

Towards Magneto-Elastomeric Nanocomposites with Supramolecular Activity

Lisa Sarah Fruhner

Schlüsseltechnologien / Key Technologies

Band / Volume 234

ISBN 978-3-95806-538-3

Forschungszentrum Jülich GmbH
Neutronen Forschung und Weiche Materie (JCNS-1)
Neutronen Forschung und Biologische Materie (IBI-8)

Towards Magneto-Elastomeric Nanocomposites with Supramolecular Activity

Lisa Sarah Fruhner

Schriften des Forschungszentrums Jülich
Reihe Schlüsseltechnologien / Key Technologies

Band / Volume 234

ISSN 1866-1807

ISBN 978-3-95806-538-3

Bibliografische Information der Deutschen Nationalbibliothek.
Die Deutsche Nationalbibliothek verzeichnet diese Publikation in der
Deutschen Nationalbibliografie; detaillierte Bibliografische Daten
sind im Internet über <http://dnb.d-nb.de> abrufbar.

Herausgeber und Vertrieb: Forschungszentrum Jülich GmbH
Zentralbibliothek, Verlag
52425 Jülich
Tel.: +49 2461 61-5368
Fax: +49 2461 61-6103
zb-publikation@fz-juelich.de
www.fz-juelich.de/zb

Umschlaggestaltung: Grafische Medien, Forschungszentrum Jülich GmbH

Druck: Grafische Medien, Forschungszentrum Jülich GmbH

Copyright: Forschungszentrum Jülich 2021

Schriften des Forschungszentrums Jülich
Reihe Schlüsseltechnologien / Key Technologies, Band / Volume 234

D 82 (Diss. RWTH Aachen University, 2020)

ISSN 1866-1807
ISBN 978-3-95806-538-3

Vollständig frei verfügbar über das Publikationsportal des Forschungszentrums Jülich (JuSER)
unter www.fz-juelich.de/zb/openaccess.



This is an Open Access publication distributed under the terms of the [Creative Commons Attribution License 4.0](https://creativecommons.org/licenses/by/4.0/),
which permits unrestricted use, distribution, and reproduction in any medium, provided the original work is properly cited.

Die vorliegende Dissertation entstand im Zeitraum von März 2016 bis Dezember 2019 im Arbeitskreis von Prof. Dr. Stephan Förster am Jülich Centre for Neutron Science, Neutronenstreuung und Weiche Materie (JCNS-1/ICS-1), bzw. dem Institut für Physikalische Chemie der RWTH Aachen, Lehrstuhl für Physikalische Chemie weicher Materie.

Eidesstattliche Erklärung

Lisa Sarah Fruhner erklärt hiermit, dass diese Dissertation und die darin dargelegten Inhalte die eigenen sind und selbstständig, als Ergebnis der eigenen originären Forschung, generiert wurden.

Hiermit erkläre ich an Eides statt

1. Diese Arbeit wurde vollständig oder größtenteils in der Phase als Doktorand dieser Fakultät und Universität angefertigt;
2. Sofern irgendein Bestandteil dieser Dissertation zuvor für einen akademischen Abschluss oder eine andere Qualifikation an dieser oder einer anderen Institution verwendet wurde, wurde dies klar angezeigt;
3. Wenn immer andere eigene- oder Veröffentlichungen Dritter herangezogen wurden, wurden diese klar benannt;
4. Wenn aus anderen eigenen- oder Veröffentlichungen Dritter zitiert wurde, wurde stets die Quelle hierfür angegeben. Diese Dissertation ist vollständig meine eigene Arbeit, mit der Ausnahme solcher Zitate;
5. Alle wesentlichen Quellen von Unterstützung wurden benannt;
6. Wenn immer ein Teil dieser Dissertation auf der Zusammenarbeit mit anderen basiert, wurde von mir klar gekennzeichnet, was von anderen und was von mir selbst erarbeitet wurde;
7. Teile dieser Arbeit wurden zuvor veröffentlicht und zwar in:
 - A. Feld, R. Koll, L. S. Fruhner, M. Krutyeva, W. Pyckhout-Hintzen, C. Weiß, H. Heller, A. Weimer, C. Schmidtke, M. S. Appavou, E. Kentzinger, J. Allgaier, H. Weller, *ACS Nano* **2017**, *11*, 3767.
 - R. Koll, L. S. Fruhner, H. Heller, J. Allgaier, W. Pyckhout-Hintzen, M. Kruteva, A. Feoktystov, R. Biehl, S. Förster, H. Weller, *Nanoscale* **2019**, *11*, 3847.
 - M. Rafipoor, R. Koll, J. Merkl, L. S. Fruhner, H. Weller, H. Lange, *Small* **2019**, *15*, 1803798.

Datum

Unterschrift

Abstract

Combining the functionality of nanoparticles and polymers leads to a novel class of materials: nanocomposites. Nanoparticles like magnetic nanoparticles or quantum dots (QDs) can be used to introduce new properties into polymeric matrices. This could be the response to a magnetic field or photoluminescence. Polymers can provide stability, add elasticity or an improved processability, they can be functionalised by supramolecular groups to allow non-permanent bonds between the polymer chains. The combination of those properties makes nanocomposites deeply interesting for a range of applications like coatings, membranes, organic solar cells or biomedicine. The additional structuring of nanoparticles within the polymer matrix allows for an even wider range of tuneable properties.

Obtaining stable nanocomposites in external fields is highly desirable but challenging due to the usually encountered aggregation of nanoparticles in polymer matrices. Therefore, compatibilization of the two components is essential to study their controlled spatial organisation. The aim of this work is the development of a route towards magneto-elastomeric nanocomposites with supramolecular activity. For this, functional nanocomposites are synthesised, and their structure characterised by small-angle scattering methods. First, the behaviour of superparamagnetic, oleic acid stabilised iron oxide nanoparticles, in a magnetic field is investigated by small-angle neutron scattering (SANS). It is found that already at low magnetic fields, the nanoparticles form chains, which are aligned parallel to the magnetic field while crystalline phases dominate the measured structures at higher field strengths. To be able to make use of this behaviour in a nanocomposite, a compatibilization of the nanoparticles and the polymer matrix is necessary. The solution developed here, relies on the coating of the nanoparticles with a polymer shell.

This is achieved in the second part of this thesis by encapsulating the nanoparticles with a polydiene-poly(ethylene oxide) (PEO) diblock copolymer. In this process the polydiene forms a cross-linkable inner shell to chemically fixate the polymer around the nanoparticle. The PEO corona allows the dispersion of the nanoparticles in water or PEO melt. Small-angle X-ray scattering (SAXS) is used to investigate the encapsulation procedure, showing that the critical step is the phase transfer from organic medium to water, and the final nanocomposites, revealing well-dispersed nanoparticles in the polymer melt. The same encapsulation procedure is used to create clusters of QDs whose distances can be tuned by different polymer sizes. The polymer shell enabled long-term stability of these materials and high-power excitations.

Finally, shifting the focus towards elastic and supramolecular materials, a polymer shell with hydrogen bonding groups is targeted. As the encapsulation procedure explained above only works for PEO based materials, another method has to be developed, in which poly(butylene oxide) PBO was chosen as the nanoparticle coating. The synthesis of these polymers involved the polymerisation of butylene oxide onto an initiator carrying a protective group and the subsequent independent functionalisation of both ends of the polymer chain with anchor group, binding to the nanoparticle surface, and hetero-associating supramolecular groups diaminotriazine (DAT) and thymine. First results showed that coating the nanoparticles with these polymeric ligands results in supramolecular interactions between DAT and thymine functionalised nanoparticles as revealed by SAXS studies and microscopy.

Kurzzusammenfassung

Die Kombination der Funktionalitäten von Nanopartikeln und Polymeren führt zu einer neuen Klasse an Materialien: Nanokomposite. Nanopartikel wie magnetische Nanopartikel oder Quantum Dots (QDs) können genutzt werden, um neue Eigenschaften in Polymermatrizen einzubringen. Dies können z.B. die Reaktion auf ein Magnetfeld sein oder Photolumineszenz sein. Polymers können für Stabilität oder Elastizität sorgen oder einfachere Verarbeitbarkeit, sie können mit supramolekularen Gruppen funktionalisiert werden, die nicht-permanente Bindungen zwischen den Polymerketten erlauben. Die Kombination dieser Eigenschaften macht Nanopartikel höchst interessant für eine Vielzahl von Anwendungen wie Beschichtungen, Membranen, organische Solarzellen oder Biomedizin. Die zusätzliche Strukturierung der Nanopartikel innerhalb der Polymermatrix ermöglicht eine noch größere Bandbreite an einstellbare Eigenschaften.

Stabile Nanokomposite in äußeren Felder zu erhalten ist äußerst wünschenswert aber auch herausfordernd aufgrund der üblicherweise vorliegenden Aggregation von Nanopartikeln in Polymermatrizen. Daher ist eine Kompatibilisierung der beiden Komponenten essentiell, um ihre kontrollierte räumliche Organisation zu untersuchen. Das Ziel dieser Arbeit ist es, einen Prozess zu magneto-elastomerischen Nanokompositen mit supramolekularer Aktivität zu entwickeln. Dafür werden funktionale Nanokomposite synthetisiert und ihre Struktur mit Kleinwinkelstreuungsmethoden untersucht. Zuerst wird das Verhalten von superparamagnetischen, Ölsäure stabilisierten Eisenoxid-Nanopartikeln in einem Magnetfeld mit Kleinwinkelneutronenstreuung untersucht. Dabei wird gezeigt, dass die Nanopartikel bereits in sehr schwachen Magnetfeldern Ketten bilden, die parallel zum Feld angeordnet sind, während kristalline Phasen die gemessenen Strukturen bei höheren Feldstärken dominieren. Um dieses Verhalten im Nanokomposit nutzen zu können, ist eine Kompatibilisierung der Nanopartikel mit der Polymermatrix nötig. Die hier entwickelte Lösung beruht auf der Beschichtung der Nanopartikel mit einer Polymerhülle.

Dies wird im zweiten Teil der Arbeit durch Verkapseln der Nanopartikel mit einem Polydien-Polyethylenoxid (PEO) Diblockcopolymer erreicht. In diesem Prozess bildet das Polydien eine vernetzbare innere Hülle, um das Polymer chemisch um den Nanopartikel herum zu fixieren. Die PEO-Korona ermöglicht die Dispersion der Nanopartikel in Wasser oder PEO-Schmelze. Kleinwinkelröntgenstreuung wird genutzt, um den Prozess der Verkapselung zu untersuchen und zeigt, dass der kritische Schritt der Phasentransfer aus dem organischen

Medium ins Wasser ist. Die Untersuchung der finalen Nanokomposite zeigt gut verteilte Nanopartikel in der Polymerschmelze. Derselbe Prozess kann verwendet werden, um Cluster von QDs zu erzeugen, deren Abstand durch verschieden lange Polymere variiert werden kann.

Der letzte Teil rückt den Fokus auf elastische und supramolekulare Materialien und zielt auf eine Polymerhülle mit funktionalen Gruppen ab, die Wasserstoffbrücken ermöglichen. Da die oben beschriebene Verkapselungsmethode auf PEO basierenden Materialien beruht, wurde eine andere Methode entwickelt, in der Polybutylenoxid (PBO) als Nanopartikelbeschichtung verwendet wird. Die Synthese des Polymers beinhaltet die Polymerisation von Butylenoxid auf einen Initiator, der eine Schutzgruppe trägt, sowie die konsekutive und unabhängige Funktionalisierung beider Kettenenden mit einer Kopfgruppe, die auf die Nanopartikeloberfläche bindet bzw. die heteroassoziierenden supramolekularen Gruppen Diaminotriazin (DAT) und Thymin (Thy). Erste Ergebnisse aus Untersuchungen mit Kleinwinkelröntgenstreuung und Mikroskopie zeigen, dass das Beschichten von Nanopartikeln mit diesen Polymerliganden zu supramolekularen Wechselwirkungen zwischen den Thy- und DAT-beschichteten Nanopartikeln führt.

Table of Contents

<i>Abstract</i>	<i>VII</i>
<i>Kurzzusammenfassung</i>	<i>IX</i>
<i>Abbreviations</i>	<i>XV</i>
1 Introduction	1
1.1 References	4
2 Theoretical Principles	7
2.1 Nanoparticles	7
2.1.1 Magnetic Nanoparticles	9
2.1.2 Quantum Dots	11
2.2 Polymers	14
2.2.1 Supramolecular Polymers	17
2.3 Polymeric nanocomposites	18
2.3.1 Supramolecular Nanocomposites	20
2.4 References	21
3 Small-Angle Scattering	27
3.1 Basics of Scattering Theory	27
3.2 Small-Angle Scattering Experiments	37
3.3 References	42
4 Self-Assembly of Iron Oxide Nanocrystals in Magnetic Fields up to 3 T Studied by Small-Angle Neutron Scattering	43
4.1 Introduction	44
4.2 Results and Discussion	45
4.2.1 Structural exploration	45
4.2.2 Searching for Phase Transition	56
4.3 Conclusion	63
4.4 Materials and Methods	64
4.4.1 Transmission Electron Microscopy (TEM)	64
4.4.2 Small-Angle X-Ray Scattering (SAXS)	64
4.4.3 Small-Angle Neutron Scattering (SANS)	65

4.5	References	66
5	<i>Nanocomposites of Highly Monodisperse Encapsulated Superparamagnetic Iron Oxide Nanocrystals Homogeneously Dispersed in a Poly(ethylene Oxide) Melt</i>	69
5.1	Abstract	71
5.2	Introduction	71
5.3	Results and Discussion	73
5.3.1	Encapsulation of SPIONs	73
5.3.2	Dispersion Properties of AIBN Cross-Linked Polydiene Shells.....	74
5.3.3	Dispersion Properties of HDT-AIBN Cross-Linked Shells.....	76
5.3.4	Step-by-Step Characterization of the Encapsulation Reactions	79
5.3.5	TEM Investigations of SPION Shell in Aqueous solution.....	81
5.3.6	Chemical Composition of the Block Copolymer Coated SPIONs.....	84
5.4	Conclusion	85
5.5	Materials and Methods	86
5.5.1	Materials	86
5.5.2	Polymer Synthesis.....	86
5.5.3	Polymer Characterisation.....	88
5.5.4	Encapsulation of SPIONs and Dispersing into a PEO Matrix	89
5.5.5	Transmission Electron Microscopy (TEM).....	89
5.5.6	Elemental Analysis.....	90
5.6	Acknowledgements	90
5.7	References	91
6	<i>Creating a synthetic platform for the encapsulation of nanocrystals with covalently bound polymer shells</i>	95
6.1	Abstract	97
6.2	Introduction	97
6.3	Results and Discussion	98
6.3.1	Encapsulation of SPIONs	98
6.3.2	Examination of different crosslinking pathways	99
6.3.3	Variation of the diblock copolymer chain length.....	103
6.3.4	Attachment of supramolecular group to SPIONs.....	110
6.3.5	Attempts to exchange of PEO in the diblock copolymer	112
6.3.6	Investigation of the ligand exchange step	113

6.4	Experimental	115
6.4.1	Materials	115
6.4.2	Polymer synthesis	116
6.4.3	Polymer characterisation	119
6.4.4	Encapsulation of SPIONs and nanocomposite synthesis	120
6.4.5	Transmission electron microscopy (TEM)	121
6.4.6	Small angle X-ray scattering (SAXS)	121
6.4.7	Small angle neutron scattering (SANS)	121
6.5	Conclusions	122
6.6	Acknowledgements	123
6.7	Supporting Information.....	124
6.8	References	128
7	<i>Resonant Energy Transfer can Trigger Multiexciton Recombination in Dense Quantum Dot Ensembles</i>	<i>131</i>
7.1	Abstract.....	132
7.2	Introduction	132
7.3	Conclusions	152
7.4	Experimental Section	152
7.4.1	Materials	152
7.4.2	Micellar Encapsulation.....	153
7.4.3	Sample Characterisation	153
7.4.4	SAXS.....	153
7.4.5	Optical Spectroscopy	154
7.5	Acknowledgements	154
7.6	References	155
8	<i>Synthesis and Characterisation of Polymer Coated Supramolecular Magnetic Nanocrystals.....</i>	<i>159</i>
8.1	Introduction	160
8.2	Results and Discussion	162
8.2.1	Synthesis of DETA-PBO5k-Thy and DETA-PBO5k-DAT	162
8.2.2	Nanocomposites and self-assembly	172
8.3	Conclusion and Outlook.....	179

8.4	Materials and Methods	181
8.4.1	Nanocrystal synthesis	181
8.4.2	Polymer synthesis	181
8.4.3	Exchange of oleic acid against the (supramolecular) polymer ligands	185
8.4.4	Polymer characterisation:	186
8.4.5	Transmission electron microscopy (TEM)	186
8.4.6	Dynamic light scattering (DLS).....	187
8.4.7	Small-angle X-ray scattering (SAXS)	187
8.5	Acknowledgements	187
8.6	Supporting Information.....	188
8.7	References	200
9	<i>Conclusion and Outlook</i>	203
9.1	References	207
	<i>Acknowledgements</i>	209
	<i>Curriculum Vitae</i>	213

Abbreviations

18C6	crown ether 18-crown-6
AIBN	2,2'azobis(2-methylpropionitrile)
bcc	body-centred cubic
bct	body centered tetragonal
BO	1,2-butylene oxide
CaH ₂	calcium hydride
CDI	1,1'-carbonyldiimidazole
CdS	cadmium sulfide
CdSe	cadmium selenide
DAT	4,6-diamino-1,3,5-triazine
DAT-F	2-fluoro-4,6-diamino-1,3,5-triazine
DETA	diethylenetriamine
DEVP	diethyl vinylphosphonate
DFG	Deutsche Forschungsgemeinschaft
DIPEA	<i>N,N</i> -diisopropylethylamine
DLS	dynamic light scattering
DMA	<i>N,N</i> -dimethylacetamide
DMF	<i>N,N</i> -dimethylformamide
DMPA	2,2-dimethoxy-2-phenyl-acetophenone
DNA	deoxyribonucleic acid
EMA	European Medicines Agency
FDA	US Food and Drug Administration
FRET	Förster resonance energy transfer
FRMII	Forschungs-Neutronquelle Heinz Maier-Leibnitz
GALAXI	gallium anode low angle X-ray instrument
HDT	1,6-hexanedithiol
HPA	hexylphosphonic acid
ISO	International Organization for Standardization
IUPAC	International Union of Pure and Applied Chemistry
KOtBu	potassium <i>tert</i> -butoxide
LED	light-emitting diode
MLZ	Heinz Maier-Leibnitz Zentrum

MNPs	magnetic nanoparticles
NC	nanocrystal
NMR	nuclear magnetic resonance
OA	oleic acid
ODPA	octadecylphosphonic acid
PA	phosphonic acid
PB	polybutadiene
PBO	poly(butylene oxide)
Pd/C	palladium/charcoal activated
PEO	poly(ethylene oxide)
PET	poly(ethylene terephthalate)
PI	polyisoprene
PL	photoluminescence
QDs	quantum dots
QRs	quantum rods
RMSD	root mean squared displacement
SANS	small-angle neutron scattering
SAS	small-angle scattering
SAXS	small-angle X-ray scattering
SEC	size exclusion chromatography
SLD	scattering length density
SPIONs	superparamagnetic iron oxide nanoparticles
TA	transient absorption
TBAF	tetrabutylammonium fluoride
TBTU	<i>o</i> -(benzotriazole-1-yl)- <i>N,N,N',N'</i> -tetramethyluronium tetrafluoroborate
TEM	transmission electron microscopy
THF	tetrahydrofuran
Thy	thymine
ThyAcOH	thymine-1-acetic acid
TNT	trinitrotoluene
UV	ultraviolet

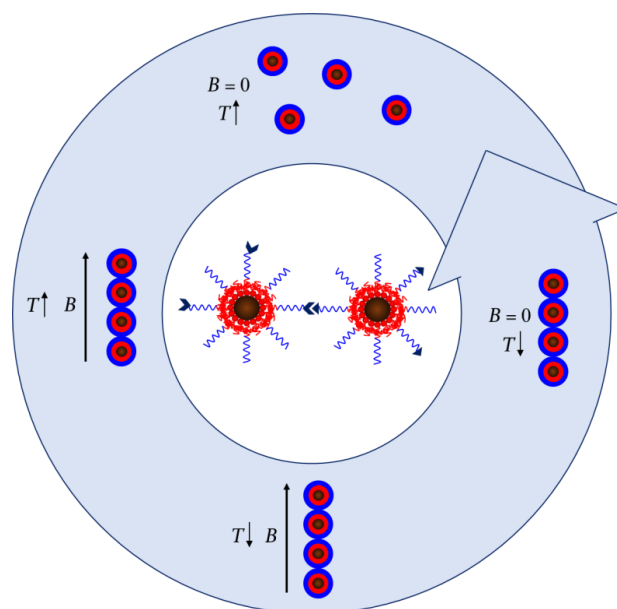
1 Introduction

Nowadays and probably unbeknownst to most people, our everyday life is inherently supported by functional materials based on composite structures. One of the best-known examples is reinforced concrete, which allows us to build higher and more durable buildings. Yet the employment of composite materials is beneficial for our lives and wallets also in much smaller length scales. Coatings and packaging made of nanocomposites usually outperform their classic counterparts, as the additives for example increase the barrier properties of the materials.^[1] Keeping the air inside a tennis ball or the carbon dioxide inside a PET soda bottle increases the shelf life of these products.^[2,3] In addition, cultural heritage like the last judgment mosaic in Prague is conserved thanks to nanocomposite coatings.^[2] In airplanes or cars, a lot of materials already consist of polymeric nanocomposites as they surpass materials based on metal due to their light weight, saving a considerable amount of fuel during the lifetime of these means of transportation.^[4,5]

Nanomaterials are not solely synthetically produced materials as various representatives of this class of materials can be found in nature. One example are clay minerals which typically have a thickness of a few nanometre with the other two dimensions in the micrometre range. Stacks of hundreds or thousands of these layers are held together by van der Waals and electrostatic forces.^[6-9] Without any kind of knowledge about them, nanomaterials have already been used during ancient and medieval times, resulting in intriguingly colourful products like stained glass in church windows, Maya blue or the famous Lycurgus cup.^[10,11] The industrial production of nanomaterials started in the 20th century by adding carbon black nanoparticles to car tires.^[10] This is also a great example for the advantages of a composite material: not only is the carbon black responsible for the typical colour of the tires, which would be milky white otherwise, but also does it increase the durability and therefore the lifetime of the tire. From this example it can be learned that the combination of different materials leads to products which outperform the individual components. In addition, nanocomposites are superior compared to micro- or neat counterparts due to the availability of large numbers of nanoparticles with huge interfacial areas and confinement of polymer chains at the nano-level.^[12]

In the centre of interest are multifunctional nanocomposites due to their broad range of applications including flame retardants, smart coatings, organic solar cells and

(bio)medicine.^[11,13-18] This work presents a pathway towards magneto-elastomeric nanocomposites with supramolecular activity (Scheme 1.1). Magnetic nanoparticles in a polymeric matrix can be aligned in a magnetic field, reinforcing the composite by chain formation. Similarly, depending on the chosen polymer matrix, structures can be introduced by shearing the system. Without external field or mechanical force, the so obtained structures will simply dissolve. This can be prevented by forming bonds between the nanoparticles to stabilise the structures. Compared to covalent bonds, supramolecular bonds like hydrogen bonds are advantageous as they enable the rebuilding of the structures. At elevated temperatures the bonds are broken, and structure formation can be induced. Cooling down the material then freezes the structures. If necessary, the bonds can be broken again to restart the cycle.



Scheme 1.1 The envisioned functionality of magneto-elastomeric nanocomposites with supramolecular activity. Nanoparticles encapsulated in a polymer shell are aligned in a magnetic field. The structures can be “frozen” by non-permanent connections between the particles to stabilize the structures even without applied field. Raising the temperature breaks up the nanoparticle structures to restart this cycle.

Several steps are necessary to obtain these materials: investigating the structure formation of magnetic nanoparticles in magnetic fields, encapsulating the nanoparticles with a polymer shell to make them miscible with a polymeric matrix, attaching supramolecular groups to the nanoparticles and studying the interactions between the nanoparticles because of these functionalities.

Superparamagnetic iron oxide nanoparticles can be synthesised in large quantities and high qualities, especially regarding their monodispersity^[19] which is a key factor for defined magnetic properties. In addition, they are considered as safe-to-use and are already employed for various medical applications.^[20] The self-assembly of magnetic nanoparticles is by itself an important research topic as it is a bottom-up approach towards applications like high density data storage^[21,22] or artificial cilia actuated by magnetic fields^[23]. The first part of this thesis will display the investigation of structures formed by iron oxide nanoparticles in magnetic fields up to 3 T using small-angle neutron scattering. When combining nanoparticles with a polymeric matrix, the properties of the nanocomposite can be influenced by an external magnetic field.^[24-26] It is of utmost importance to achieve a homogeneous dispersion of the nanoparticles within the surrounding matrix as the nanocomposite properties strongly depend on the local organisation of the nanoparticles.^[27]

Coating the nanoparticles with a brush-like layer of the polymer is a suitable method to make those two materials miscible.^[28] To prevent aggregation of the nanoparticles, a tightly bound polymer shell around them is highly desirable. In addition, a versatile process that can be used for various systems of nanoparticles is targeted. In the second part of this thesis, an encapsulation procedure based on amphiphilic diblock copolymers which can partially be crosslinked is developed to obtain stable and well-dispersed nanoparticles in a polymer matrix. The resulting encapsulated nanoparticles and the final nanocomposite are investigated by small-angle scattering methods, revealing the structure of the nanoparticle and their polymer shell as well as the dispersion state of the materials.

Fundamental as well as application-oriented research is conducted towards the exploration of supramolecular nanocomposites and potential applications like artificial skin, sensors, drug delivery or artificial nacre have already been discussed in the literature.^[29-35] To study the interactions of polymer coated nanoparticles which carry hydrogen bonding groups, a synthesis protocol for an α,ω -functionalised polymer ligand needs to be worked out which is presented in the last part of this work.

Next to complementary methods like microscopy, the main investigation method used in this work is small-angle scattering (SAS) utilising the contrast of the different components. Small-angle X-ray scattering (SAXS) is employed to study the iron oxide core of the nanoparticles and the aggregation behaviour of the nanocomposite materials. To obtain information about the surfactant or polymer shell, as well as the structure formation, small-angle neutron scattering (SANS) is used due to the favourable contrast for organic materials and the higher transmission for highly packed nanoparticle systems.

1.1 References

- [1] A. Dasari, Z.-Z. Yu, Y.-W. Mai, in *Polym. Nanocomposites Towar. Multi-Functionality* (Ed: B. Derby), Springer London, London, **2016**, pp. 279–297.
- [2] C. Sanchez, B. Julián, P. Belleville, M. Popall, *J. Mater. Chem.* **2005**, *15*, 3559.
- [3] P. Anadão, in *Nanocomposites - New Trends Dev.* (Ed: F. Ebrahimi), InTech, Rijeka, **2012**.
- [4] J. Baur, E. Silverman, *MRS Bull.* **2007**, *32*, 328.
- [5] J. M. Garcés, D. J. Moll, J. Bicerano, R. Fibiger, D. G. McLeod, *Adv. Mater.* **2000**, *12*, 1835.
- [6] H. H. Murray, in *Appl. Clay Mineral. Occur. Process. Appl. Kaolins, Bentonites, Palygorskite-Sepiolite, Common Clays* (Ed: H.H. Murray), Elsevier B.V., Amsterdam, **2006**, pp. 7–31.
- [7] P. LeBaron, *Appl. Clay Sci.* **1999**, *15*, 11.
- [8] M. F. Brigatti, E. Galan, B. K. G. Theng, in *Handb. Clay Sci.* (Eds: F. Bergaya, B.K.G. Theng, G. Lagaly), Elsevier B.V., Amsterdam, **2006**, pp. 19–86.
- [9] K. A. Carrado, A. Decarreau, S. Petit, F. Bergaya, G. Lagaly, in *Handb. Clay Sci.* (Eds: F. Bergaya, B.K.G. Theng, G. Lagaly), Elsevier B.V., Amsterdam, **2006**, pp. 115–139.
- [10] S. Horikoshi, N. Serpone, in *Microwaves Nanoparticle Synth.*, Wiley-VCH Verlag GmbH & Co. KGaA, Weinheim, Germany, **2013**, pp. 1–24.
- [11] P. Gómez-Romero, C. Sanchez, *Functional Hybrid Materials*, Wiley-VCH, **2004**.
- [12] A. Dasari, Z.-Z. Yu, Y.-W. Mai, in *Polym. Nanocomposites Towar. Multi-Functionality* (Ed: B. Derby), Springer London, London, **2016**, pp. 1–4.
- [13] M. Salavati-Niasari, D. Ghanbari, in *Adv. Divers. Ind. Appl. Nanocomposites* (Ed: B. Reddy), InTech, London, **2011**, pp. 501–520.
- [14] S. Bhattacharya, S. K. Samanta, *Chem. Rev.* **2016**, *116*, 11967.
- [15] Z. Tang, C. He, H. Tian, J. Ding, B. S. Hsiao, B. Chu, X. Chen, *Prog. Polym. Sci.* **2016**, *60*, 86.
- [16] N. Erathodiyil, J. Y. Ying, *Acc. Chem. Res.* **2011**, *44*, 925.
- [17] G. Kaur, R. Adhikari, P. Cass, M. Bown, P. Gunatillake, *RSC Adv.* **2015**, *5*, 37553.

-
- [18] A. J. T. Teo, A. Mishra, I. Park, Y.-J. Kim, W.-T. Park, Y.-J. Yoon, *ACS Biomater. Sci. Eng.* **2016**, *2*, 454.
- [19] J. Park, K. An, Y. Hwang, J.-G. Park, H.-J. Noh, J.-Y. Kim, J.-H. Park, N.-M. Hwang, T. Hyeon, *Nat. Mater.* **2004**, *3*, 891.
- [20] M. Colombo, S. Carregal-Romero, M. F. Casula, L. Gutiérrez, M. P. Morales, I. B. Böhm, J. T. Heverhagen, D. Prospero, W. J. Parak, *Chem. Soc. Rev.* **2012**, *41*, 4306.
- [21] D. Speliotis, *J. Magn. Magn. Mater.* **1999**, *193*, 29.
- [22] A. K. Boal, in *Nanoparticles Build. Blocks Nanotechnol.* (Ed: V.M. Rotello), Springer Science+Business Media, New York, **2004**, pp. 1-27.
- [23] J. J. Benkoski, R. M. Deacon, H. B. Land, L. M. Baird, J. L. Breidenich, R. Srinivasan, G. V. Clatterbaugh, P. Y. Keng, J. Pyun, *Soft Matter* **2010**, *6*, 602.
- [24] J. Belardi, N. Schorr, O. Prucker, J. Rühle, *Adv. Funct. Mater.* **2011**, *21*, 3314.
- [25] J. Hussong, N. Schorr, J. Belardi, O. Prucker, J. Rühle, J. Westerweel, *Lab Chip* **2011**, *11*, 2017.
- [26] S. N. Khaderi, C. B. Craus, J. Hussong, N. Schorr, J. Belardi, J. Westerweel, O. Prucker, J. Rühle, J. M. J. den Toonder, P. R. Onck, *Lab Chip* **2011**, *11*, 2002.
- [27] C. Chevigny, F. Dalmas, E. Di Cola, D. Gigmes, D. Bertin, F. Boué, J. Jestin, *Macromolecules* **2011**, *44*, 122.
- [28] S. Ehlert, S. M. Taheri, D. Pirner, M. Drechsler, H.-W. Schmidt, S. Förster, *ACS Nano* **2014**, *8*, 6114.
- [29] C. Hou, T. Huang, H. Wang, H. Yu, Q. Zhang, Y. Li, *Sci. Rep.* **2013**, *3*, 3138.
- [30] B. C. K. Tee, C. Wang, R. Allen, Z. Bao, *Nat. Nanotechnol.* **2012**, *7*, 825.
- [31] Y. Chen, W. Cheng, L. Teng, M. Jin, B. Lu, L. Ren, Y. Wang, *Macromol. Mater. Eng.* **2018**, *303*, 1700660.
- [32] G. Cai, J. Wang, K. Qian, J. Chen, S. Li, P. S. Lee, *Adv. Sci.* **2017**, *4*, 1600190.
- [33] J. Cao, C. Lu, J. Zhuang, M. Liu, X. Zhang, Y. Yu, Q. Tao, *Angew. Chemie Int. Ed.* **2017**, *56*, 8795.
- [34] X. Ran, Q. Qu, X. Qian, W. Xie, S. Li, L. Li, L. Yang, *Sensors Actuators B Chem.* **2018**, *257*, 362.
-

- [35] Y. Wang, T. Li, P. Ma, S. Zhang, H. Zhang, M. Du, Y. Xie, M. Chen, W. Dong, W. Ming, *ACS Nano* **2018**, *12*, 6228.

2 Theoretical Principles

2.1 Nanoparticles

Nanoparticles are defined by the International Organization for Standardization (ISO) as “nano-object(s) (...) with all external dimensions in the nanoscale (...) where the lengths of the longest and the shortest axes of the nano-object do not differ significantly”.^[1] The word fragment “nano” is derived from the Greek word “nanos” meaning dwarf. Nanoscale represents length scales typically in the range of 1 to 100 nm which corresponds to 10^{-9} to 10^{-7} m.^[1]

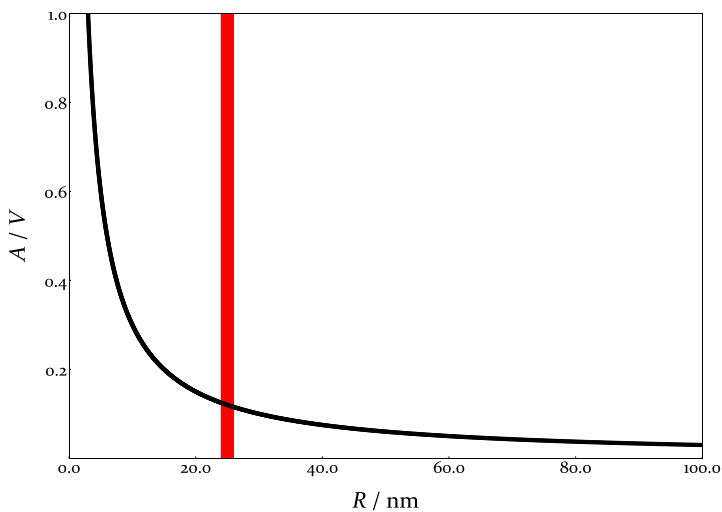


Figure 2.1 The surface to volume ratio of a spherical nanoparticle as a function of its radius R . The red line demonstrates the critical size at which properties tend to change.

Due to their size, nanoparticles are considered as intermediates between the bulk material and single atoms or molecules.^[2] Their properties often differentiate from the bulk material, the critical size for the change in properties is around 20-30 nm.^[3,4] Examples for this are the melting point of nanoparticles compared to their respective bulk counterparts^[5], superparamagnetism of magnetic nanoparticles^[4] or the biocidal activity of silver nanoparticles which is non-existent in bulk silver^[6]. Properties can also be strongly size-dependent for the nanoparticles themselves; the electroluminescence of semi-conductor nanoparticles can

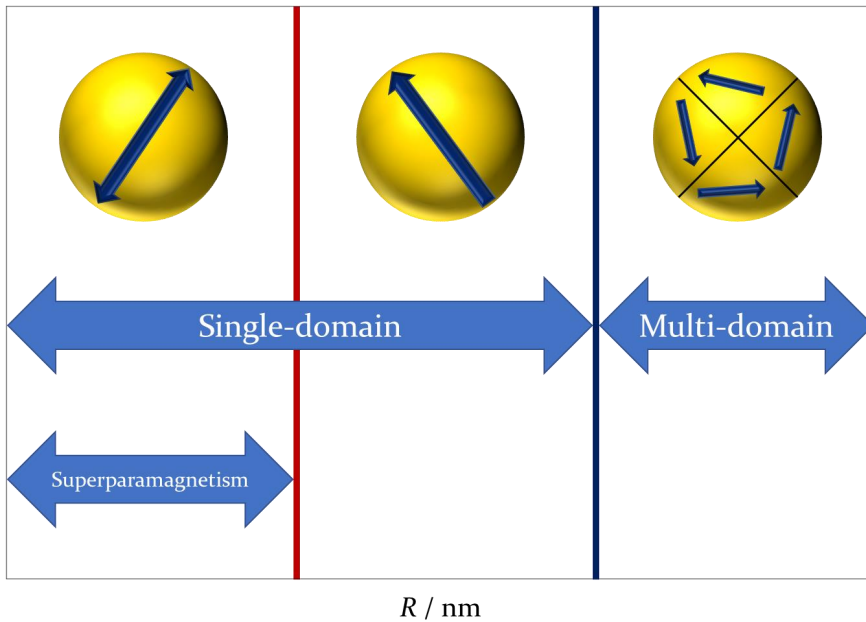
already be tuned by small changes in size.^[2,4] One reason for these effects is the high surface-to-volume ratio in nanoparticles (Figure 2.1). Reducing the size of an object immediately leads to an increase of the fraction of its surface atoms.^[3]

There are various procedures for the synthesis of nanoparticles. Generally, they can be divided into two approaches: top-down and bottom-up. Top-down describes the breakdown of a solid material into small particles, for example by grinding or ultrasonication. Bottom-up can be understood as the formation of particles starting from single atoms or molecules. This can happen in the solid phase by chemical or physical vapor deposition or in the liquid phase where numerous processes like solvothermal synthesis, sol-gel, co-precipitation or hydrolysis are well-known. The most important factors for nanoparticle synthesis are the control over shape, size, size distribution, chemical composition and crystal structure, their stability as well as high yields at low costs and a good reproducibility. These factors vary between the different synthesis procedures.^[7] For the nanoparticles used in this work, thermal decomposition was chosen as synthesis method as it allows the precise control of size and shape of the nanoparticles which is important for the target materials described here. It is done by controlled heating of a precursor material until it decomposes. The single atoms then start to form clusters which grow into nanoparticles. One key parameter is the presence of surfactants in the reaction mixture as they stabilise the intermediate clusters as well as the final nanoparticles. The used surfactants must be chosen carefully as their binding strength to the atoms which form the nanoparticles must be neither too large nor too small. A too high affinity between the surfactant and the surface would prohibit the growth of the cluster and a too low affinity results in aggregates.^[2] Changing the parameters of this reaction (surfactant and its amount, end temperature, reaction time, heat rate etc.) allows precise control over size and shape of the nanoparticles.^[8-10]

Usually, surface modification of the nanoparticles is necessary to stabilise them against aggregation in a medium which can for example be a solvent or a polymer melt. Additional reasons for modifications are applications where self-assembly into one, two or three dimensions is required to achieve certain properties.^[4] Typical methods for surface modification is the grafting of surfactants or polymer ligands, the adsorption of charged molecules or the attachment of biological molecules.^[4]

2.1.1 Magnetic Nanoparticles

Magnetic nanoparticles (MNPs) are nanoparticles that react to magnetic fields. Due to their numerous possible applications, they have been extensively studied in recent years.^[11] Examples for typical applications of MNPs are ferrofluids, magnetic data storage arrays, magneto-optical switches, novel photoluminescent materials and biomedicine where they are used for biosensors, for tumour treatment by magnetic hyperthermia or as contrast agents for MRI among other applications.^[8,11,12] MNPs usually are either metallic nanoparticles or oxides, mostly ferrites. They do not reach the saturation magnetisation of their bulk counterparts because of the disorder of the spins at the surface of the nanoparticles.^[13] However, due to their size, they have other unique properties.



Scheme 2.1 Size-dependent magnetic properties of MNPs.

The magnetic properties of MNPs strongly depend on their size (Scheme 2.1). Above a critical diameter, the magnetic structure is divided into Weiss domains. Decreasing the size leads to only a single domain remaining in the MNP with the magnetisation along a certain direction of the crystal. For smallest MNPs, the magnetisation becomes instable, it can flip by 180° due to thermal energy. This behaviour is known as superparamagnetism.^[13] Although each particle might be ferromagnetic, the particles together behave as a paramagnetic material. They

are magnetised uniformly along an applied magnetic field but lose this magnetisation due to thermal fluctuation without external field.^[14] The main contrast to classical paramagnets is the high magnetic moment of superparamagnetic particles in a magnetic field which leads to a high susceptibility. At room temperature, no hysteresis can be found in their magnetisation curve as the particles are in thermal equilibrium.^[15] However, at low temperatures, the thermal energy is not sufficient to flip the magnetisation of the particles and therefore, they show the typical hysteresis of a ferromagnetic material.^[16,17] The temperature that divides these two states is called the blocking temperature T_B , it depends for example on the nanoparticles' size, chemical composition and anisotropy. Applying an alternating magnetic field to superparamagnetic nanoparticles can lead to two different responses of the MNPs: above T_B the magnetic moment within the MNP flips (Néel relaxation), below T_B the particle itself rotates with the field direction (Brown relaxation). The latter effect is used for magnetic hyperthermia where the mechanical movement of the MNPs creates heat due to friction.^[12]

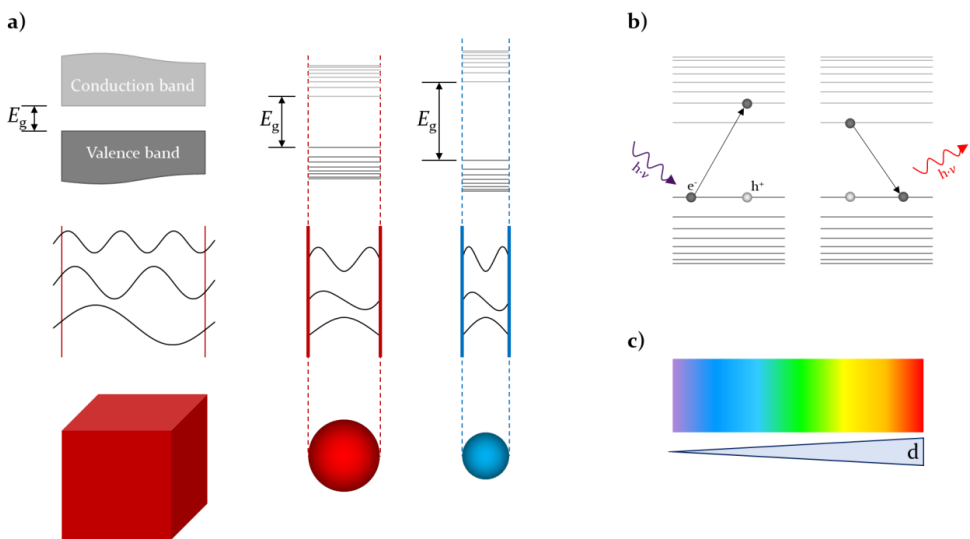
Iron oxide nanoparticles are the most common MNPs, especially as superparamagnetic iron oxide nanoparticles (SPIONs). Not only are iron oxides the longest used permanent magnets in human history but iron also surpasses all other magnetic elements in abundance by far.^[18] Next to applications in other fields, iron oxide nanoparticles are the number one MNPs for bioapplications due to their biocompatibility.^[8] Both the US Food and Drug Administration (FDA) and the European Medicines Agency (EMA) permit the medical use of these nanoparticles.^[12] Next to magnetic hyperthermia, they fulfil important roles in medicine as drug carriers and contrast agents.^[8]

The most important synthesis procedure for MNPs is thermal decomposition due to the control over size, shape and composition which is essential for the design of smart nanomaterials.^[8] For applications like high-density data storage^[19], electrical transport or magnetic switching^[20], the ordering of the MNPs is of utmost importance. Field-directed self-assembly is a widely used bottom-up approach to obtain 1-, 2- or 3-dimensional structures of MNPs.^[21] In a large enough magnetic field, MNPs are theoretically and experimentally known to form chain-like structures with head-to-tail configuration of their dipoles.^[22,23]

2.1.2 Quantum Dots

Next to magnetic properties, there are several other properties of nanoparticles that depend strongly on their size. One example for this is the quantum confinement in semiconducting nanoparticles which leads to their well-known labelling as quantum dots (QDs).

Although quantum dots have already been discovered by Ekimov^[24] and Brus^[25] in 1981 and 1983 respectively, the term “quantum dot” has only been used since 1986^[26]. Quantum dot on the one hand reflects on the dimensions of the particle which are theoretically described as point like (zero dimensional system) and on the other hand originates in the quantisation of its energy levels.^[2] As this is comparable to atoms, QDs are often described as “artificial atoms”.^[27,28] A common approach to explain this quantisation is to start from the bulk material and decrease all three dimensions to a few nanometers.



Scheme 2.2 Electronic structure of Quantum Dots; a) Comparison between a bulk semiconductor and a QD and the size dependence of the band gap; b) exciton creation by absorption of light and resulting fluorescence; c) colour spectrum of QDs with a band gap of visible light and its size-dependence.

In bulk semiconductors the electrons are delocalised and considered as “free electron gas”.^[2] As their wavelengths are much smaller than the dimensions of the bulk material, periodic boundary conditions can be assumed. This is a mathematical concept to create an “infinite solid”, meaning that an electron near the border of the solid is not affected by it. The possible energy states for the electrons are quasi-continuous and are usually described as the

valence band, which is filled with electrons, and its empty counterpart, the conduction band. The energy gap E_g between them obtains values between a fraction of an eV up to a few eV.^[2,29]

For QDs, the periodic boundary condition is no longer valid as the wavelength of the electrons is in the range of the diameter of the QD. The electrons are therefore confined inside the QD, they can be considered as a particle trapped inside a “box”. While the potential energy inside of this box is zero, it is infinite at the walls. So, only wave functions which vanish at the walls are allowed, leaving only discrete levels of the energy.

Exciting an electron from the valence band into the conduction band creates a hole in the valence band. The couple of electron and hole is called an exciton. For the generation of an exciton, the minimum energy required is the gap energy of the QD, $E_g(\text{dot})$, which is the sum of the gap energy of the bulk material $E_g(\text{bulk})$, the confinement energy E_{well} and the Coulomb interaction between electron and hole, E_{Coul} :

$$E_g(\text{dot}) = E_g(\text{bulk}) + E_{\text{well}} + E_{\text{Coulomb}} = E_g(\text{bulk}) + \frac{h^2}{2m^*d^2} - \frac{1.8e^2}{2\pi\epsilon\epsilon_0d} \quad (2.1)$$

With h as Planck’s constant, m^* the reduced mass of the exciton which consists of the mass of the electron m_e and the mass of the hole m_h : $\frac{1}{m^*} = \frac{1}{m_e} + \frac{1}{m_h}$, e the elementary charge, ϵ the dielectric constant of the semiconductor, ϵ_0 the vacuum permittivity and d the diameter of the QD.^[2] Equation (2.1) shows the relation between the diameter of the QD and its gap energy, resulting in increasing values for the gap energy for decreasing particle size which can also be seen in Scheme 2.2a.

In most cases, the absorbed energy for the excitation is higher than E_g (left part of Scheme 2.2b). Therefore, the electron firstly releases energy *via* internal conversion. When the electron and the hole recombine, the exciton is annihilated and the energy is released as photons of a wavelength larger than the excitation wavelength (fluorescence, right part of Scheme 2.2b). This difference between excitation and emission wavelength is commonly known as “Stokes shift”. Due to the size-dependence of E_g and therefore the wavelength of the emitted photons, a broad range of optical emission is accessible (see Scheme 2.2c for possible luminescence colours of visible light emitting QDs).

There are several possibilities to obtain various types of QDs like lithographically defined QDs, epitaxially self-assembled QDs and colloidal QDs. The first two methods lead to QDs embedded in a matrix material while the latter are synthesised by wet chemical methods and are free-standing nanoparticles in solution. Typical synthetic procedures for colloidal QDs are the inverse micellar approach at room temperature or the “hot injection” method at elevated

temperatures which provides better results concerning size distribution.^[30] The optical properties also differentiate between the free QDs and the embedded ones. The emission spectra of colloidal QDs are much broader than those of the embedded QDs as they interact with their local, non-constant environment. This effect is known as “spectral diffusion”. Another property that is much more prominent in colloidal QDs than in the self-assembled ones is “blinking”.^[31] “Blinking” describes the on/off behaviour of the fluorescence of the QDs which arises due to Auger recombination taking place instead of the emission of a photon. Auger recombination can happen if two excitons are present at the same time in a QD and the energy from the annihilation of one of those excitons is transferred to the other one. The so obtained energy is then released *via* thermal vibrations as a non-radiative process and therefore “switching off” the fluorescence during a short time frame.

Colloidal QDs usually possess a high crystallinity with a low number of internal defects. Although they exhibit a strong luminescence their emission efficiency is rather low with values of 5 to 15 %.^[30] The emission efficiency is the ratio of emitted to absorbed photons and is usually called quantum yield. The low quantum yields of colloidal QDs originate in defects or surface trap states which can easily trap charge carriers leading to non-radiative recombination of the exciton. This process, which is also known as “trapping”, is much faster than the radiative recombination of an exciton.^[32] Most of the trap states are located on the surface of the QD as the surface atoms possess unsatisfied chemical bonds (dangling bonds). These bonds enable additional energy states within the band gap which can efficiently trap charge carriers. Therefore, a versatile approach to improve the quantum yield of a QD is to passivate the surface by coating it with either a shell of another inorganic material^[33] or suitable organic ligands^[34].

Another possibility for an exciton to recombine without emitting a photon is resonant energy transfer which is best known as Förster resonance energy transfer (FRET), named after the German scientist Theodor Förster.^[35] For this process to take place, a QD needs to be in close proximity to another QD. One of the QDs (donor) can then transfer an exciton to the other one (acceptor) which can be observed by time-resolved photoluminescence spectroscopy.^[32]

Typical QDs are among others CdSe, CdS, Si, GaAs, PbSe, and InP.^[30] Applications of QDs can first and foremost be found in optics, for example in lasers, light-emitting diodes (LEDs) and photovoltaics^[2,36,37], but also in electronics for example as field-effect devices^[38] and in biology for example as fluorescent markers^[2,39].

2.2 Polymers

The term “polymer” is made up of two Greek words, “poly” meaning many and “meros” meaning part. Fittingly, it describes chemical compounds that consist of many small subunits, the so called “monomers” (“mono” in Greek means single). Although plastics and rubbers are the most likely materials to be directly recognised as polymers, the general definition for a polymer according to the International Union of Pure and Applied Chemistry (IUPAC) is “A substance composed of macromolecules”.^[40] In return, a macromolecule is “A molecule of high relative molecular mass, the structure of which essentially comprises the multiple repetition of units derived, actually or conceptually, from molecules of low relative molecular mass”. Macromolecules can be the typical organic carbon main chains but also inorganic (without carbon, e.g. sulphur chains) or hybridic (carbon-free main chain, e.g. polysiloxanes) but also natural compounds like DNA, cellulose, polypeptides etc.^[41] Besides their chemical constituents, macromolecules can also be classified due to their architectures as linear, branched, brushes, star-like, dendritic, cross-linked or hyperbranched.^[41] Another important criteria is the number of different monomers that can be found inside the polymer’s structure. If this number is one, the polymer is called a “homopolymer”, for numbers larger than one a “copolymer”. An important class of copolymers are block copolymers which consist of two or more connected blocks which each are built of one species of monomers.

Polymers can be synthesised by many different reactions which are known as polymerisation reactions. In general, they are divided into two procedures: step-growth and chain-growth polymerisation. The difference between them is the distribution of reactive centres during the reaction. For step-growth, each monomer has at least two reactive centres, allowing them to react with any other monomer or already assembled larger units. An example for this type of reaction are polyadditions or polycondensations. In contrast, chain-growth relies on an initiator to produce one or more reactive centres which can then add one monomer at a time to one reactive centre while the reactive centre is passed to the end of the chain. The monomers cannot simply react with each other.^[42]

One of the most important characteristics of a polymer is its molecular weight¹ as the properties of polymers are inherently size-dependent.^[42] The molecular weight is connected to the number of monomer units, the so called degree of polymerisation. As the product of a

¹ In this work, the term molecular weight is used as a synonym for the molar mass of the polymer (typical unit: g/mol) as this is the common term used in polymer chemistry. Regarding to the definition of IUPAC, the molecular weight (or relative molecular mass) is the “Ratio of the mass of a molecule to the unified atomic mass unit” and therefore dimensionless.^[40]

polymerisation has a certain molecular weight distribution, the obtained number of the molecular weight differs depending on the calculation method. The two most important quantities are the number-average molecular weight M_n and the weight-average molecular weight M_w . By dividing the total weight of all molecules w by the number of molecules N_{total} , M_n can be calculated. Another approach is to measure the molecular weights of a certain number of molecules and sort them by their number of monomer units i . Summing the products of the corresponding numbers N and masses M of each unit i and dividing by the total amount of molecules again yields M_n :

$$M_n = \frac{w}{N_{\text{total}}} = \frac{\sum_i N_i M_i}{\sum_i N_i} \quad (2.2)$$

M_w is determined by summing over the products of the weight fraction w_i of molecules with molecular weight M_i and their number N_i :

$$M_w = \sum_i w_i N_i = \frac{\sum_i N_i M_i^2}{\sum_i N_i M_i} \quad (2.3)$$

The ratio of M_w and M_n is defined as the polydispersity \mathcal{D} and is a measure for the width of the molecular weight distribution:

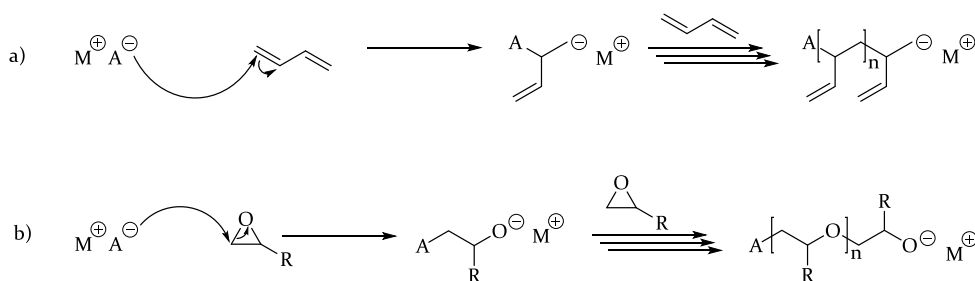
$$\mathcal{D} = \frac{M_w}{M_n} \quad (2.4)$$

Suitable methods for the molecular weight characterisation of a polymer are size exclusion chromatography (SEC) and nuclear magnetic resonance (NMR) spectroscopy.

The choice of the polymerisation technique depends on the thermodynamics and kinetics of the desired reactions.^[42] The most classical approach for chain-growth polymerisations is free radical polymerisation. As the name implies, the reactions are based on the formation and propagation of radicals as the reactive centres. The process is started by the decomposition of an initiator leading to the first reactive centres. They react with a monomer which then becomes the next reactive centre. A polymer chain is formed *via* propagation by adding more and more monomers. Eventually, this process is terminated by chemical reactions which remove the reactive centre from the chain. Due to these termination reactions, the resulting molecular weight distributions are rather broad.

Another polymerisation method which was exclusively used during this work is anionic polymerisation. Instead of radicals, the reactive centres are now made up of a negative charge, turning the whole molecule into an anion with a corresponding free counterion. As an initiator,

organometallic compounds are used. This restricts the possible solvents to aliphatic and aromatic hydrocarbons or cyclic ethers. Esters, ketones or halogenated solvents might react with carbanions and therefore cannot be used for this type of polymerisation. As initiators, organometallic compounds are widely employed with alkyllithium compounds among the most used ones, especially for carbon-carbon double bonds. The mechanism of the anionic polymerisation of 1,3-butadiene resulting in 1,2-polybutadiene can be found in Scheme 2.3a. The carbanion reacts with the double bond of the monomer to produce a larger carbanion with a new reactive centre. This reaction starts immediately when the initiator is added to the mixture resulting in exactly as many reactive centres as initiator molecules being present. If termination reactions inside the reaction mixture can be excluded, a so called living polymerisation is achieved. Even after all monomer units are connected, the polymer anion is still reactive and can continue the polymerisation if more monomer is added. This could be the same monomer for homopolymers or a different one for block copolymers. The living polymerisation is then terminated by the addition of a proton donor like water, alcohols or carbonic acids. As all hydrogen impurities could terminate the reaction prematurely, a considerable amount of care must be taken to remove all impurities like moisture from the reaction mixture. Some monomers tend to undergo side reactions but those can be suppressed by polymerisations at low temperatures. Ligands like crown ethers can be used to increase the reaction rate as they complex counterions like lithium. The counterions tend to associate with carbanions, thus decreasing their reactivity. Binding them in a complex and breaking up their connections to the carbanions can therefore lead to much higher reaction rates.



Scheme 2.3 Reaction scheme for a) anionic polymerisation of 1,3-butadiene and b) anionic ring-opening polymerisation of epoxides.

Anionic polymerisation can also be used on cyclic monomers like epoxides as a ring-opening polymerisation (Scheme 2.3b). Although cyclic ethers can usually only be polymerised in a cationic polymerisation due to the ether oxygen acting as a Lewis base, epoxides are an

exception as three-membered ring possess a high degree of strain. The reaction proceeds similar to the anionic polymerisation of monomers with C-C double bonds.

2.2.1 Supramolecular Polymers

Supramolecular chemistry was described as “the chemistry of the intermolecular bond, covering the structures and functions of the entities formed by association of two or more chemical species” by Jean-Marie Lehn who obtained the Nobel Prize in Chemistry in 1987 for his contributions to this field of chemistry.^[43] As “chemistry beyond the molecule”, it focuses on the connection of molecules instead of atoms by intermolecular bonds instead of covalent bonds. This approach can be extended to polymer chemistry, resulting in supramolecular polymers which are considered as one of the most promising classes for self-healing materials as they can go through multiple cycles of self-healing.^[44–47]

In general, supramolecular bonds can be formed *via* five approaches: π - π stacking, ionomers, metal bonding, host-guest interactions or hydrogen bonding.^[44] π - π stacking originates in the interactions between π -systems of large, usually aromatic molecules. For effective supramolecular bonds, charge-transfer structures of electron-deficient and electron-rich end groups are most suited.^[48] Ionomers are a class of polymers that contain up to 15 mol% of ionic groups.^[49] The most used group for this type of supramolecular bonds are carboxylate groups with sodium or zinc as counterions.^[48] Metal bonding results from the complexation of metal ions by organic ligands like terpyridine.^[50] The choice of the metal ion is able to change the dynamics of supramolecular metal bonding networks.^[51] Host-guest interactions can arise from several types of interactions like van der Waals, charge-transfer, ion-dipole, and hydrophobic interactions.^[48] The first system of these materials was based on β -cyclodextrin and ferrocene.^[52] Hydrogen bonding relies on the formation of multiple hydrogen bonds between the polymer chains. They are especially interesting due to their flexibility as the bonding strength can be tuned by external stimuli.^[53] As hydrogen bonds are quite weak (0.5–40 kJ/mol) compared to for example a carbon-carbon bond (~345 kJ/mol), the amount of hydrogen bonds formed is a key to tune the interactions. As a rule of thumb, each additional hydrogen bond increases the interaction by around 7.4 kJ/mol.^[47] Therefore, a lot of hydrogen-bonding motifs have been employed which usually consist of an interacting pair like the well-known thymine (Thy) and diamino-triazine (DAT) couple. On the other hand, also homo-associating molecules like urazole or ureidopyrimidone (UPy) can be found.^[48]

Supramolecular interactions influence the properties of the polymers like mechanical strength, viscosity and flow and introduce a stimuli-responsiveness that allows applications like self-healing.^[47] Including only 2 mol% of hydrogen bonds into polybutadiene can change the thermal and mechanical behaviour tremendously, turning the soft polymer into a thermoplastic material.^[54] If mechanical stress is applied to a material that contains covalent as well as supramolecular bonds, the latter will fail due to their weaker binding strength and can then reform to heal the material.^[47]

2.3 Polymeric nanocomposites

Composites are materials that consist of two or more components with different chemical and physical properties. Usually, one component is a continuous phase and therefore called the matrix while the other component(s) are called fillers. For nanocomposites, at least one component has one or more dimensions in the nanometre range.^[40] Considering polymeric nanocomposites, the matrix is made up of a polymer while the fillers can be selected from various types of inorganic nanoparticles. In general, fillers are used to improve existing or add new properties to the polymer. Examples for applications of polymeric nanocomposites are flame retardants^[55], membranes or adsorbents for waste water treatment^[56,57], catalysts^[58], organic solar cells^[58], food packaging^[59], soft electronics^[60] or biomedical applications like drug delivery, gene therapy, bioimaging, tissue engineering and regenerative medicine^[61-64].

Magnetic nanocomposites as stimuli-responsive materials have been the centre of interest due to their usage in smart or intelligent devices.^[65] Depending on the chosen polymers, applications range from deformable soft materials over magnetically guided objects (e.g. cells, drug loaded nanoparticles) to magnetically actuated materials allowing controlled drug delivery or shape memory materials.

Important for such applications is a good dispersion of the fillers inside and specific interactions with the matrix.^[55,66,67] Unfortunately, the miscibility of polymers and inorganic nanoparticles is often quite poor leading to aggregation of the particles. This inhibits the desired improvement of targeted properties and can even result in a decrease in functionality of the material. Possibilities to overcome this problem have been sought after for years, producing different approaches, each of them with their own advantages and disadvantages. The simplest methods rely on mixing both materials and extruding them together as a melt or film casting a

solution of the mixture with following evaporation of the solvent. Those methods can be used to process quite large amounts of material but do not allow precise control of the distribution of the nanoparticles in the final product. Another approach is the *in-situ* generation of nanoparticles in polymers for example by reducing a metal salt using the polymer matrix as a template.^[68] This method is limited regarding the nanoparticles that can be synthesised under such conditions.

To establish a chemical connection between nanoparticles and polymer two main approaches are used: “grafting-to” and “grafting-from”. Grafting-to stands for the coupling of a preformed polymer to the nanoparticle surface by suitable functionalities on both sides. If the functional group is introduced only to one end of the polymer this can be used to create brush-like layers around the nanoparticle. However, it is difficult to reach high grafting densities by this method. Grafting-from requires the creation of centres on the nanoparticle surface from which the polymer is created for example by a free or living radical polymerisation. This can be achieved by attaching initiator molecules or a monomer unit to the nanoparticle. The resulting grafting densities are higher, but a precise control of the polymer is often not trivial.

In this work, another method was used which is known as “polymer ligand exchange”^[69]. The ligand exchange relies on the end-functionalisation of polymer chains with head groups which possess a high affinity for the surface of the nanoparticle. Depending on the type of nanoparticle, this includes amines, thiols, carbonic acids, phosphonic acids or phosphines. In contrast to the grafting-to method, the nanoparticle surface does not need to be modified as only a physical connection between the polymer and the surface is established. It enables high grafting densities ($> 1 \text{ nm}^{-2}$) due to the strong interaction between the head group and the nanoparticle surface combined with the mobility of the polymer chain on the surface because of the non-permanent connection. Next to the functionalised polymer, nanoparticles stabilised by their native surfactants are the starting materials for this procedure which are mixed in a good solvent for both constituents. By precipitation and solving steps the polymer coated nanoparticles can be separated from the surfactant and excess polymer ligand. The so obtained polymer coated nanoparticles can then be mixed with additional polymer, allowing high contents of nanoparticles inside the polymer matrix.^[70]

2.3.1 Supramolecular Nanocomposites

In 1999, Jean-Marie Lehn encouraged the combination of supramolecular chemistry and “nanoparticles which, fitted with suitable recognition groups, may serve as instructed building blocks for the spontaneous but controlled generation of highly complex, functional architectures of both basic and applied interest”.^[71] Nowadays, it is well-known that fillers like carbon fibres or carbon nanotubes can increase the modulus of supramolecular materials, while they do not disturb the reversible bonding.^[72-78] In addition, they can enhance the self-healing abilities as they induce new properties into the system. Magnetic nanoparticles can be used to generate heat for self-healing^[79,80], other materials use light as a trigger for self-healing^[76,81,82].

Supramolecular interactions like hydrogen bonding can be used to attach nanoparticles on surfaces^[83,84], an approach that is especially applied for the targeted deposition of nanoparticles on block copolymer structures^[85-87]. If the nanoparticles are already incorporated into the block copolymer before structure formation, they influence the obtained structures.^[88,89] In addition, nanoparticles which are either supramolecularly functionalised^[90,91] or whose surface serves as coordination centres for supramolecular groups^[92] can be used as crosslinkers for polymeric materials.

Potential applications of supramolecular nanocomposites include for example artificial skin^[93,94], self-healing piezoresistive strain sensors^[95], self-healing surgical dressings^[82], drug delivery^[96,97], adsorbents for synergetic adsorption of heavy metal ions and organic pollutants^[98], pH controlled cargo release systems^[99], sensors for human-machine interactions^[100], electrochemical sensors for trinitrotoluene (TNT) detection^[101] and artificial nacre for potential applications in energy conversion, temperature sensor, and thermo-driven actuator^[102].

2.4 References

- [1] “ISO/TS 80004-2:2015(en), Nanotechnologies — Vocabulary — Part 2: Nano-objects,” can be found under <https://www.iso.org/obp/ui/#iso:std:iso:ts:80004:-2:ed-1:vl:en>, **2015**.
- [2] W. J. Parak, L. Manna, F. C. Simmel, D. Gerion, P. Alivisatos, in *Nanoparticles* (Ed: G. Schmid), Wiley-VCH Verlag GmbH & Co. KGaA, Weinheim, FRG, **2004**, pp. 4–49.
- [3] M. Auffan, J. Rose, J.-Y. Bottero, G. V. Lowry, J.-P. Jolivet, M. R. Wiesner, *Nat. Nanotechnol.* **2009**, *4*, 634.
- [4] R. Nagarajan, in *Nanoparticles Synth. Stab. Passiv. Funct.* (Eds: R. Nagarajan, T. Alan Hatton), American Chemical Society, **2008**, pp. 2–14.
- [5] A. P. Chernyshev, *Mater. Lett.* **2009**, *63*, 1525.
- [6] J. R. Morones, J. L. Elechiguerra, A. Camacho, K. Holt, J. B. Kouri, J. T. Ramírez, M. J. Yacaman, *Nanotechnology* **2005**, *16*, 2346.
- [7] S. Horikoshi, N. Serpone, in *Microwaves Nanoparticle Synth.*, Wiley-VCH Verlag GmbH & Co. KGaA, Weinheim, Germany, **2013**, pp. 1–24.
- [8] E. Polo, P. del Pino, A. Pardo, P. Taboada, B. Pelaz, in *Nanooncology. Nanomedicine and Nanotoxicology* (Ed: T.G. Gonçalves G.), Springer, Cham, **2018**, pp. 239–279.
- [9] J. Park, K. An, Y. Hwang, J.-G. Park, H.-J. Noh, J.-Y. Kim, J.-H. Park, N.-M. Hwang, T. Hyeon, *Nat. Mater.* **2004**, *3*, 891.
- [10] W. W. Yu, J. C. Falkner, C. T. Yavuz, V. L. Colvin, *Chem. Commun.* **2004**, 2306.
- [11] A. K. Boal, in *Nanoparticles Build. Blocks Nanotechnol.* (Ed: V.M. Rotello), Springer Science+Business Media, New York, **2004**, pp. 1–27.
- [12] M. Colombo, S. Carregal-Romero, M. F. Casula, L. Gutiérrez, M. P. Morales, I. B. Böhm, J. T. Heverhagen, D. Prospero, W. J. Parak, *Chem. Soc. Rev.* **2012**, *41*, 4306.
- [13] C. Caizer, in *Handb. Nanoparticles*, Springer International Publishing, Cham, **2016**, pp. 475–519.
- [14] M. Naitō, T. Yokoyama, K. Hosokawa, K. Nogi, *Nanoparticle Technology Handbook*, Elsevier, **2018**.

- [15] H. R. Rezaie, A. Shokuhfar, F. Arianpour, in *New Front. Nanoparticles Nanocomposite Mater.* (Eds: A. Öchsner, A. Shokuhfar), Springer Berlin Heidelberg, Berlin, Heidelberg, **2013**, pp. 171–232.
- [16] X.-C. Sun, *Mol. Phys.* **2002**, *100*, 3059.
- [17] J. I. Gittleman, B. Abeles, S. Bozowski, *Phys. Rev. B* **1974**, *9*, 3891.
- [18] J. M. D. Coey, M. Venkatesan, H. Xu, in *Funct. Met. Oxides*, Wiley-VCH Verlag GmbH & Co. KGaA, Weinheim, Germany, **2013**, pp. 1–49.
- [19] D. Speliotis, *J. Magn. Magn. Mater.* **1999**, *193*, 29.
- [20] Y. Sahoo, M. Cheon, S. Wang, H. Luo, E. P. Furlani, P. N. Prasad, *J. Phys. Chem. B* **2004**, *108*, 3380.
- [21] S. Singamaneni, V. N. Bliznyuk, C. Binek, E. Y. Tsybal, *J. Mater. Chem.* **2011**, *21*, 16819.
- [22] P.-G. de Gennes, P. A. Pincus, *Phys. der Kondens. Mater.* **1970**, *11*, 189.
- [23] M. Grzelczak, J. Vermant, E. M. Furst, L. M. Liz-Marzán, *ACS Nano* **2010**, *4*, 3591.
- [24] A. I. Ekimov, A. A. Onushchenko, *Pis'ma Zh. Eksp. Teor. Fiz.* **1981**, *34*, 363.
- [25] R. Rossetti, S. Nakahara, L. E. Brus, *J. Chem. Phys.* **1983**, *79*, 1086.
- [26] M. A. Reed, *J. Vac. Sci. Technol. B Microelectron. Nanom. Struct.* **1986**, *4*, 358.
- [27] D. B. Hayrapetyan, H. A. Sarkisyan, E. M. Kazaryan, *Fundamental Absorption of Semiconductor Quantum Dots*, SPIE, **2018**.
- [28] M. A. Kastner, *Phys. Today* **1993**, *46*, 24.
- [29] A. F. Holleman, E. Wiberg, N. Wiberg, *Lehrbuch Der Anorganischen Chemie*, Walter De Gruyter & Co., Berlin, **2007**.
- [30] H. Skaff, T. Emrick, in *Nanoparticles Build. Blocks Nanotechnol.* (Ed: V.M. Rotello), Springer Science+Business Media, New York, **2004**, pp. 29–52.
- [31] A. Kurzmam, A. Ludwig, A. D. Wieck, A. Lorke, M. Geller, *Nano Lett.* **2016**, *16*, 3367.
- [32] R. Koole, E. Groeneveld, D. Vanmaekelbergh, A. Meijerink, C. de Mello Donegá, in *Nanoparticles Work. Nanosci.* (Ed: C. De Mello Donegá), Springer Berlin Heidelberg, Berlin, Heidelberg, **2014**, pp. 13–51.
- [33] P. Reiss, M. Protière, L. Li, *Small* **2009**, *5*, 154.

-
- [34] C. de M. Donegá, *Chem. Soc. Rev.* **2011**, *40*, 1512.
- [35] T. Förster, *Ann. Phys.* **1948**, *437*, 55.
- [36] G. H. Carey, A. L. Abdelhady, Z. Ning, S. M. Thon, O. M. Bakr, E. H. Sargent, *Chem. Rev.* **2015**, *115*, 12732.
- [37] A. J. Nozik, M. C. Beard, J. M. Luther, M. Law, R. J. Ellingson, J. C. Johnson, *Chem. Rev.* **2010**, *110*, 6873.
- [38] D. V. Talapin, J.-S. Lee, M. V. Kovalenko, E. V. Shevchenko, *Chem. Rev.* **2010**, *110*, 389.
- [39] D. Bera, L. Qian, T.-K. Tseng, P. H. Holloway, *Materials (Basel)*. **2010**, *3*, 2260.
- [40] A. D. McNaught, A. Wilkinson, *IUPAC Compendium of Chemical Terminology (the "Gold Book")*, Blackwell Scientific Publications, Oxford, **1997**.
- [41] D. Braun, H. Cherdrón, M. Rehahn, H. Ritter, B. Voit, *Polymer Synthesis: Theory and Practice*, Springer Berlin Heidelberg, Berlin, Heidelberg, **2013**.
- [42] G. Odian, *Principles of Polymerization*, John Wiley & Sons, Inc., Hoboken, NJ, USA, **2004**.
- [43] J.-M. Lehn, *Angew. Chemie Int. Ed. English* **1988**, *27*, 89.
- [44] D. Döhler, P. Michael, W. H. Binder, in *Self-Healing Polym.* (Ed: W.H. Binder), Wiley-VCH Verlag GmbH & Co. KGaA, Weinheim, Germany, **2013**, pp. 5–60.
- [45] J.-M. Lehn, *Polym. Int.* **2002**, *51*, 825.
- [46] W. H. Binder, R. Zirbs, in *Adv. Polym. Sci. 207* (Ed: W.H. Binder), Springer Berlin Heidelberg, Berlin, Heidelberg, **2006**, pp. 1–78.
- [47] F. Herbst, W. H. Binder, in *Self-Healing Polym.* (Ed: W.H. Binder), Wiley-VCH Verlag GmbH & Co. KGaA, Weinheim, Germany, **2013**, pp. 273–300.
- [48] M. Enke, D. Döhler, S. Bode, W. H. Binder, M. D. Hager, U. S. Schubert, in *Adv. Polym. Sci. 273* (Eds: M.D. Hager, S. van der Zwaag, U.S. Schubert), Springer International Publishing, Basel, **2015**, pp. 59–112.
- [49] I. Capek, *Adv. Colloid Interface Sci.* **2005**, *118*, 73.
- [50] A. Winter, U. S. Schubert, *Chem. Soc. Rev.* **2016**, *45*, 5311.
- [51] M. Hess, E. Roeben, A. Habicht, S. Seiffert, A. M. Schmidt, *Soft Matter* **2019**, *15*, 842.
- [52] M. Nakahata, Y. Takashima, H. Yamaguchi, A. Harada, *Nat. Commun.* **2011**, *2*, 511.
-

- [53] A. W. Bosnian, L. Brunsveld, B. J. B. Folmer, R. P. Sijbesma, E. W. Meijer, *Macromol. Symp.* **2003**, *201*, 143.
- [54] R. Stadler, *Kautschuk Gummi Kunststoffe* **1993**, *46*, 619.
- [55] M. Salavati-Niasari, D. Ghanbari, in *Adv. Divers. Ind. Appl. Nanocomposites* (Ed: B. Reddy), InTech, London, **2011**, pp. 501–520.
- [56] X. Qu, J. Brame, Q. Li, P. J. J. Alvarez, *Acc. Chem. Res.* **2013**, *46*, 834.
- [57] G. Lofrano, M. Carotenuto, G. Libralato, R. F. Domingos, A. Markus, L. Dini, R. K. Gautam, D. Baldantoni, M. Rossi, S. K. Sharma, M. C. Chattopadhyaya, M. Giugni, S. Meric, *Water Res.* **2016**, *92*, 22.
- [58] S. Bhattacharya, S. K. Samanta, *Chem. Rev.* **2016**, *116*, 11967.
- [59] M. Carbone, D. T. Donia, G. Sabbatella, R. Antiochia, *J. King Saud Univ. - Sci.* **2016**, *28*, 273.
- [60] S. Choi, S. I. Han, D. Kim, T. Hyeon, D.-H. Kim, *Chem. Soc. Rev.* **2019**, *48*, 1566.
- [61] Z. Tang, C. He, H. Tian, J. Ding, B. S. Hsiao, B. Chu, X. Chen, *Prog. Polym. Sci.* **2016**, *60*, 86.
- [62] N. Erathodiyil, J. Y. Ying, *Acc. Chem. Res.* **2011**, *44*, 925.
- [63] G. Kaur, R. Adhikari, P. Cass, M. Bown, P. Gunatillake, *RSC Adv.* **2015**, *5*, 37553.
- [64] A. J. T. Teo, A. Mishra, I. Park, Y.-J. Kim, W.-T. Park, Y.-J. Yoon, *ACS Biomater. Sci. Eng.* **2016**, *2*, 454.
- [65] J. Thévenot, H. Oliveira, O. Sandre, S. Lecommandoux, *Chem. Soc. Rev.* **2013**, *42*, 7099.
- [66] T. Krasia-Christoforou, in *Hybrid Hierarchical Compos. Mater.* (Eds: C.-S. Kim, C. Randow, T. Sano), Springer International Publishing, Cham, **2015**, pp. 11–63.
- [67] S. P. Ehlert, Preparation of Fully Miscible Nanocomposites Dissertation, University of Bayreuth; Germany, **2014**.
- [68] A. Sanyal, T. B. Norsten, V. M. Rotello, in *Nanoparticles. Build. Blocks Nanotechnology* (Ed: V.M. Rotello), Springer Science+Business Media, New York, **2004**, pp. 201–224.
- [69] S. Ehlert, S. M. Taheri, D. Pirner, M. Drechsler, H.-W. Schmidt, S. Förster, *ACS Nano* **2014**, *8*, 6114.
- [70] S. Ehlert, C. Stegelmeier, D. Pirner, S. Förster, *Macromolecules* **2015**, *48*, 5323.

-
- [71] J.-M. Lehn, N. Laureate, *J. Nanoparticle Res.* **1999**, *1*, 7.
- [72] L. R. Hart, J. L. Harries, B. W. Greenland, H. M. Colquhoun, W. Hayes, *Polym. Chem.* **2013**, *4*, 4860.
- [73] J. Fox, J. J. Wie, B. W. Greenland, S. Burattini, W. Hayes, H. M. Colquhoun, M. E. Mackay, S. J. Rowan, *J. Am. Chem. Soc.* **2012**, *134*, 5362.
- [74] R. Vaiyapuri, B. W. Greenland, H. M. Colquhoun, J. M. Elliott, W. Hayes, *Polym. Int.* **2014**, *63*, 933.
- [75] Q. Ding, X. Xu, Y. Yue, C. Mei, C. Huang, S. Jiang, Q. Wu, J. Han, *ACS Appl. Mater. Interfaces* **2018**, *10*, 27987.
- [76] M. V. Biyani, E. J. Foster, C. Weder, *ACS Macro Lett.* **2013**, *2*, 236.
- [77] A. Hashemi, N. Jouault, G. A. Williams, D. Zhao, K. J. Cheng, J. W. Kysar, Z. Guan, S. K. Kumar, *Nano Lett.* **2015**, *15*, 5465.
- [78] B. Zhu, R. Merindol, A. J. Benitez, B. Wang, A. Walther, *ACS Appl. Mater. Interfaces* **2016**, *8*, 11031.
- [79] C. C. Corten, M. W. Urban, *Adv. Mater.* **2009**, *21*, 5011.
- [80] E. Oglioni, L. Yu, I. Javakhishvili, A. L. Skov, *RSC Adv.* **2018**, *8*, 8285.
- [81] H. Zhang, H. Xia, Y. Zhao, *J. Mater. Chem.* **2012**, *22*, 845.
- [82] E. Zhang, T. Wang, L. Zhao, W. Sun, X. Liu, Z. Tong, *ACS Appl. Mater. Interfaces* **2014**, *6*, 22855.
- [83] R. Zirbs, F. Kienberger, P. Hinterdorfer, W. H. Binder, *Langmuir* **2005**, *21*, 8414.
- [84] W. H. Binder, M. Lomoschitz, R. Sachsenhofer, G. Friedbacher, *J. Nanomater.* **2009**, *2009*, 1.
- [85] A. Haryono, W. H. Binder, *Small* **2006**, *2*, 600.
- [86] W. H. Binder, C. Kluger, C. J. Straif, G. Friedbacher, *Macromolecules* **2005**, *38*, 9405.
- [87] S. G. Jang, E. J. Kramer, C. J. Hawker, *J. Am. Chem. Soc.* **2011**, *133*, 16986.
- [88] Y.-R. Wu, Y.-C. Wu, S.-W. Kuo, *Macromol. Chem. Phys.* **2013**, *214*, 1496.
- [89] T. Ye, X. Chen, X. Fan, Z. Shen, *Soft Matter* **2013**, *9*, 4715.

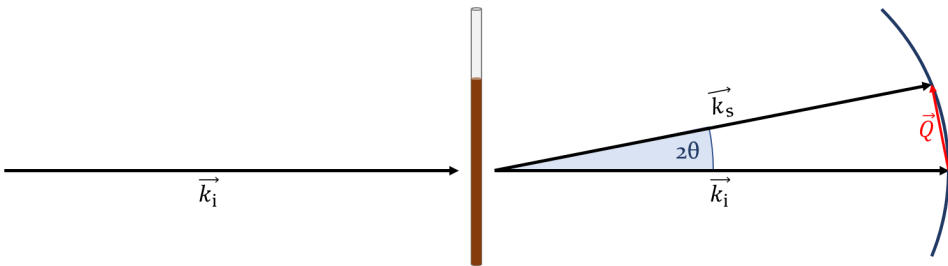
- [90] R. Vaiyapuri, B. W. Greenland, S. J. Rowan, H. M. Colquhoun, J. M. Elliott, W. Hayes, *Macromolecules* **2012**, *45*, 5567.
- [91] R. Shenhar, E. Jeoung, S. Srivastava, T. B. Norsten, V. M. Rotello, *Adv. Mater.* **2005**, *17*, 2206.
- [92] Q. Li, D. G. Barrett, P. B. Messersmith, N. Holten-Andersen, *ACS Nano* **2016**, *10*, 1317.
- [93] C. Hou, T. Huang, H. Wang, H. Yu, Q. Zhang, Y. Li, *Sci. Rep.* **2013**, *3*, 3138.
- [94] B. C. K. Tee, C. Wang, R. Allen, Z. Bao, *Nat. Nanotechnol.* **2012**, *7*, 825.
- [95] G. Cai, J. Wang, K. Qian, J. Chen, S. Li, P. S. Lee, *Adv. Sci.* **2017**, *4*, 1600190.
- [96] Y. Chen, W. Cheng, L. Teng, M. Jin, B. Lu, L. Ren, Y. Wang, *Macromol. Mater. Eng.* **2018**, *303*, 1700660.
- [97] X. Li, X. Wang, M. Hua, H. Yu, S. Wei, A. Wang, J. Zhou, *ACS Biomater. Sci. Eng.* **2019**, *5*, 2399.
- [98] J. Wang, W. Zhang, J. Wei, *J. Mater. Chem. A* **2019**, *7*, 2055.
- [99] Q. Zhang, T.-Y. Xu, C.-X. Zhao, W.-H. Jin, Q. Wang, D.-H. Qu, *Chem. - An Asian J.* **2017**, *12*, 2549.
- [100] J. Cao, C. Lu, J. Zhuang, M. Liu, X. Zhang, Y. Yu, Q. Tao, *Angew. Chemie Int. Ed.* **2017**, *56*, 8795.
- [101] X. Ran, Q. Qu, X. Qian, W. Xie, S. Li, L. Li, L. Yang, *Sensors Actuators B Chem.* **2018**, *257*, 362.
- [102] Y. Wang, T. Li, P. Ma, S. Zhang, H. Zhang, M. Du, Y. Xie, M. Chen, W. Dong, W. Ming, *ACS Nano* **2018**, *12*, 6228.

3 Small-Angle Scattering

The following chapter is a summary of various text books and journal articles about scattering theory, especially for small-angle scattering. For further details, the reader is referred to the original literature.^[1-10]

3.1 Basics of Scattering Theory

In general, scattering describes the deflection of something in arbitrary direction due to interactions with something else. This can be a billiard ball hitting another billiard ball or a light beam hitting raindrops to form a rainbow. For small-angle scattering (SAS), a beam of X-rays or neutrons is directed onto a sample and scattered there due to interactions with the material of the sample. The basic principle can be seen in Scheme 3.1.



Scheme 3.1 Basic scattering experiment.

An important assumption for the following considerations is a monochromatic beam meaning that the beam consists of particles of one distinct energy which corresponds to a distinct wavelength. The incident beam is described as a plane wave with the vector \vec{k}_i . In Scheme 3.1, it hits the sample, represented by a thin capillary containing a solution of nanoparticles, and is partially scattered: A part of the incoming beam will pass through the sample unchanged but another part of it will change its direction by a certain angle 2θ , forming the scattered beam \vec{k}_s . Assuming elastic scattering, the energy of the scattered particle and thus the magnitude of the vector is constant.

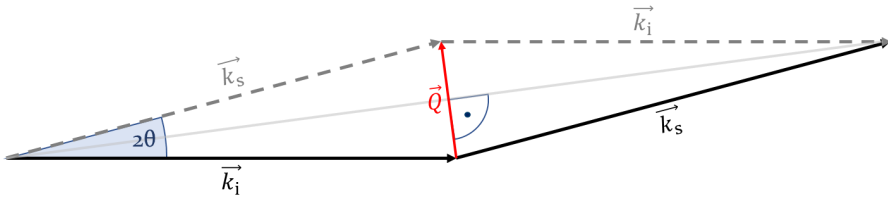
$$|\vec{k}_1| = |\vec{k}_s| = k \quad (3.1)$$

The difference between the scattered and the incoming beam defines the scattering vector, \vec{Q} :

$$\vec{Q} = \vec{k}_s - \vec{k}_i \quad (3.2)$$

All possible scattering vectors are located on a sphere with radius k , the so-called Ewald sphere. However, for SAS experiments, only small values for the angle 2θ between the scattered and the incoming beam are taken into account.

To calculate the magnitude of \vec{Q} , a simple geometrical construction can be used (Scheme 3.2):



Scheme 3.2 Geometrical construction to illustrate the mathematical relation between Q , k and θ .

By reproducing the incoming and scattered beam, a rhombus is created allowing the calculation of Q by considering the definition of the wavevector $k = \frac{2\pi}{\lambda}$, with λ being the wavelength of the beam.

$$\sin \theta = \frac{Q}{2k} \Rightarrow Q = 2k \sin \theta \Rightarrow Q = \frac{4\pi}{\lambda} \sin \theta \quad (3.3)$$

This equation shows an important relation for scattering experiments. To study large structures, small angles are needed. Using incident wavelengths of about one to several Å, typical length scales for SAS are in the nm range.

Instead of the amplitudes of the scattered beams, the intensity is measured in SAS experiments which is its absolute square. The amplitude is the Fourier transform of the scattering length density $\rho(\vec{r})$.

$$A(\vec{Q}) = \int_V \rho(\vec{r}) e^{i\vec{Q}\vec{r}} d\vec{r} \quad (3.4)$$

The vectors \vec{r} describe the relative locations of all scattering centres relative to an arbitrary chosen centre and the product $\vec{Q}\vec{r}$ represents the phase shift between the scattered waves from different centres. For SAS experiments, often the magnitude of \vec{Q} and \vec{r} is sufficient due to isotropic scattering. Therefore, the vector notation is omitted for simplicity from here on. The scattering length density is directly related to the chemical composition and thus varies between different materials. This will be explained later in this chapter.

The intensity as its square is then calculated by multiplication of the amplitude with its complex conjugate $A^*(Q)$.

$$I(Q) = |A(Q)|^2 = A(Q) \cdot A^*(Q) = \iint_V \rho(r)\rho'(r')e^{iQ(r-r')}drdr' \quad (3.5)$$

Because of the squared amplitude, the phase information from $\vec{Q}\vec{r}$ cannot be extracted from the measured intensity, resulting in the so-called phase problem of scattering. This disables the reconstruction of the full original information which would be necessary to obtain an image like it is done in microscopy methods.

Two assumptions are made to simplify equation (3.5): the sample consists of i) only two phases with their respective scattering length densities, thus the product $\rho(r)\rho'(r')$ can be reduced to $\Delta\rho^2$ and ii) an assembly of N_p identical particles with volume V_p . The scattered intensity per unit volume can then be calculated for dilute solutions by

$$I(Q) = \frac{N_p}{V} V_p^2 \Delta\rho^2 \left[\int_{V_p} e^{iQr} dr \right]^2 = \Phi V_p^2 \Delta\rho^2 P(Q) \quad (3.6)$$

with $\Phi = \frac{N_p}{V}$ the volume fraction of the particles and $P(Q)$ the particle form factor. For a spherical particle, the amplitude of the form factor can be calculated by taking into account the spherical symmetry of the particle, resulting in equation (3.7):

$$P_{\text{sphere}}(Q) = \left[\frac{3(\sin(qR) - qR \cos(qR))}{(qR)^3} \right]^2 \quad (3.7)$$

The radius R of synthesised nanoparticles cannot be considered as one discrete size. Therefore, this parameter is usually folded with a distribution function which can be for example the normal distribution with the standard deviation σ , as presented in Figure 3.1.

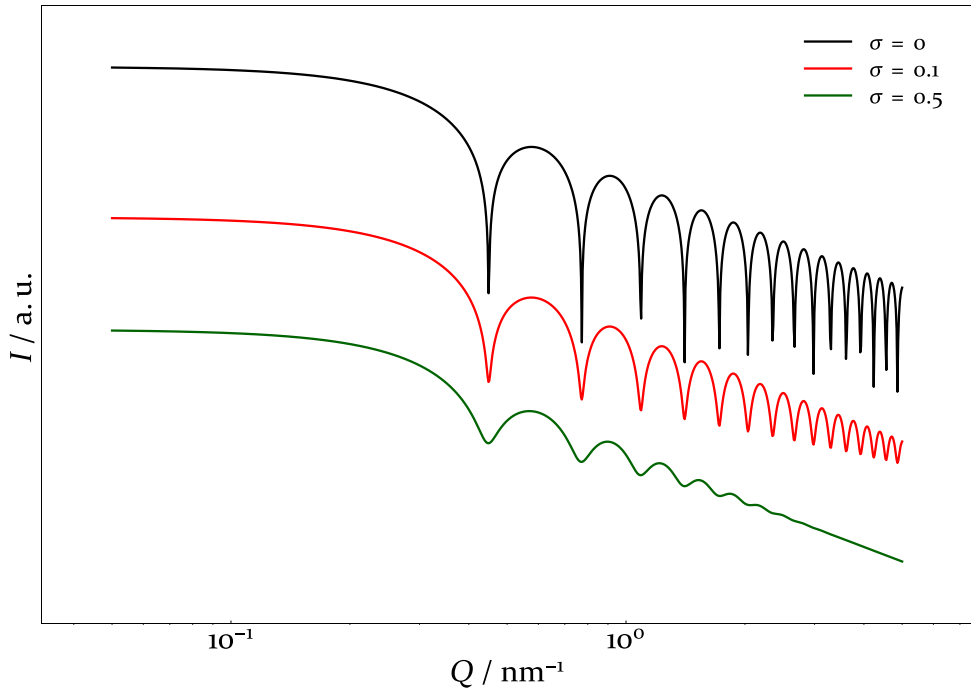


Figure 3.1 Scattering curves for spherical particles with 10 nm radius. The black curves shows the monodisperse form factor, the red and green curve display polydisperse spheres with a standard deviation of 0.1 or 0.5 nm respectively. Intensities are arbitrarily shifted.

The minima of the form factor are becoming less pronounced with increasing polydispersity due to the variation of the radius, which directly corresponds to the location of the minima.

In case of finite concentrations, interference between the particles are included, equation (3.6) is supplemented by the structure factor $S(Q)$.

$$I(Q) = \Phi V_p^2 \Delta\rho^2 P(Q) S(Q) \quad (3.8)$$

While the form factor in general provides information about the shape of the particles, the structure factor includes information about the arrangement and correlations of the particles and approaches 1 for large distances between the particles. Therefore, the structure factor can most often be disregarded for dilute solutions. However, if structure formation of the nanoparticles is induced, a correct interference function needs to be chosen to describe the ordering of the particles.

Various models exist to describe the scattering of chain-like structures of particles. As chains of particles are not necessarily linear, the pearl necklace chain model by Schweins and

Huber^[11] is chosen to describe small agglomerates of nanoparticles in this work. The original model describes spherical particles in a freely jointed chain which are connected by rod like segments of length l (Scheme 3.3a).



Scheme 3.3 Pearl necklace model: a) Original model by R. Schweins and K. Huber, b) adapted model for small, chain-like agglomerates of nanoparticles.

The intramolecular structure factor of this model consists of contributions from the interference between sphere-sphere, rod-rod and sphere-rod. As there are no connecting rods between nanoparticles, the model is reduced to the interference between the spheres (Scheme 3.3b), resulting in

$$S_{\text{intra}}(Q) = \frac{2}{N^2} \left[\frac{N}{1 - \frac{\sin(Q(l+2R))}{(Q(l+2R))}} - \frac{N}{2} \frac{1 - \left(\frac{\sin(Q(l+2R))}{(Q(l+2R))} \right)^N}{\left(1 - \frac{\sin(Q(l+2R))}{(Q(l+2R))} \right)^2} \frac{\sin(Q(l+2R))}{(Q(l+2R))} \right] \quad (3.9)$$

with N the number of spheres in a chain and R the radius of the spheres. For $N = 1$, S_{intra} becomes 1, leading to the pure form factor. Higher values for N change the form of the curve at low Q s, introducing an additional slope, as can be seen in Figure 3.2.

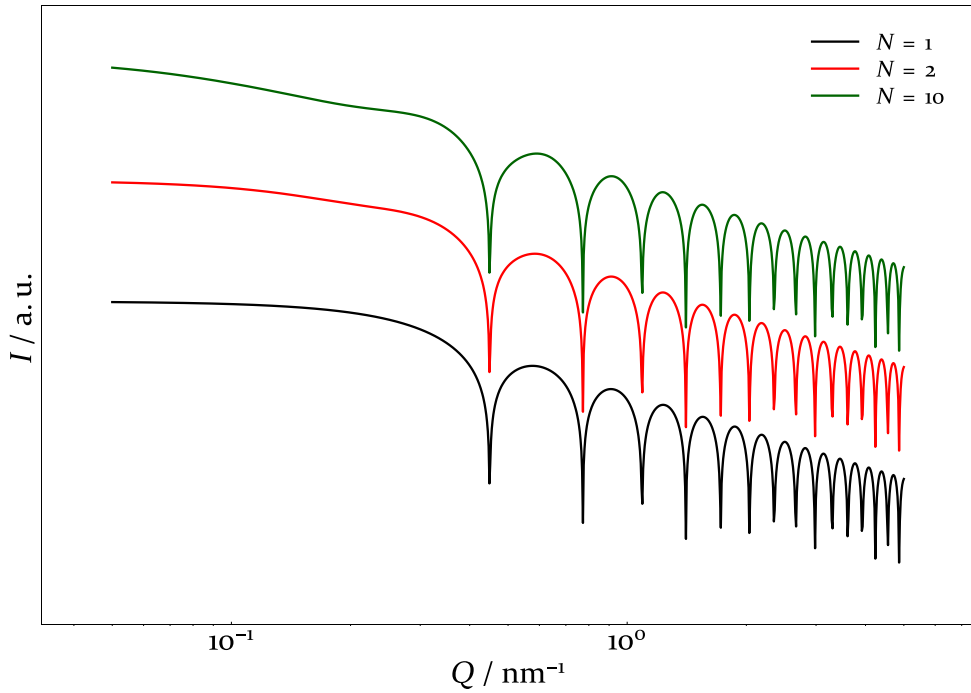


Figure 3.2 Resulting scattering curves for the adapted pearl necklace model with $R = 10$ nm, $l = 2$ nm for different values of N . Intensities are arbitrarily shifted.

Therefore, from this model, information regarding the number of particles in chain-like structures, which represents the size of the aggregates, as well as the distance between them can be obtained.

At high concentrations, the nanoparticles can form periodic lattices for which the structure factor can be described as:

$$S(Q) = 1 + \beta(Q) (Z(Q) - 1) G(Q) \quad (3.10)$$

with $\beta(Q)$ representing the diffuse scattering due to particle polydispersity leading to an intensity increase at high Q s, $Z(Q)$ the lattice factor and $G(Q)$ the isotropic Debye-Waller factor.

The lattice factor $Z(Q)$ determines the shape of the function and can be calculated for an ideal, undistorted lattice by:

$$Z(Q) = \frac{(2\pi)^{d-1} c}{nV_d \Omega_d Q^{d-1}} \sum_{\{hkl\}} m_{hkl} f_{hkl}^2 L_{hkl}(Q) \quad (3.11)$$

Here, d denotes the dimension of the unit cell, c the Porod constant ($c \approx 1$), n the number of particles per unit cell, V_d the volume of the unit cell, Ω_d the solid angle. The Miller indices (hkl) describe lattice planes in the crystal leading to a Bragg reflex and depend on the crystal symmetry. The intensity and locations of the peaks are defined by peak multiplicity m_{hkl} and symmetry factor f_{hkl} which takes into account symmetry-related extinction rules while its shape is characterised by the function $L_{hkl}(Q)$ for which for example a Lorentzian or Gaussian function can be used. The sum is then made over all reflections $\{hkl\}$.

In the following, some effects which influence the experimental scattering pattern are explained. As an example, the scattering patterns of a body-centred cubic and a body-centred tetragonal lattice structure factor are displayed in Figure 3.3.

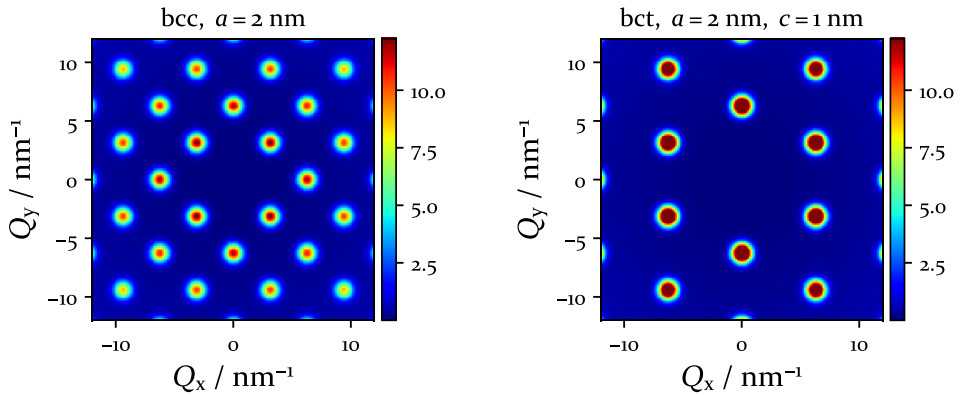


Figure 3.3 2D scattering patterns of bcc and bct lattice structure factor. Axis c and viewing direction along 001.

The scattering patterns reveal narrow peaks which are typical for well-ordered lattices with large domain sizes. Intrinsically the domain size determines the peak width. The difference between cubic and tetragonal lattice is the third lattice spacing, c , which is of the same length as a and b for the cubic lattice but differentiates for the tetragonal lattice. This corresponds to the difference of the peak positions in Figure 3.3.

In experiments, the intensity of the peaks is usually decreased due to small domain sizes which is shown in Figure 3.4. Reducing the domain size by 10 % leads to a significant drop of the peak intensity and broader peaks.

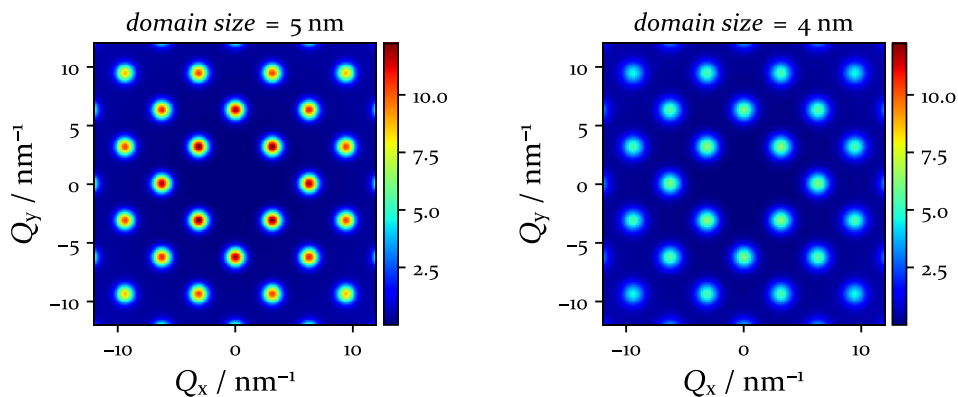


Figure 3.4 Decrease of intensity due to smaller domain sizes.

In the scattering patterns shown so far, a decrease in intensity can be found for the peaks at higher Q values. The most prominent reason for this is the Debye-Waller factor which arises from the thermal displacement of the particles around their lattice positions and can be written as:

$$G(Q) = e^{-\sigma_D^2 Q^2 d_p^2} \quad (3.12)$$

While d_p represents the nearest neighbour distance, σ_D^2 is the mean squared displacement. The effect of an increase of the root mean squared displacement (*RMSD*) can be seen in Figure 3.5.

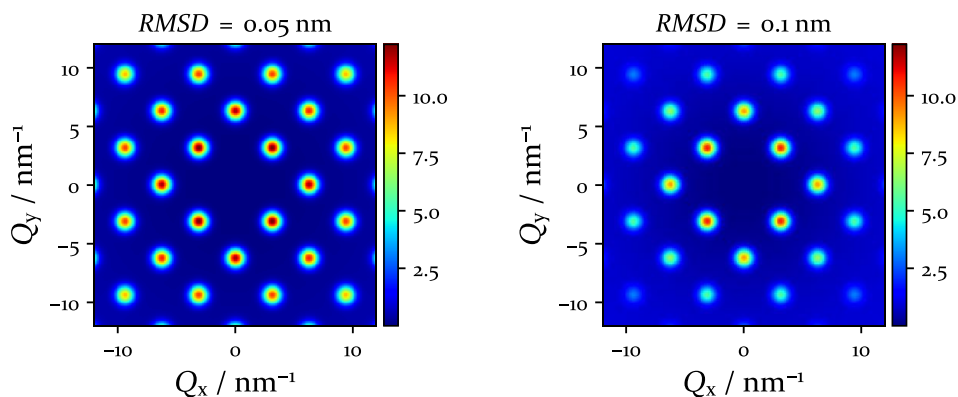


Figure 3.5 Decrease in intensity of higher order peaks because of increasing root mean squared displacement.

Doubling the *RMSD* leads to a decrease in intensity for all peaks but especially for the peaks at large Q values due to the Q^2 in equation (3.12). Additionally, we observe an increase of the background intensity between the peaks at larger Q . The reason is that the missing intensity in the peaks contributes to the diffuse scattering appearing as a background between peaks. The Debye-Waller factor gains importance if the distances of the particles within the crystal or the displacements are large.

In addition to these effects which show a decrease in intensity, often an asymmetric broadening of the peaks can be observed. This arises from rotational disorder of the lattices and is showcased in Figure 3.6.

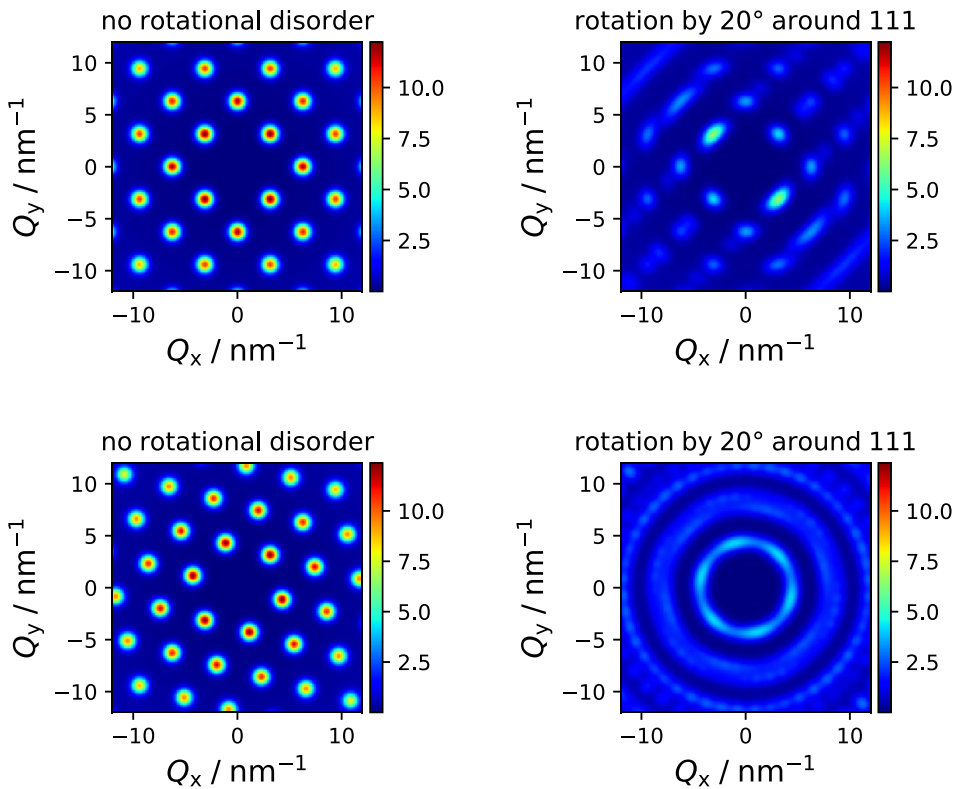
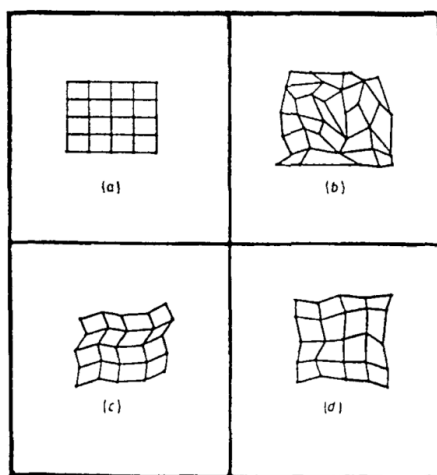


Figure 3.6 Scattering patterns demonstrating the effect of orientational disorder of the crystalline lattice. For the images in the second row, the viewing direction is along the III axis.

Rotating the lattice by 10° around the III axis leads not only to a smearing of the peak intensity in this direction but also to additional peaks arising from quasi-forbidden symmetries.

An explanation for the origin of these peaks can be found in [8]. If the disorder becomes large, the peaks evolve into Debye-Scherrer rings. This can be seen more easily if the lattice is observed along the rotated direction.

If the ordering of the lattice is reduced to medium range, paracrystalline structures can be obtained.^[12] To explain the differences between crystalline, amorphous and paracrystalline lattices, they are schematically shown in Scheme 3.4.



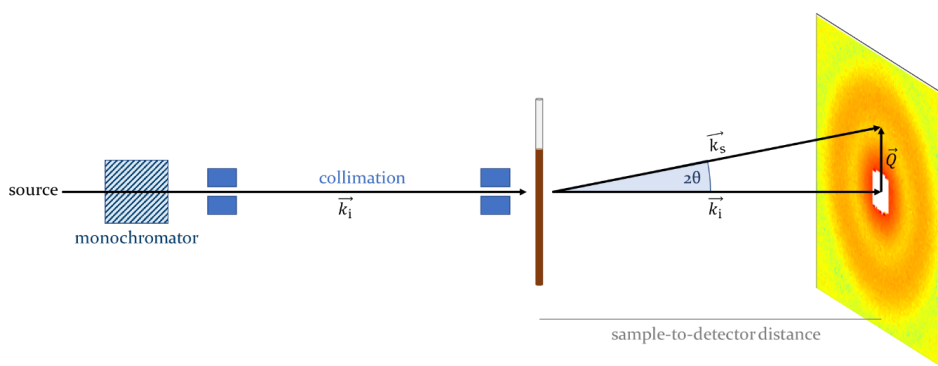
Scheme 3.4 Schematic representations of different types of point lattices in two dimensions: (a) crystal, (b) amorphous, (c) ideal paracrystal, (d) real paracrystal. Reprinted from [12] with permission from Taylor & Francis.

All structures are based on quadrilaterals, but their individual appearance and distribution differ. In a crystal, the quadrilaterals are identical and perfectly ordered in rows and columns while for the amorphous case, every form is individual and their positions to each other highly distorted. The ideal paracrystal shows parallelepipeds which can be easily enumerated even though their forms are not identical. In a real paracrystal, each side of the quadrilaterals has different direction and magnitude, but the assembly can still be divided in rows and columns.

3.2 Small-Angle Scattering Experiments

The next section will deal with the set-up and conduction of a SAS experiment. Unless otherwise stated, everything explained here holds true for both X-rays and neutrons.

A schematic drawing of the basic set-up of a SAS instrument is shown in Scheme 3.5. Originating from the source, the beam is guided towards the sample position and due to interaction with the sample scattered onto the detector where the intensity for each value of Q is counted and transferred to electronic data.



Scheme 3.5 Schematic set-up of a small-angle scattering instrument.

For the generation of X-rays, two cases have to be distinguished, the laboratory setup and the synchrotron. Synchrotrons are large-scale facilities consisting of long storage rings for particles like electrons or positrons. These are periodically accelerated perpendicular to the propagation direction by magnet arrays like undulators, producing X-rays of high brilliance. A range of wavelengths is accessible by this method. Laboratory SAXS instruments create X-rays from metal anodes. The wavelength is restricted to the K_α -line of the anode material by optics. Typical wavelengths are 1.54 Å for copper or 1.34 Å for gallium. The X-rays are then collimated by an arrangement of slits.

Neutron sources are usually not found in a laboratory but in large-scale facilities as only nuclear processes like fission or spallation produce enough flux for scattering experiments.^[7] The material used in fission reactions is the uranium isotope ^{235}U . When hit by a neutron, the uranium atom is split into smaller nuclei and releases on average 2.5 neutrons which are either used to continue the fission reaction or extracted from the reactor core for experiments. These neutrons have high energies in the MeV range which corresponds to wavelengths of about

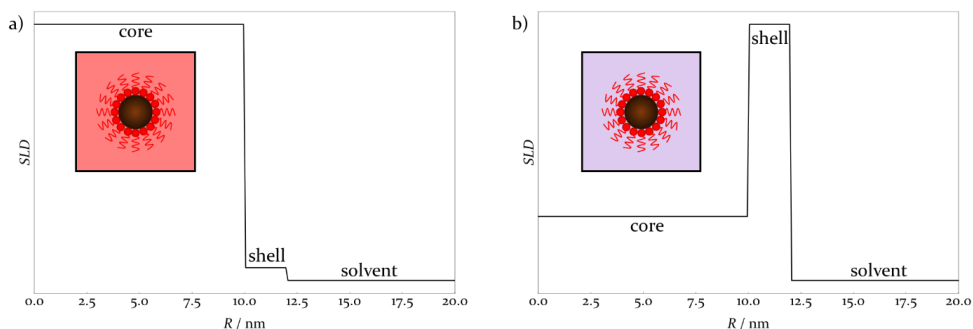
10^{-5} Å. As the desired wavelengths for SANS are much larger (several Å), the neutrons have to be slowed (“cooled”) down. This is done by elastic impacts with another material, which is known as “moderation”. For SANS at the FRM II reactor at the MLZ in Garching, Germany, liquid deuterium is used as the “cold source” which releases neutrons of suitable wavelengths. The neutrons are then transported to the instrument *via* neutron guides. Using total reflection, the neutrons are prohibited from leaving the guide and the beam arrives with only very small intensity loss at the instrument. At that point, the neutron beam still includes a large distribution of wavelengths. To select a certain wavelength for the experiment, monochromators like velocity selectors are used. These consist of rotating tilted lamellae which can only be traversed by neutrons with the correct velocity. Similar to X-rays, the neutrons are then collimated by slits.

In the scattering process, the two probes show different behaviours. While X-rays interact with and are scattered by the electron clouds of the atoms, neutrons are scattered by the nuclei of the atoms. This directly leads to one main difference for the two methods as well as a reason why their combination is highly beneficial for the analysis of many kinds of materials. Heavy elements possess a high probability for the scattering of X-rays due to their high amount of electrons. This probability is known as scattering cross section and is inherently different for neutrons where the value of the scattering cross sections varies strongly for consecutive atoms in the periodic table as well as for different isotopes of the same element. Although hydrogen is hardly visible for X-rays, especially if heavier atoms are present, it is well-distinguishable for neutrons. For organic materials like polymers, the possibility to selectively deuterate is a great benefit to study distinct parts of the sample. To describe this, the concept of the scattering length density (SLD) is introduced as

$$\rho = \frac{\sum_i b_i}{V_p} \quad (3.13)$$

with b_i as the scattering length of the atom. For X-rays, the scattering length can be calculated by the number of electrons, while tabulated values for each isotope exist in the case of neutron scattering.

The different SLDs between X-rays and neutrons as well as between different isotopes for neutrons can be used for contrast matching experiments. A good example for this is inorganic nanoparticles with an organic shell consisting of surfactants or polymers in deuterated organic solvents or polymer melts which is displayed in Scheme 3.6.



Scheme 3.6 Hypothetical contrasts for the same sample, consisting of an inorganic core stabilised with an organic shell and dispersed in a deuterated organic solvent, for X-rays (a) and neutrons (b).

Due to the much higher number of electrons in the nanoparticle core as compared to shell and solvent, it can easily be studied with X-rays. The difference in SLD between the shell and the solvent is small for X-rays, even if the solvent is deuterated as this does not change the number of electrons. A neutron scattering experiment will clearly show the protonated shell as the SLD differentiates significantly between hydrogen and deuterium. Therefore, the combination of SAXS and SANS is beneficial to obtain information about the whole sample.

After passing the sample, the part of the beam which scattered in the correct angular region for SAS is collected on the detector. To prevent the high intensity of the primary beam from hitting the detector, a beam-stop is installed which absorbs the incoming neutrons or X-rays. Typical materials are cadmium or boron carbide for neutrons and heavy elements like tungsten or lead for X-rays. Detectors fulfil the task of converting the incoming photons or neutrons to an electric signal. For X-rays, detectors are for example CCD cameras or hybrid photon counting detectors which use the photoelectric effect. Commonly used SANS detectors are based on scintillation or fission reactions (gas proportional counters) to produce charged particles. Materials with a high absorption cross section for neutrons are needed for these devices, including ${}^6\text{Li}$ for scintillators and ${}^3\text{He}$ for the gas proportional counters.

Next to the contributions stated in equation (3.8), the counted intensities on the detectors depend on the incident beam intensity I_0 , the irradiated area A , the transmission of the sample Tr , as well as its thickness t :

$$I(Q) = I_0 \cdot A \cdot Tr \cdot t \cdot \Phi V_p^2 \Delta\rho^2 P(Q) S(Q) \quad (3.14)$$

These parameters are either known from the experimental set-up or have to be determined in reference measurements to be able to obtain the scattered intensity of the sample in absolute units. For isotropically scattering samples, the intensities are usually radially

averaged to gain high statistics for each Q value. By separately measuring the pure solvent, the background from this component can be subtracted.

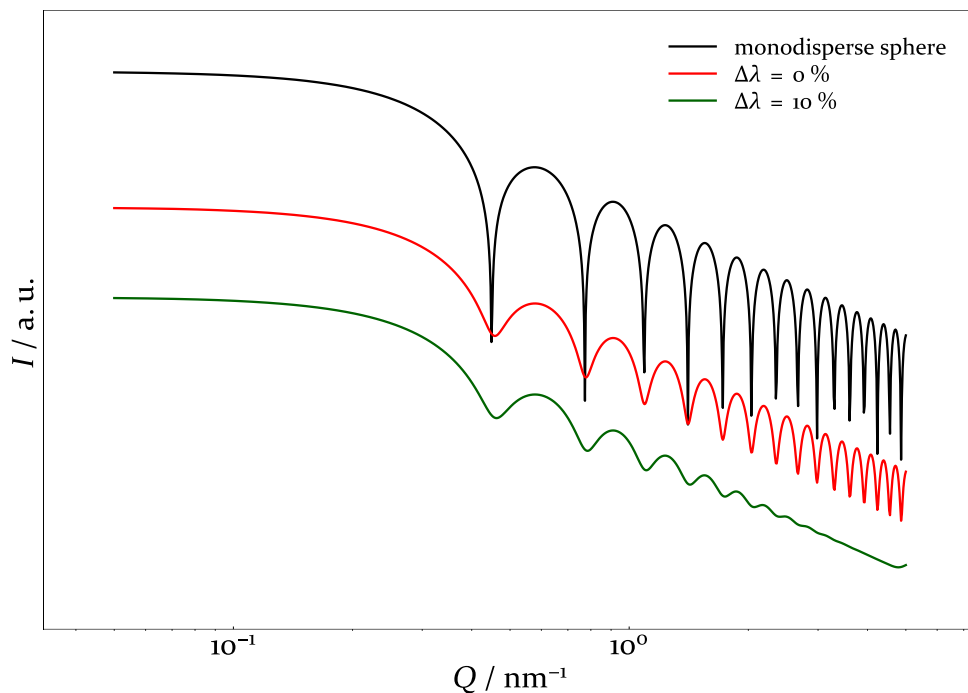


Figure 3.7 Scattering curves for monodisperse spheres considering the resolution of the instrument. The black curve shows only the monodisperse sphere form factor, the red and green curves use Pedersen's resolution function to account for the decrease in resolution due to instrument parameters (20 m collimation and detector distance, 50·50 mm² collimation aperture and 10·10 mm² sample aperture, $\lambda = 5 \text{ \AA}$) and wavelength spread $\Delta\lambda$.

In contrast to SAXS instruments where the wavelength of the probe is very well-defined, SANS instruments rely on the trade-off between narrow wavelength distributions and required intensity levels. They typically have wavelength spreads of about 10 % when using devices like velocity selectors to monochromatize the beam. In combination with geometrical factors originating from the collimation of the beam, the wavelength spread influences the resolution of the measurement. Therefore, it needs to be included into the evaluation of the data. For pin-hole instruments, an approach for this was developed by Jan Skov Pedersen.^[B] The influence of the resolution is displayed in Figure 3.7 in which the black curve shows the monodisperse sphere form factor from before. The red and green curves were calculated using Pedersen's approach, with the green one showing only the difference in resolution due to the instrument

geometry. As a result, the minima of the form factor are smeared which intensifies for the green curve where a wavelength spread of 10 % was assumed.

Because of the phase problem of scattering, a Fourier transformation of the experimental data to obtain the real space structure is usually impossible. Therefore, suitable models have to be found to describe the data, revealing the sought-for parameters for the characterisation of the sample by fitting them to the experimental data. Complementary methods like microscopy are beneficial to gain first insights regarding the structure of the sample, which is helpful to choose the correct models to fit the data.

3.3 References

- [1] I. Grillo, *Soft-Matter Charact.* **2008**, DOI 10.1115/ICES2006-1436.
- [2] B. Hammouda, *Probing Nanoscale Structures - The SANS Toolbox*, National Institute Of Standards And Technology, Gaithersburg, **2009**.
- [3] T. Li, A. J. Senesi, B. Lee, *Chem. Rev.* **2016**, *116*, 11128.
- [4] T. Brückel, in *Lab. Course Neutron Scatt. Lect.* (Eds: T. Brückel, S. Förster, G. Roth, R. Zorn), Forschungszentrum Jülich GmbH Zentralbibliothek, Jülich, **2018**, pp. 2.1-2.34.
- [5] S. Jaksch, in *Scatt. Soft, Funct. Quantum Mater. Lect. Notes* (Eds: M. Angst, T. Brückel, S. Förster, K. Friese, R. Zorn), Forschungszentrum Jülich GmbH Zentralbibliothek, Jülich, **2019**, p. D1.1-D1.29.
- [6] H. Frielinghaus, in *Lab. Course Neutron Scatt. Lect.* (Eds: T. Brückel, S. Förster, G. Roth, R. Zorn), Forschungszentrum Jülich GmbH Zentralbibliothek, Jülich, **2018**, pp. 5.1-5.43.
- [7] J. Voigt, in *Lab. Course Neutron Scatt. Lect.* (Eds: T. Brückel, S. Förster, G. Roth, R. Zorn), Forschungszentrum Jülich GmbH Zentralbibliothek, Jülich, **2018**, pp. 3.1-3.15.
- [8] S. Förster, A. Timmann, C. Schellbach, A. Frömsdorf, A. Kornowski, H. Weller, S. V. Roth, P. Lindner, *Nat. Mater.* **2007**, *6*, 888.
- [9] S. Förster, A. Timmann, M. Konrad, C. Schellbach, A. Meyer, S. S. Funari, P. Mulvaney, R. Knott, *J. Phys. Chem. B* **2005**, *109*, 1347.
- [10] H. Schnablegger, Y. Singh, *Ant. Paar GmbH* **2013**, DOI 10.1006/aphy.1994.1055.
- [11] R. Schweins, K. Huber, *Macromol. Symp.* **2004**, *211*, 25.
- [12] R. Hosemann, A. M. Hindeleh, *J. Macromol. Sci. Part B* **1995**, *34*, 327.
- [13] J. S. Pedersen, D. Posselt, K. Mortensen, *J. Appl. Crystallogr.* **1990**, *23*, 321.

4 Self-Assembly of Iron Oxide Nanocrystals in Magnetic Fields up to 3 T Studied by Small-Angle Neutron Scattering

I characterised the samples *via* Small-Angle X-Ray Scattering and analysed the results. I successfully applied for the first beamtime at the MLZ and assisted in composing the proposal for the second beamtime. I performed the SANS experiments at KWS-I and fitted the 1D and 2D data. All parts of this manuscript unless otherwise stated were written by myself. Walter Van Herck developed the models, programmed the code for BornAgain and started the evaluation of the 2D SANS data. He prepared a first draft for the detailed description of the BornAgain data evaluation which can be found in the Supporting Information. Artur Feld and Agnes Weimer synthesised and oxidised the nanocrystals, performed and evaluated the TEM measurements and prepared the samples for the SANS measurements. Artur Feld applied for the second beamtime at the MLZ and was part of the experimental team for this experiment. Artem Feoktystov and Lester Barnsley helped me during the experiments at KWS-I, treated the SANS data and provided information about instrument parameters for the analysis of the data. Ralf Biehl, Margarita Kruteva and Jürgen Allgaier assisted me with helpful discussions and in writing this manuscript. Stephan Förster established the cooperation for the SANS 2D data analysis with BornAgain and did the first fit of the 3 T data with which he determined the bct crystal lattice.

4.1 Introduction

The self-assembly of magnetic nanocrystals (NCs) is a versatile approach towards many kinds of applications like high density data storage^[1,2], electrical transport and magnetic switching^[3] or even the arrangement of non-magnetic matter^[4]. In addition, biological applications like biosensors, contrast agents, drug delivery, hyperthermia^[5] or even responsive 1D mesostructures like artificial cilia actuated by magnetic fields^[6] are nowadays important topics for research. A thorough investigation of the self-assembly behaviour of these NCs in solution is highly desirable as the self-assembly of nanoprobe inside of cells or the body in general is necessary for various applications.^[7]

Iron oxide nanocrystals are the most used magnetic NCs as they are considered safe for medical usage by both the US Food and Drug Administration (FDA) and the European Medicines Agency (EMA).^[5] Furthermore, they can be synthesised in large quantities and high qualities, especially regarding their monodispersity^[8] which is a key factor for defined magnetic properties.

Due to their magnetic dipole in external fields, magnetic NCs tend to form chain-like structures.^[9,10] Highly ordered structures built from NCs have so far mostly been obtained by evaporation of the solvent leading to two- or three-dimensional structures.^[11,12] For large NCs with diameters of around 200 nm, colloidal crystals have been observed to form with and without magnetic fields.^[13,14] Both approaches rely on the (at least partial) separation of the NCs and their matrix. In contrast to the large colloidal particles, smaller NCs are stable in solution but are much harder to assemble, especially if they do not possess any kind of shape anisotropy.^[15] Therefore, literature about the reversible self-assembly of small spherical NCs is rather scarce. Fu and co-workers studied iron oxide NCs with a diameter of 17 nm dispersed in toluene and observed the formation of a face-centred cubic (fcc) lattice already at a field strength of 0.1 T which became more pronounced at higher field strengths.^[16]

The aim of this study is to investigate the structure formation of iron oxide NCs in a magnetic field. The magnetic field induces self-assembly of the NCs of about 20 nm in diameter. Small-angle scattering (SAS) contains information about shape of the NCs and their 3D assembly because the scattered intensity $I(Q)$ depends on the form factor $P(Q)$ and the structure factor $S(Q)$ as^[17]

$$I(Q) \cong P(Q) \cdot S(Q) \tag{4.1}$$

We use small angle X-ray scattering (SAXS) to study the formfactor and small-angle neutron scattering (SANS) to examine how structure evolves. Already at low fields the NCs show ordering and at higher field strengths a highly ordered body-centred tetragonal crystal lattice appears.

4.2 Results and Discussion

The nanocrystals were synthesised *via* thermal decomposition of an iron precursor resulting in oleic acid (OA) stabilised iron oxide NCs.^[18] Prior to the measurements in magnetic fields, the NCs were oxidised to obtain one crystal phase of iron oxide (maghemite). This is beneficial for their magnetic properties as multiple iron oxide modifications are usually present in iron oxide NCs after their synthesis. As these procedures are not a part of this thesis, it will not be discussed here.

4.2.1 Structural exploration

SAXS and TEM – Characterisation of the NC core

A first characterisation of the NCs was done *via* transmission electron microscopy (TEM) and SAXS.

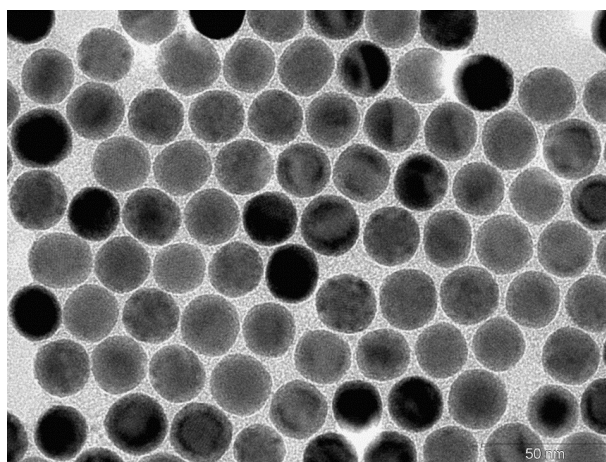


Figure 4.1 TEM image of iron oxide NCs.

In Figure 4.1, a TEM image of the used iron oxide NCs is shown. The NCs are highly monodisperse and a radius of $10.55 \text{ nm} \pm 5.6\%$ could be determined from TEM measurements. The SAXS experiment reveals sharp minima which stress the low polydispersity of the NCs (Figure 4.2).

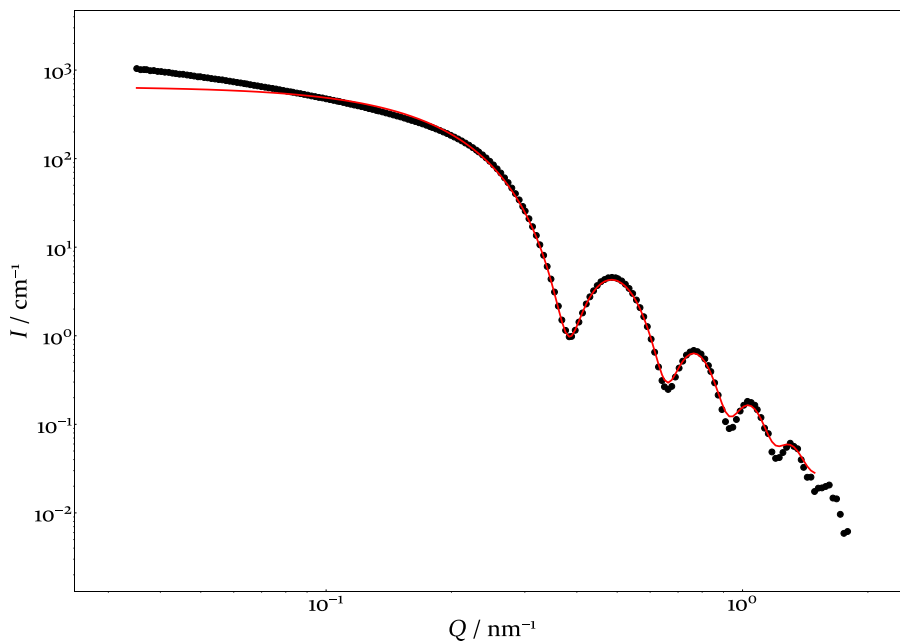


Figure 4.2 SAXS data of iron oxide NCs in toluene.

While the contrast of the scattering length densities of the NC core to the surrounding solvent is rather high in SAXS, the surfactant shell only has a very small contrast and is therefore negligible. The data was fitted with a spherical form factor considering the polydispersity of the radius of the NCs by means of a Gaussian distribution. The radius was determined to be 11.93 nm with a polydispersity of 0.73 nm (6%). Due to scattering probing the bulk of the sample instead of a fraction of the sample in dried form like TEM does, the result for the core radius from SAXS is chosen for the following evaluations. For low Q values, the form factor does not describe the data sufficiently. The slope at low Q is of the order of $Q^{-0.9}$ which hints to smaller aggregates as dimers or trimers while larger aggregates would lead to a Q^{-3} - Q^{-4} power law. The aggregation is most likely a result of the oxidation process as rather harsh conditions are used.

SANS – Experiment in magnetic fields up to 3 T

The NCs were dispersed in deuterated toluene ($c_{\text{NCs}} \sim 30 \text{ mg/ml}$) and filled into a rectangular Quartz cell of 1 mm thickness (Hellma, Müllheim). The setup of the experiment at KWS-1 can be seen in Figure 4.3.

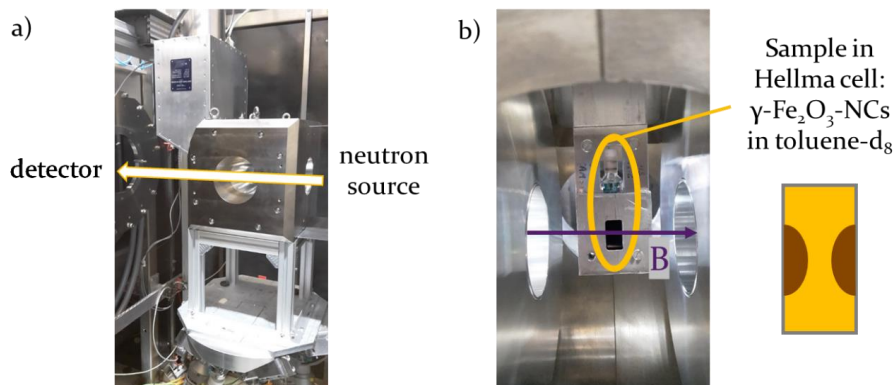


Figure 4.3 Setup of SANS experiment at KWS-1. a) Sample environment with hexapod and cryomagnet. b) Position of sample inside the magnet.

The 3 T cryomagnet was mounted on a hexapod to allow an easy alignment of the sample environment (Figure 4.3a). The cell was fixated in a sample holder that could be installed from the top of the magnet (Figure 4.3b). The sample aperture was chosen to match the dimensions of the cell as close as possible to get a full view of the sample. During the experiment at higher field strengths, the NCs formed self-assembled structures at positions in the cell where the concentration was locally increased (scheme on the right of Figure 4.3b). This indicates a field inhomogeneity as magnetic NCs tend to assemble at positions where the force of the magnetic field is highest.^[19] Because of the full cell being illuminated by the beam, not only the highly concentrated regions but also the parts with low particle density contribute to the obtained scattering patterns. Without magnetic field, the NCs could simply be homogenised by shaking the cell, showing the reversibility of the self-assembly.

SANS – Characterisation of the NC shell

At 0.0 T the 2D data was isotropic, and radial averaging could be applied. For neutrons, the contrast between surfactant shell and solvent is high (much higher than the contrast between the NC core and the solvent). Thus, SANS gains information about the surfactant shell in addition to the NC core and a core-shell form factor was used to describe the data:

$$P(q) = [V_c \cdot (\rho_c - \rho_s) \cdot A_1 + V \cdot (\rho_s - \rho_m) \cdot A_2]^2 \quad (4.2)$$

$$A_1 = 3 \frac{\sin(qR_c) - qR_c \cdot \cos(qR_c)}{(qR_c)^3} \quad (4.3)$$

$$A_2 = 3 \frac{\sin(qR) - qR \cdot \cos(qR)}{(qR)^3} \quad (4.4)$$

where V_c is the core volume, V the total volume of core and shell, ρ_c , ρ_s and ρ_m the scattering length densities of core, shell and medium, R_c the radius of the core and R the total radius of core and shell. For each detector distance, the corresponding resolution function was used for the fits.^[20] The core radius was fixed to the value obtained from SAXS. The scattering length densities were fixed to the theoretical values of $\rho_c = 6.656 \cdot 10^{-6} \text{ \AA}^{-2}$, $\rho_s = 7.762 \cdot 10^{-8} \text{ \AA}^{-2}$ and $\rho_m = 5.664 \cdot 10^{-6} \text{ \AA}^{-2}$.

The 1D data is much more sensitive to deviations from the ideal core-shell model than the 2D data and was therefore used to identify a suitable model. As the available BornAgain script allows only one polydisperse parameter, a choice had to be made between the core radius and the shell thickness. For the low Q data, we observe deviations from a single particle model indicating aggregation within the sample which results in a rather high value for χ^2 allowing only a relative comparison.

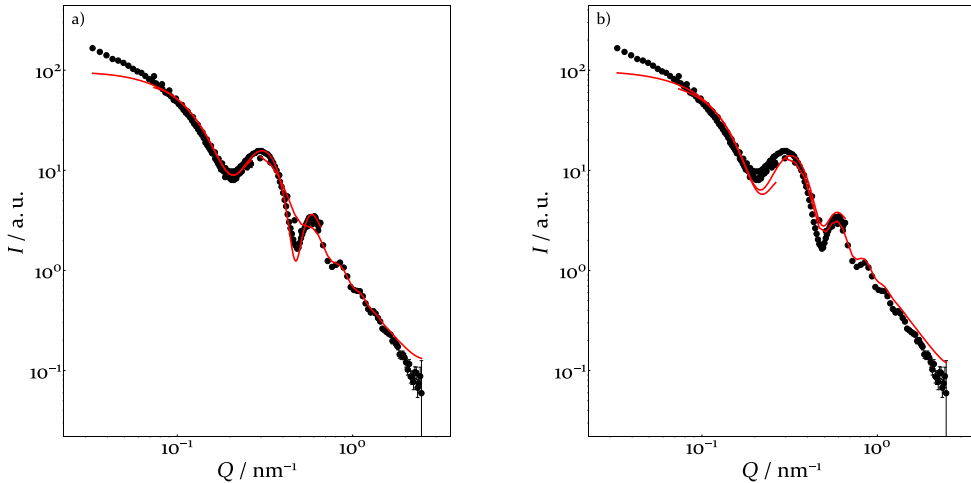


Figure 4.4 SANS data of iron oxide NCs at 0 T, black dots: experimental data, red solid line: fit with respective core-shell model taking into account either a) a lognormal distribution for the shell thickness or b) a Gaussian distribution for the core radius.

Two models were tested to fit the data: 1) A Gaussian distribution was employed for the core radius (see Figure 4.4b) which had already been used to describe the SAXS data, the standard deviation was fixed to the one obtained from the SAXS fit. 2) For the shell thickness, a lognormal distribution was assumed (see Figure 4.4a). The second model led to a significantly better result (four times smaller χ^2). As a result, the polydispersity of the shell thickness was chosen to be included into the core-shell model, resulting in a value of 0.82 nm for the shell thickness with a standard deviation of 0.37 nm (45 %). The available BornAgain model describes core and shell by constant scattering length densities, which might not be an accurate description for the oleic acid shell as this is only valid for a rather compact structure. This must not necessarily be the case for the shell around a NC, especially for lower grafting densities or at distances further away from the core.

Small-Angle Neutron Scattering (SANS) – Ordering in magnetic field

Data were obtained at five different field strengths: 0.0, 0.1, 0.5, 1.0 and 3.0 T. The scattering patterns with their corresponding fits are displayed in Figure 4.5.

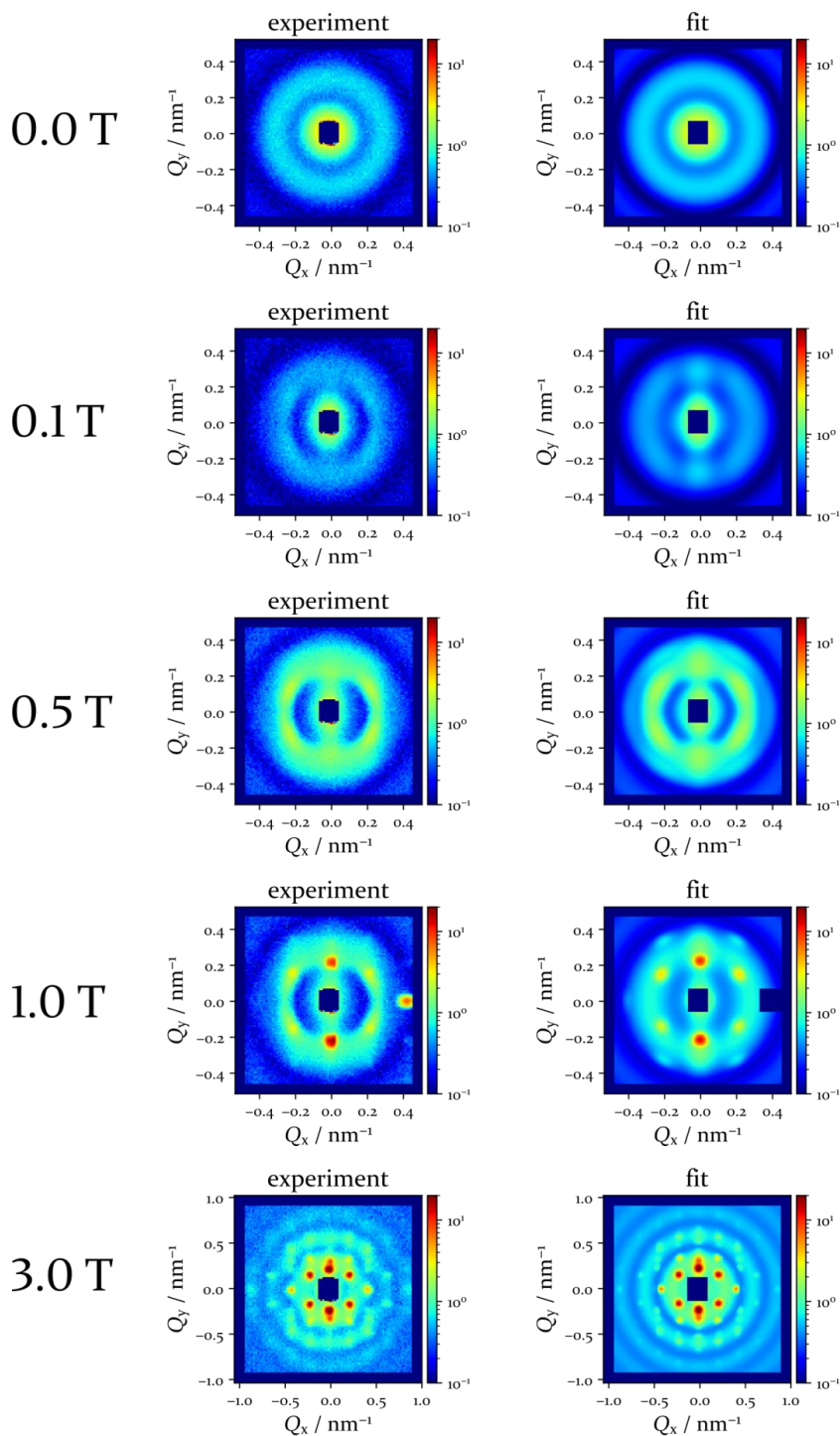


Figure 4.5 Scattering patterns at different field strengths and corresponding fits. All images share the same scale of the intensity coloring.

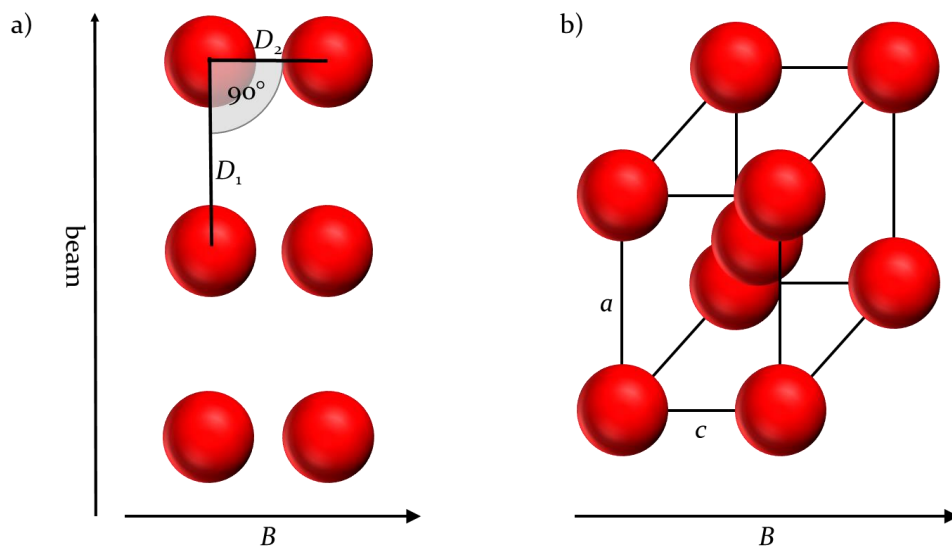
Besides the data at 0.0 T, all scattering patterns are clearly anisotropic. Applying a magnetic field of 0.1 T immediately induced an ordering, that becomes more pronounced with increasing field strength. This corresponds to the NCs aligning themselves in linear chains alongside the magnetic field vector.^[9,21] At 3 T, sharp Bragg peaks can be observed, indicating a defined crystal structure. It is well-known that spherical particles at high concentrations form structures like body- or face-centred cubic (bcc/fcc) or body-centred tetragonal (bct) which coexist with linear chains.^[14,16,21] Due to the asymmetry, a cubic lattice can be excluded for our measurement. The bright peak at high Q s was masked for the fit of the 1 T image due to a slight misalignment of the sample with respect to the beam. The data at 3 T were taken at a detector distance of 4 m to obtain an image of the whole scattering pattern on the detector. In addition, the misalignment was corrected. Now, one can observe peaks of higher orders, indicating larger crystals in a well oriented sample.

To fit the data, a combined model based on the spherical core-shell form factor F that was used for the radially averaged data was employed. Three states of the assembly can be present in the solution at the same time with varying fractions φ in dependence of the applied field: 1) the disordered state of nanoparticles without interactions ($S = 1$); 2) a paracrystal to represent the linear chains ($S_{\text{paracrystal}}$) and 3) a bct lattice (S_{bct}):

$$I(Q) = \varphi_{\text{disorder}} P(Q) + \varphi_{\text{partial order}} P(Q) S_{\text{paracrystal}}(Q) + \varphi_{\text{bct}} P(Q) S_{\text{bct}}(Q) \quad (4.5)$$

The core radius was fixed to the value obtained from the SAXS experiment for all 2D data. The SLDs were fixed to the values stated above and the shell thickness was again fitted by using a lognormal distribution.

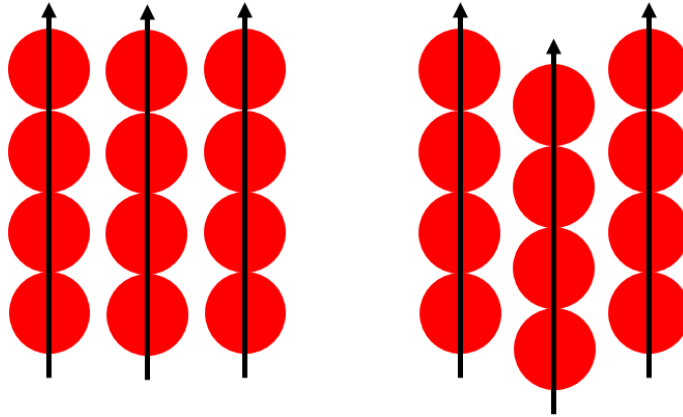
The partial ordering corresponding to the linear chains was described by a finite 2D paracrystal^[22], consisting of three lattice sites in beam direction (Q_z) and two horizontally (Q_x) (see Scheme 4.1a).



Scheme 4.1 Structures formed by NCs in magnetic fields: a) 2D paracrystal; b) bct lattice.

In the paracrystal, the NCs are arranged as a rectangular lattice with an angle of 90° between the basis vectors, a distance D_1 in beam direction and a much shorter distance D_2 in field direction. This model was chosen to represent the structures that are expected to form for magnetic NCs in external fields^[9]. In field direction, the NCs form chain-like structures with minimal distance between each other because of attractive dipole-dipole interactions between them. Perpendicular to this direction, the interactions between the NCs are repulsive and therefore, the distance does not obtain a similar value as in the field direction.

The body-centred crystal lattice (Scheme 4.1b) is a commonly appearing structure for colloidal assemblies and it fits well into the predicted phase diagram for dipolar hard and soft spheres.^[21] Usually, a cubic lattice were to be expected, but due to the dipoles of the NCs, a tetragonal lattice is formed in these experiments. Here, the short c axis is oriented parallel to the field. The reason why it makes sense for particles to form this structure is the minimisation of the distance of dipolar chains as depicted in Scheme 4.2.



Scheme 4.2 Dipolar chain assemblies.

In magnetic fields, the particles tend to form chains alongside the field direction (left side of Scheme 4.2). Due to the dipoles having the same direction, the force between them is repulsive. If one of the chains is shifted in the direction of the field, the repulsion between the chains is decreased leading to a much more energetically favourable and therefore stable configuration.^[21]

The averaging of the orientations of the crystals is taken into account by using a wrapped normal distribution to account for the periodicity of the angle.

SANS –Results from 2D Data

In Figure 4.6, the fractions for the used models are collected. Without magnetic field, the NCs are in the disordered state and can be described by the form factor only. A small magnetic field of 0.1 T induces the alignment of the NCs into linear chains. Therefore, the paracrystal is used to account for the partial ordering. Already at 0.5 T the peaks are too pronounced to be sufficiently described by the paracrystal and the bct lattice is added to the fit. The same is true for the higher magnetic fields of 1 and 3 T. For 3 T, the fraction of the bct lattice decreases compared to the 1 T data.

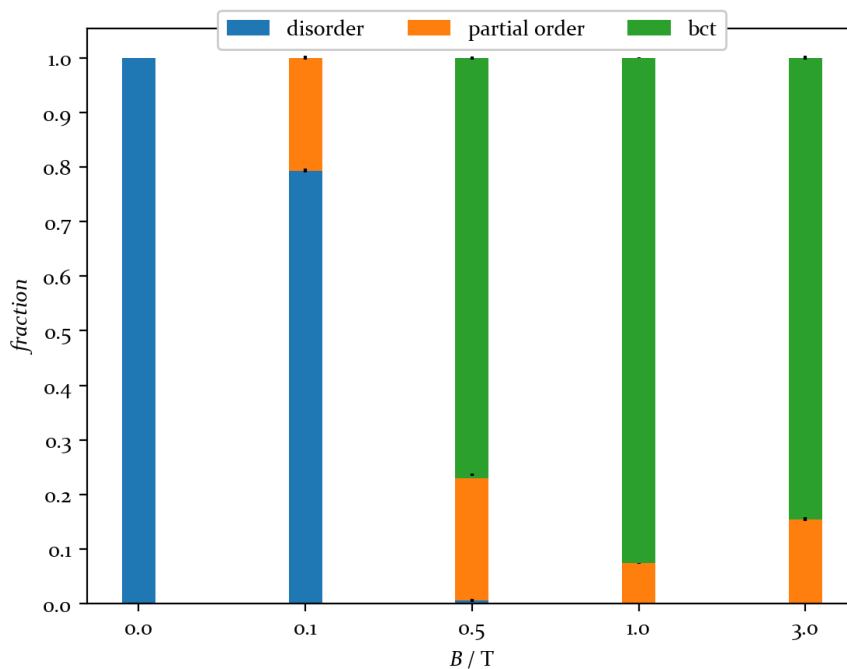


Figure 4.6 Fractions for used models.

The shell thickness of 0.85 nm at 0.0 T is in a good agreement to the result from the 1D data evaluation but the polydispersity is much higher for the 2D data (0.82 nm (96 %)). For these parameters, the 1D data is more trustworthy than the 2D data as the scattering curve is much more sensitive to the form factor oscillations. Increasing the field strength leads to a reduction of the shell thickness (Figure 4.7a) indicating a compression of the surfactant molecules. The change of the distances in the paracrystal can be seen in Figure 4.7b. For D_2 which is parallel to B , a value of about 25 nm could be obtained while D_1 is significantly larger at the beginning with 260 nm but decreases to about 52 nm at 3.0 T. By increasing the field strength, the nanoparticle chains move closer together, ultimately leading to the formation of the bct crystal structure.

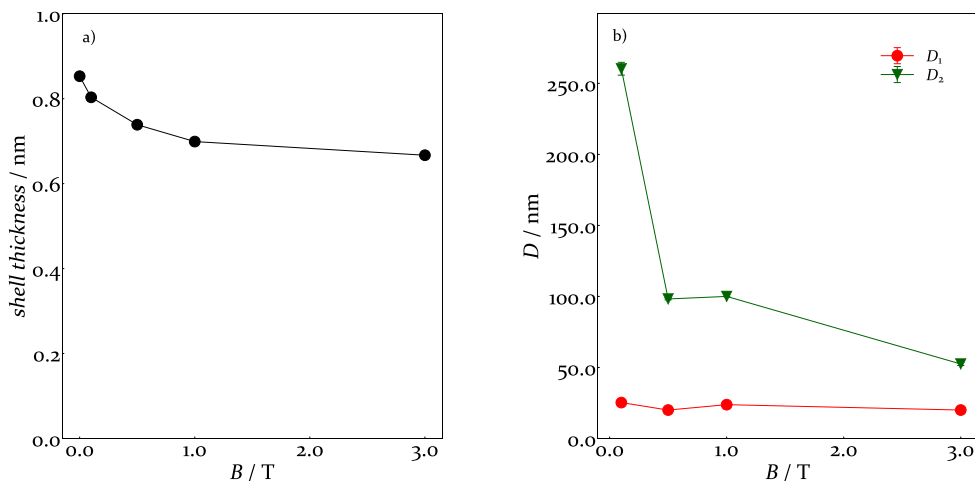


Figure 4.7 Dependence of shell thickness (a) and distances in paracrystal (b) on the magnetic field strength. Lines are added as guide for the eye.

This coincides with the decreasing of the lattice constants in the bct crystal structure (Figure 4.8a). They change from $a = 40.56$ nm and $c = 29.00$ nm (0.5 T) to $a = 38.68$ nm and $c = 28.50$ nm (3.0 T). Using the so obtained lattice constants in combination with the total diameter of the NCs as a sum of core radius and shell thickness, the distances between the NC surfaces in the bct lattice can be calculated while taking into account the core radius and the obtained effective shell thickness.

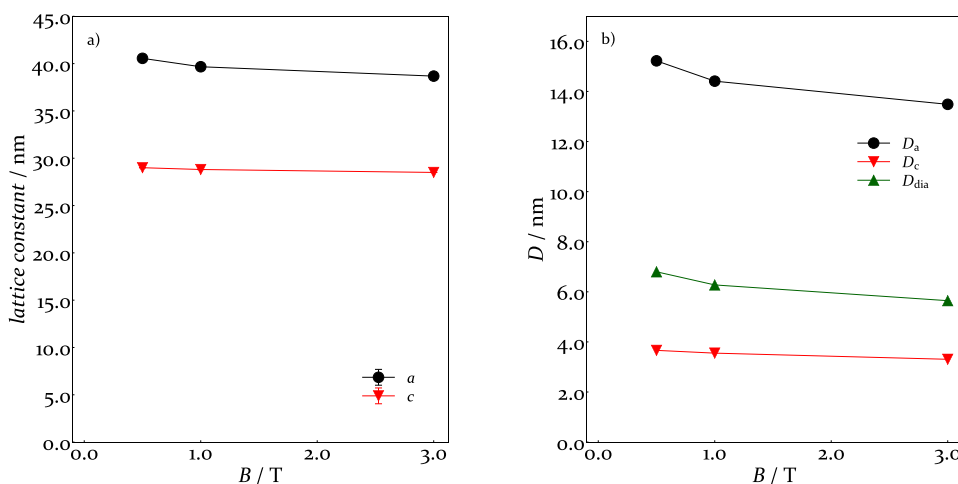


Figure 4.8 Dependence of the lattice constants and thus the distances of the NCs in the bct lattice on the magnetic field strength. Lines are added as guide for the eye.

The resulting values for the distance along a (D_a) and c (D_c), as well as along the diagonal (D_{dia}) are displayed in Figure 4.8b. The closest distance between the NCs is along the short c axis. This is high enough that a compression of the surfactant shell would not be required.

The results from this experiment clearly show the self-assembly of the NCs with linear chains forming at lower field strengths which approach each other until they form a bct lattice. While a homogeneous magnetic field could explain the chain formation, attractive interactions leading to locally increased NC concentration relies on inhomogeneous field where the NCs are driven towards the region of the highest field. Although the high concentration itself can already be the reason for crystalline phases as is known for colloidal particles^[13], the bct phase is a result of the dipole moment of the NCs in the magnetic field^[14,21]. For more precise information about the phase transitions between paracrystal and bct, more field steps are necessary.

There are two main reasons for the smearing of the peaks in the experimental data. First, the finiteness of the crystal is contributing to the broadening of the peaks. Second, there is disorder due to rotation and distribution of lattice lengths. Additionally the force on the NC dipole that drives the formation of high concentration regions depends on the local field gradient. This is not constant within the bct domain and might lead to small changes in the lattice constant dependent on position in the bct domain. The higher order peaks are suppressed by the displacement of the NCs inside the lattice (Debye-Waller factor). The mean-square-displacement in this structure is of the order of 7 nm² at 0.5 T and reduces to 5 nm² at 3 T.

4.2.2 Searching for Phase Transition

A new batch of oxidised NCs was created which was again first characterised *via* TEM and SAXS.

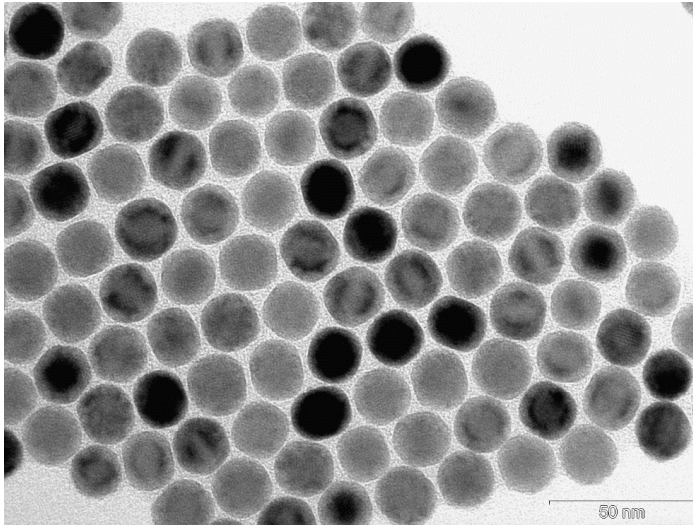


Figure 4.9 TEM image of second batch of NCs.

The radius obtained from the TEM experiments was $9.14 \text{ nm} \pm 5.5 \%$ showing that the second batch of NCs is as monodisperse as the first batch. This was further confirmed by a SAXS measurement.

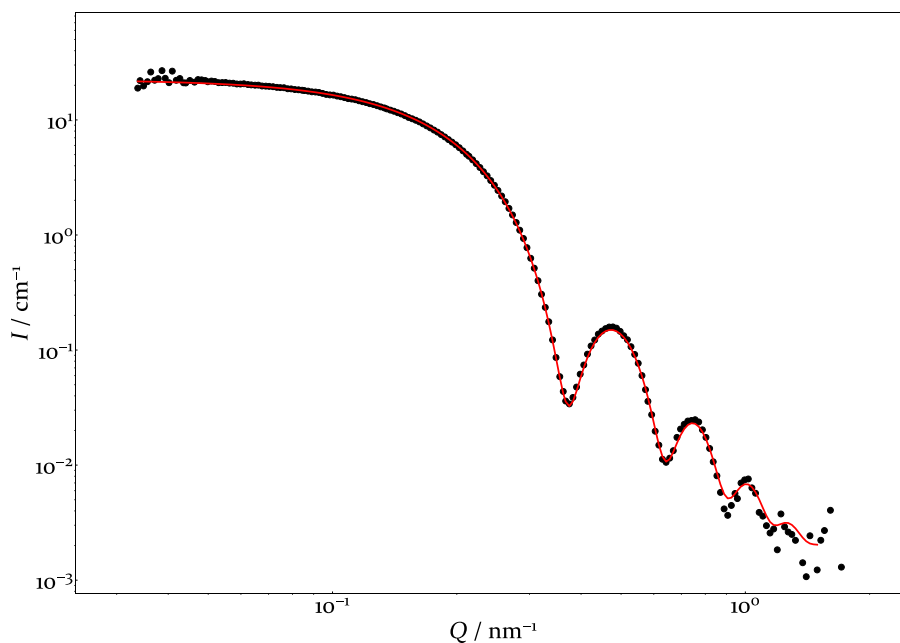


Figure 4.10 SAXS data for second batch of NCs, black dots: experimental data, red solid line: fit with sphere form factor.

As can be seen in Figure 4.10, the data can be well described with a sphere form factor this time indicating that no aggregates are present in this sample. The radius was determined to be 12.23 nm with a polydispersity of 0.74 nm (6%).

The same instrumental setup as for the first SANS experiment was used. The magnetic field was varied between 0 and 2.95 T in 0.05 T increments. The 1D data of the radial average at 0 T was fitted by the core-shell model with polydispersity assumed for the shell of the NCs or for the core of the NCs (Figure 4.11).

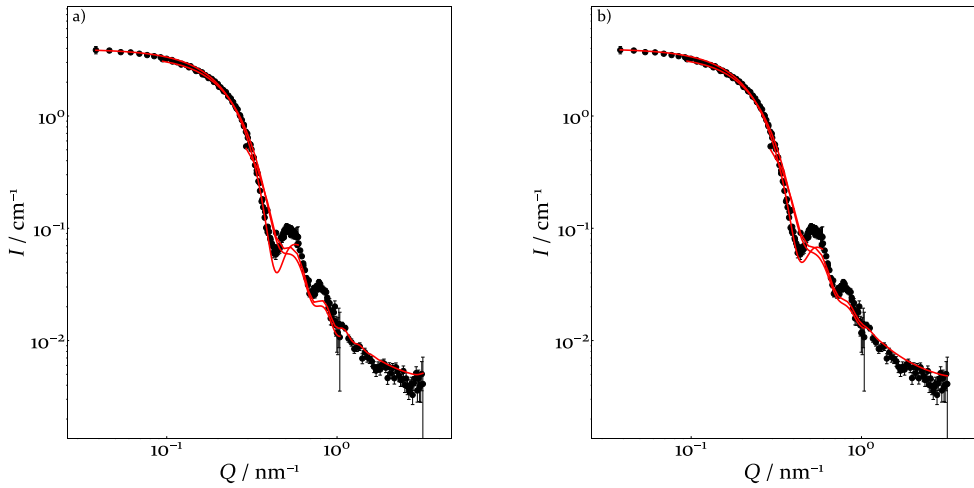


Figure 4.11 SANS data of iron oxide NCs at 0 T from second experiment, black dots: experimental data, red solid line: fit with respective core-shell model taking into account either a) a lognormal distribution for the shell thickness or b) a Gaussian distribution for the core radius.

The model containing the lognormal distribution for the shell thickness (Figure 4.11a) fits slightly better than the model with the Gaussian distribution for the core radius (Figure 4.11b), therefore this model is again chosen for the following 2D data evaluation.

The same radius and polydispersity for the core were used as were determined from the SAXS data of this NCs and the same scattering length densities as for the first experiment. The shell thickness was found to be 0.28 nm with a negligible polydispersity of 0.001 nm. This hints at a lower grafting density of oleic acid around the NCs. The even smaller result for the shell thickness in comparison to the first SANS experiment could be a reason for the similar fit results for both models as the influence of the shell decreases with its volume.

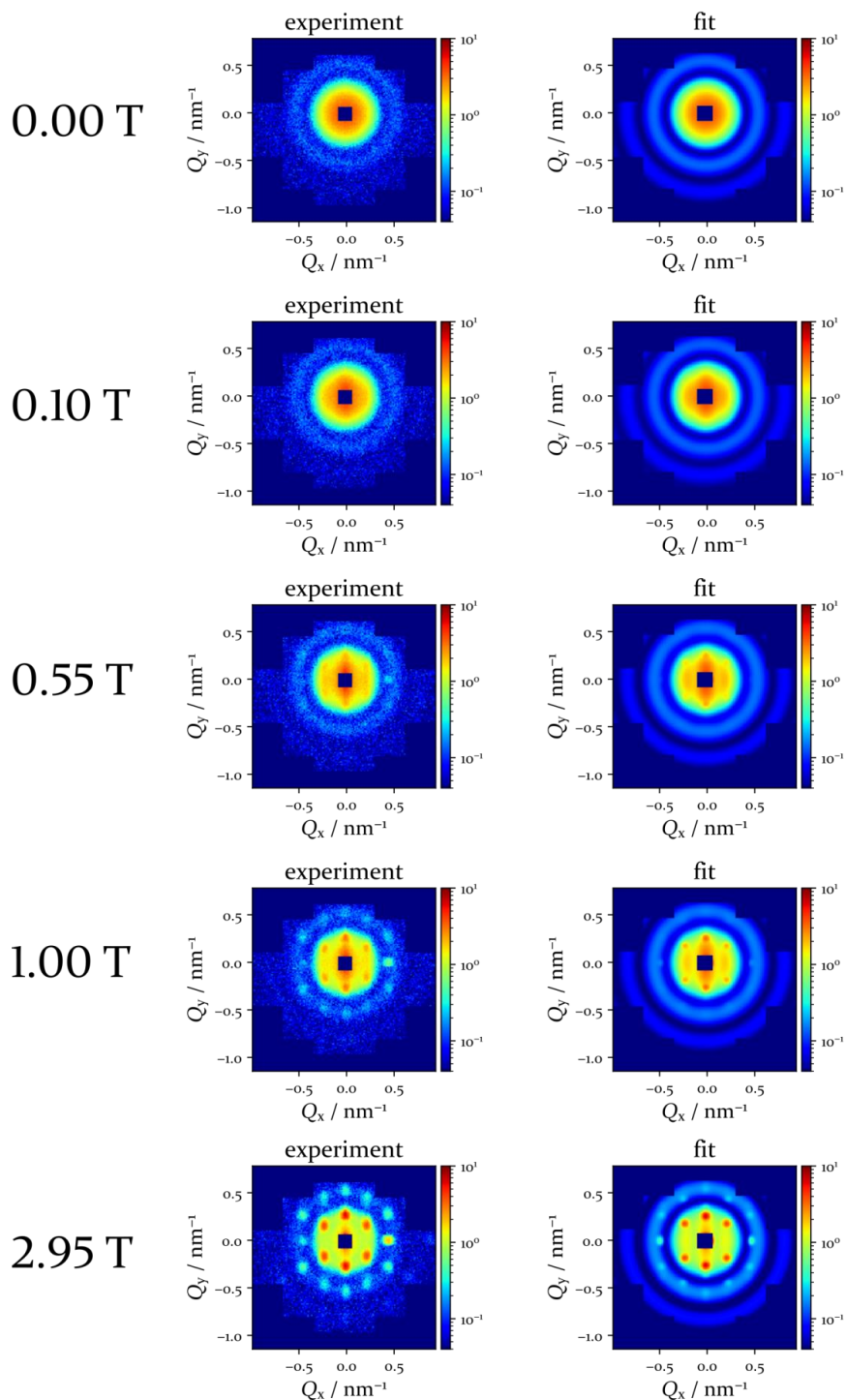


Figure 4.12 Selected 2D scattering patterns for second SANS experiment. All images share the same scale of the intensity coloring.

For the 2D data evaluation, the same models as before were used. A selection of the experimental data and fits are shown in Figure 4.12. For the shell thickness at 0.0 T, a value of 0.33 nm could be obtained. This corresponds well to the 1D result. The mask looks different compared to the first experiment, as the new Helium-3 detector of KWS-1 has a different dimension and layout compared to the old one.

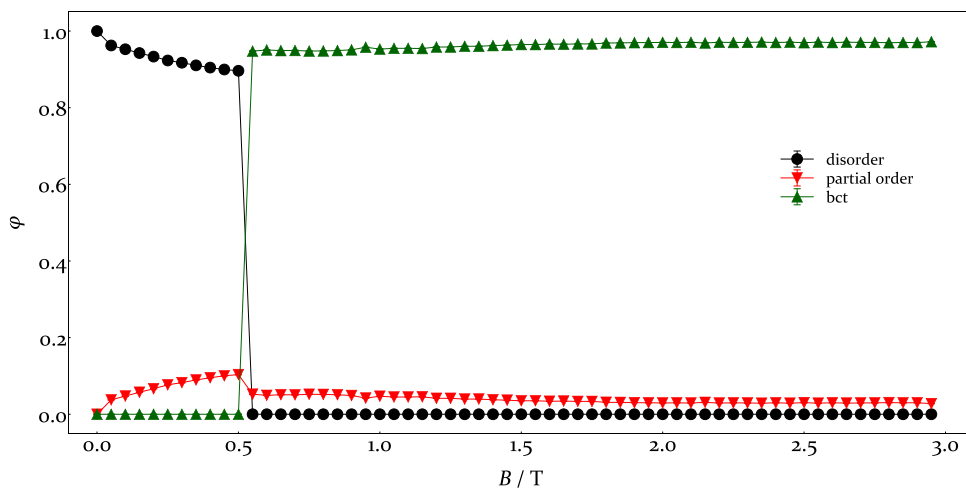


Figure 4.13 Fractions of used models. Lines are added as guide for the eye.

As can be seen in Figure 4.13, for the field strengths up to 0.5 T, only the disorder and the paracrystal were used to describe the data (for 0 T only the disorder). The fraction of the paracrystal increases from 3.8 % at 0.05 T to 10.4 % at 0.5 T. From 0.55 T on, the bct model is necessary to sufficiently describe the model while the disorder is not relevant anymore and is discarded for the rest of the field strengths. The fraction of the paracrystal declines in favour of the bct fraction which is very high from the beginning at a value of 94.8 % until 97.2 % at 2.95 T.

These results show that the NCs assemble already at low field strengths, as an anisotropy can already be detected at 0.05 T. A clear change in the ordering can be observed at 0.55 T where the structures are dominated by the bct lattice. Afterwards, the structures are rather constant.

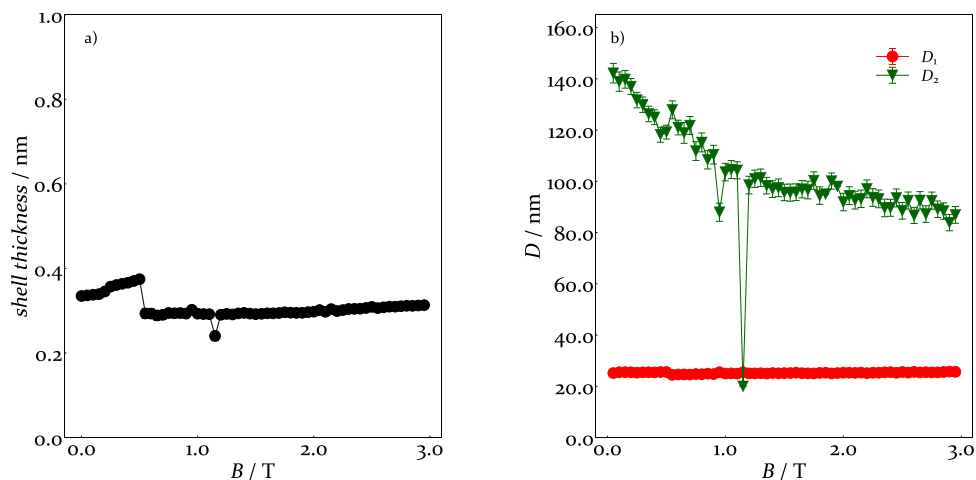


Figure 4.14 Dependence of a) shell thickness and b) distances inside the paracrystal on the magnetic field strength. Lines are added as guide for the eye.

The shell thickness only shows a small dependence on the strength of the magnetic field for the second experiment (Figure 4.14a). Instead of decreasing during the experiment as before, it seems to increase slightly. For the distances in the paracrystal, a similar trend compared to the measurement before can be found (Figure 4.14b). The shorter distance D_2 between NCs in field direction is nearly constant while the larger distance D_1 in beam direction decreases with increasing field strength.

The lattice spacings in the bct crystal structure are displayed in Figure 4.15a. They are smaller than in the first experiment which can only partially be explained by the lower shell thickness, hinting at a different assembly of the NCs. The lattice spacings do not change much during this experiment, indicating that the structure formation is already completed at 0.55 T. Additionally, the root mean squared displacement for the NCs inside the bct lattice is shown in Figure 4.15a, starting with a rather high value of 4.7 nm which then decreases until it reaches a nearly constant value of around 2.8 nm.

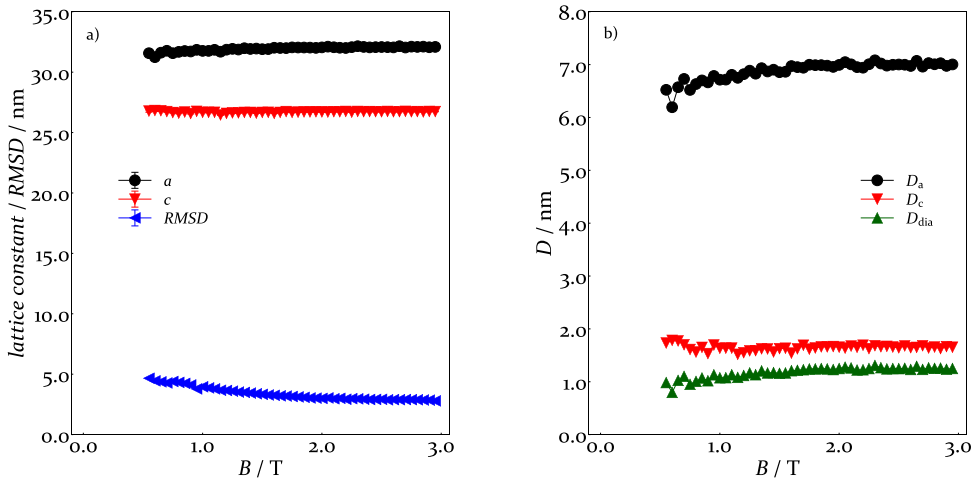


Figure 4.15 Dependence of the lattice constants and thus the distances of the NCs in the *bct* lattice on the magnetic field strength. Lines are added as guide for the eye.

Similar to the lattice spacings, the distances of the NCs inside the lattice are more or less constant with a slight increase at lower field strengths (Figure 4.15b). The NCs are much closer together in all directions. As the effective shell thickness is smaller for these NCs than in the first experiment, the mobility of the oleic acid molecules on the NC surface is much higher. This makes it easier for the NCs to change their distance. Interestingly, the smallest distance between the NCs is now along the diagonal instead of c . This corresponds well to the different lattice spacings, showing a differently assembled structure.

Although the lattice does not change much during the experiment, the size of the crystalline domains, becomes larger leading to sharper peaks on the scattering patterns. In contrast to the first experiment, the scattering patterns of 0.55 T and the highest field strength of 2.95 T are much more similar to each other, as only the peak intensities are changing and the smearing of the peak decreases.

4.3 Conclusion

Highly monodisperse iron oxide nanocrystals were investigated in magnetic fields up to 3 T. At 0 T, the data could be described by a simple core-shell form factor. Increasing the field strength leads to pronounced ordering effects. First, the NCs form a partial order which can be

described as a two-dimensional paracrystal. The second experiment stressed that already at field strengths of about 0.5 T, the NCs form a body-centred tetragonal superlattice which dominates the present structures in the sample. The distance of the NCs in the paracrystal as well as in the bct lattice decreased with increasing field strength in the first experiment. The shell thickness also decreased in the first experiment indicating a compression of the organic layer around the NCs. In the second experiment, the lattice spacings and the shell thickness were rather constant as the shell was more compact from the beginning. Furthermore, the distances between the NCs are smaller than before with the shortest distance now being along the diagonal which is in contrast to the first experiment in which the distance along c was shortest. This hints at a slightly different structure formation for the second experiment, making a comparison of both experiments difficult.

4.4 Materials and Methods

4.4.1 Transmission Electron Microscopy (TEM)

TEM experiments were performed using a Jeol JEM-1011 microscope (100 keV) at the University of Hamburg. To investigate the NCs, a drop of the diluted colloidal solution was deposited on a carbon-coated 400 mesh TEM grid. The excess of solvent was removed with a filter paper and the grid was air-dried.

4.4.2 Small-Angle X-Ray Scattering (SAXS)

SAXS experiments were performed in the Q -range from 0.04 to 1.79 nm⁻¹ at the Gallium Anode Low-Angle X-ray Instrument (GALAXI)^[23] at Forschungszentrum Jülich. The incident wavelength is 1.34 Å and the detector distance was set to 3.5 m. All samples were sealed in glass capillaries of 2 mm inner diameter. The data were background corrected and calibrated to absolute intensities by relating them to a standard sample (fluorinated ethylene propylene). Data correction and analysis has been done using the Python based project jscatter.^[24]

4.4.3 Small-Angle Neutron Scattering (SANS)

SANS experiments were performed at the instrument KWS-1^[25,26] at the MLZ in Garching, Germany. The incident neutron wavelength λ was 5 Å for the first experiment and 4.93 Å for the second experiment ($\Delta\lambda/\lambda = 10\%$). The data were obtained from three to four different detector and collimation distances. For the first experiment: the detector distances of 1.555 m, 4.055 m and 8.055 m with a collimation distance of 8 m and the detector distance of 20.055 m with 20 m collimation distance leading to a total Q range of 0.03 to 2.47 nm⁻¹. For the second experiment: detector distances of 2.185 m and 7.885 m with a collimation distance of 8 m and the detector distance of 13.885 m with a collimation distance of 14 m leading to a total Q range of 0.04 to 3.19 nm⁻¹. The samples were measured at room temperature in quartz cells with beam path of 2 mm. For the magnetic field, an HTS-110 electromagnet was used. The size of the sample aperture was set as 7 × 10 mm for the first experiment and 10 × 12 mm for the second experiment. The data presented here were corrected taking into account the sample thickness, transmission and the background from electronic noise, the solvent and the quartz cell. For the second experiment, the data were calibrated to absolute units by relating them to a standard sample (plexiglass). Data reduction has been done using the QtiKWS software,^[27] data analysis has been done using the Python based project jscatter^[24] for the 1D data and the BornAgain software^[28] for the 2D data.

4.5 References

- [1] D. Speliotis, *J. Magn. Magn. Mater.* **1999**, *193*, 29.
- [2] A. K. Boal, in *Nanoparticles Build. Blocks Nanotechnol.* (Ed: V.M. Rotello), Springer Science+Business Media, New York, **2004**, pp. 1–27.
- [3] Y. Sahoo, M. Cheon, S. Wang, H. Luo, E. P. Furlani, P. N. Prasad, *J. Phys. Chem. B* **2004**, *108*, 3380.
- [4] B. B. Yellen, O. Hovorka, G. Friedman, *Proc. Natl. Acad. Sci.* **2005**, *102*, 8860.
- [5] M. Colombo, S. Carregal-Romero, M. F. Casula, L. Gutiérrez, M. P. Morales, I. B. Böhm, J. T. Heverhagen, D. Prospero, W. J. Parak, *Chem. Soc. Rev.* **2012**, *41*, 4306.
- [6] J. J. Benkoski, R. M. Deacon, H. B. Land, L. M. Baird, J. L. Breidenich, R. Srinivasan, G. V. Clatterbaugh, P. Y. Keng, J. Pyun, *Soft Matter* **2010**, *6*, 602.
- [7] Z. Hai, G. Liang, *Adv. Biosyst.* **2018**, *2*, 1800108.
- [8] J. Park, K. An, Y. Hwang, J.-G. Park, H.-J. Noh, J.-Y. Kim, J.-H. Park, N.-M. Hwang, T. Hyeon, *Nat. Mater.* **2004**, *3*, 891.
- [9] P.-G. de Gennes, P. A. Pincus, *Phys. der Kondens. Mater.* **1970**, *11*, 189.
- [10] M. Grzelczak, J. Vermant, E. M. Furst, L. M. Liz-Marzán, *ACS Nano* **2010**, *4*, 3591.
- [11] J. J. Brunner, M. Krumova, H. Cölfen, E. V Sturm (née Rosseeva), *Beilstein J. Nanotechnol.* **2019**, *10*, 894.
- [12] L. Li, Y. Yang, J. Ding, J. Xue, *Chem. Mater.* **2010**, *22*, 3183.
- [13] V. Malik, A. V. Petukhov, L. He, Y. Yin, M. Schmidt, *Langmuir* **2012**, *28*, 14777.
- [14] A. Pal, V. Malik, L. He, B. H. Erné, Y. Yin, W. K. Kegel, A. V. Petukhov, *Angew. Chemie Int. Ed.* **2015**, *54*, 1803.
- [15] S. Mehdizadeh Taheri, M. Michaelis, T. Friedrich, B. Förster, M. Drechsler, F. M. Römer, P. Bösecke, T. Narayanan, B. Weber, I. Rehberg, S. Rosenfeldt, S. Förster, *Proc. Natl. Acad. Sci.* **2015**, *112*, 14484.
- [16] Z. Fu, Y. Xiao, A. Feoktystov, V. Pipich, M.-S. Appavou, Y. Su, E. Feng, W. Jin, T. Brückel, *Nanoscale* **2016**, *8*, 18541.

- [17] B. Hammouda, *Probing Nanoscale Structures - The SANS Toolbox*, National Institute Of Standards And Technology, Gaithersburg, **2009**.
- [18] W. W. Yu, J. C. Falkner, C. T. Yavuz, V. L. Colvin, *Chem. Commun.* **2004**, 2306.
- [19] J. B. Tracy, T. M. Crawford, *MRS Bull.* **2013**, 38, 915.
- [20] J. S. Pedersen, D. Posselt, K. Mortensen, *J. Appl. Crystallogr.* **1990**, 23, 321.
- [21] A.-P. Hynninen, M. Dijkstra, *Phys. Rev. Lett.* **2005**, 94, 138303.
- [22] "BornAgain - Interference function of 2D paracrystal," can be found under <https://www.bornagainproject.org/documentation/working-with-python/interference/para2d/>, **n.d.**
- [23] E. Kentzinger, M. Krutyeva, U. Rücker, *J. large-scale Res. Facil. JLSRF* **2016**, 2, A61.
- [24] R. Biehl, *PLoS One* **2019**, 14, e0218789.
- [25] Heinz Maier-Leibnitz Zentrum, *J. large-scale Res. Facil. JLSRF* **2015**, 1, 1.
- [26] A. V. Feoktystov, H. Frielinghaus, Z. Di, S. Jaksch, V. Pipich, M.-S. Appavou, E. Babcock, R. Hanslik, R. Engels, G. Kemmerling, H. Kleines, A. Ioffe, D. Richter, T. Brückel, *J. Appl. Crystallogr.* **2015**, 48, 61.
- [27] V. Pipich, "QtiKWS," **2007**.
- [28] J. Burle, C. Durniak, J. M. Fisher, M. Ganeva, G. Pospelov, W. Van Herck, J. Wuttke, D. Yurov, **2018**.

5 Nanocomposites of Highly Monodisperse Encapsulated Superparamagnetic Iron Oxide Nanocrystals Homogeneously Dispersed in a Poly(ethylene Oxide) Melt

The following chapter was published in *ACS Nano*, Vol. II, No. 9, pages 3767-3775, 2017 in cooperation with Artur Feld¹, Rieke Koll¹, Margarita Kruteva², Wim Pyckhout-Hintzen², Christine Weiß², Hauke Heller¹, Agnes Weimer¹, Christian Schmidtke¹, Marie-Sousai Appavou³, Emmanuel Kentzinger⁴, Jürgen Allgaier², and Horst Weller^{1,5}. Reprinted with permission from *ACS Nano*, Vol. II, No. 9, pages 3767-3775, 2017. Copyright 2017 American Chemical Society.

I performed most of the SAXS experiments. I corrected and analysed the resulting data. I wrote the corresponding part in the manuscript and participated in reviewing and finalising the whole manuscript. Artur Feld had the idea to use the thiol-ene clickreaction for the encapsulation of the nanocrystals. Artur Feld and Agnes Weimer synthesised the iron oxide particles and analysed them by TEM, DLS and TGA. Agnes Weimer worked as a student of Artur Feld for 10 weeks on the sample preparation for the first SAXS measurements. Rieke Koll and Artur Feld developed the material preparation and synthesized the nanocomposites. They analysed the nanocomposites using TEM and DLS and evaluated the data. Margarita Kruteva and Jürgen

¹ Institute of Physical Chemistry, University of Hamburg, Grindelallee 117, 20146 Hamburg, Germany.

² JCNS-1 and ICS-1, Forschungszentrum Jülich GmbH, Leo-Brandt-Straße, 52425 Jülich, Germany.

³ Jülich Centre for Neutron Science (JCNS) at MLZ, Forschungszentrum Jülich GmbH, 52425 Garching, Germany.

⁴ Jülich Centre for Neutron Science JCNS and Peter Grünberg Institut PGI, JARA-FIT, Forschungszentrum Jülich GmbH, 52425 Jülich, Germany.

⁵ The Hamburg Center for Ultrafast Imaging, University of Hamburg, Luruper Chaussee 149, 22761 Hamburg, Germany;
Center for Applied Nanotechnology (CAN) GmbH, Grindelallee 117, 20146 Hamburg, Germany;
Department of Chemistry, Faculty of Science, King Abdulaziz University, P.O. Box 80203, Jeddah 21589, Saudi Arabia.

Allgaier successfully applied for funding of this project from the Deutsche Forschungsgemeinschaft and established the cooperation with the colleagues in Hamburg. Margarita Kruteva and Wim Pyckhout-Hintzen helped me with the evaluation and interpretation of the SAXS data. Christine Weiß synthesised and characterised the polymers. Hauke Heller contributed to this work in many discussions with Jürgen Allgaier, Margarita Kruteva, Artur Feld, Rieke Koll and Horst Weller. Margarita Kruteva, Wim Pyckhout-Hintzen, Jürgen Allgaier, Artur Feld and Hauke Heller chose the analytical methods. Christian Schmidtke was involved *via* many discussions with Artur Feld, Rieke Koll, Hauke Heller and Horst Weller and in writing the manuscript. Marie-Sousai Appavou performed the TEM measurements of the nanocomposites. Emmanuel Kentzinger performed the remaining SAXS experiments together with Rieke Koll. Jürgen Allgaier formulated the original task. He performed the elemental analysis of the encapsulated nanoparticles and analysed the results. Hauke Heller, Margarita Kruteva, Rieke Koll and Artur Feld wrote the framework of the paper. Jürgen Allgaier and Horst Weller supervised the investigations. All authors participated during all stages of the process.

5.1 Abstract

Nanocomposite materials based on highly stable encapsulated superparamagnetic iron oxide nanocrystals (SPIONs) were synthesized and characterized by scattering methods and transmission electron microscopy (TEM). The combination of advanced synthesis and encapsulation techniques using different diblock copolymers and the thiol-ene click reaction for cross-linking the polymeric shell results in uniform hybrid SPIONs homogeneously dispersed in a poly(ethylene oxide) matrix. Small-angle X-ray scattering and TEM investigations demonstrate the presence of mostly single particles and a negligible amount of dyads. Consequently, an efficient control over the encapsulation and synthetic conditions is of paramount importance to minimize the fraction of agglomerates and to obtain uniform hybrid nanomaterials.

5.2 Introduction

Blending of soft polymer matrices with nanocrystals (NCs) displaying high surface-to-volume ratios has led to hybrid materials with exceptional properties, so called nanocomposites.^[1-5] Especially, multifunctional nanocomposites are in the focus of research due to application areas ranging from sensors and plasmonics, through stretchable electronics and smart coatings, to energy conversion and (bio)medicine.^[6-10] In particular, responsive polymeric nanocomposites that are able to adapt to different surrounding environments are playing an increasingly important role. These materials per definition show a built-in ability to respond to physical or chemical stimuli *via* controlled molecular design. A subset of such functional systems is based on superparamagnetic iron oxide nanoparticles (SPIONs).^[11-14] Due to the magnetic behavior of these NCs, the properties of the composite can be changed by an external magnetic field.^[15-17] Often the reported composites consist of SPIONs with broad size distributions.^[18] This results in inhomogeneous magnetic and distribution properties in the polymer matrix.^[13,14] In addition, an unstable ligand shell may lead to strong agglomeration of the SPIONs and, therefore, increases the inhomogeneity in the nanocomposite. However, it shall be stated here that attractive forces between the carrier material (micelle, capsule, or ligand system) may also induce reversible agglomeration. All of these inhomogeneities are especially evident when investigation methods like small-angle X-ray scattering (SAXS) are used, which are sensitive to size and size distributions in the sample.^[19]

Any further development of these kinds of functional nanocomposites requires, however, a more profound control and insight with regard to the interactions between the NC and their host matrix in the nanocomposite. Generally, the corresponding properties of the nanocomposites are strongly influenced by the specific properties of the NC, their ligand shell, its coverage density, the NC concentration, and the self-assembly step.^[20,21]

The challenge for the synthesis of homogeneous polymer-NC nanocomposites is the dispersion of the NC into the polymer matrix, because of the immiscibility of the inorganic NC with an organic phase. Several approaches to overcome this difficulty exist, especially by grafting polymer chains on the particle surface of the same chemical nature as the matrix polymer.^[22] Even this advanced method leads to agglomeration processes resulting in self-assembly of the NC under a broad range of conditions into a variety of superstructures.^[19] This can be prevented by introducing a robust ligand shell, which is cross-linked by covalent bonds and, therefore, provides maximum stability during the mixing step.

Pöselt et al. developed a preparation method for nanocomposites, which is based on the micellar encapsulation of NC in a polyisoprene-*block*-poly(ethylene oxide) (PI-*b*-PEO) diblock copolymer shell with subsequent radically initiated cross-linking of the PI block.^[23-25] This allows for the originally hydrophobic NC to be transferred into water and provides a very robust shell in comparison to non-cross-linked shells regarding inertness, dilution, and long-term stability, especially in biologically relevant media. Micellar encapsulation is based on the hydrophobic part of amphiphilic polymers intercalating with the hydrophobic ligand shell of the particle, while the hydrophilic part is reaching into the aqueous solution.^[26,27] The hydrophilic part often consists of poly(ethylene oxide) (PEO). Various types of NCs can be incorporated in the micelles to combine different functionalities,^[28,29] e.g., magneto-plasmonic and magneto-fluorescent properties.^[30-33]

SPIONs of various radii (3-8 nm) have been studied in the literature by scattering in both pristine and grafted states, dispersed in melts and solvents. A formation of magnetic particle-chains was evidenced directly in emulsions and in a melt state, if a modest magnetic field of the order of 0.01 T was applied during the drying process.^[12-14,34-37] It is evident that for such applications a homogeneous distribution of the NCs in the matrix under zero-field conditions is a prerequisite for a strong magneto response. Any in situ proof of the structural behavior of grafted particles in solvents or low-to-intermediate viscosity media is lacking, though.

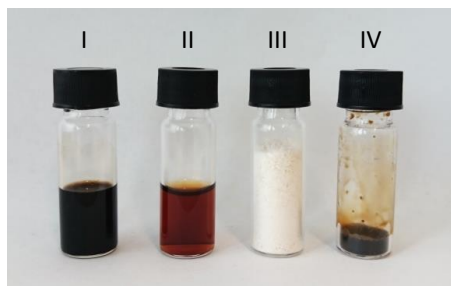
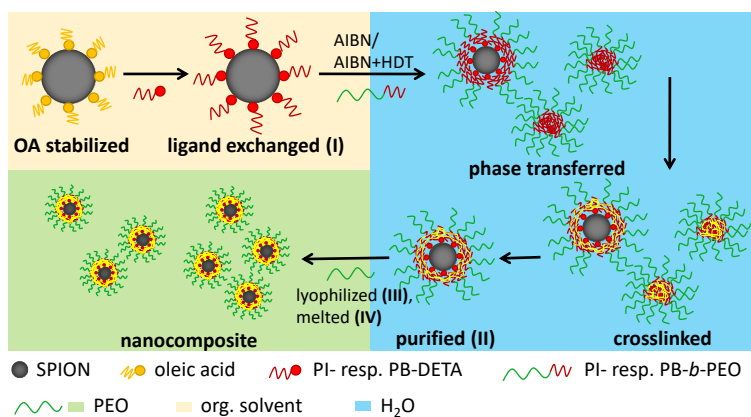
In this work, we apply the diblock copolymer encapsulation for the preparation of nanocomposites and focus on the homogeneous dispersion of monodisperse SPIONs in a

polymer matrix. We present an extensive step-by-step characterization during the different stages of preparation by small-angle X-ray scattering (SAXS) and transmission electron microscopy (TEM), with both methods complementing each other in a perfect manner. Based on that, we will show that cross-linking of the polydiene block surrounding the SPIONs is a crucial parameter for the homogeneous distribution of NC within the polymer matrix.

5.3 Results and Discussion

5.3.1 Encapsulation of SPIONs

The encapsulation of the SPIONs was routinely carried out in a three-step process. A schematic illustration of the preparation of the encapsulated SPIONs and the composites is shown in Scheme 5.1. The SPIONs consist of magnetite (Fe_3O_4), while small fractions of maghemite ($\gamma\text{-Fe}_2\text{O}_3$) may coexist due to oxidation processes during purification and phase transfer.^[38]



Scheme 5.1 Schematic illustration of the preparation of nanocomposites based on the SPION-polymer hybrid nanoparticles and photograph of the material at different stages of the preparation.

First, the native oleic acid ligands of the NC were exchanged with PI-DETA in an equilibrium process in *n*-hexane as solvent. PI-DETA is polyisoprene equipped with a 2,2'-diaminodiethylamine headgroup. Then, the SPIONs, PI-*b*-PEO, and 2,2'-azobis(2-methylpropionitrile) (AIBN) were mixed and phase transferred into water. PI-*b*-PEO acted as emulsifying agent and served as shell material. Finally, the double bonds of the PI shell were cross-linked at 80 °C in a radical reaction with AIBN as radical initiator. Empty micelles were removed by means of a magnetic column. The encapsulated SPIONs, dispersed in water, were mixed with an aqueous PEO solution, lyophilized, and melted at 60 °C to yield the nanocomposite.

Alternatively, the existing encapsulation process was modified/optimized by two measures. First, PI-DETA and PI-*b*-PEO were replaced by their polybutadiene (PB) analogues. Second, the cross-linking of the polydiene shell was carried out using a radically initiated thiol-ene click reaction with 1,6-hexanedithiol (HDT) and AIBN. An overview of the nanocomposites is shown in Table 5.1. The illustrated samples are representative for each different encapsulation. Every step was checked several times, thereby proving the reproducibility and stability of the system.

Table 5.1 Overview of the nanocomposites based on differently produced SPIONs in a PEO matrix. The SPION volume concentrations and core radii as determined by TEM, $R_{c,TEM}$, are given.

$R_{c,TEM}$ [nm]	PI- <i>b</i> -PEO		PB- <i>b</i> -PEO	
	AIBN crosslinking	AIBN-HDT crosslinking	AIBN crosslinking	AIBN-HDT crosslinking
5.7	PI_AIBN_5.7 (0.2 vol%)	PI_HDT_5.7 (0.1 vol%)	PB_AIBN_5.7 (0.3 vol%)	PB_HDT_5.7 (0.1 vol%)
7.7		PI_HDT_7.7 (0.1 vol%)		PB_HDT_7.7 (0.1 vol%)

5.3.2 Dispersion Properties of AIBN Cross-Linked Polydiene Shells

To stabilize the SPIONs in the polymer matrix and minimize agglomeration, different synthesis parameters were used. The volume concentrations of the SPIONs were always ≤ 0.3 vol % (Table 5.1), i.e., small to avoid interparticle interaction, but enough to observe a

reasonable scattering signal. Stabilization of SPIONs with PI-*b*-PEO and with PB-*b*-PEO diblock copolymer was used to clarify the influence of the cross-linked polymer (PI or PB) on the distribution within the PEO matrix and, therefore, the stability of the polymer shell regarding the lyophilization. In Figure 5.1a, the SAXS results for two samples, where the PI or PB part was cross-linked in a radical reaction using AIBN, are presented. For those samples, the SPIONs with 5.7 nm radius were used, and the radius was determined by TEM (Figure 5.1b and Figure 5.1c). In the intermediate to large Q -limit, the form-factor of spherical NCs with well-defined minima is seen reflecting the narrow SPION size distribution. The position of the first minimum of the form-factor determines the radius of the particles by $Q_{\min}R_{\text{SPION}} = 4.49$, this corresponds to 6.3 nm.^[39] In the low Q limit, the presence of an effective power law, close to Q^{-2} , is the signature of an agglomerate formation.^[39] The exponent ~ 2 signifies open branched agglomerates. Linear agglomeration would yield to Q^{-1} . For both samples, the intermediate Q scattering intensity demonstrates a structural peak at $Q \sim 0.45 \text{ nm}^{-1}$, which is related to an intra-agglomerate structure factor $S_{\text{intra}}(Q)$. As a first estimate, the distance between the centers inside the agglomerate is about $\frac{2\pi}{0.45 \text{ nm}^{-1}} = 14.0 \text{ nm}$.

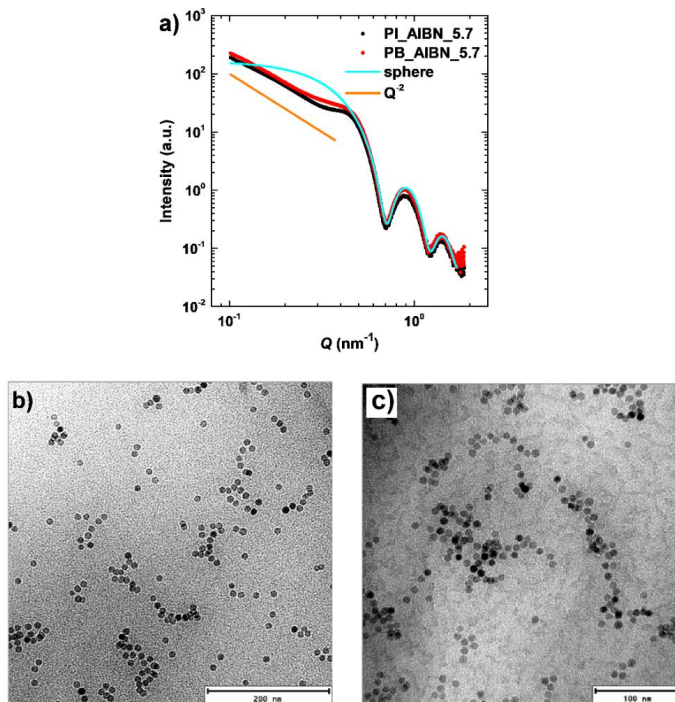


Figure 5.1 (a) SAXS results for the samples PI_AIBN_5.7 and PB_AIBN_5.7 (from Table 5.1) obtained by cross-linking in a radical reaction and the fits for spheres and Q^{-2} . (b) TEM image of PB_AIBN_5.7 in PEO matrix. c) TEM image of PI_AIBN_5.7 in PEO matrix.

This distance between the centres of the SPIONs is therefore about twice the radius of the NCs without the polymer shell. It may indicate that the polymer shell in these agglomerates is partially damaged during the synthesis of the nanocomposite and allows the SPIONs to interact. Such agglomerates as well as one dimensional agglomerates can be seen in the TEM images of the samples in Figure 5.1b and Figure 5.1c. Equally, for the larger SPIONs with an iron oxide core radius of 7.7 nm, not shown here, similar structural conclusions can be drawn. However, no differences between PI and PB can be observed.

5.3.3 Dispersion Properties of HDT-AIBN Cross-Linked Shells

Figure 5.2 shows the scattering curves of the samples cross-linked *via* HDT-AIBN with both dienes, PI and PB, and SPION radii 5.7 and 7.7 nm. While the samples cross-linked in a radical reaction with AIBN show a peak at intermediate Q due to agglomeration (Figure 5.1a), the scattering curves of the samples HDT-AIBN cross-linked lack such a peak (Figure 5.2a). This indicates a significantly better distribution, suggesting that we have a robust and stable polymer shell. As an appropriate model, the scattering curves were fitted by the pearl-necklace model of Schweins and Huber.^[40] The model was developed to describe the scattering of polymer particles connected by cylindrical rods consisting of the same component to form chain-like structures.

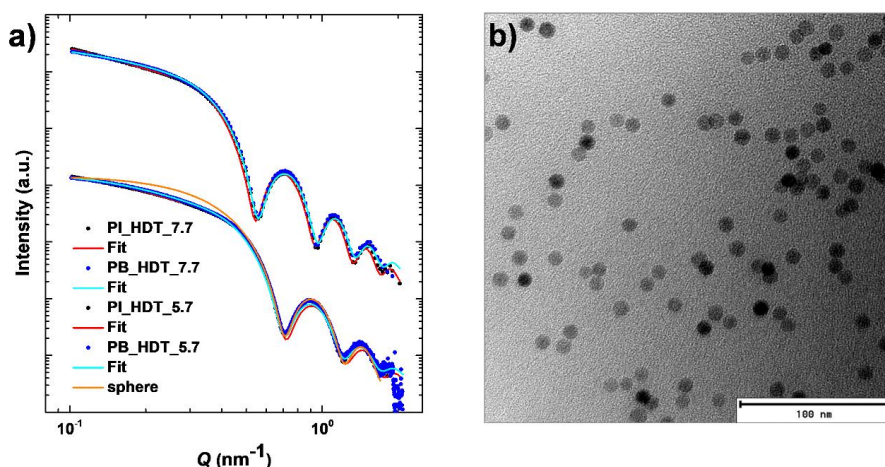


Figure 5.2 (a) SAXS results for the samples with 5.7 and 7.7 nm SPIONs with PI and PB, respectively, and cross-linked with HDTAIBN. (b) TEM image of PB_HDT_5.7 in PEO matrix.

As our crystals are not expected to have any kind of rod-like connections, we adapt the model to make it suitable for our system. The scattering intensity is proportional to

$$I(Q) \cong P(Q)S_{\text{intra}}(Q) \quad (5.1)$$

Where

$$P(Q) = \left[3 \frac{\sin(QR_c) - (QR_c) \cos(QR_c)}{(QR_c)^3} \right]^2 \quad (5.2)$$

is the normalized form-factor of a spherical nanoparticle with radius R_c and an intra-agglomerate structure factor

$$S_{\text{intra}}(Q) = \frac{2}{N^2} \left[\frac{N}{1 - \frac{\sin(Q(l+2 \cdot R_c))}{(Q(l+2 \cdot R_c))}} - \frac{N}{2} \frac{1 - \left(\frac{\sin(Q(l+2 \cdot R_c))}{(Q(l+2 \cdot R_c))} \right)^N}{\left(1 - \frac{\sin(Q(l+2 \cdot R_c))}{(Q(l+2 \cdot R_c))} \right)^2} \frac{\sin(Q(l+2 \cdot R_c))}{(Q(l+2 \cdot R_c))} \right] \quad (5.3)$$

which can be interpreted as the scattering from spherical NCs, interacting via $S_{\text{intra}}(Q)$, given by the chain-like organization. For the number of SPIONs per “particle chain”, N , we included a Poisson distribution and determine the amount of single SPIONs, dyads, and longer chains in the samples. Additionally, we assumed that the core radius R_c is characterized by its own distribution, which showed to be necessary to improve the fitting quality at high scattering angles. For this purpose, a normal distribution was included with the standard deviation σ . Furthermore, these fits enabled to estimate a virtual distance l between the crystals building chain-like structures. In the pearlnecklace model, which we applied for our chain-like structures, l does not contribute to the scattering but controls the separation of the beads in the necklace. The results for the samples are shown in Table 5.2.

Table 5.2 Fitting results using the Pearl-Necklace model. $\langle N \rangle_w$ is the weight-averaged number, R_c is the SPION core radius, σ is the standard deviation, and l is the average (virtual) distance between the surfaces of two neighboring crystals. The relative fractions of agglomerates comply well with the Poisson distribution (Figure 5.3). The error bars of the fitted parameters do not exceed 5%.

$R_{c,TEM}$ [nm]	σ_{TEM} [nm]	polymer	$\langle N \rangle_w$	$R_{c,SAXS}$ [nm]	σ_{SAXS} [nm]	l [nm]
5.7	0.4	PI	1.41	6.35	0.41	4.09
5.7	0.4	PB	1.26	6.44	0.43	3.31
7.7	0.4	PI	1.48	8.32	0.42	5.39
7.7	0.4	PB	1.19	8.14	0.42	5.64

The average core radii are reliably found at around 6.4 ± 0.4 and 8.2 ± 0.4 nm, respectively. Considering that the radii evaluated by TEM are number-averaged, while the radii calculated by SAXS are weight-averaged, these values correspond well with each other. The average virtual distance between the SPION surfaces in the chain l is situated between 3.7 ± 0.4 and 5.5 ± 0.1 nm. The mean value for the chain length $\langle N \rangle_w$ is 1.23 in the case of the PB shell and 1.45 in the case of the PI shell, indicating a very comparable agglomeration for PI and PB encapsulated SPIONs. Within the assumption for the distribution, they are equivalent. This is also corroborated by the weight distribution of N (Figure 5.3), where most of the particles in the samples are singly encapsulated, some form dyads and a minor amount triads and higher, in accordance to the expectation.

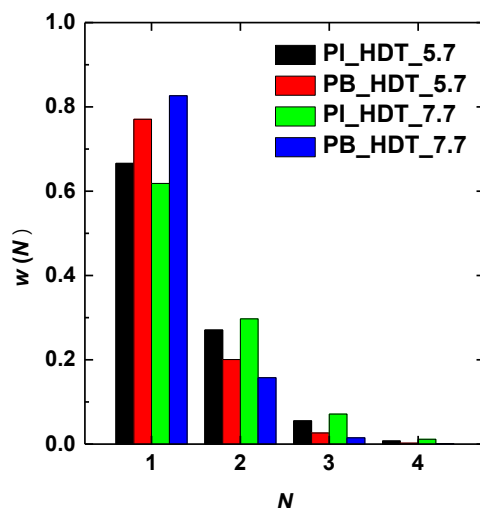


Figure 5.3 Weight distribution $w(N)$ obtained from the SAXS curves for the samples with 5.7 and 7.7 nm, respectively, SPIONs with a PI and PB, respectively, HDT-AIBN cross-linked shell in PEO matrix.

The results from the SAXS experiments show that using HDT-AIBN cross-linking allows an improvement of the polymer shell stability. The SAXS results suggest that there is a different degree of tendency to agglomerate for PI and PB encapsulated SPIONs, when using PI and PB with a similar molecular mass. This is suggested by a number of SAXS measurements performed on PI and PB encapsulated SPIONs of different sizes (Table 5.3). To further ensure these findings, more studies with identical connectivity of the polymers are needed.

Table 5.3 Parameters obtained from the fit of different batches of the nanocomposites.

sample	$R_{c,TEM}$ [nm]	polymer	$\langle N \rangle_w$	$R_{c,SAXS}$ [nm]	σ_{SAXS} [nm]	l [nm]
1	5.7	PI	1.41	6.35	0.41	4.09
2	7.7	PI	1.48	8.32	0.42	5.39
3	7.7	PI	1.72	8.07	0.43	2.29
4	5.7	PB	1.26	6.44	0.43	3.31
5	5.7	PB	1.18	6.45	0.45	9.06
6	5.7	PB	1.26	6.42	0.42	8.78
7	5.7	PB	1.29	6.38	0.42	3.45
8	7.7	PB	1.19	8.14	0.42	5.64
9	7.7	PB	1.22	8.10	0.40	6.73

Preliminary small angle neutron scattering experiments (SANS) clearly indicate magnetic alignment of the NCs under magnetic field also in the composite. Details of the magnetic behavior will be published in a forthcoming paper.

5.3.4 Step-by-Step Characterization of the Encapsulation Reactions

To clarify the details of the SPION agglomeration, we performed SAXS characterizations of sample PB_HDT_5.7 for all encapsulation steps, as presented in Scheme 5.1. The SPIONs stabilized with oleic acid, which are used as a starting material, show a perfect single particle form factor (Figure 5.4a) in organic media. The SPIONs are spherical and have narrow size distributions (5–6%). Basically, no agglomerated particles can be detected. The same is true for the SPIONs that are ligand exchanged with PB-DETA. Evidence of SPION agglomeration appears after the phase transfer step from the organic solvent into water using a diblock copolymer, which has also been observed for other NPs, like quantum dots (QDs), elongated quantum dots in quantum rods (QDQRs), etc.^[41,42] The fitting procedure with the pearl-necklace model shows a measurable amount of chain-like agglomerates (Figure 5.4b). During the cross-linking step and the purification, where empty micelles are removed, no further agglomeration takes place. The phase transfer results in weight distributions where the percentage of singly encapsulated SPIONs varies by about 10%. This observation shows that the rather small differences between the distributions of the NCs in PEO using PI and PB are insignificant, because the transfer into water as well as the lyophilization are the crucial steps.

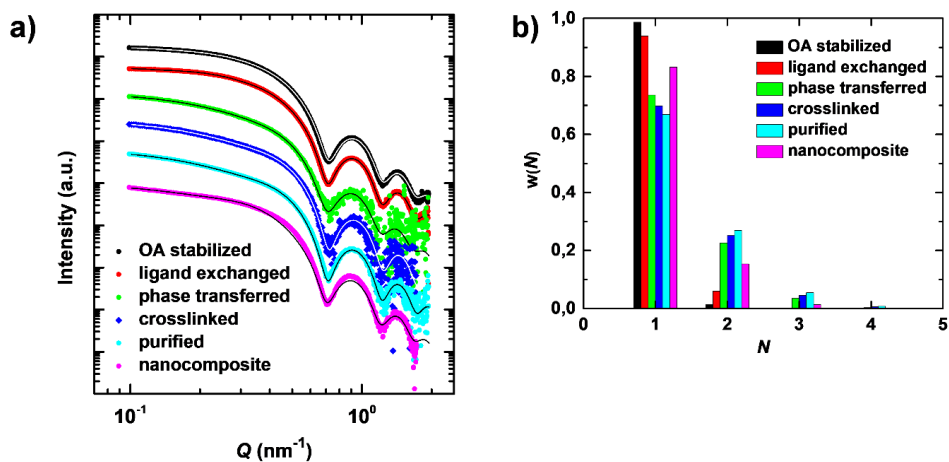


Figure 5.4 (a) Experimental scattering curves (arbitrarily shifted) characterizing each step of the encapsulation procedure from the SPION synthesis (OA stabilized) to embedding in a polymer matrix (nanocomposite). (b) Distribution for N for the samples related to different encapsulation steps.

Interestingly, there are fewer agglomerates in the PEO nanocomposite than in the purified aqueous solution. Furthermore, this result is reproducible for all samples. We note that the computation of the scattering curve for the nanocomposite sample is slightly underestimating the experimental intensity at both $Q \sim 0.5$ and 0.9 nm^{-1} . Simultaneously, the lowest Q -scattering corroborates the lower agglomeration in the nanocomposite since almost single particle scattering is detected. The fit curve minimized the deviation of experimental and calculated intensities in the full Q -range and therefore yields the best overall description. The obtained parameters can be found in Table 5.4.

Table 5.4 Fitting results of the samples related to different encapsulation steps using pearlnecklace model. The error bars for the values do not exceed 5%.

step	$\langle N \rangle_w$	$R_{c,SAXS}$ [nm]	σ_{SAXS} [nm]	l [nm]
OA stabilised	1	6.32	0.44	-
ligand exchanged	1	6.40	0.42	-
phase transferred	1.31	6.45	0.50	1.23
crosslinked	1.36	6.29	0.37	2.20
purified	1.40	6.38	0.37	2.51
nanocomposite	1.18	6.45	0.45	9.06

Apparently, from a thermodynamic point of view, PEO turns out to be a better solvent for the encapsulated SPIONs than water. To investigate this phenomenon in more detail, SANS experiments on a similar system were performed. These experiments allowed to determine the exact shell sizes of core-shell-shell particles (PB-*b*-PEO encapsulated SPIONs) and will be described elsewhere.

5.3.5 TEM Investigations of SPION Shell in Aqueous solution

In order to obtain more information about the encapsulation, TEM investigations of the SPION shells were performed. Primarily, the PEO shells of the encapsulated SPIONs were stained with phosphotungstic acid, leading to a dark corona around the crystals in aqueous solution. Figure 5.5 shows the direct comparison of samples PI_ and PB_AIBN_5.7 cross-linked with AIBN (Figure 5.5a,b) and samples PI_ and PB_HDT_5.7 cross-linked with HDT-AIBN (Figure 5.5c,d). The TEM images showed no visible differences between PI and PB. The AIBN cross-linked samples show a less sharply defined and less visible polymer corona in comparison to the particles, whose double bonds were cross-linked with HDT-AIBN.

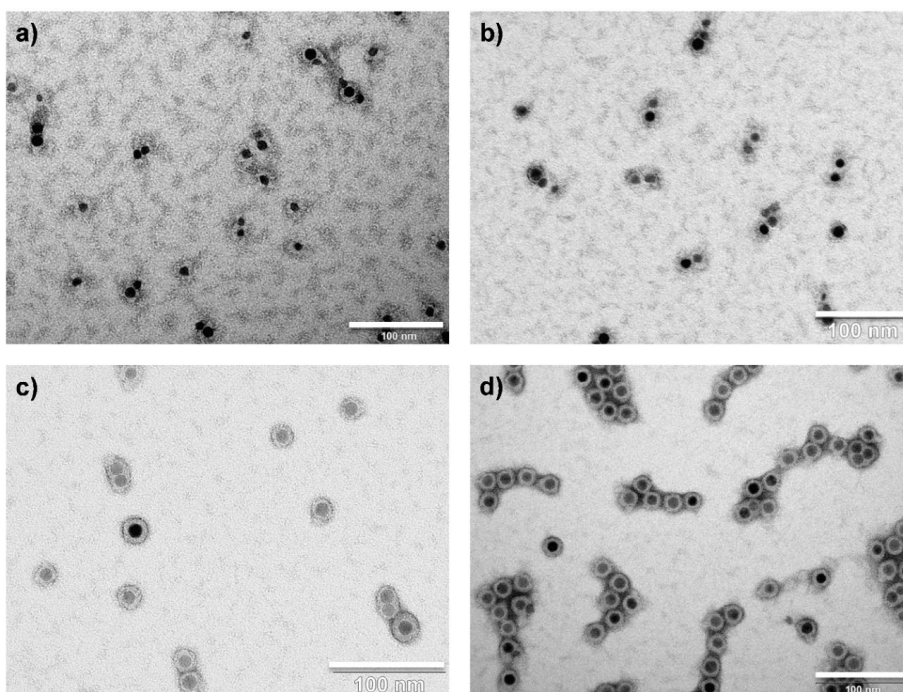


Figure 5.5 TEM images showing hybrid SPIONs after purification, whose shell was cross-linked with AIBN for PI (a) and for PB (b), and hybrid nanoparticles, whose shell was HDT-AIBN cross-linked for PI (c) and for PB (d). All scale bars are 100 nm.

Furthermore, the AIBN cross-linked samples show a lot of etched and therefore small and irregularly shaped NCs (Figure 5.5a,b). This is due to a permeability of the polymer shell for phosphotungstic acid, which mediates corrosion. As comparison, TEM images of native SPIONs can be seen in Figure 5.6. It is clearly visible that the outer SPIONs are considerably etched.

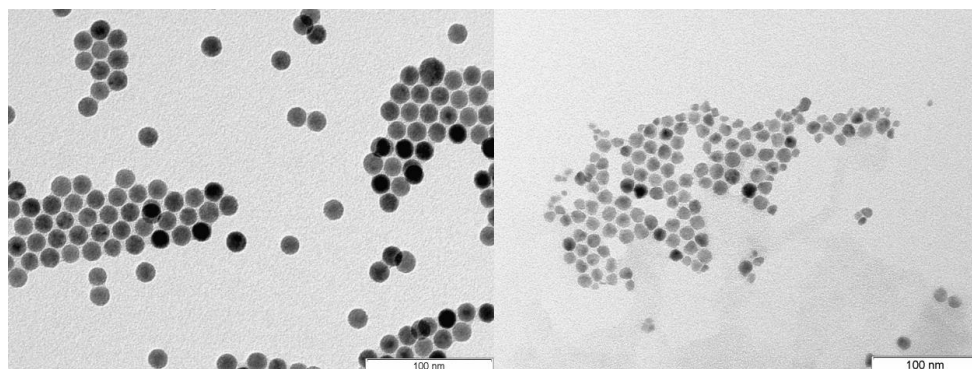


Figure 5.6 TEM images of native SPIONs unstained (left) and stained with phosphotungstic acid (right).

The permeability of AIBN cross-linked shells using relative small diblock copolymers could also be observed for QDs.^[43] In contrast, the HDT-AIBN cross-linked samples demonstrate only very few etched SPIONs, indicating a less permeable shell. TEM images of the samples with different shells and SPION sizes are presented in Figure 5.7.

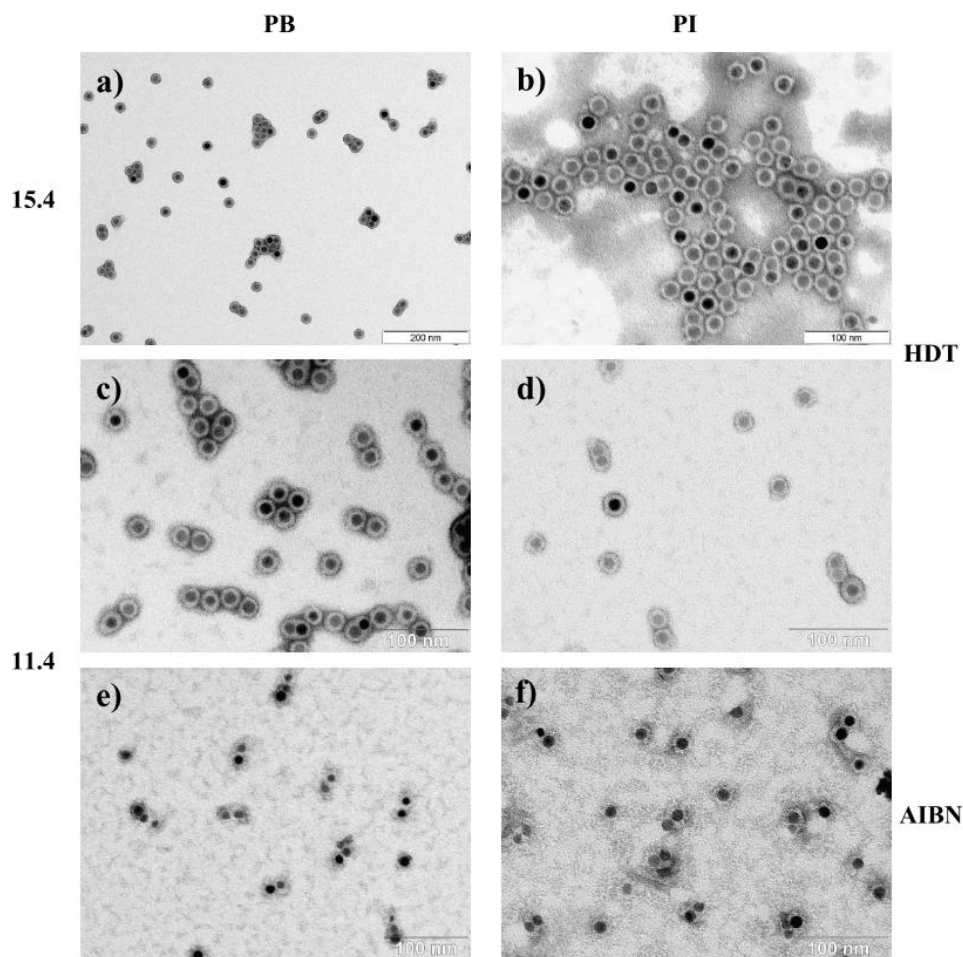


Figure 5.7 TEM images of PB encapsulated SPIONs (a, c, e) and PI encapsulated SPIONs (b, d, f), crosslinked with HDT-AIBN (a-d), and with AIBN (e-f), both with 15.4 nm SPIONs (a, b), and with 11.4 nm SPIONs (c-f).

Those observations suggest that staining of the HDT-AIBN cross-linked polymer shell leads to a well-defined polymer corona around the NC because of an attachment of phosphotungstic acid on the hydrophilic-hydrophobic phase interface. When using AIBN for the cross-linking, phosphotungstic acid can diffuse through the permeable polymer shell leading to a more diffuse staining and etching of the NC.

5.3.6 Chemical Composition of the Block Copolymer Coated SPIONs

Elemental analysis was performed exemplarily on sample PB_HDT_7.7 (see Table 5.1). The iron content of 33.9 mass % (Table 5.5) translates into a fraction of 48.5 mass % of γ -Fe₂O₃ in this sample.^[38] Additionally, the elemental composition of the organic material allows a detailed insight into the structure of the organic shell. The key element here is oxygen, which is only present in PEO if residual oleic acid is neglected. As in the combustion process of the elemental analysis where iron oxide is partially reduced, the measurement of the organic fraction was carried out after removal of the iron oxide by dissolution in hydrochloric acid. This measure ensured detecting only the oxygen of the organic material. From the oxygen content, the PEO fraction of the organic shell was calculated to be 54.4 mass %. The amount of cross-linker HDT, fixed at PB chains, was determined from the sulphur content to be 10.9 mass % of the organic fraction. From the remaining carbon, the fraction of PB was calculated to be 34.5 mass %. The molar ratio of butadiene monomer units to HDT is 8.8.

Table 5.5 Elemental analysis of the sample PB_HDT_7.7.

	mass %				
	Fe	C	H	S	O
overall sample	33.9				
separated organic part		65.5	9.93	4.65	19.76

This translates into 8 cross-linking sites per PB chain, assuming quantitative cross-linking efficiency. This indicates a high crosslinking density of the PB shell, even if the HDT had not reacted quantitatively with both functionalities. In addition, some AIBN radicals contribute to the cross-linking of the PB as well, which also indicates a high cross-linking density. Taking into account the diblock copolymer composition measured by ¹H NMR, 63% of the PB is attributed to the diblock copolymer and 37% to PB-DETA. The accuracy of the elemental analysis is underlined if the calculations above are carried out using the hydrogen content instead of the carbon content. The mismatch between both methods is only 0.1%.

The organic material used for the elemental analysis precipitated during the dissolution process of the iron oxide. In addition, a small quantity of soluble organic material was extracted from the hydrochloric acid phase and was analyzed by SEC and ¹H NMR. The measurements detected mainly PEO homopolymer, an impurity of the original PB-*b*-PEO, and some non-cross-

linked diblock copolymer. The latter corresponded to 2.5% of the diblock copolymer measured in the elemental analysis. This confirms the high cross-linking density of the PB shell. In addition, a marginal quantity of oleic acid was found, indicating its efficient replacement by PB-DETA in the ligand exchange step.

If the fraction of soluble diblock copolymer is considered and bulk densities are assumed for the components, the sample PB_HDT_7.7 is composed of 15.2 vol % of iron oxide core, 42.6 vol % of inner cross-linked PB shell, and 42.2 vol % of outer PEO shell. Taking now into account the iron oxide particle radius of 7.7 nm, the thickness of the cross-linked PB shell is 4.3 nm. This calculated value corresponds well with the thickness of the unstained and, therefore, light PB shell of single SPIONs in the TEM image (Figure 5.5d), which is about 3 nm. The PEO chains are anchored on the PB shell with a density of 1 chain per 4.2 nm² of PB surface. This grafting density is comparable with the density of PEO chains in aqueous micelles of amphiphilic diblock polymers of 1 chain per 1.6 nm² of interfacial area and therefore indicates a reasonable stabilization of the NCs by the PEO corona.^[44]

5.4 Conclusion

In conclusion, polymer nanocomposites consisting of homogeneously dispersed SPIONs in a poly(ethylene oxide) matrix could be synthesized. Detailed step-by-step analysis by SAXS and TEM allowed to identify the crucial steps determining the degree of agglomeration within polymer matrix, i.e., pre-encapsulation of the NCs into a cross-linked polydiene poly(ethylene oxide) diblock copolymer and the consecutive phase transfer into aqueous environment. Likewise, the subsequent cross-linking of the inner polydiene shell influences strongly the structural homogeneity and the agglomerate formation of the encapsulated NCs. SAXS and TEM investigations clearly showed that the radical initiated thiol–ene click reaction with HDT and AIBN is superior to the classical free radical cross-linking approach with only AIBN. In the latter case, the dispersion of the NCs into poly(ethylene oxide) leads to an increased fraction of agglomerates, whereas the nature of the polydiene is of minor importance. Best nanocomposites consist of 80–90% of single, homogeneously dispersed particles and only 10–20% of linear agglomerates of two or three NCs. To the best of our knowledge, such a detailed sequence of NC synthesis, modification, nanocomposite formation, and structural characterization has not yet been reported in literature.

The presented advanced method will enable the applications of magneto-rheological nanocomposites as adaptive materials, in which the core functionality of the SPIONs is exploited.

5.5 Materials and Methods

5.5.1 Materials

The following chemicals were used as received.

Tetrahydrofuran (THF, 99.7%), *n*-hexane (96%), and ethanol (99.98%) were purchased from VWR. 1,6-Hexanedithiol (HDT, 97%) was obtained from Alfa Aesar. 2,2'-Azobis(2-methylpropionitrile) (AIBN, 98%), hydrochloric acid (37%, ACS reagent grade), and chloroform ($\geq 99.8\%$) were purchased from Sigma-Aldrich. Water was purified using a Millipore-Q System (18.2 M Ω cm). SPIONs were synthesized according to Yu et al.^[45] The synthesized SPIONs were initially stabilized with oleic acid. 1,2-Polybutadiene (PB) with molecular weight $M_n = 1940$ g/mol and molecular weight distribution $M_w/M_n = 1.05$ and 3,4-polyisoprene (PI) with $M_n = 1800$ g/mol and $M_w/M_n = 1.08$ were synthesized with OH head groups. The block copolymers PB-*b*-PEO ($M_n = 6790$ g/mol and $M_w/M_n = 1.02$) and PI-*b*-PEO ($M_n = 6600$ g/mol and $M_w/M_n = 1.23$) were synthesized by polymerizing ethylene oxide onto the polydiene polymers and used for the encapsulation. The synthesis of these polymers and the synthesis of PB-DETA and PI-DETA are presented in the Supporting Information. The matrix polymer poly(ethylene oxide) had a M_n of 3.080 g/mol, and M_w/M_n was determined to be 1.04. SPIONs encapsulated with a polymer shell in solution and the nanocomposites were characterized by TEM and SAXS. TEM experiments were performed at MLZ Garching/Munich using a Jeol JEM 2200 FS EFTEM instrument and in Hamburg using Jeol JEM1011 microscope (100 keV). The high brilliance laboratory small-angle X-ray scattering instrument GALAXI at JCNS was used for SAXS measurements.^[46]

5.5.2 Polymer Synthesis

General procedures. All manipulations were carried out at a high vacuum line or in a glove box filled with argon (M Braun, Unilab). The water level in the glove box was below 1 ppm and the oxygen level below 0.1 ppm. The flasks for all manipulations were equipped with Teflon

stopcocks (Young®), which allowed the transfer of materials between the vacuum line and glove box without contamination with air. The flasks that were exposed to overpressure were pressure-tested to 4-12 bar depending on the size of the flask.

Materials. Butadiene (Fluka, ≥99.6%) and isoprene (Aldrich, 99%) were degassed, condensed on solvent free di-*n*-butylmagnesium, stirred at 0 °C over-night, condensed on solvent free *n*-butyllithium, stirred at -20 °C for 20 min and directly used by condensing the monomers into the polymerization flask. Ethylene oxide (EO) (Chemogas, ≥99.9%) was condensed into a flask, degassed, and stirred twice over CaH₂ for 1-2 days, before being condensed into the reaction flask. THF (Merck, 99.9%) was degassed, pre-dried over CaH₂, and dried with potassium and benzophenone before use. *tert*-Butyllithium solution (1.7 M) in *n*-pentane (Aldrich), 1,1'-carbonyldiimidazole (CDI) (Aldrich, ≥97%) and diethylenetriamine (Aldrich, 99%) were used as received.

Polymerization reactions. The synthesis of polyisoprene end functionalized with an OH-group (PI-OH), PI-DETA, and PI-*b*-PEO is described elsewhere.^[23] 1,2-Polybutadiene end functionalized with an OH-group (1,2-PB-OH) was obtained by polymerizing 21.7 g of butadiene with 12.8 mmol of *tert*-butyllithium in 350 mL of THF at -60 °C for 4 h, followed by 0 °C for 2 h. Afterwards, 3 g of EO (68 mmol) were added by vacuum distillation and the reaction mixture was allowed to warm up to room temperature over-night. About half of the solvent was removed by vacuum distillation in order to eliminate excess EO, 1 mL of acetic acid was added, insoluble salt was removed by filtration, and after concentrating the solution to a volume of about 100 mL, the polymer was precipitated in methanol, washed with methanol, and finally, dried under high vacuum conditions. The 1,2-PB-*b*-PEO block copolymer was synthesized by dissolving 3.47 g of 1,2-PB-OH in 22 mL of THF and titrating the alcoholic end groups with potassium naphthalenide solution. The potassium naphthalenide solution was obtained by dissolving 1.44 g of sublimed naphthalene (11.2 mmol) in THF, adding 0.375 g of potassium (9.6 mmol) and stirring the mixture over-night. The polymer solution was diluted with 40 mL of THF and 7.12 g of EO were cryo-distilled into the reactor. After four days at 40 °C, 0.5 mL of acetic acid was added, the solvent was distilled off at reduced pressure, the solid residue was dissolved in about 200 mL of chloroform, and washed four times with 50 mL of water. After having removed the solvent at reduced pressure, the block copolymer was dissolved in 200 mL of warm ethanol, precipitated at -20 °C, washed twice with cold ethanol, and dried under high vacuum conditions. The refunctionalization of 1,2-PB-OH in order to obtain the diethylenetriamine functionalized variant 1,2-PB-DETA was conducted by mixing 2.0 g of dry 1,2-PB-OH, dissolved in 15 mL of dry dichloromethane with 3.42 g of CDI (21.1 mmol, 20 eq.). The suspension was stirred under argon atmosphere at room temperature for 17 h. It was then

transferred into a separating funnel and washed twice with 5 to 10 mL of water to hydrolyze the excess of CDI. After drying with MgSO₄, 2.2 g of diethylenetriamine (21.3 mmol, 20 eq.) were added slowly. The mixture was stirred at 45 °C for 22 h. The precipitate which was formed during the reaction was filtered off. After replacing the solvent dichloromethane by toluene, the polymer was precipitated in methanol, washed with methanol, and dried under high vacuum conditions.

5.5.3 Polymer Characterisation

The molecular weight distributions M_w/M_n of samples 1,2-PB-OH and 1,2-PB-*b*-PEO were determined by size exclusion chromatography (SEC) using a Polymer Laboratories PL 220 SEC instrument equipped with a differential refractive index detector and with three PolyPore columns at 50 °C. The eluent was a solution of THF and DMA (85 : 15 by volume) at a flow rate of 1 mL/min. PEO standards were used for calibration. The molecular weights and weight distributions can be found in Table 5.6.

Table 5.6 Molecular weight characterization of the polymers used for the SPION encapsulation processes.

	polydiene block		block copolymer	
	M_n (NMR) [g/mol]	M_w/M_n (SEC)	M_n (NMR) [g/mol]	M_w/M_n (SEC)
PI- <i>b</i> -PEO	1800	1.08	6600	1.23
PB- <i>b</i> -PEO	1940	1.05	6790	1.02

The number average molecular weight (M_n) of 1,2-PB-OH was determined by ¹H-NMR in CDCl₃ comparing the signal intensities of PB between 1.0 and 2.2 ppm and between 4.8 and 5.7 ppm with the signal intensity of the *tert*-butyl initiating group at 0.84 ppm. For determining M_n of the PEO block in 1,2-PB-*b*-PEO, the same procedure was used by considering the PEO signal intensity between 3.4 and 3.8 ppm. The microstructure of the sample 1,2-PB-OH was extracted from the ¹H-NMR signal between 4.8 and 5.1 ppm (2 protons of the 1,2-microstructure) and the signal between 5.2 and 5.7 ppm (1 proton of the 1,2-microstructure and 2 protons of the 1,4-microstructure). The 1,2-fraction was calculated to be 91%. ¹H-NMR was also used to determine the functionalization of 1,2-PB-DETA with diethylenetriamine units. The signal of the CH₂-protons next to the OH-group in 1,2-PB-OH at 3.65 ppm moved to 4.05 ppm

in the spectrum of 1,2-PB-DETA. The absence of the signal at 3.65 ppm indicated the quantitative conversion of the alcohol end group.

5.5.4 Encapsulation of SPIONs and Dispersing into a PEO Matrix

Encapsulation of the SPIONs took place in three steps. First, the oleic acid ligands were exchanged with PI-DETA or PB-DETA. Therefore, the oleic acid-coated SPIONs and a 3000-fold excess of PI- and PB-DETA, respectively, were dispersed in *n*-hexane and stored for 20 h. The NCs were precipitated with ethanol and redispersed in THF. Then, the NCs, a 3000-fold excess of PI-*b*-PEO or PB-*b*-PEO, respectively, and either AIBN (1/3 of isoprene and butadiene units present in the diblock copolymer) or a mixture of HDT (1/12 of isoprene and butadiene units) and AIBN (1/4 of isoprene and butadiene units) were mixed in THF to yield a 2 μ M solution. The solution was transferred into the 10-fold volume of water with a programmable flow system.^[42] PI-*b*-PEO and PB-*b*-PEO acted as emulsifying agent and served as shell material, respectively. Finally, the double bonds of the PI or PB part were cross-linked at 80 °C for 4 h either in a radical initiated reaction with AIBN as radical initiator or in a radical initiated thiol-ene click reaction with HDT as a cross-linker and AIBN as radical initiator. The encapsulated SPIONs were purified by means of magnetic column.^[47] The encapsulated SPIONs, dispersed in water, were mixed with an aqueous PEO solution. The mixture was lyophilized and melted at 60 °C to get the nanocomposites.

5.5.5 Transmission Electron Microscopy (TEM)

For the TEM images presented in Figure 5.1b and Figure 5.2b, the nanocomposite samples were obtained by scratching the matrix and then smashed into powder deposited onto MultiA carbon-coated grid. After a few minutes, excess powder was carefully removed. The specimen was inserted into a hightilt-specimen retainer (EM-2131HTR, JEOL, Tokyo, Japan) and inserted into an adapted tube connected to a membrane pump. The specimen holder with the inserted specimen was put under vacuum at 10^{-6} mbar for a couple of hours (2-4 h). Then, the specimen holder was transferred to a JEM 2200 FS EFTEM instrument (JEOL, Tokyo, Japan). Examinations were carried out at room temperature. The transmission electron microscope was operated at an acceleration voltage of 200 kV. Zero-loss filtered images were recorded digitally by a bottom-mounted 16 bit CCD camera system (FastScan F214, TVIPS, Munich, Germany). Images have been taken with EMenu 4.0 image acquisition program (TVIPS, Munich, Germany). For the TEM images presented in Figure 5.4, the PEO parts of the polymer shells

were stained with phosphotungstic acid. To achieve this, the aqueous solution of the NCs was partially dried on a carboncoated copper grid, and excess solution was removed. A drop of an aqueous phosphotungstic acid solution (10%) was added and carefully removed after 30 s. Afterward, the crystals on the grid were washed two times with a water drop. Small Angle X-ray Scattering (SAXS). SAXS experiments were performed on all samples presented in Table 5.1 in the Q -range from 0.1 to 2 nm^{-1} at the GALAXI. All samples were sealed in glass capillaries of 2 mm inner diameter and measured at $65\text{ }^{\circ}\text{C}$, i.e., above the PEO melting point (melting temperature of PEO is $60\text{ }^{\circ}\text{C}$). The data were background corrected.

5.5.6 Elemental Analysis

The elemental composition of the polymer functionalized SPIONs was exemplarily measured for sample PB_HDT_7.7 (Table 5.1). The iron content was determined by inductively coupled plasma optical emission spectroscopy (ICP-OES). The contents of carbon, hydrogen, oxygen, and sulfur were determined by elemental analysis using the combustion technique. Before this measurement, the iron oxide was removed by stirring a fraction of PB_HDT_7.7 with 1 M hydrochloric acid for 3 days. The insoluble organic material was isolated by centrifugation, washed first with 1 M hydrochloric acid and then with water. The elemental composition is summarized in Table 5.5. The combined aqueous solutions of the iron oxide dissolution process were extracted with chloroform in order to determine soluble organic material. SEC and ^1H NMR measurements showed that the soluble organic fraction consisted mainly of PEO homopolymer. In addition, small quantities of PB-*b*-PEO and oleic acid were found. They corresponded to 1.8 and 0.4 mass % of the organic fraction.

5.6 Acknowledgements

This work was supported by SFB 986 (M3) and SPP 1681 (project 3929/2-1) of the German Research Foundation (DFG). We thank Dr. Johannes Ostermann (Center for Applied Nanotechnology (CAN) GmbH) and Robin Eggers (University of Hamburg, Institute of Physical Chemistry) for support and helpful discussions.

5.7 References

- [1] W. Caseri, *Macromol. Rapid Commun.* **2000**, *21*, 705.
- [2] J. R. Potts, D. R. Dreyer, C. W. Bielawski, R. S. Ruoff, *Polymer (Guildf)*. **2011**, *52*, 5.
- [3] C. Yang, H. Wei, L. Guan, J. Guo, Y. Wang, X. Yan, X. Zhang, S. Wei, Z. Guo, *J. Mater. Chem. A* **2015**, *3*, 14929.
- [4] R. Gupta, E. Kennel, K.-J. Kim, Eds. , *Polymer Nanocomposites Handbook*, CRC Press, **2009**.
- [5] A. C. Balazs, T. Emrick, T. P. Russell, *Science (80-.)*. **2006**, *314*, 1107.
- [6] A. D. B. L. Ferreira, P. R. O. Nóvoa, A. T. Marques, *Compos. Struct.* **2016**, *151*, 3.
- [7] Q. Wang, L. Zhu, in *Funct. Polym. Nanocomposites Energy Storage Convers.* (Ed: Intergovernmental Panel on Climate Change), Cambridge University Press, Cambridge, **2010**, pp. ix–xii.
- [8] B. Gao, M. J. Rozin, A. R. Tao, *Nanoscale* **2013**, *5*, 5677.
- [9] S. Kalia, S. Kango, A. Kumar, Y. Haldorai, B. Kumari, R. Kumar, *Colloid Polym. Sci.* **2014**, *292*, 2025.
- [10] P. Gómez-Romero, C. Sanchez, *Functional Hybrid Materials*, Wiley-VCH Verlag GmbH & Co. KGaA, Weinheim, FRG, **2003**.
- [11] M. Nisar, C. Bergmann, J. Geshev, R. Quijada, G. B. Galland, *Polymer (Guildf)*. **2016**, *97*, 131.
- [12] J. Jestin, F. Cousin, I. Dubois, C. Ménager, R. Schweins, J. Oberdisse, F. Boué, *Adv. Mater.* **2008**, *20*, 2533.
- [13] A.-S. Robbes, F. Cousin, F. Meneau, F. Dalmas, R. Schweins, D. Gigmes, J. Jestin, *Macromolecules* **2012**, *45*, 9220.
- [14] A.-S. Robbes, J. Jestin, F. Meneau, F. Dalmas, O. Sandre, J. Perez, F. Boué, F. Cousin, *Macromolecules* **2010**, *43*, 5785.
- [15] J. Belardi, N. Schorr, O. Prucker, J. Rühle, *Adv. Funct. Mater.* **2011**, *21*, 3314.
- [16] J. Hussong, N. Schorr, J. Belardi, O. Prucker, J. Rühle, J. Westerweel, *Lab Chip* **2011**, *11*, 2017.

- [17] S. N. Khaderi, C. B. Craus, J. Hussong, N. Schorr, J. Belardi, J. Westerweel, O. Prucker, J. Ruhe, J. M. J. den Toonder, P. R. Onck, *Lab Chip* **2011**, *11*, 2002.
- [18] M. Yoonessi, B. A. Lerch, J. A. Peck, R. B. Rogers, F. J. Sol-Lopez, M. A. Meador, *ACS Appl. Mater. Interfaces* **2015**, *7*, 16932.
- [19] P. Akcora, H. Liu, S. K. Kumar, J. Moll, Y. Li, B. C. Benicewicz, L. S. Schadler, D. Acehan, A. Z. Panagiotopoulos, V. Pryamitsyn, V. Ganesan, J. Ilavsky, P. Thiyagarajan, R. H. Colby, J. F. Douglas, *Nat. Mater.* **2009**, *8*, 354.
- [20] M. A. Boles, D. Ling, T. Hyeon, D. V. Talapin, *Nat. Mater.* **2016**, *15*, 141.
- [21] A. Demortiere, P. Panissod, B. P. Pichon, G. Pourroy, D. Guillon, B. Donnio, S. Bgin-Colin, *Nanoscale* **2011**, *3*, 225.
- [22] S. Ehlert, C. Stegelmeier, D. Pirner, S. Frster, *Macromolecules* **2015**, *48*, 5323.
- [23] E. Pselt, C. Schmidtke, S. Fischer, K. Peldschus, J. Salamon, H. Kloust, H. Tran, A. Pietsch, M. Heine, G. Adam, U. Schumacher, C. Wagener, S. Frster, H. Weller, *ACS Nano* **2012**, *6*, 3346.
- [24] C. Schmidtke, H. Lange, H. Tran, J. Ostermann, H. Kloust, N. G. Basts, J.-P. Merkl, C. Thomsen, H. Weller, *J. Phys. Chem. C* **2013**, *117*, 8570.
- [25] H. Weller, J. Ostermann, C. Schmidtke, H. Kloust, *Zeitschrift fr Phys. Chemie* **2014**, *228*, 183.
- [26] T. Pellegrino, L. Manna, S. Kudera, T. Liedl, D. Koktysh, A. L. Rogach, S. Keller, J. Rdler, G. Natile, W. J. Parak, *Nano Lett.* **2004**, *4*, 703.
- [27] Y. Kang, T. A. Taton, *Angew. Chemie Int. Ed.* **2005**, *44*, 409.
- [28] B.-S. Kim, T. A. Taton, *Langmuir* **2007**, *23*, 2198.
- [29] B. L. Sanchez-Gaytan, W. Cui, Y. Kim, M. A. Mendez-Polanco, T. V. Duncan, M. Fryd, B. B. Wayland, S.-J. Park, *Angew. Chemie Int. Ed.* **2007**, *46*, 9235.
- [30] W. Li, S. Liu, R. Deng, J. Wang, Z. Nie, J. Zhu, *Macromolecules* **2013**, *46*, 2282.
- [31] A. Snchez-Iglesias, M. Grzelczak, T. Altantzis, B. Goris, J. Prez-Juste, S. Bals, G. Van Tendeloo, S. H. Donaldson, B. F. Chmelka, J. N. Israelachvili, L. M. Liz-Marzn, *ACS Nano* **2012**, *6*, 11059.

- [32] A. Feld, J.-P. Merkl, H. Kloust, S. Flessau, C. Schmidtke, C. Wolter, J. Ostermann, M. Kampferbeck, R. Eggers, A. Mews, T. Schotten, H. Weller, *Angew. Chemie Int. Ed.* **2015**, *54*, 12468.
- [33] A. Feld, J.-P. Merkl, H. Kloust, S. Flessau, C. Schmidtke, C. Wolter, J. Ostermann, M. Kampferbeck, R. Eggers, A. Mews, T. Schotten, H. Weller, *Angew. Chemie* **2015**, *127*, 12645.
- [34] P. Domínguez-García, M. A. Rubio, *Colloids Surfaces A Physicochem. Eng. Asp.* **2010**, *358*, 21.
- [35] M. Bonini, E. Fratini, P. Baglioni, *Mater. Sci. Eng. C* **2007**, *27*, 1377.
- [36] M. Hagenbüchle, J. Liu, *Appl. Opt.* **1997**, *36*, 7664.
- [37] M. J. a Hore, J. Ford, K. Ohno, R. J. Composto, B. Hammouda, *Macromolecules* **2013**, *46*, 9341.
- [38] E. Wetterskog, C.-W. Tai, J. Grins, L. Bergström, G. Salazar-Alvarez, *ACS Nano* **2013**, *7*, 7132.
- [39] J. S. Higgins, H. Benoît, *Polymers and Neutron Scattering*, Clarendon Press, Oxford, **1996**.
- [40] R. Schweins, K. Huber, *Macromol. Symp.* **2004**, *211*, 25.
- [41] J. Dimitrijevic, L. Krapf, C. Wolter, C. Schmidtke, J.-P. Merkl, T. Jochum, A. Kornowski, A. Schüth, A. Gebert, G. Hüttmann, T. Vossmeier, H. Weller, *Nanoscale* **2014**, *6*, 10413.
- [42] C. Schmidtke, R. Eggers, R. Zierold, A. Feld, H. Kloust, C. Wolter, J. Ostermann, J.-P. Merkl, T. Schotten, K. Nielsch, H. Weller, *Langmuir* **2014**, *30*, 11190.
- [43] J. Ostermann, J.-P. Merkl, S. Flessau, C. Wolter, A. Kornowski, C. Schmidtke, A. Pietsch, H. Kloust, A. Feld, H. Weller, *ACS Nano* **2013**, *7*, 9156.
- [44] J. Allgaier, A. Poppe, L. Willner, D. Richter, *Macromolecules* **1997**, *30*, 1582.
- [45] W. W. Yu, J. C. Falkner, C. T. Yavuz, V. L. Colvin, *Chem. Commun.* **2004**, 2306.
- [46] E. Kentzinger, M. Krutyeva, U. Rücker, *J. large-scale Res. Facil. JLSRF* **2016**, *2*, A61.
- [47] H. Kloust, C. Schmidtke, A. Feld, T. Schotten, R. Eggers, U. E. a Fittschen, F. Schulz, E. Pöselt, J. Ostermann, N. G. Bastús, H. Weller, *Langmuir* **2013**, *29*, 4915.

6 Creating a synthetic platform for the encapsulation of nanocrystals with covalently bound polymer shells

The following chapter was published in *Nanoscale*, Vol. 11, No. 9, pages 3847-3854, 2019 in cooperation with Rieke Koll¹, Hauke Heller¹, Jürgen Allgaier², Wim Pyckhout-Hintzen², Margarita Kruteva², Artem Feoktystov³, Ralf Biehl², Stephan Förster^{2,4}, and Horst Weller¹. Reproduced from Ref. *Nanoscale*, Vol. 11, No. 9, pages 3847-3854, 2019 with permission from the Royal Society of Chemistry.

Together with Rieke Koll, I formulated the original task and chose the analytical methods. I synthesised most of the polymers and characterised them *via* NMR and SEC. The synthesis route for the phosphonic acid functionalised polymers was researched and developed by me. I performed all of the SAXS experiments and one SANS experiment and analysed all of the small-angle scattering data. I wrote the corresponding parts of the manuscript and developed a first draft of the manuscript together with Rieke Koll. I participated in revising and finalising the manuscript. Rieke Koll developed and optimised the synthesis procedure for the encapsulation of the nanocrystals. She characterised the encapsulated nanocrystals *via* TEM, DLS and TGA, analysed the results and prepared the corresponding parts of the manuscript. Hauke Heller contributed to this work in many discussions with Rieke Koll, Jürgen Allgaier, Margarita Kruteva, Wim Pyckhout-Hintzen, Ralf Biehl, Horst Weller and myself. Jürgen Allgaier was involved into the synthesis and characterisation of the polymers. Together with Margarita Kruteva, he successfully applied for funding of this project from the Deutsche Forschungsgemeinschaft. They established the connection to the colleagues in Hamburg. Wim Pyckhout-Hintzen provided help concerning the interpretation of the SANS data. Margarita Kruteva performed

¹ Institute of Physical Chemistry, Fraunhofer CAN, Grindelallee 117, 20146 Hamburg, Germany.

² Jülich Centre for Neutron Science (JCNS-1) and Institute for Complex Systems (ICS-1), Forschungszentrum Jülich GmbH, Leo-Brandt-Straße, 52425 Jülich, Germany.

³ Forschungszentrum Jülich GmbH, Jülich Centre for Neutron Science (JCNS) at MLZ, Lichtenbergstrasse 1, 85748 Garching, Germany.

⁴ Institute of Physical Chemistry, RWTH Aachen University, Landoltweg 2, 52056 Aachen, Germany.

most of the SANS experiments. Artem Feoktystov assisted during all SANS experiments and treated the resulting data. Ralf Biehl helped me regarding the data evaluation using Jscatter. Margarita Kruteva, Stephan Förster and Horst Weller supervised the investigations. All authors participated during all stages of the process.

6.1 Abstract

We present a platform for the encapsulation of superparamagnetic iron oxide nanocrystals (SPIONs) with a highly stable diblock copolymer shell allowing a homogeneous dispersion of the nanocrystals into a polymer matrix in the resulting nanocomposites. High polymer shell stability was achieved by crosslinking the inner polydiene shell for example in a persulfate based redox process. The advantage of this crosslinking reaction is the avoidance of heat and UV light for the initiation, making it suitable for heat or UV sensitive systems. In addition, we were able to minimize the ligand excess needed for the encapsulation and showcased a variation of molecular weight and composition as well as different ligands which lead to stable micelles. The encapsulated nanocrystals as well as the nanocomposite materials were characterized by transmission electron microscopy (TEM) and small angle scattering (SAXS and SANS).

6.2 Introduction

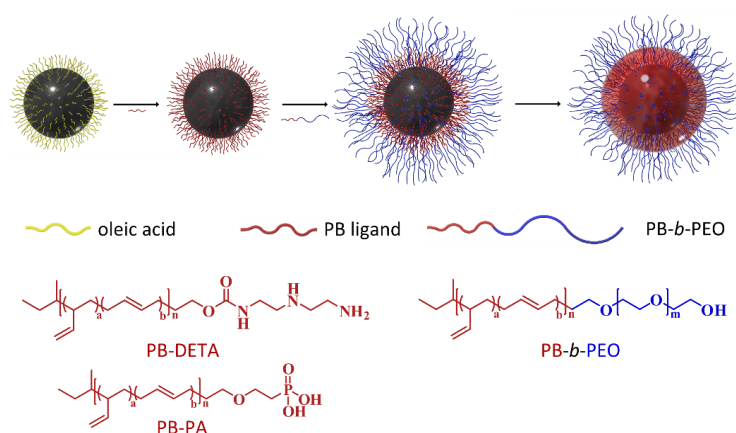
Polymer encapsulation is a key technological step for nanocrystal (NC) applications ranging from high performance nanocomposites^[1-4] over quantum converter films in display and lighting^[5,6] to contrast agents and drug delivery systems^[7-13] in nanomedicine. The role of the encapsulation is twofold: it allows solubility adjustment and ensures stability and compatibility in the respective environment. A very powerful method is based on amphiphilic diblock copolymers. Here, hydrophobic NCs act as nucleation centres for micelle formation of the copolymers around the NCs. For the system polyisoprene-*block*-poly (ethylene oxide) (PI-*b*-PEO) it was shown that radical initiated crosslinking of the polyisoprene core significantly enhances the biocompatibility due to shielding effects of the NCs against the surrounding medium.^[14] An important parameter is the control of the number of NCs within one micelle, in which in many applications just one NC per micelle is the target structure. In nanocomposites, moreover, it is mostly desirable to achieve a homogeneous dispersion of individually encapsulated NCs within the surrounding matrix material as the nanocomposite properties strongly depend on the local organization of the NCs.^[15] Here we report a combined transmission electron microscopy (TEM) and small angle X-ray and neutron scattering (SAXS and SANS) study on structure formation during the encapsulation process of superparamagnetic iron oxide nanocrystals (SPIONs) in a poly(ethylene oxide) matrix. We have

chosen 1,2-polybutadiene-*block*-poly(ethylene oxide) (PB-*b*-PEO) of various molar masses for the encapsulation and compare different crosslinking techniques of the hydrophobic micellar core. Furthermore, we present how a homogeneous distribution of the SPIONs can be achieved by adjustment of PEO block lengths of the diblock copolymers and the PEO matrix material, respectively. The excess of polymer ligand needed for encapsulation was minimized by choosing a NC specific anchoring group, facilitating a future upscale of the process. In addition, a SANS contrast variation study was employed to examine the details of the polymer shell.

6.3 Results and Discussion

6.3.1 Encapsulation of SPIONs

In order to avoid agglomeration and to get a homogeneous distribution of the nanocrystals inside the PEO matrix, the SPIONs have to be stabilized. We used SPIONs with a TEM determined diameter of $15.4 \text{ nm} \pm 5\%$. The stabilization of the SPIONs was achieved by encapsulation with PB-*b*-PEO and crosslinking of the inner PB shell. The encapsulation of SPIONs serves as a model system due to their well-known synthesis of high quality nanocrystals. Nevertheless, the presented procedure is adaptable to various types of nanocrystals.^[14,16–20] The encapsulation was achieved in three steps; a schematic illustration is presented in Scheme 6.1.

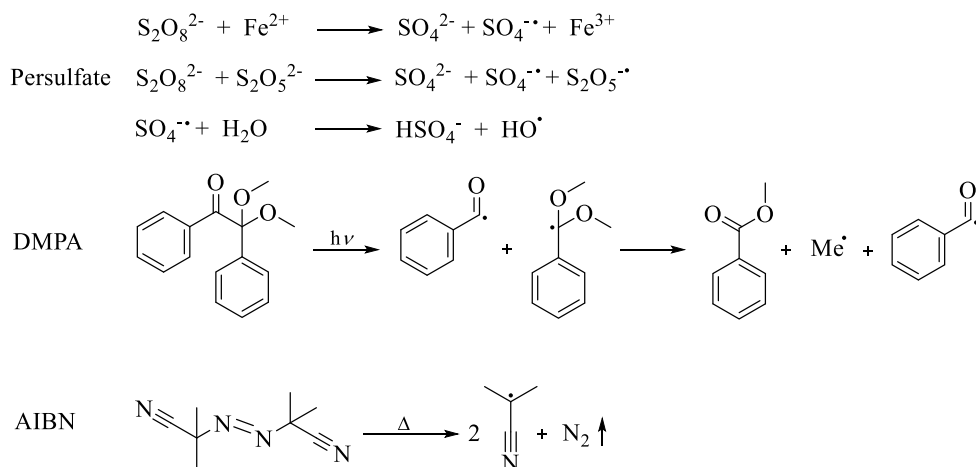


Scheme 6.1 Schematic illustration of the encapsulation process. First, the native oleic acid ligands are exchanged against a polymer ligand. Then, the SPIONs are mixed with a diblock copolymer and transferred into water, where the micelle formation takes place. Finally, the double bonds of the inner polymer shell are crosslinked.

The first step is the exchange of the native oleic acid ligands by a polymeric ligand in an equilibrium process. As ligands the 2,2'-diamino-diethylamine functionalized polybutadiene (PB-DETA) and phosphonic acid functionalized polybutadiene (PB-PA) were used. The polymer ligand serves as seed for the following micelle formation. Afterwards, the polymer ligand stabilized SPIONs were mixed with PB-*b*-PEO and were transferred into water. The diblock copolymer acts in this process as emulsifying agent. In a final step, the double bonds of the inner PB shell were crosslinked. In order to remove empty micelles, the encapsulated SPIONs were purified using a magnetic column. The purified encapsulated SPIONs, dispersed in water, were then mixed with an aqueous PEO solution, lyophilized and melted at 65 °C to yield the nanocomposite.

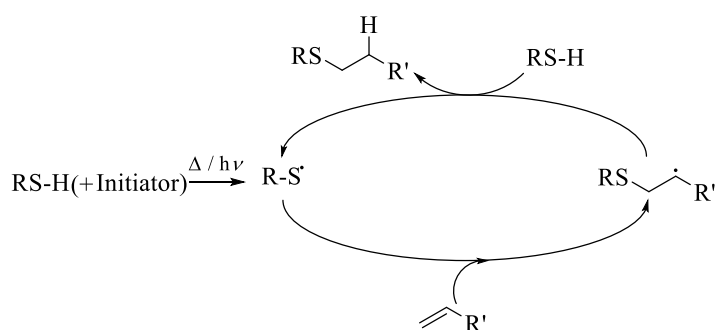
6.3.2 Examination of different crosslinking pathways

For the crosslinking of the inner polymer shell, several different pathways are possible. We already introduced the thiol-ene click reaction with 1,6-hexanedithiol (HDT) to be a suitable method to crosslink and therefore stabilize the polymer shell in order to obtain homogeneously dispersed nanocrystals in a PEO matrix.^[21] The thiol-ene clickreaction can be initiated with either a thermal radical initiator like 2,2'-azobis(2-methylpropionitrile) (AIBN) or with a photoinitiator like 2,2-dimethoxy-2-phenyl-acetophenone (DMPA). Both initiation techniques are unsuitable for heat or UV sensitive materials. An alternative crosslinking method is provided by a common redox reaction using potassium persulfate as a water soluble radical initiator. The persulfate decomposition at room temperature is catalyzed by a redox system comprising sodium metabisulfite and iron(II) sulfate heptahydrate.^[22,23]



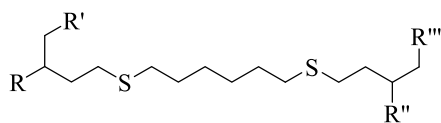
Scheme 6.2 Decomposition reactions of the used initiators to start the crosslinking process.

All three crosslinking reactions start with the formation of radicals (Scheme 6.2) which then initiate the polymerisation reaction.^[23-26] The crosslinking of polydienes is well-known, information on the mechanism can be found in the literature.^[27,28] The reaction mechanism of the thiol-ene clickreaction can be found in Scheme 6.3.^[29] An additional advantage of the persulfate based redox process is the direct crosslinking of the polymer without integration of crosslinker into the shell. This is the case for example for the thiol-ene click reactions, where large disulfide moieties are incorporated between the polymer chains (Scheme 6.4).



Scheme 6.3 Reaction mechanism of the thiol-ene clickreaction.

The fixation of micellar structures formed by amphiphilic diblock copolymers *via* the persulfate based redox reaction has already been published,^[30] but in combination with nanocrystals it is still unknown.



Scheme 6.4 Polymer structure after crosslinking with HDT as crosslinker.

The completeness of the encapsulation process was examined by TEM. In these experiments the PEO shell was selectively stained with phosphotungstic acid, leading to a dark corona around the SPIONs. Combining TEM imaging with this staining agent is a suitable method to study the completeness of the encapsulation process due to possible etching of the SPIONs by the staining agent. Etching is only prevented in case of a homogeneous and stable polymer shell.^[21] Figure 6.1 shows representative TEM images of encapsulated SPIONs, crosslinked with HDT/AIBN (a), HDT/UV (b), HDT/DMPA/UV (c) and persulfate (d). As can be seen here, all crosslinking procedures lead to closed polymer shells of a high quality.

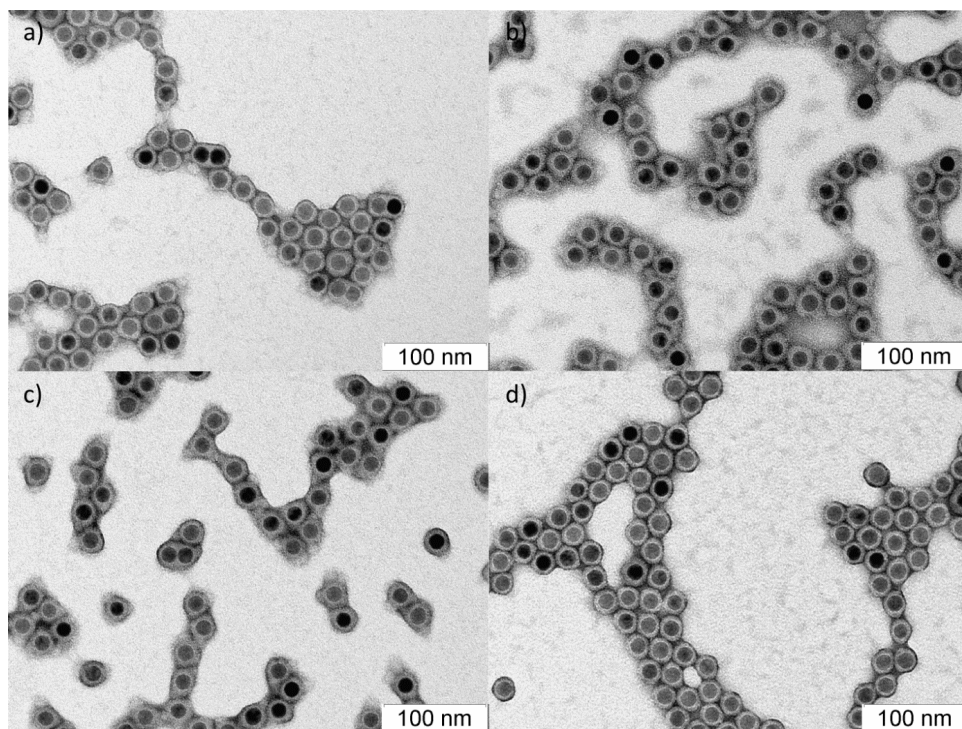


Figure 6.1 TEM images of HDT/AIBN (a) HDT/UV (b) HDT/DMPA/UV (c) and persulfate (d) crosslinked encapsulated SPIONs, stained with phosphotungstic acid. The diblock copolymers PB5k-PEO10k (b, c) and PB3k-PEO4k (a, d) were used.

The encapsulated SPIONs, crosslinked with the persulfate based redox reaction or the thiol–ene clickreaction, were dispersed in a polymer matrix and the resulting nanocomposites were analyzed with SAXS. Figure 6.2a shows the scattering curves for the different crosslinked samples. All scattering curves exhibit a form factor of spherical SPIONs with well-defined minima indicating the narrow size distribution of the used SPIONs. The form factor oscillations can be described by a SPION radius of 8.2 ± 0.4 nm, which is in a good agreement to the TEM determined radius of 7.7 nm, as the SAXS radius is weight-averaged and the TEM radius is number-averaged. To get information about the number of individually encapsulated SPIONs and therefore the dispersion state, the scattering curves were fitted with the pearl-necklace model.^[21,31] This gives the number of encapsulated SPIONs N forming a “chain” (agglomeration number).

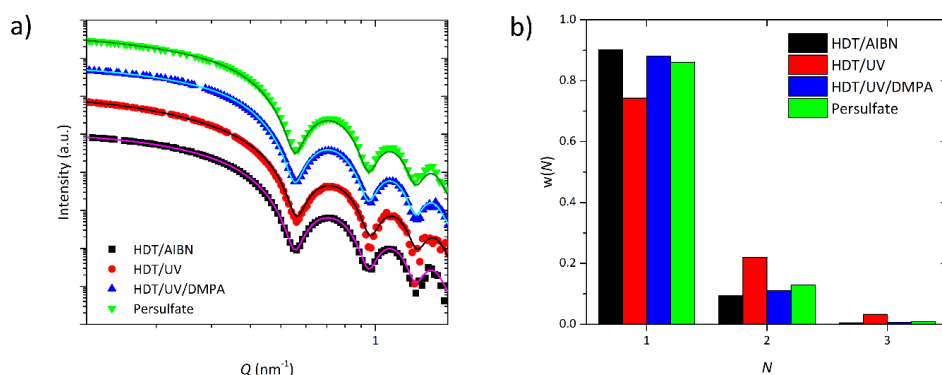


Figure 6.2 a) SAXS curves (arbitrarily shifted) of differently crosslinked samples. b) Distribution of the agglomeration number N for each sample.

The distribution of N is presented in Figure 6.2b. Both the persulfate based redox reaction and the thermally and photochemically initiated thiol–ene clickreaction lead to a stable polymer shell, which enables a homogeneous distribution of the SPIONs inside the PEO matrix with a ratio of single SPIONs of around 90%. The remaining SPIONs form mainly dyads and to a marginal amount triads. We already clarified the origin of dyads and triads coming from a multiple encapsulation during the phase transfer step from organic solvent into water.^[21] Slight differences in the relative amount of single SPIONs arise from different encapsulation processes during the phase transfer step. In contrast, the sample crosslinked photochemically without the photoinitiator DMPA shows only 75% of single SPIONs, which indicates insufficient polymer shell stability. This can be explained by a lack of radical polymerization of the PB

double bonds when DMPA is missing. The same effect has been shown when using the radical initiator AIBN with and without HDT.^[21]

6.3.3 Variation of the diblock copolymer chain length

For the SPION encapsulation we varied the chain length and the composition of the diblock copolymers. PB5k-PEO10k, PB3k-PEO4k and PB2k-PEO5k were used, while the chain length of the polymer ligand PB-DETA was kept constant at 2k. The polymer shells were crosslinked with HDT/AIBN and analyzed with TEM. Furthermore, we dispersed the encapsulated SPIONs in PEO and investigated the dispersion state with SAXS measurements. To obtain further knowledge about the polymer shells, SANS experiments of SPIONs encapsulated with two different diblock copolymers were performed. Typical TEM images of samples with a PB5k-PEO10k and a PB2k-PEO5k polymer shell are presented in Figure 6.3. The PEO shell was stained with phosphotungstic acid. Independent from the diblock copolymer chain length, all samples indicate a PB shell thickness of about 3 nm, which is represented by the unstained yet slightly darkened area around the SPIONs.

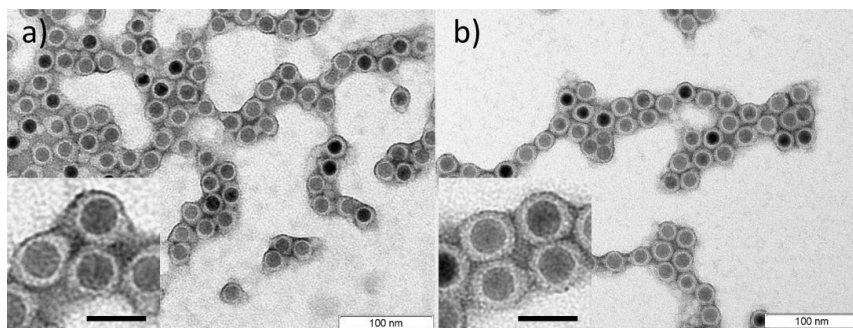


Figure 6.3 TEM images after drying of PB-b-PEO encapsulated SPIONs with a (a) PB5k-PEO10k and a (b) PB2k-PEO5k polymer shell. The scale bars in the inserts correspond to 25 nm.

This area darkens in additional TEM images, where the PB was selectively stained with osmium tetroxide (see Figure 6.4). This shell primarily consists of diblock PB and to a smaller extent of PB-DETA. Nevertheless, its thickness is independent of the PB length in the diblock.

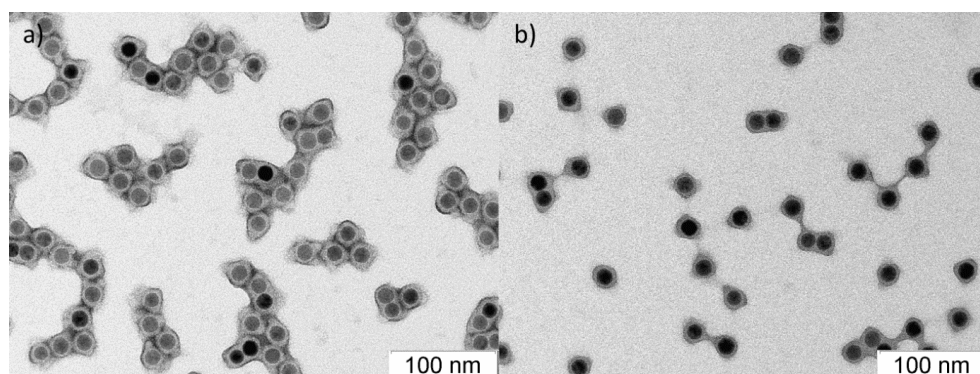


Figure 6.4 TEM images of encapsulated SPIONs with phosphotungstic acid (a) and osmium tetroxide (b) stained polymer shells. The polymer shell consists of PB3k-PEO4k and was crosslinked with HDT/AIBN.

Hence, the grafting density of the PEO corona decreases with increasing PB block length. This was confirmed by thermogravimetric analysis (TGA) measurements, where the mass loss due to the polymer depended only slightly on its chain length (see Figure 6.5).

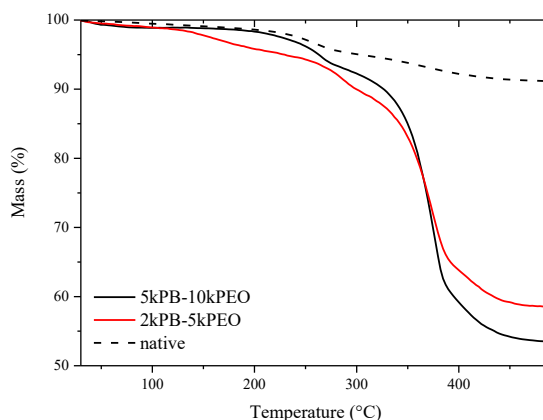


Figure 6.5 Exemplary TGA results for PB2k-PEO5k and PB5k-PEO10k encapsulated SPIONs, crosslinked with HDT/AIBN, and TGA results for oleic acid stabilized SPIONs for comparison.

The replacement of the oleic acid by the polymeric ligand was omitted for these samples to ensure that the organic compound mostly consists of the diblock copolymer. The diblock copolymer and NC mass fractions were calculated from the relative mass losses between 100 °C and 450 °C and the residual mass at 450 °C, whereat a mass loss of 9% for oleic acid was subtracted. Considering the masses of the diblock chains and the NCs, the number of polymer

chains per NC was calculated to be 230 chains for PB5k-PEO10k coated NCs and 360 chains for the PB2k-PEO5k coated NCs.

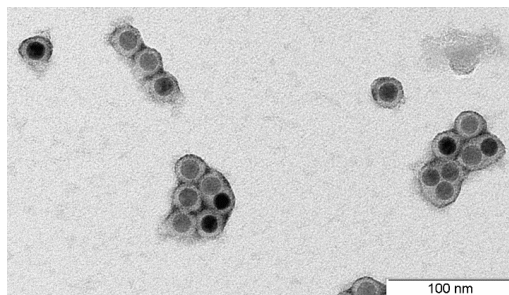


Figure 6.6 TEM image of PB-b-PEO encapsulated SPIONs with a PB5k-PEO10k polymer shell and a 5 kDa polymer ligand.

In further experiments, where the PB-DETA molecular weight was increased from 2k to 5k, the PB shell thickness stayed constant at 3 nm (see Figure 6.6). However, the total size of the micelles increases with increasing diblock copolymer size which was ascertained with dynamic light scattering (DLS) measurements (see Figure 6.7).

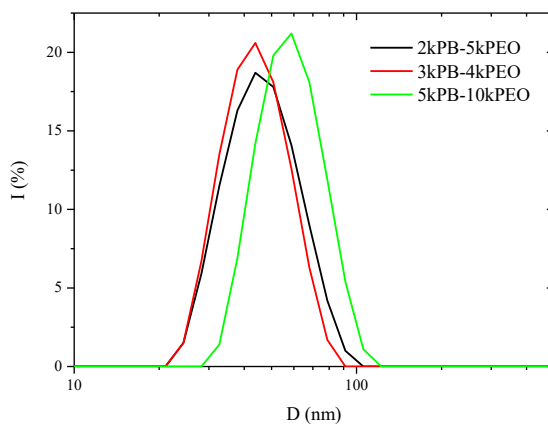


Figure 6.7 Intensity weighted size distributions from DLS analysis for SPIONs encapsulated with different weighted diblock copolymers.

The polymer shell thickness was exemplarily analyzed with SANS for the PB2k-PEO5k and PB5k-PEO10k. In the case of PB2k-PEO5k a contrast variation study was conducted using four different contrast scenarios which are illustrated in Figure 6.8: (1) hPB-dPEO in dPEO3k;

(2) hPB-hPEO in dPEO3k; (3) hPBdPEO in D₂O; (4) hPB-hPEO in D₂O. For PB5k-PEO10k, only the second contrast (in dPEO10k) was measured to compare the polymer shell dimensions for different block copolymer lengths. As the scattering length density (SLD) of iron oxide is very close to the values for the deuterated matrices, the highest contribution to the scattering intensity arises from the hydrogenous polymers.

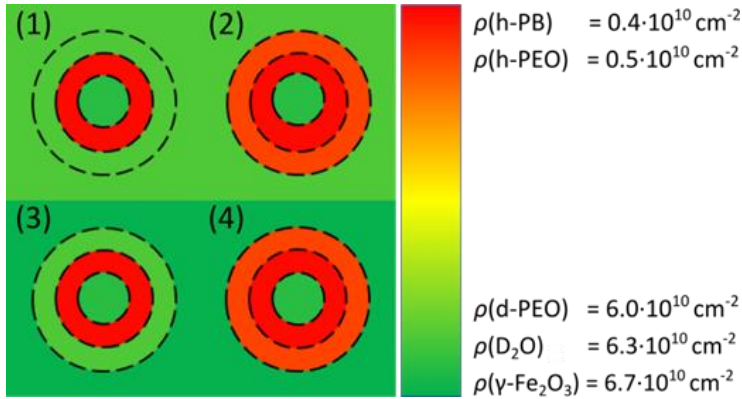


Figure 6.8 SANS contrast scenarios for SPIONs encapsulated with hPB-dPEO in dPEO (1), hPB-hPEO in dPEO (2), hPB-dPEO in D₂O (3) and hPB-hPEO in D₂O (4) and calculated values of scattering length densities.

Therefore, the pearl-necklace model was modified by using a spherical core-shell-shell form factor implying a step profile for the SLDs. Our extended pearl-necklace model consists of a spherical core-shell-shell form factor $P(Q)$ and an intra-agglomerate structure factor $S_{\text{intra}}(Q)$:

$$I(Q) \cong P(Q) \cdot S_{\text{intra}}(Q) \quad (6.1)$$

The form factor contains contributions from the core and both shells including R as the radius of the full particle with $R = R_c + t_{\text{PB}} + t_{\text{PEO}}$:

$$P(Q) = \left[\frac{4\pi}{3} (\rho_c - \rho_m) \cdot R_c^3 \cdot A_1 + \frac{4\pi}{3} (\rho_{\text{PB}} - \rho_m) \cdot (R_c + t_{\text{PB}})^3 \cdot A_2 + \frac{4\pi}{3} (\rho_{\text{PEO}} - \rho_m) \cdot R^3 \cdot A_3 \right]^2 \quad (6.2)$$

The three contributions to the form factor are as follows:

$$A_1 = 3 \frac{\sin(QR_c) - QR_c \cdot \cos(QR_c)}{(QR_c)^3} \quad (6.3)$$

$$A_2 = 3 \frac{(\sin(Q(R_c + t_{\text{PB}})) - Q(R_c + t_{\text{PB}}) \cdot \cos(Q(R_c + t_{\text{PB}}))) - (\sin(QR_c) - QR_c \cdot \cos(QR_c))}{(Q(R_c + t_{\text{PB}}))^3 - (QR_c)^3} \quad (6.4)$$

$$A_{3=3} = \frac{(\sin(QR) - QR \cdot \cos(QR)) - (\sin(Q(R_c + t_{PB})) - Q(R_c + t_{PB}) \cdot \cos(Q(R_c + t_{PB})))}{QR^3 - Q(R_c + t_{PB})^3} \quad (6.5)$$

The structure factor is the same as in the original model:

$$S_{\text{intra}}(Q) = \frac{2}{N^2} \left[\frac{N}{1 - \frac{\sin(Q(l+2R))}{Q(l+2R)}} - \frac{N}{2} \frac{1 - \left(\frac{\sin(Q(l+2R))}{Q(l+2R)} \right)^N \sin(Q(l+2R))}{\left(1 - \frac{\sin(Q(l+2R))}{Q(l+2R)} \right)^2 Q(l+2R)} \right] \quad (6.6)$$

The value for the core radius of 8.2 nm was taken from the SAXS data evaluation. Due to the low contrast between SPION core and matrix, the influence of the SPION polydispersity is small and can be neglected. The SLD of the matrix ρ_m and the inner PB shell ρ_{PB} were fixed to calculated values of $\rho_{PB} = 0.4 \cdot 10^{10} \text{ cm}^{-2}$ and $\rho_m = 6.0 \cdot 10^{10} \text{ cm}^{-2}$ for deuterated PEO and $\rho_m = 6.3 \cdot 10^{10} \text{ cm}^{-2}$ for deuterated water. Experimental SANS curves with corresponding fits are displayed in Figure 6.9.

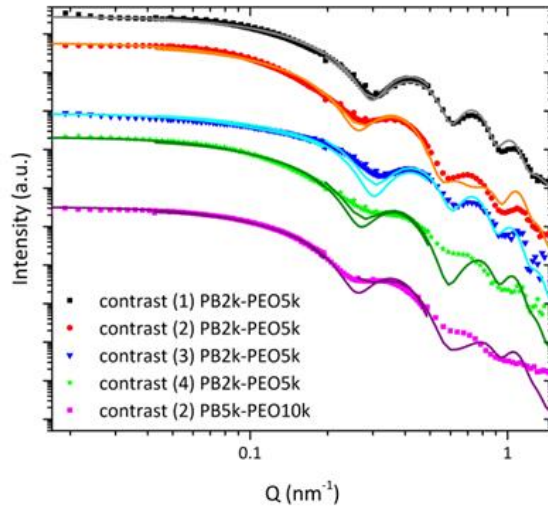


Figure 6.9 SANS curves with corresponding fits for hPB-dPEO in dPEO (1), hPB-hPEO in dPEO (2), hPB-dPEO in $D_2O(3)$ and hPB-hPEO in D_2O (4), obtained from three different detector distances with corresponding resolution functions.

We used contrast (1) to determine the SLD of the SPION core ρ_c and the thickness t_{PB} of the PB shell, resulting in values of $\rho_c = 6.7 \pm 0.1 \cdot 10^{10} \text{ cm}^{-2}$ which conforms to the theoretical value for maghemite and $t_{PB} = 4.3 \pm 0.1 \text{ nm}$. This corresponds well to the values for the PB shell thickness found *via* TEM and complementary methods.^[21] The well pronounced minima

indicate a narrow distribution of the PB shell thickness. The PEO shell is invisible under these contrast conditions. The fraction of singly encapsulated SPIONs was determined to be 76%.

For the contrast (3) the data could be described by the model and the predetermined values quite well. The PEO shell contributes to the scattering curve due to a small difference between SLD of D₂O and PEO. As a consequence, the minima are less pronounced.

Fixing t_{PB} , ρ_c and N from contrast (1) for the examination of contrast (2) and (4) with h-PEO shells, we were able to obtain reliable values for the thickness t_{PEO} of the outer PEO shell. For contrast (2) t_{PEO} was equal to 4.5 ± 0.1 nm and for contrast (4) in D₂O the value was 5.3 ± 0.3 nm. The PEO shell thicknesses can be compared with the sizes of the free PEO chains by taking their end-to-end distances R_{ee} as a measure. For PEO5k in a theta solvent R_{ee} is about 6.92 nm using the equations $R_{ee} = \sqrt{6} R_g$. and $R_g^2 = 4.08 \cdot 10^{-18} M_w^{1.16} cm^2$ ^{[32]5}

For small molecular weights, it is known that chain dimensions are similar in good and theta solvents. Therefore, the PEO5k shell results of t_{PEO} , 4.5 nm in the nanocomposite and 5.3 nm in water indicate rather dense PEO shells whereby the PEO chains are only marginally stretched. Although the molecular weight of the PEO is doubled when using PB5k-PEO10k, the dimension of the PEO shell in the melt increases only slightly to 4.9 ± 0.1 nm compared to the calculated value of $R_{ee} = 8.9$ nm.^[33] The fraction of singly encapsulated SPIONs was determined to be 83%. From prior investigations it is known that for SPIONs encapsulated with the procedure presented here, a grafting density of PEO chains on the PB surface is approximately one chain per 4.2 nm².^[21] One notes, that the quality of the fits becomes worse with increasing scattering contribution of the PEO shell due to the used simplified step profile. For this reason, the thickness of the PEO shell may be underestimated in our study. Nevertheless, we have to assume a rather dense PEO shell. This is confirmed by the absence of individual chain scattering (PEO form factor) characterized by the power law $I(Q) \sim Q^{-1.6}$ in the high Q -range, which is normally seen in micellar systems.^[34]

Additional parameters of the fits are the SLDs of the PEO shells ρ_{PEO} . The values for PB2k-PEO5k and contrast (2) is $3.4 \pm 0.2 \cdot 10^{10}$ cm⁻² and contrast (4) $3.5 \pm 0.5 \cdot 10^{10}$ cm⁻². Together with the SLD of pure protonated PEO of $0.5 \cdot 10^{10}$ cm⁻² this translates into a volume fraction of PEO (φ_{PEO}) of 49% for contrast (2) and 33% for contrast (4). These are high values if compared for example with the swelling degree of free PEO5k at the overlap concentration c^* which is 21%.^[35] For PB5k-PEO10k the situation is similar with a volume fraction of PEO in the

⁵ In the published version of this chapter, an equation for polymers in the melt was used for both the melt and the solution. This was corrected here, leading to a different value. In addition, the value for the melt was wrong and therefore corrected here as well.

shell of 44%. All the parameters are listed in Table 6.2. The distance l between the particles in chain-like aggregates was fixed to zero as in contrast to SAXS, the polymer shell which determines this distance is now visible and this parameter does not play a role and can even be negative if polymer shells are overlapping.

Combining the PEO content of the outer shell with the PB and PEO shell thicknesses, the composition of the polymer shell can be calculated from the SANS data (Table 6.3) The mass fraction w_{PEO} was calculated using the obtained volume fractions of PEO in the outer shell to determine the volume of PEO. The volume for PB was calculated directly from the obtained shell thickness t_{PB} . Both volumes were transferred into the corresponding masses using densities of 0.9 g/cm^3 for PB and 1.1 g/cm^3 for PEO. The resulting values for w_{PEO} match very well to the prior result of 54.4% from elemental analysis.^[21]

We further varied the molecular weight ratio of the grafted PEO chains to the free matrix PEO chains. The encapsulated SPIONs with the different diblock copolymer shells were dispersed in a PEO10k or a PEO3k matrix. The molecular weight ratio R of grafted to free chains ranged from 0.5 to 3.33. The nanocomposites were analysed by SAXS.

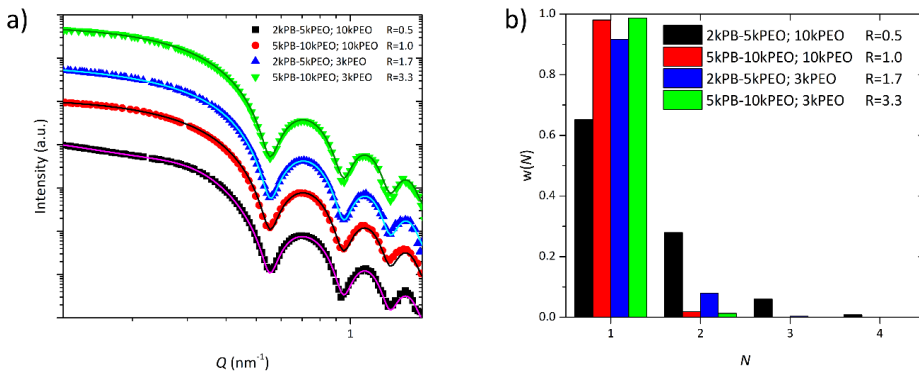


Figure 6.10 a) SAXS curves (arbitrarily shifted). b) Distribution for N for nanocomposites with different grafted to free chain length ratios.

Several groups^[15,36-38] identified R to be an important parameter for the dispersion state of the NCs in a polymer matrix. For R smaller than 1 the interpenetration of free chains into the PEO corona is conformationally unfavored, leading to an expulsion from the grafted chains and therefore to attractive interactions between the NCs. In the case of R of 1 or larger than 1 the smaller free chains act as a solvent for the grafted chains, which causes repulsive interactions between the NCs and induces an individual dispersion. We also observed this parameter to be a suitable way of adjusting the solubilization state of the SPIONs inside the nanocomposite

(Figure 6.10). The original SPION samples encapsulated with PB2k-PEO5k and PB5k-PEO10k contained mainly singly encapsulated SPIONs (see Figure 6.11).

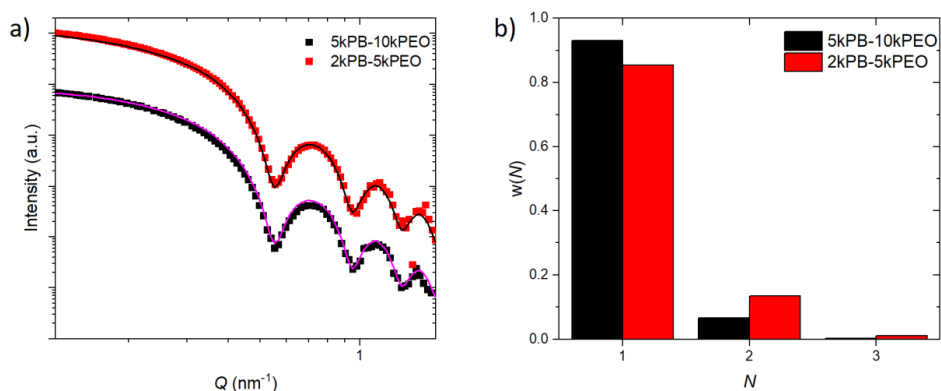


Figure 6.11 a) Experimental scattering curves (arbitrarily shifted) for 2kPB-5kPEO and 5kPB-10kPEO encapsulated SPIONs in water. b) Distribution for N .

The dispersion in PEO caused a visible agglomeration if SPIONs encapsulated with PB2k-PEO5k were mixed into a PEO10k matrix ($R = 0.5$). In contrast, no additional agglomeration appeared if PB2k-PEO5k encapsulated SPIONs were mixed with PEO3k or PB5k-PEO10k SPIONs were mixed with both PEO3k and PEO10k ($R \geq 1$). The samples with $R = 0.5$ and $R = 1.7$, that were phase transferred and crosslinked with the same PB2k-PEO5k diblock copolymer, necessarily had the same amount of singly encapsulated SPIONs and the same polymer shell stability. Therefore, multiple encapsulation and shell stability can be excluded as causes for the increase in agglomeration in the case of $R = 0.5$. Insofar, our findings are in good agreement with prior results.

6.3.4 Attachment of supramolecular group to SPIONs

Including a supramolecular group into the system allows additional interactions between the SPIONs and their surrounding matrix as well as between the encapsulated SPIONs themselves. We chose the hydrogen bonding group thymine (Thy) to be introduced to our system by attaching it to the PEO end of the diblock copolymer. Using thymine-*l*-acetic acid as a precursor for the Thy functionality, two possible pathways exist to connect it to a hydroxy end group of a polymer: 1) the transfer of the hydroxy group to an amino group *via* an azide intermediate and the succeeding coupling of thymine by an amide bond; 2) directly in an esterification reaction following the activation of the acid functionality by carbonyldiimidazole

(CDI). During the crosslinking reaction, the encapsulated SPIONs are heated to 80 °C for four hours. To check if the ester bonds withstand these conditions, a test was done with a double functionalised PEG homopolymer, Thy-PEG4.6k-Thy. The Thy functionality was attached *via* the same esterification process as for PB3k-PEO4k-Thy. After stirring for four hours at 80 °C, the polymer lost 9 % of Thy functionality. As the remaining amount of Thy groups is still sufficient for supramolecular interactions and the direct approach 1) requires less reaction steps, the second pathway is chosen. The diblock copolymer PB3k-PEO4k-Thy was successfully synthesised by this approach with 90 % Thy functionalisation. It could be used equivalently to the non-supramolecularly functionalised copolymers for the encapsulation of the SPIONs. Figure 6.12 displays a comparison between SPIONs encapsulated with the diblock copolymers PB3k-PEO4k and PB3k-PEO4k-Thy.

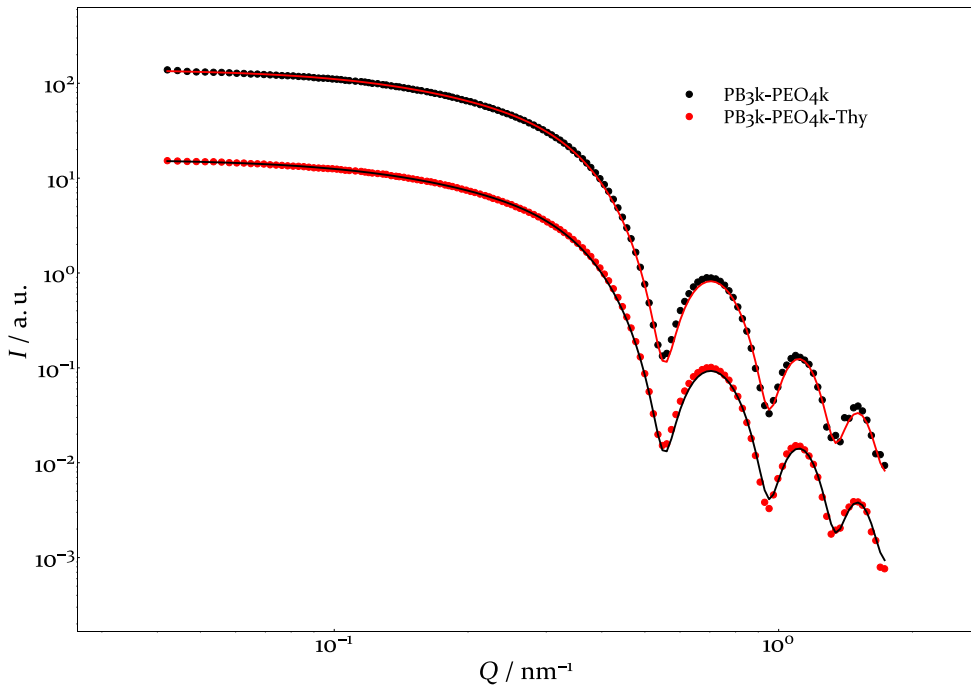


Figure 6.12 SAXS curves for PB3k-PEO4k and PB3k-PEO4k-Thy encapsulated SPIONs in PEO.

The SAXS data reveals homogeneously dispersed SPIONs in the PEO melt. The fraction of single nanoparticles obtained from the fit is about 90 % for both samples. This clearly shows that the Thy groups do not decrease the solubility of the encapsulated SPIONs in the melt.

6.3.5 Attempts to exchange of PEO in the diblock copolymer

To obtain elastomeric nanocomposites, it was desired to exchange PEO in the diblock copolymer against an elastomeric polymer. Poly(butylene oxide) PBO was chosen as a suitable replacement due to its chemical similarity to PEO. Butylene oxide (BO) can be polymerised in anionic ring opening reactions similar to EO and narrow molecular weight distributions can be obtained if the reaction temperature is low.^[39] To overcome the low reaction rates at these temperatures, crown ethers are used to complex the counter ion and increase the reactivity of the polymer anion. Additionally, the end group of the PBO block can be used to include another functionality which is desirable for future applications towards supramolecular systems. In a first approach, PB5k-OH which was also the precursor material for the PB5k-PEO10k diblock copolymer was deprotonated and polymerised with butylene oxide for four days at -10 °C in THF using the crown ether 18-crown-6 (18C6). The procedure was chosen to be as similar to the one used for the preparation of the PB-PEO diblock copolymers. Differences are the reaction temperature and the addition of the crown ether which are necessary to suppress side reactions of BO. Two reactions were done in parallel to obtain diblock copolymers of two compositions: PB5k-PBO5k and PB5k-PBO10k. The analysis of the polymer *via* SEC and NMR revealed narrow molecular weight distributions (PDI = 1.00) but the molecular weight of the PBO block was much smaller than desired, resulting in PB5k-PBO1.5k and PB5k-PBO4k. As the obtained block ratios are not favourable for our encapsulation procedure, another approach was tried using toluene as a solvent which is reported to be favourable for the polymerisation of PBO over THF.^[39] Instead of PB5k-OH, the precursor material for PB3k-PEO4k and PB3k-DETA, PB3k-OH was used. The resulting polymer was PB3k-PBO4k with a narrow molecular weight distribution (PDI = 1.00).

Several solvents were tested for micelle formation of the diblock copolymer. Ethanol, acetone, dimethylacetamide, benzyl alcohol and ethyl acetate proved to be good solvents for both blocks as no micelles could be found in DLS measurements. Isopropanol and dimethylformamide did not give clear results as structures were found but with large size distributions. For DMF, a temperature dependence was found as the polymer was insoluble below 75 °C but soluble for higher temperatures. Water and methanol were bad solvents for the whole diblock copolymer. For the encapsulation of the SPIONs, ethanol and methanol were tested but the SPIONs precipitated during the phase transfer.

6.3.6 Investigation of the ligand exchange step

The ligand exchange step was examined by varying the amount of polymeric ligand and using two different head groups. PB-DETA contains a 2,2'-diaminodiethylamine head group and PB-PA is equipped with a phosphonic acid head group, both polymers having a molecular weight of 2k. In the past experiments a high ligand amount of about 3000 PB-DETA chains per SPION was used. This value translates into 4.0 PB-DETA chains per nm^2 of iron oxide surface considering the diameter to be 15.4 nm. Starting without polymer ligand we increased the amount of PB-DETA to determine the minimum quantity for full encapsulation. The same procedure was applied for PB-PA. The SPIONs encapsulated with PB3k-PEO4k were analyzed with TEM using phosphotungstic acid as staining reagent. TEM images showed that the encapsulation without polymer ligand lead to an irregular polymer shell with SPIONs partially etched by the staining agent, phosphotungstic acid (Figure 6.13a).

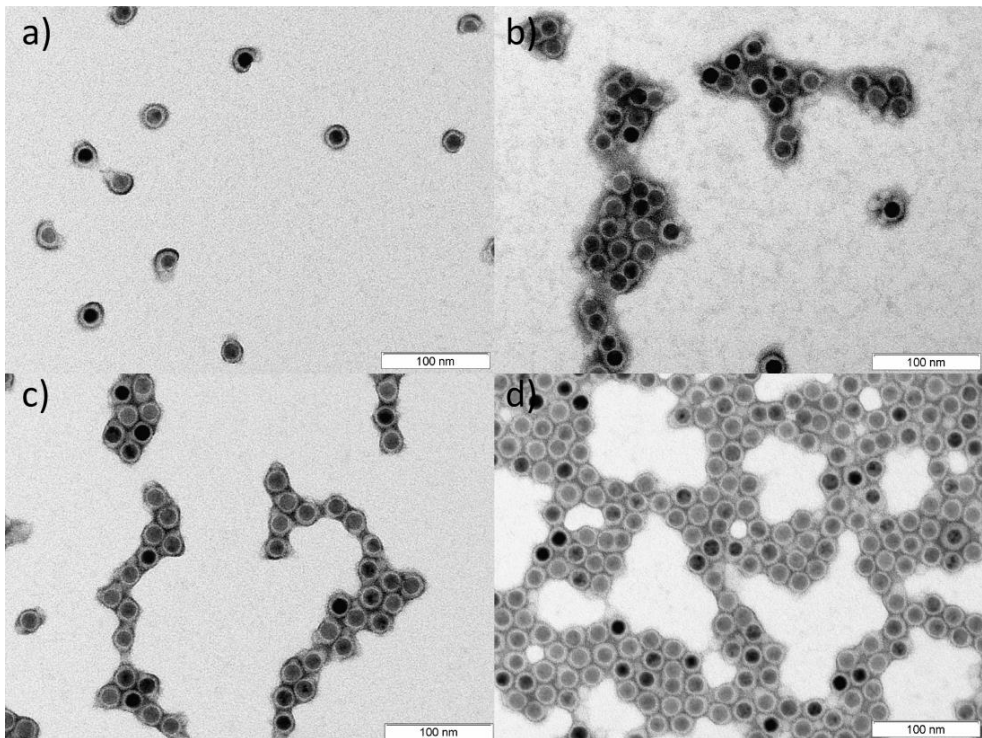


Figure 6.13 TEM images after drying of SPIONs encapsulated with PB3kPEO4k, stabilized with (a) oleic acid, (b) a 100-fold PB-DETA excess (0.1 chains per nm^2), (c) a 250-fold PB-DETA excess (0.3 chains per nm^2) and (d) a 100-fold PB-PA excess (0.1 chains per nm^2).

The same was observed if only 0.1 PB-DETA chains per nm^2 of iron oxide surface were added (Figure 6.13b). Increasing the amount of PB-DETA to 0.3 chains per nm^2 iron oxide surface resulted in completely closed polymer shells where the SPIONs are protected against the etching by phosphotungstic acid (Figure 6.13c).

For PB-PA already the addition of 0.1 chains per nm^2 iron oxide surface was sufficient to gain closed polymer shells and to protect the encapsulated SPIONs against etching. This is understandable as phosphonic acid has a higher affinity to the NC surface than DETA.^[40] In addition, PB-DETA may form an ion pair with the released oleic acid leading to a decreased amount of free PB-DETA, which increases the required ligand excess.^[41] As the maximum grafting density of polymeric ligands is about 1 chain per nm^2 .^[42,43] A complete exchange of the native oleic acid ligands is not required in order to obtain closed polymer shells. Additional TEM images of PB2k-PEO5k and PB5k-PEO10k encapsulated SPIONs are presented in Figure 6.16 where the results are similar to these of PB3k-PEO4k. The SPIONs encapsulated with different ligand quantities were dispersed in PEO and the distribution was analysed by SAXS. The scattering curves were fitted with the pearl necklace model to calculate the fraction of single SPIONs inside the nanocomposite.

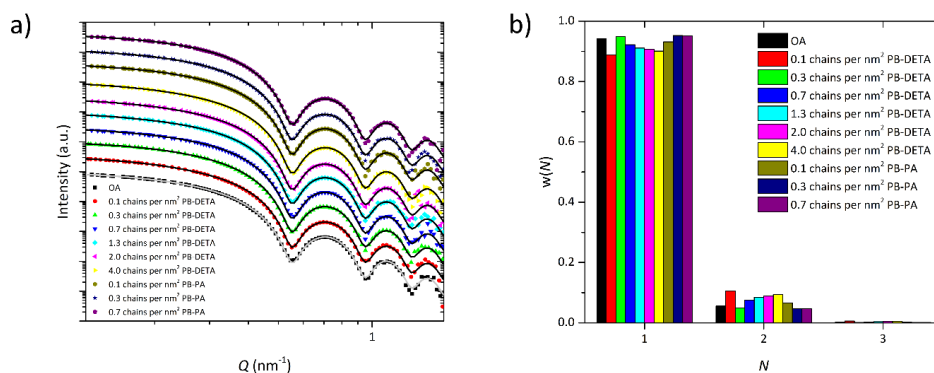


Figure 6.14 a) SAXS curves (arbitrarily shifted). b) Distribution for N for nanocomposites with PB3k-PEO4k encapsulated SPIONs, stabilized with different ligands and excess.

The scattering curves and the distribution of N for PB3k-PEO4k encapsulated SPIONs with different ligands and ligand excess are shown in Figure 6.14. The scattering curves and the ratio of single SPIONs inside the nanocomposite for PB2k-PEO5k and PB5k-PEO10k encapsulated SPIONs are presented in Figure 6.15.

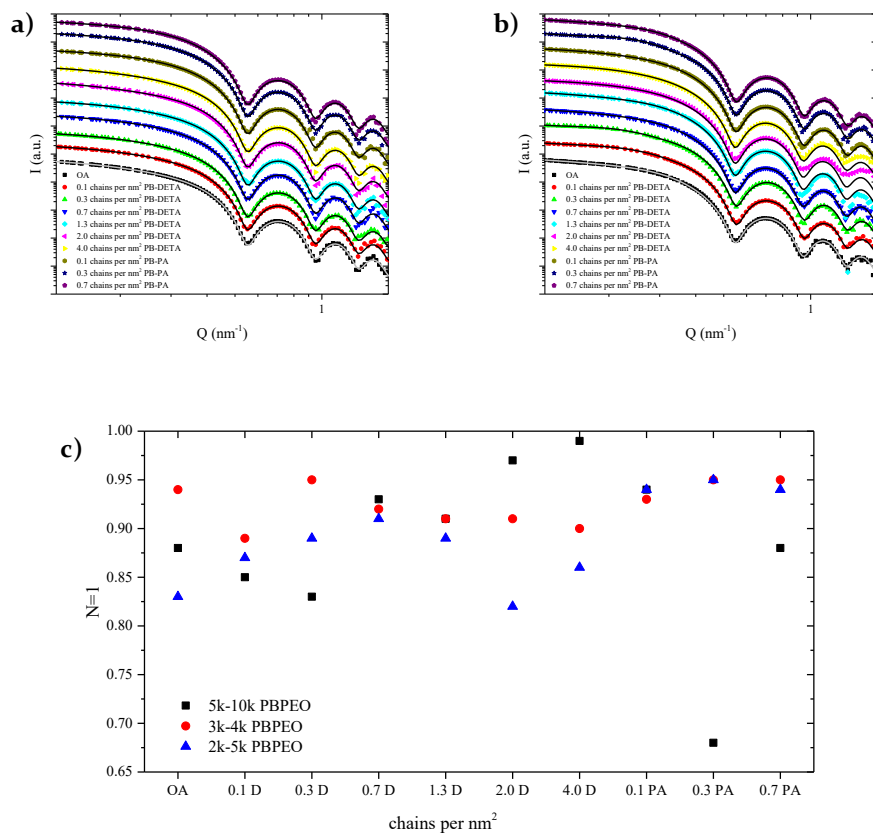


Figure 6.15 Experimental scattering curves (arbitrarily shifted) for nanocomposites with 2kPB-5kPEO (a) and 5kPB-10kPEO (b) encapsulated SPIONs, stabilized with different ligands and ligand excess. (c) Ratio of single NCs inside the nanocomposite for samples with different diblock copolymer sizes, different ligands and ligand excess.

Regardless of the ligand and the ligand amount, all samples exhibit a fraction of single SPIONs of 80% to nearly 100%.

6.4 Experimental

6.4.1 Materials

The following chemicals were used as received. Tetrahydrofuran (THF, 99.7%), *n*-hexane (96%) and ethanol (99.98%) were purchased from VWR. 1,6-Hexanedithiol (HDT, 97%) was obtained from Alfa Aesar. 2,2'-Azobis(2-methyl-propionitrile) (AIBN, 98%), 2,2-

dimethoxy-2-phenylaceto-phenone (DMPA, 99%), potassium persulfate ($K_2S_2O_8$, 99.0%), iron(II) sulfate heptahydrate ($FeSO_4 \cdot 7H_2O$, 99%), osmium tetroxide solution (OsO_4 , 4% in H_2O) and poly(ethylene oxide) ($M_n \sim 2.05$ kDa, 3.1 kDa and 10.4 kDa) were purchased from SigmaAldrich. Sodium metabisulfite ($Na_2S_2O_5$, 98.0%) was obtained from Merck. Water was purified using an ELGA PURELAB® flex 2 system (18.2 M Ω). SPIONs were synthesized according to Yu et al.^[44] and were initially stabilized with oleic acid. DLS data were collected with a Zetasizer Nano ZS system (Malvern).

6.4.2 Polymer synthesis

General procedures. All manipulations were carried out at a high vacuum line or in a glove box filled with Argon (M Braun, Unilab). The water level in the glove box was below 1 ppm and the oxygen level below 0.1 ppm. The flasks for all manipulations were equipped with Teflon stopcocks (Young® or Gebr. Rettberg GmbH), which allowed the transfer of materials between the vacuum line and glove box without contamination with air. The flasks that were exposed to overpressure were pressure-tested to 4-12 bar depending on the size of the flask.

Materials. Butadiene (Aldrich, $\geq 99.6\%$) was degassed, condensed on solvent free di-*n*-butylmagnesium, stirred at RT overnight, condensed on solvent free *n*-butyllithium, stirred at -20 °C for 20 min and directly used by condensing the monomer into the polymerization flask. Ethylene oxide (EO) (Chemogas, $\geq 99.9\%$) was condensed into a flask, degassed and stirred twice over CaH_2 for 1-2 days, before being condensed into the reaction flask. 1,2-Butylene oxide (BO) (Aldrich, 99%) was degassed and stirred twice over calcium hydride (CaH_2) for several days. Crown ether 18-crown-6 (18C6) (Sigma-Aldrich, 99%) was freeze dried with benzene prior to use under high vacuum conditions. THF (VWR, $\geq 99.5\%$) was degassed and dried with potassium and benzophenone before use. Toluene (Merck, 99.9%) was degassed, distilled into another flask which contained sodium metal, stirred over the sodium for at least 24 hours before being degassed again and heated to 110-115 °C for 3-4 hours. Dimethyl chlorophosphate (Sigma-Aldrich, 96%) was filled into a flask and degassed to remove traces of hydrogen chloride before use. Iodomethane (Sigma-Aldrich, $>99\%$) was degassed and dried by stirring over CaH_2 before use. Diethylen glycol monomethyl ether (Sigma-Aldrich, 99.5%) was degassed before use. Methanol (VWR, $\geq 99.8\%$), dichloromethane (Sigma-Aldrich, $\geq 99.9\%$), acetic acid (Sigma-Aldrich $\geq 99.8\%$), ethyl acetate (Sigma-Aldrich, $\geq 99.7\%$), 1-methyl-2-pyrrolidone (Sigma-Aldrich, 99.5%), sodium bromide (AlfaAesar, $\geq 99.5\%$), trimethylsilyl chloride (Fluka, $\geq 99.0\%$), potassium *tert*-butoxide (Sigma-Aldrich 99.9%) diethyl

vinylphosphonate (Sigma-Aldrich, 97%), potassium (Acros Organics, $\geq 98\%$) and DMF (Sigma-Aldrich, 99.8%) were used as received.

Polymerization reactions. The synthesis of polybutadiene end functionalized with an OH-group (PB-OH), the PB-PEO diblock and PB-DETA is described elsewhere.^[21] For the largest PB block with a molecular weight of about 4750 g/mol the synthesis procedure was changed slightly so that the polymerization took place at $-60\text{ }^{\circ}\text{C}$ for the whole time and the ethylene oxide was distilled into the flask at $-60\text{ }^{\circ}\text{C}$ instead of $0\text{ }^{\circ}\text{C}$ leading to an almost quantitative functionalization of the polymer end. For the largest block copolymer the synthesis procedure was also slightly changed to replace ethanol by acetone during the purification process. The block copolymer PB2k-*b*-dPEO5k was synthesized as described elsewhere^[21] by replacing hydrogenous ethylene oxide (h-EO) by deuterated ethylene oxide (d-EO, Cambridge Isotope Laboratories, deuteration degree 98%).

The synthesis of PB3k-PEO4k-Thy was done in two steps. First, 0.648 g (3.52 mmol) thymine-1-acetic acid was suspended in 5 mL DMA and 0.560 g (3.15 mmol) of CDI were added under argon. The reaction is stirred for one day at room temperature. During this time, the stopcock is left slightly open for the forming carbon dioxide. In a second step, 9.638 g (1.25 mmol) of the polymer PB3k-PEO4k were dissolved in 20 mL of THF. In a glove box, the polymer solution is added to the activated thymine-1-acetic acid and stirred at $40\text{ }^{\circ}\text{C}$ for three days. Afterwards, the solvent is removed by vacuum distillation. The polymer is dissolved in 350 mL of a 5 wt% solution of sodium bicarbonate (NaHCO_3). The polymer is extracted with 200 mL of chloroform. The extraction is repeated twice with 100 mL of chloroform. The organic phases are collected, washed with 100 mL of distilled water and the solvent is evaporated. The same purification process for the polymer as employed before^[21] was used from here.

PB3k-PBO4k was synthesised by reacting 14.47 g (5.36 mmol) of PB3k-OH with 0.555 g (4.95 mmol) potassium *tert*-butoxide in toluene under argon. A white precipitate could be observed. The solvent and formed *tert*-butanol were removed under high vacuum conditions. The alcoholate was dissolved twice in toluene and dried again to remove any remaining alcohol. In a glovebox, 0.654 g (2.48 mmol) crown ether (18C6) and 14 g of toluene were added, yielding a reddish-brown solution. The flask was degassed in an ice bath and 36.39 g (504.65 mmol) BO was distilled into the flask by locally cooling it with liquid nitrogen. The polymerisation was conducted at $-10\text{ }^{\circ}\text{C}$ for one day. During this time, the colour changed from dark red to dark green. The reaction was terminated with 5 ml of acetic acid. The polymer was precipitated in 1.4 L of methanol and washed two times with 250 mL of methanol. The product was dried under high vacuum conditions, yielding 33.843 g of the dry polymer.

Two methods were tried to obtain 1,2-polybutadiene end functionalized with a phosphonic acid group (PB2k-PA and PB5k-PA).^[45]

1) 1,2-Polybutadiene was obtained by polymerizing 8.45 g of butadiene with 4.2 mmol of *sec*-butyllithium in 50 ml of THF at -60 °C for 2 h. Afterwards, 3.03 g of dimethyl chlorophosphate was added under Argon and the reaction mixture was allowed to warm up to room temperature over-night leading to the precipitation of a white solid which dissolved upon the addition of 2 ml of methanol. After stirring for 5 min, the solvent was partially removed by vacuum distillation. The polymer was precipitated in methanol, washed with methanol and dried under vacuum conditions. NMR analysis revealed incomplete functionalization of the polymer. To separate the polymer fraction with phosphonate end group, the product was purified *via* column chromatography using first dichloromethane to elute the non-functionalized polymer (70%) and afterwards a 1 : 1 mixture of ethyl acetate and methanol for the functionalized polymer (26%). The latter was washed three times with methanol and dried in vacuum. To cleave the ester groups, the functionalized polymer was dissolved in 20 ml of 1-methyl-2-pyrrolidone. Upon addition of 0.295 g of sodium bromide and 400 μ l of trimethylsilyl chloride, the solution was stirred for 17 h at 50 °C. After removal of the solvent by vacuum distillation, the polymer was washed two times with methanol and dried under high vacuum conditions. The purity of the functionalized product was checked *via* thin-layer chromatography (TLC).

2) 1.038 g (0.2 mmol) of 1,2-polybutadiene end functionalized with an OH-group ($M = 5000$ g/mol) was added to a Schlenk flask and degassed under high vacuum conditions. In a glovebox, 0.0248 g potassium *tert*-butoxide (0.2 mmol) was dissolved in dry THF and added to the flask. After stirring for 3 h, solvent and formed *tert*-butanol were removed under high vacuum conditions. 30 ml of THF, 10 ml of DMF and 0.3625 g (2.2 mmol) of diethyl vinylphosphonate were added to the flask in a glovebox. The reaction was terminated after 27 h by removal of the solvent under high vacuum conditions. The ester hydrolysis and purification steps were the same as described in 1). The full functionalization of the polymer was confirmed by the absence of the signal for the CH₂-OH protons in the ¹H NMR spectrum of the product in deuterated pyridine.

The PEO homopolymers PEO3k and dPEO3k were synthesized from h-EO and d-EO using the techniques described elsewhere.^[21] The potassium salt of diethylene glycol monomethyl ether (KDGME) was used as initiator and dry toluene as solvent. The mass fraction of EO in the toluene/EO mixture was about 10% and the reaction temperature was increased from 35 °C to 55 °C over two days and kept at 55 °C for another 3 days. The polymerization

reactions were terminated with a tenfold excess of dry hydrogenous iodomethane. After four hours the excess of iodomethane and the solvent were removed by vacuum distillation. The raw products were dissolved in chloroform, washed with water and after removal of most of the solvent precipitated in heptane. The products were finally dried under vacuum conditions. KDGME was synthesized by reacting potassium metal with a small excess of diethylene glycol monomethyl ether in a triple amount of dry toluene. After the disappearance of the potassium, the solvent was distilled off and the excess of the alcohol was removed under high vacuum conditions at 80 °C. dPEO10k was synthesized using triethylene glycol as initiator, metallated to 15% with potassium. Dry THF was the solvent. The polymerization was carried out in a metal reactor at 100 °C overnight. The reaction was terminated with acetic acid. The purification steps are the same as for the PEO3k.

6.4.3 Polymer characterisation

The molecular weight distributions M_w/M_n of samples 1,2-PB-OH and 1,2-PB-*b*-PEO were determined by size exclusion chromatography (SEC) using a SEC instrument consisting of Agilent 1260 Infinity pump (G1310B) and autosampler (G1329B), three Agilent PlusPore GPC columns with a continuous pore size distribution, a Shimadzu CTO-20AC column oven and a differential refractive index (Wyatt Optilab T-rEX) as well as a light scattering detector (Wyatt DAWN Heleos-2). The eluent was a mixture of THF and DMA (85 : 15 by volume) at a flow rate of 1 mL/min at 50 °C. The data were evaluated using ASTRA6.1 software, determining the refractive index increment from the polymer peak and calculating the absolute molecular weights from the light scattering signal. The molecular weight characterization of the PB-DETA and PB-PA samples were carried out with the polymers prior to the functionalization reaction due to the absorption of the functionalized polymers on the SEC columns. The microstructure of the PB block as well as the functionalization of the polymer ligands were defined *via* $^1\text{H-NMR}$ as described elsewhere.^[21] The functionalisation degree of PB3k-PEO4k-Thy was determined *via* $^1\text{H-NMR}$ by the remaining signals from the $\text{CH}_2\text{-OH}$ protons, revealing 90 % functionalisation.

Table 6.1 Molecular weight characterization of the polymers used for the SPION encapsulation processes.

polymer	M_n [g/mol]	M_w/M_n
PB2k-dPEO5k	6580	1.02
PB2k-PEO5k	6790	1.02
PB3k-PEO4k	7710	1.00
PB3k-PEO4k-Thy	7850	1.03
PB5k-PEO10k	14830	1.01
PB3k-PBO4k	6740	1.00
PB2k-DETA	1920	1.02
PB3k-DETA	2930	1.01
PB2k-PA	2180	1.03
PB5k-PA	4750	1.00
PEO3k*	3020	1.04
dPEO3k*	2940	1.03
dPEO10k*	10500	1.03
PEO3k (Sigma-Aldrich)	3370	1.03
PEO10k (Sigma-Aldrich)	10420	1.06

* These data were evaluated using a standard calibration for PEO

6.4.4 Encapsulation of SPIONs and nanocomposite synthesis

To exchange the oleic acid ligands, SPIONs were incubated with different quantities of PB-DETA or PB-PA in *n*-hexane for more than 20 h. Before encapsulation, the SPIONs were precipitated with ethanol and centrifuged. The polymer-coated SPIONs were dispersed in THF and mixed with a 3000-fold excess of PB-*b*-PEO in THF to yield a 0.8 μ M solution.

For HDT/AIBN crosslinking HDT (ratio HDT to butadiene units present in the diblock copolymer of 1 : 12) and AIBN (ratio AIBN to butadiene units present in the diblock copolymer of 1 : 4) was added to the SPION-polymer mixture. The mixture was transferred into the 10-fold volume of water with a programmable flow system^[20] and heated up to 80 °C for 4 h. Finally, the SPIONs were purified using a magnetic column.

For HDT/UV and HDT/UV/DMPA crosslinking the SPION-polymer solution was mixed with HDT (ratio HDT to butadiene units present in the diblock copolymer of 1 : 4) and DMPA (ratio DMPA to HDT of 1 : 7), transferred into the 10-fold volume of water and irradiated with UV light (four PL-S 9W/2P BLB UV lamps from Philips with 9 W power each and 366 nm wavelength) for 4 h. Then, the encapsulated SPIONs were purified using a magnetic column.

For crosslinking with the redox reaction, the SPION-polymer mixture was transferred into the 10-fold volume of water. $K_2S_2O_8$ (ratio $K_2S_2O_8$ to butadiene units present in the diblock copolymer of 1 : 2.5) was added and the mixture was stirred at room temperature. After 3 h $Na_2S_2O_5$ (ratio $Na_2S_2O_5$ to $K_2S_2O_8$ of 1 : 1.4) and $FeSO_4 \cdot 7H_2O$ (ratio $FeSO_4 \cdot 7H_2O$ to $K_2S_2O_8$ of 1 : 49) were added successively. After 45 min the encapsulated SPIONs were purified using a magnetic column. To get the nanocomposites, the encapsulated SPIONs, dispersed in water, were mixed with an aqueous PEO solution, lyophilized and melted at 65 °C.

6.4.5 Transmission electron microscopy (TEM)

TEM experiments were performed using a Jeol JEM-1011 microscope (100 keV) at the University of Hamburg. For TEM images, the aqueous SPIONs solution was partially dried on a carbon-coated copper grid and excess solution was removed. An aqueous phosphotungstic acid solution (10%) was added and removed after 30 s. Afterwards, the sample on the grid was washed with water two times. For osmium tetroxide staining, encapsulated SPIONs deposited on a carboncoated copper grid were stained with osmium tetroxide vapor for 1 h using an osmium tetroxide solution (4% in H_2O).

6.4.6 Small angle X-ray scattering (SAXS)

SAXS experiments were performed in the Q-range from 0.12 to 1.7 nm^{-1} at the Gallium Anode Low-Angle X-ray Instrument (GALAXI)^[46] at Forschungszentrum Jülich. The incident wavelength is 1.34 Å and the detector distance was set to 3.5 m. All samples were sealed in glass capillaries of 2 mm inner diameter. Nanocomposite samples were measured above the PEO glass transition temperature. The concentrations of the SPIONs in each sample were 0.1 vol% to avoid interparticle interaction and to get a sufficient scattering signal. The data were background corrected and calibrated to absolute intensities. Data analysis has been done using the Python based project jscatter.^[47]

6.4.7 Small angle neutron scattering (SANS)

SANS experiments were performed at the instrument KWS-1^[48,49] at the MLZ in Garching, Germany. The incident neutron wavelength λ was 7 Å ($\Delta\lambda/\lambda = 10\%$). The data were obtained from three different detector and collimation distances: the detector distances of 1.5 m

and 8 m with a collimation distance of 8 m and the detector distance of 20 m with 20 m collimation distance leading to a total Q range of 0.017 to 1.5 nm⁻¹. The samples were measured in quartz cells with beam path of 2 mm. For the samples in deuterated water, the measurements were done at room temperature, for the nanocomposite samples, the measurements were done at 70 °C, e.g. above the melting temperature of PEO. The size of the sample aperture was set as 6 × 6 mm. The data presented here were converted to an absolute intensity unit of cm⁻¹ taking into account the sample thickness, transmission, the scattering from a standard sample and the background from electronic noise, the solvent and the quartz cell. Data reduction has been done using the QtiKWS software,^[50] data analysis has been done using the Python based project jscatter^[47] including resolution smearing dependent on the measurement geometry.^[51]

6.5 Conclusions

Superparamagnetic iron oxide nanocrystals (SPIONs) were successfully encapsulated with a highly stable diblock copolymer shell. The inner part of the shell was crosslinked using a thermally or photochemically initiated thiol–ene click reaction or a persulfate based redox process at room temperature. The major advantage of the latter crosslinking reaction is the avoidance of heat or UV light for the initiation, making it suitable for heat or UV sensitive systems and facilitating a future upscaling of the process. The presented procedure is adaptable to various types of nanocrystals, whereas the encapsulation of SPIONs serves as a model system due to their well-known synthesis of high quality nanocrystals.

We could show by TEM, SAXS and SANS that the size of the polymer shell is not considerably influenced by the polymer molecular weight and composition. Thymine as a hydrogen bonding group was successfully attached to the diblock copolymer and used for the encapsulation of the SPIONs. The resulting nanocomposite was of as high quality as the ones without supramolecular functionality. Replacing the PEO block by PBO led to a diblock copolymer with a narrow molecular weight distribution but it could not be used to encapsulate SPIONs.

By minimizing the ligand excess during the encapsulation, the process was further improved with regard to a future upscaling whereby PB-PA allows an even smaller ligand excess than PB-DETA. The exchange of oleic acid by the polymeric ligand is necessary to obtain a closed polymer shell around the SPIONs. This is of great importance for example in the case of biomedical applications. However, a high fraction of single SPIONs in the PEO matrix can also be achieved if the ligand exchange is omitted.

The SANS examination performed with different contrasts indicates that (i) the inner shell contains only PB and has a size comparable to prior results and (ii) the PEO shell is rather dense.

6.6 Acknowledgements

This work was supported by SPP 1681 (projects KR 3929/2-1 and KR 3929/2-2) of the German Research Foundation (DFG). The authors acknowledge Artur Feld for support with iron oxide nanocrystals.

6 Creating a synthetic platform for the encapsulation of nanocrystals with covalently bound polymer shells

6.7 Supporting Information

Table 6.2 Fit parameters for SANS data. Highlighted in grey are the fixed values for the fits, R_c was taken from the SAXS results, ρ_{PB} and ρ_m are calculated values.

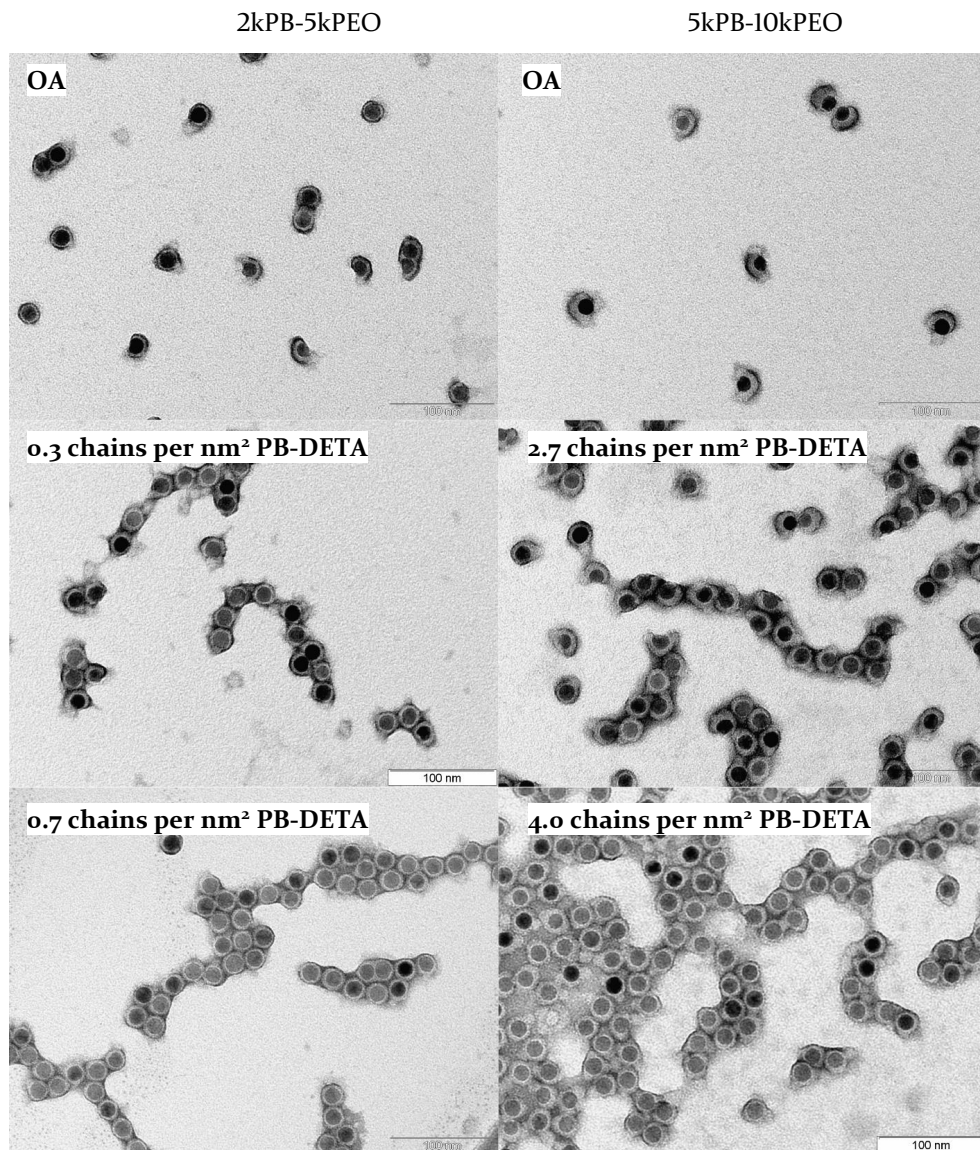
contrast	diblock	matrix	ρ_m [10^{10} cm^{-2}]	R_c [nm]	ρ_c [10^{10} cm^{-2}]	ρ_{PB} [10^{10} cm^{-2}]	t_{PB} [nm]
(1)	PB2k-PEO5k	dPEO3k	6.0	8.2	6.7 ± 0.1	0.4	4.3 ± 0.1
(2)	PB2k-PEO5k	dPEO3k	6.0	8.2	6.7	0.4	4.3
	PB5k-PEO10k	dPEO10k	6.0	8.2	6.7	0.4	4.3
(3)	PB2k-PEO5k	D ₂ O	6.3	8.2	6.7	0.4	4.3
(4)	PB2k-PEO5k	D ₂ O	6.3	8.2	6.7	0.4	4.3

contrast	diblock	matrix	outer shell	t_{PEO} [nm]	ρ_{PEO} [10^{10} cm^{-2}]	$\langle N \rangle$	l [nm]
(1)	PB2k-PEO5k	dPEO3k	dPEO	$1.1 \cdot 10^{-6} \pm 0.4$	6.0	1.3 ± 0.0	0
(2)	PB2k-PEO5k	dPEO3k	hPEO	4.5 ± 0.1	3.3 ± 0.2	1.3	0
	PB5k-PEO10k	dPEO10k		4.9 ± 0.1	3.6 ± 0.1	1.2 ± 0.0	0
(3)	PB2k-PEO5k	D ₂ O	dPEO	6.0 ± 1.9	6.3 ± 0.1	1.3	0
(4)	PB2k-PEO5k	D ₂ O	hPEO	5.3 ± 0.3	3.5 ± 0.5	1.3	0

Table 6.3 Calculated values of the volume fraction of PEO in the polymer shell from SANS analysis.

contrast	diblock	t_{PEO} [nm]	V_{total} [nm ³]	$V_{\text{PEO shell}}$ [nm ³]	ρ_{PEO} [10 ¹⁰ cm ⁻²]	ϕ_{PEO}	V_{PEO} [nm ³]	m_{PEO} [10 ⁻²¹ g]	m_{polymer} [10 ⁻²¹ g]	w_{PEO}
(2)	PB2k-PEO5k	4.5	20579.5	12398.3	3.4	0.49	5904.0	6744.1	12028.6	0.56
	PB5k-PEO10k	4.9	22449.3	14268.1	3.5	0.44	6533.0	6713.8	11998.3	0.56
(4)	PB2k-PEO5k	5.3	18816.6	10635.3	3.5	0.33	5685.6	5603.3	10887.8	0.51

TEM of samples with different ligands and ligand excess



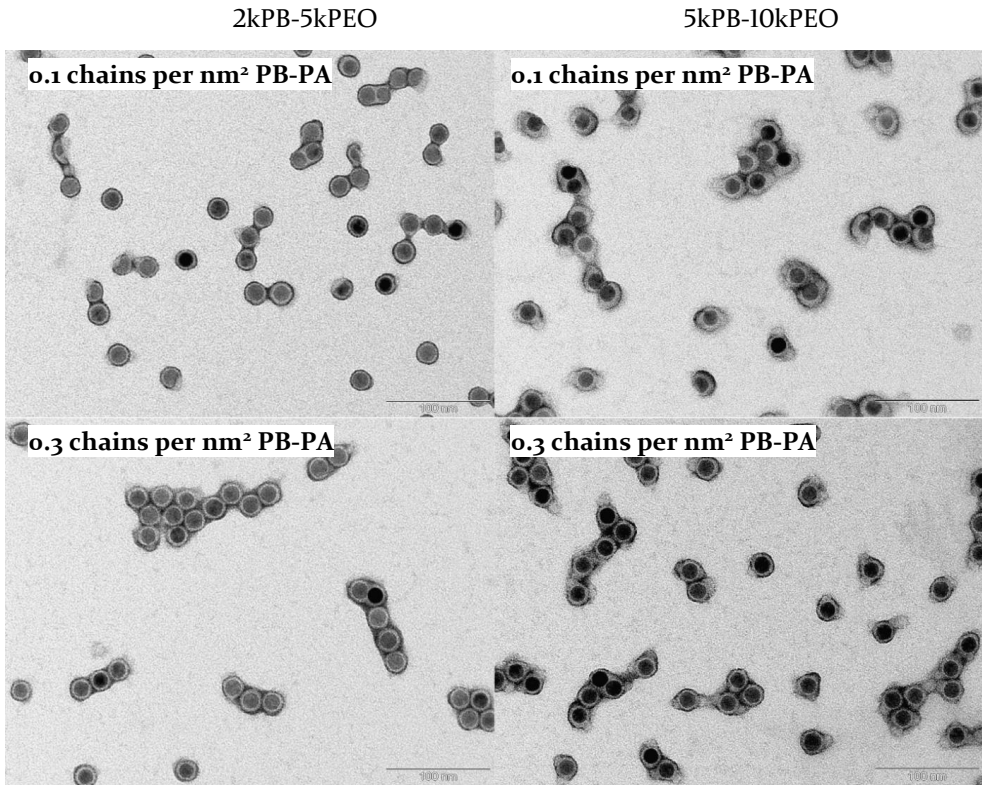


Figure 6.16 TEM images of SPIONs, encapsulated with a 2kPB-5kPEO and 5kPB-10kPEO diblock copolymer, stabilized with different ligands and ligand excess

6.8 References

- [1] A.-S. Robbes, F. Cousin, F. Meneau, F. Dalmas, F. Boué, J. Jestin, *Macromolecules* **2011**, *44*, 8858.
- [2] S. K. Kumar, N. Jouault, B. Benicewicz, T. Neely, *Macromolecules* **2013**, *46*, 3199.
- [3] D. Maillard, S. K. Kumar, B. Fragneaud, J. W. Kysar, A. Rungta, B. C. Benicewicz, H. Deng, L. C. Brinson, J. F. Douglas, *Nano Lett.* **2012**, *12*, 3909.
- [4] C. Yang, H. Wei, L. Guan, J. Guo, Y. Wang, X. Yan, X. Zhang, S. Wei, Z. Guo, *J. Mater. Chem. A* **2015**, *3*, 14929.
- [5] F. Jin, M.-L. Zheng, M.-L. Zhang, Z.-S. Zhao, X.-M. Duan, *RSC Adv.* **2014**, *4*, 33206.
- [6] C. Woelfle, R. O. Claus, *Nanotechnology* **2007**, *18*, 025402.
- [7] A. K. Gupta, M. Gupta, *Biomaterials* **2005**, *26*, 3995.
- [8] S. Kalia, S. Kango, A. Kumar, Y. Haldorai, B. Kumari, R. Kumar, *Colloid Polym. Sci.* **2014**, *292*, 2025.
- [9] L. Dykman, N. Khlebtsov, *Chem. Soc. Rev.* **2012**, *41*, 2256.
- [10] K. Ferji, I. Hamouda, C. Chassenieux, B. Nadal, B. Dubertret, C. Gaillard, E. Nicol, *J. Colloid Interface Sci.* **2016**, *476*, 222.
- [11] M. S. Nikolic, M. Krack, V. Aleksandrovic, A. Kornowski, S. Förster, H. Weller, *Angew. Chemie* **2006**, *118*, 6727.
- [12] Z. Chen, Z. Liu, Z. Li, E. Ju, N. Gao, L. Zhou, J. Ren, X. Qu, *Biomaterials* **2015**, *39*, 15.
- [13] Z. Chen, Z. Li, Y. Lin, M. Yin, J. Ren, X. Qu, *Chem. - A Eur. J.* **2013**, *19*, 1778.
- [14] E. Pöselt, C. Schmidtke, S. Fischer, K. Peldschus, J. Salamon, H. Kloust, H. Tran, A. Pietsch, M. Heine, G. Adam, U. Schumacher, C. Wagener, S. Förster, H. Weller, *ACS Nano* **2012**, *6*, 3346.
- [15] C. Chevigny, F. Dalmas, E. Di Cola, D. Gigmes, D. Bertin, F. Boué, J. Jestin, *Macromolecules* **2011**, *44*, 122.
- [16] M. S. Nikolic, M. Krack, V. Aleksandrovic, A. Kornowski, S. Förster, H. Weller, *Angew. Chemie Int. Ed.* **2006**, *45*, 6577.

- [17] C. Schmidtke, E. Pösel, J. Ostermann, A. Pietsch, H. Kloust, H. Tran, T. Schotten, N. G. Bastús, R. Eggers, H. Weller, *Nanoscale* **2013**, *5*, 7433.
- [18] J. Dimitrijevic, L. Krapf, C. Wolter, C. Schmidtke, J.-P. Merkl, T. Jochum, A. Kornowski, A. Schüth, A. Gebert, G. Hüttmann, T. Vossmeier, H. Weller, *Nanoscale* **2014**, *6*, 10413.
- [19] J.-P. Merkl, C. Wolter, S. Flessau, C. Schmidtke, J. Ostermann, A. Feld, A. Mews, H. Weller, *Nanoscale* **2016**, *8*, 7402.
- [20] C. Schmidtke, R. Eggers, R. Zierold, A. Feld, H. Kloust, C. Wolter, J. Ostermann, J.-P. Merkl, T. Schotten, K. Nielsch, H. Weller, *Langmuir* **2014**, *30*, 11190.
- [21] A. Feld, R. Koll, L. S. Fruhner, M. Krutyeva, W. Pyckhout-Hintzen, C. Weiß, H. Heller, A. Weimer, C. Schmidtke, M.-S. Appavou, E. Kentzinger, J. Allgaier, H. Weller, *ACS Nano* **2017**, *11*, 3767.
- [22] L. H. Peebles, *J. Appl. Polym. Sci.* **1973**, *17*, 113.
- [23] A. S. Sarac, *Prog. Polym. Sci.* **1999**, *24*, 1149.
- [24] G. S. Hammond, J. N. Sen, C. E. Boozer, *J. Am. Chem. Soc.* **1955**, *77*, 3244.
- [25] J. L. Faria, S. Steenken, *J. Chem. Soc. Perkin Trans. 2* **1997**, *0*, 1153.
- [26] C. E. Hoyle, T. Y. Lee, T. Roper, *J. Polym. Sci. Part A Polym. Chem.* **2004**, *42*, 5301.
- [27] K. Masaki, S. Ohkawara, T. Hirano, M. Seno, T. Sato, *J. Polym. Sci. Part A Polym. Chem.* **2004**, *42*, 4437.
- [28] K. Hummel, G. Kaiser, *Kolloid-Zeitschrift und Zeitschrift für Polym.* **1964**, *197*, 90.
- [29] A. B. Lowe, *Polym. Chem.* **2010**, *1*, 17.
- [30] Y. Won, K. Paso, H. T. Davis, F. S. Bates, *J. Phys. Chem. B* **2001**, *105*, 8302.
- [31] R. Schweins, K. Huber, *Macromol. Symp.* **2004**, *211*, 25.
- [32] S. Kawaguchi, G. Imai, J. Suzuki, A. Miyahara, T. Kitano, K. Ito, *Polymer (Guildf)*. **1997**, *38*, 2885.
- [33] L. J. Fetters, D. J. Lohse, S. T. Milner, W. W. Graessley, *Macromolecules* **1999**, *32*, 6847.
- [34] N. Stribeck, B. Smarsly, *Scattering Methods and the Properties of Polymer Materials*, Springer, **2005**.
- [35] M. Rubinstein, R. H. Colby, *Polymer Physics*, Oxford University Press, **2003**.

- [36] A.-S. Robbes, F. Cousin, F. Meneau, F. Dalmas, R. Schweins, D. Gigmes, J. Jestin, *Macromolecules* **2012**, *45*, 9220.
- [37] D. F. Sunday, D. L. Green, *Macromolecules* **2015**, *48*, 8651.
- [38] S. Srivastava, P. Agarwal, L. a. Archer, *Langmuir* **2012**, *28*, 6276.
- [39] J. Allgaier, S. Willbold, T. Chang, *Macromolecules* **2007**, *40*, 518.
- [40] K. Davis, B. Qi, M. Witmer, C. L. Kitchens, B. A. Powell, O. T. Mefford, *Langmuir* **2014**, *30*, 10918.
- [41] J. De Roo, Y. Justo, K. De Keukeleere, F. Van den Broeck, J. C. Martins, I. Van Driessche, Z. Hens, *Angew. Chemie Int. Ed.* **2015**, *54*, 6488.
- [42] S. Ehlert, S. M. Taheri, D. Pirner, M. Drechsler, H.-W. Schmidt, S. Förster, *ACS Nano* **2014**, *8*, 6114.
- [43] K. Gharbi, F. Salles, P. Mathieu, C. Amiens, V. Collière, Y. Coppel, K. Philippot, L. Fontaine, V. Montebault, L. S. Smiri, D. Ciuculescu-Pradines, *New J. Chem.* **2017**, *41*, 11898.
- [44] W. W. Yu, J. C. Falkner, C. T. Yavuz, V. L. Colvin, *Chem. Commun.* **2004**, 2306.
- [45] J. Köhler, H. Keul, M. Möller, *Chem. Commun.* **2011**, *47*, 8148.
- [46] E. Kentzinger, M. Krutyeva, U. Rücker, *J. large-scale Res. Facil. JLSRF* **2016**, *2*, A61.
- [47] R. Biehl, "Jscatter, a Program for Evaluation and Analysis of Experimental Data," DOI 10.5281/ZENODO.1470307 can be found under <https://zenodo.org/record/1470307>, **2018**.
- [48] Heinz Maier-Leibnitz Zentrum, *J. large-scale Res. Facil. JLSRF* **2015**, *1*, 1.
- [49] A. V. Feoktystov, H. Frielinghaus, Z. Di, S. Jaksch, V. Pipich, M.-S. Appavou, E. Babcock, R. Hanslik, R. Engels, G. Kemmerling, H. Kleines, A. Ioffe, D. Richter, T. Brückel, *J. Appl. Crystallogr.* **2015**, *48*, 61.
- [50] V. Pipich, "QtiKWS," **2007**.
- [51] J. S. Pedersen, D. Posselt, K. Mortensen, *J. Appl. Crystallogr.* **1990**, *23*, 321.

7 Resonant Energy Transfer can Trigger Multiexciton Recombination in Dense Quantum Dot Ensembles

The following chapter was published in *Small*, Vol. 15, No. 5, pages 1803798, 2018 in cooperation with Mona Rafipoor^{12,13}, Rieke Koll², Jan-Philip Merkl², Horst Weller^{1,2}, and Holger Lange^{1,2}. Reproduced from *Small*, Vol. 15, No. 5, pages 1803798, 2018 with permission from John Wiley and Sons.

I synthesised the polybutadiene ligand and diblock copolymer and characterised them *via* NMR and SEC. I performed the SAXS investigations of the samples and participated in writing the corresponding parts in the manuscript. Mona Rafipoor was responsible for the photoluminescence decay and TA measurements and their analysis. Mona Rafipoor, Rieke Koll and Holger Lange wrote the framework of the paper. Jan-Philip Merkl contributed to this work in many discussions with Mona Rafipoor, Rieke Koll, Holger Lange and in writing the paper. Rieke Koll developed the material preparation. She synthesised the QDQR ensembles and characterised them *via* TEM, DLS, UV/VIS and photoluminescence spectroscopy. Holger Lange formulated the original task. Rieke Koll, Mona Rafipoor and Holger Lange chose the analytical methods. Horst Weller and Holger Lange supervised the investigations. All authors participated during all stages of the process.

¹² The Hamburg Centre for Ultrafast Imaging, 20146 Hamburg, Germany.

¹³ Institut für Physikalische Chemie, Universität Hamburg, 20146 Hamburg, Germany.

7.1 Abstract

Core/shell quantum dots/quantum rods are nanocrystals with typical application scenarios as ensembles. Resonance energy transfer is a possible process between adjacent nanocrystals. Highly excited nanocrystals can also relax energy by multiexciton recombination, competing against the energy transfer. The two processes have different dependencies and can be convolved, resulting in collective properties different from the superposition of the individual nanocrystals. A platform to study the interplay of energy transfer and multiexciton recombination is presented. CdSe/CdS quantum dot/quantum rods encapsulated in amphiphilic micelles with an interparticle distance control by spacer ligands are used for time-resolved photoluminescence and transient absorption experiments. At exciton populations around one, the ensemble starts to be in a state where energy transfer can trigger multiexciton Auger recombination, altering the collective dynamics.

7.2 Introduction

Colloidal semiconductor nanocrystals (NCs) [quantum dots (QDs)], attract widespread attention due to their potential use as a tunable optoelectronic material.^[1] They are efficient light emitters and absorbers and well-suited for applications such as lasing, photodetection, and solar energy conversion.^[2–8] Among the available structures, core/shell QDs, where the shell passivates the core surface atoms, are highly developed.^[9,10] The resulting reduced overlap with trap states at the surface improves the optical properties of the QDs.^[9,11] In a typical application scenario, NCs are concentrated in a dense, macroscopic ensemble, for example, within the light emitting region of a light-emitting diode (LED).^[1,4,5,12] Possible interaction between the NCs can result in properties that are different from the ones of the sum of the constituting NCs.^[13,14] This can be disadvantageous, for example, in case the interaction results in an increase of nonradiative recombination within a LED, but also advantageous, for example in case a quick extraction of energy can be realized in photovoltaic devices.

In a nonconductive environment, NCs mainly interact *via* Förster resonance energy transfer (FRET) and Dexter electron transfer, i.e., electron tunneling.^[15–17] The latter requires wavefunction overlap and is effective on sub-nanometer scales.^[18] Because of the shell dimensions and the space occupied by the passivating ligands, Dexter transfer can usually be neglected in core–shell NC ensembles. As size variations inherent in the synthesis of NCs result in a distribution of bandgaps, energy transfer is the main interaction channel between the

NCs.^[19,20] The excitation is transferred charge-neutral by dipole–dipole interaction from excited large-bandgap, “blue” NCs to “red” NCs with smaller bandgaps. Within the excited NCs, energy is relaxed by radiative and defect-related nonradiative recombination.^[21] When the NCs are highly excited, multiexciton Auger recombination is a very effective additional nonradiative recombination possibility.^[22,23] In an evenly excited ensemble of NCs with statistically distributed bandgaps, energy transfer can result in a net gradient of carrier population.^[19] This can induce inter-NC Auger recombination, effectively resulting in an interplay between excitation levels and distance dependencies.^[24,25] To be able to investigate and deconvolve the processes, a platform that allows for an interparticle distance control and that can sustain high excitation powers is required. There, measuring NCs in solution is favourable because problems with sample degradation can be avoided: The NCs can dissipate excitation-induced heat effectively and the motion within the liquid ensures that mostly fresh NCs are excited in serial experiments. NCs can be self-assembled by hydrophobic interactions and stabilized in solution within micelles. Liz-Marzán and co-workers demonstrated the possibility for a distance control by employing stabilizing polymers of different masses.^[26] Motivated by interaction signatures observed in core/shell quantum dots/quantum rods (QDs/QRs) stabilized in micelles,^[27] we expanded our encapsulation technique accordingly. The interparticle distance within the micelles can be controlled by functionalizing the NCs with polymer ligands of defined mass. Block co-polymers then allow to stabilize clusters of the hydrophobic NCs in micelles.^[28,29] The clustered NCs are long-term stable and can then be investigated by ensemble measurements in solution. With time-resolved photoluminescence spectroscopy and pump–probe experiments, we observed interesting ensemble dynamics: At low excitation power (average exciton populations below one), the collective dynamics is only influenced by energy transfer. At high excitation levels (average exciton populations above two), multiexciton Auger recombination dominates the dynamics. In between, at exciton populations around one, energy transfer can trigger a multiexciton recombination and the ensemble features a collective dynamic, governed by its largest bandgap constituent.

Because of the maturity and the developed state in applications,^[30] CdSe/CdS QDs/QRs served as exemplary NCs. To arrange the QDs/QRs into ensembles with different average interparticle distances, a micellar encapsulation approach was adapted. Scheme 7.1 visualizes the general protocol. The QDs/QRs are synthesized with octadecylphosphonic acid (ODPA) and hexylphosphonic acid (HPA) as passivating ligands. ODPA and HPA are then exchanged with larger hydrophobic polymer ligands of different molar mass.

The polymer ligands act as a seed for the following micelle formation and allow the adjustment of the distance between the QDs/QRs inside the micelles. Three different weighted polymer ligands were used, a 2,2'-diaminodiethylamine functionalized polyisoprene (PI-DETA) ($M_n \approx 1.1$ kDa) and two phosphonic acid functionalized polybutadiene (PB-PA) ($M_n \approx 2.2$ and 4.8 kDa). Amphiphilic diblock copolymers polyisoprene-*block*-poly(ethylene oxide) (PI-*b*-PEO) and polybutadiene-*block*-poly(ethylene oxide) (PB-*b*-PEO) were added to the polymer-stabilized QDs/QRs and the mixture was transferred into aqueous solution. This led to a micelle formation, where the hydrophobic QDs/QRs are stabilized in the hydrophobic micelle interior.

In the last step, the copolymer was crosslinked by radical initiated polymerization to stabilize the construct. In principle, the micelle size, the amount of NCs per micelle and the minimum interparticle distance can be controlled by the copolymer molar mass, the relative concentrations of copolymers and NCs, and by the molar mass of the substituting polymer ligands. We performed broad parameter studies and found the amount of NCs per micelle to be a negligible parameter in comparison to the interparticle distance, as exemplarily evidenced with the sample "cluster 1". For the detailed investigations, we employed individual NCs in micelles (single), one reference sample of large micelles with long average interparticle distance (cluster 1) and three sets of micelles with the same sizes and decreasing interparticle distances (clusters 2-4). TEM images of all those samples can be found in Figure 7.1.

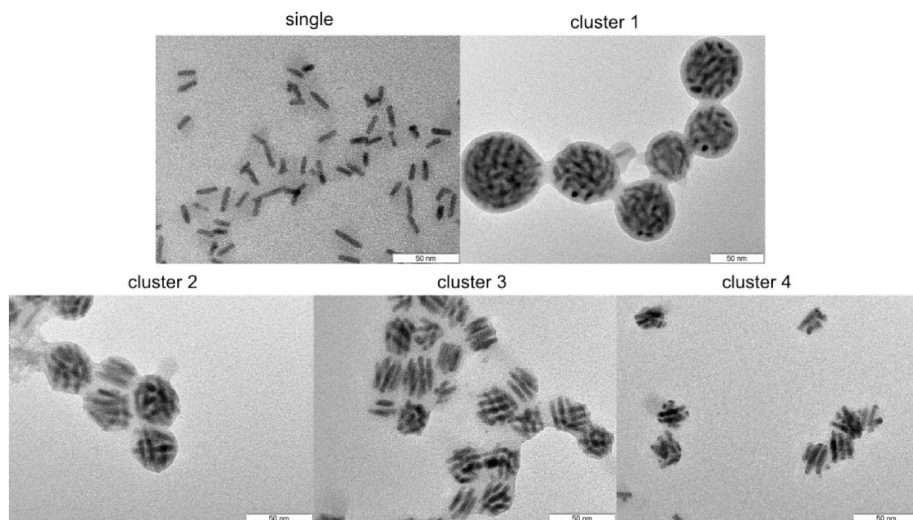


Figure 7.1 TEM images of all samples.

From the TEM images, the numbers of QDs/QRs per micelles were counted. The resulting histograms are shown in Figure 7.2.

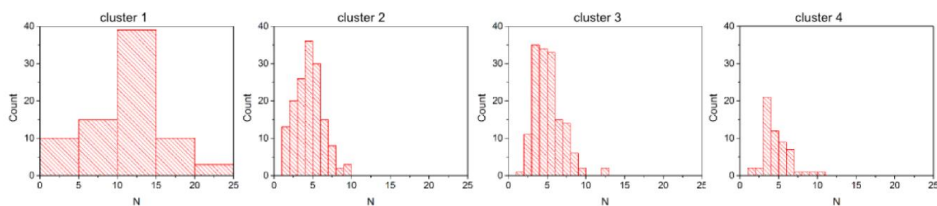


Figure 7.2 Histograms of counted QDs/QRs per micelle via TEM analysis.

In addition, two samples with a PI ligand of the same size as the PB ligand used for cluster 2 were prepared and investigated which possessed the same interparticle distance as cluster 2 (clusters 5-6).

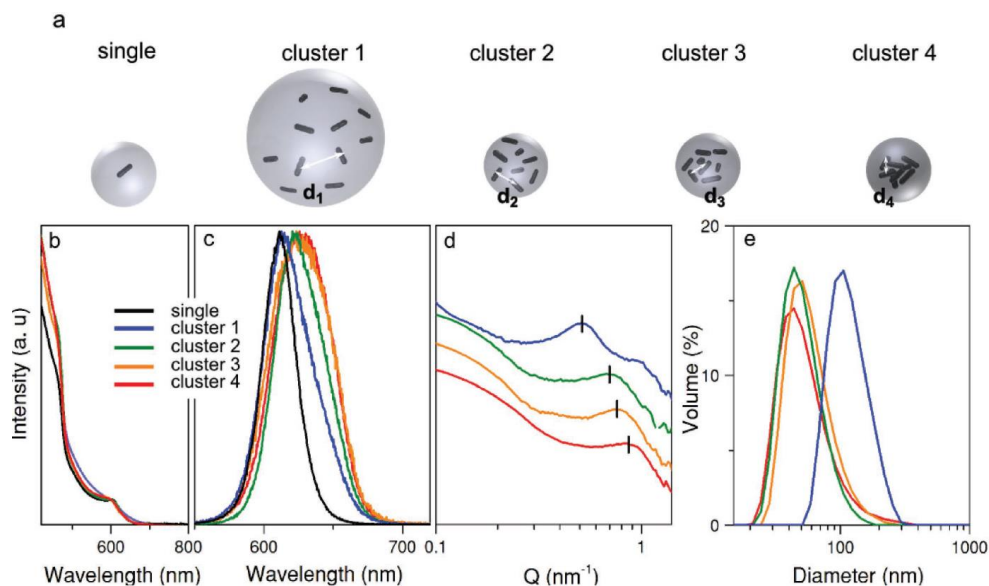


Figure 7.3 a) Schematic representations of the employed samples, highlighting the decreasing interparticle distances and different micelle sizes. b) Steady state absorption, c) photoluminescence and d) SAXS spectra of the samples. e) DLS statistics of the samples.

Figure 7.3 summarizes the basic characterization of the employed samples. The single and clustered NCs were analysed by transmission electron microscopy (TEM), steady-state absorption and photoluminescence (PL) spectroscopy, small-angle X-ray scattering (SAXS) and dynamic light scattering (DLS). The TEM and DLS measurements (Figure 7.3a,e) confirm that the clusters prepared with native ligands and with smaller polymer ligands (clusters 2-4) all have similar sizes and the clusters prepared with the heavier 4.8 kDa polymer ligand (cluster 1) are larger. The absorption spectra (Figure 7.3b) feature the CdSe correlated absorption around 600 nm and a broad CdS shell-related absorption at shorter wavelengths (460 nm). The PL spectra (Figure 7.3c) show first signatures of a resonant energy transfer: the PL of the clustered NCs is broadened and red-shifted relative to the single NCs. The probability for a resonant energy transfer increases with decreasing interparticle distance. Thus, the shorter the interparticle distance, the higher the probability for blue NCs to redistribute their excitation within the environment, effectively shifting the spectrum to the red.^[19]

Our earlier studies suggest that the polymer functionalization of the core-shell NCs has negligible impact on the optical properties of the individual NCs.^[27] Nevertheless, the processes of the NC ligand exchange and the cluster formation involve harsh chemistry, especially the cross-linking. It was found in earlier studies that the extension of the shell of the CdSe/CdS QD/QRs is sufficient to avoid changes of the optical properties by the sample preparation alone.

To ensure that the reported changes of the optical properties are purely distance and exciton-power dependent, we performed the preparation steps without clustering of the NCs. Figure 7.4 summarizes the optical characterization.

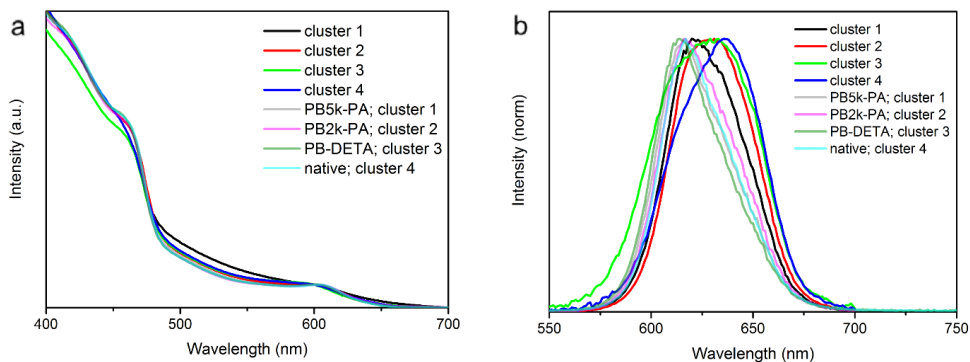


Figure 7.4 a) Comparison of absorption spectra from the clustered NCs with ligand exchanged NCs that were not clustered, labelled by the respective ligand. b) PL spectra from the clustered NCs in comparison with their ligand exchanged, not clustered NC counterparts.

Compared to the effect of the clustering, the difference between the ligand-exchanged NCs is negligible.

Within the micelle, the NCs are randomly oriented. Due to the lack of 3D information, the interparticle distance determination is difficult with TEM. In the SAXS spectra (Figure 7.3d), we observe a structural peak stemming from a regular average distance between the NCs. The shift to larger Q -values from cluster 1 to cluster 4 indicates a decreasing interparticle distance between the NCs. The distance between the centres of the QDs/QRs inside the clusters can be approximated by $2\pi/Q$,^[31,32] resulting in an average interparticle distance of 12.3 nm for cluster 1, 9.1 nm for cluster 2, 8.3 nm for cluster 3, and 7.3 nm for cluster 4, as summarized in Table 7.1.

Table 7.1 Comparison of the obtained interparticle distances between the NCs in the micelles from SAXS and FRET analysis. The FRET time constant is long for larger distances, the analysis of cluster 1 resulted in no significant FRET contribution.

Experiment	$d_{\text{cluster 1}}$ [nm]	$d_{\text{cluster 2}}$ [nm]	$d_{\text{cluster 3}}$ [nm]	$d_{\text{cluster 4}}$ [nm]
SAXS	12.3	9.1	8.3	7.3
FRET	-	9.8	7.9	7.3

The results from SAXS agree well with the distances obtained from FRET analyses of the samples. The details of the FRET evaluation will be explained later on in this chapter.

Cluster 5 and 6 were prepared with PI-DETA, a polymer ligand of the same size as the polymer ligand used for cluster 2. For the synthesis of cluster 5, the diblock copolymer excess was reduced, leading to a higher number of encapsulated QDs/QRs per micelle compared to cluster 2. In the case of cluster 6, the diblock copolymer excess was increased, whereby the number of QDs/QRs per micelle was reduced. Figure 7.5 displays a summary of investigations of these two clusters.

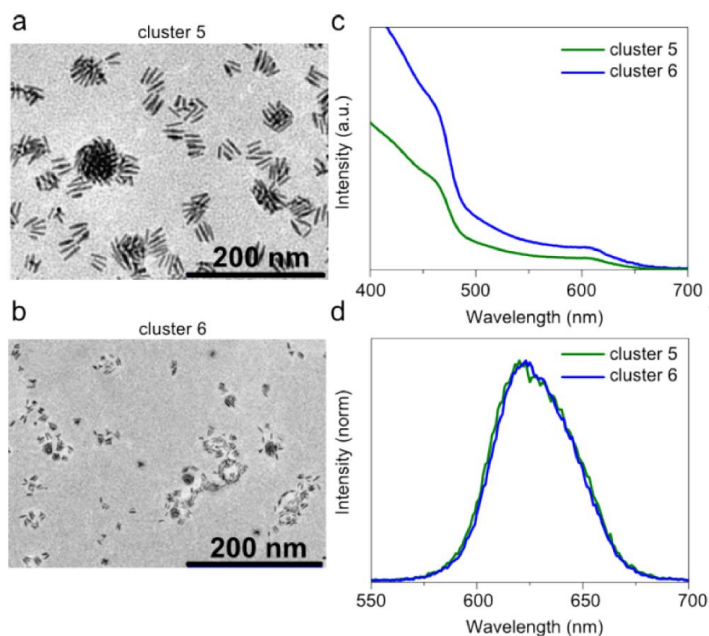


Figure 7.5 Clusters 5-6. a,b) TEM images of clusters 5 and 6, absorption c) and PL spectra d) of the clusters.

The interparticle distance is similar as in cluster 2. Table 7.2 summarizes the sample's chemical compositions and the geometry of all cluster samples is summarized in Table 7.3.

Table 7.2 Composition of the cluster samples. The samples vary by the stabilizing ligand (M_n : Number average molar mass), which defines the interparticle distance and the used copolymer and its excess, which altogether define the micelle geometry.

Cluster	Ligand	M_n (Ligand) [kDa]	Diblock copolymer	Copolymer excess
1	PB-PA	4.8	PB- <i>b</i> -PEO	200
2	PB-PA	2.2	PB- <i>b</i> -PEO	200
3	PI-DETA	1.1	PI- <i>b</i> -PEO	500
4	ODPA, HPA	0.335, 0.166	PI- <i>b</i> -PEO	500
5	PI-DETA	2.0	PI- <i>b</i> -PEO	250
6	PI-DETA	2.0	PI- <i>b</i> -PEO	1000

Table 7.3 Summary of the geometry of the cluster samples. n is the load of QDs/QRs per micelle, which is an additional geometry parameter to the average interparticle distance.

		Interparticle distance [nm]			
		7.4	8.3	9.1	12.3
$n \uparrow$					cluster 1
				cluster 5	
		cluster 4	cluster 3	cluster 2	
				cluster 6	

The knowledge of the average exciton population per NC $\langle N \rangle$ is important for a detailed discussion of potential multiexciton contributions. In our case, this quantity is difficult to obtain from absorption measurements as the exact absorption volumes and the focal conditions within the solution are complicated. We employ an approach established by Klimov et al. to calibrate the initial exciton population $\langle N \rangle$.^[22] Increasing the excitation power generates more excitons per NC. Figure 7.6a displays spectral-integrated PL decays of single NCs for increasing excitation powers. For low excitation powers, the NCs PL shows a monoexponential single-exciton decay. After crossing the threshold for multiexciton generation, Auger recombination becomes highly probable and leads to a fast decay. The Auger process annihilates the additional excitons and results in a single exciton which recombines regularly, effectively leading to a multistep decay. Normalizing the PL decay to the long-duration tail allows to distinguish the different excitation regimes, single exciton, biexciton and higher exciton populations, as well as their relative contributions (Figure 7.6b). The onset of biexciton recombination is at 10 μW

excitation power (Figure 7.6b, inset). The PL decays can again be normalized to this biexciton contribution and an onset of three excitons at 20 μW can be resolved. Assuming a constant photon density seen by the NCs in the micelles, 10 μW generate one exciton per NC in average ($\langle N \rangle = 1$).

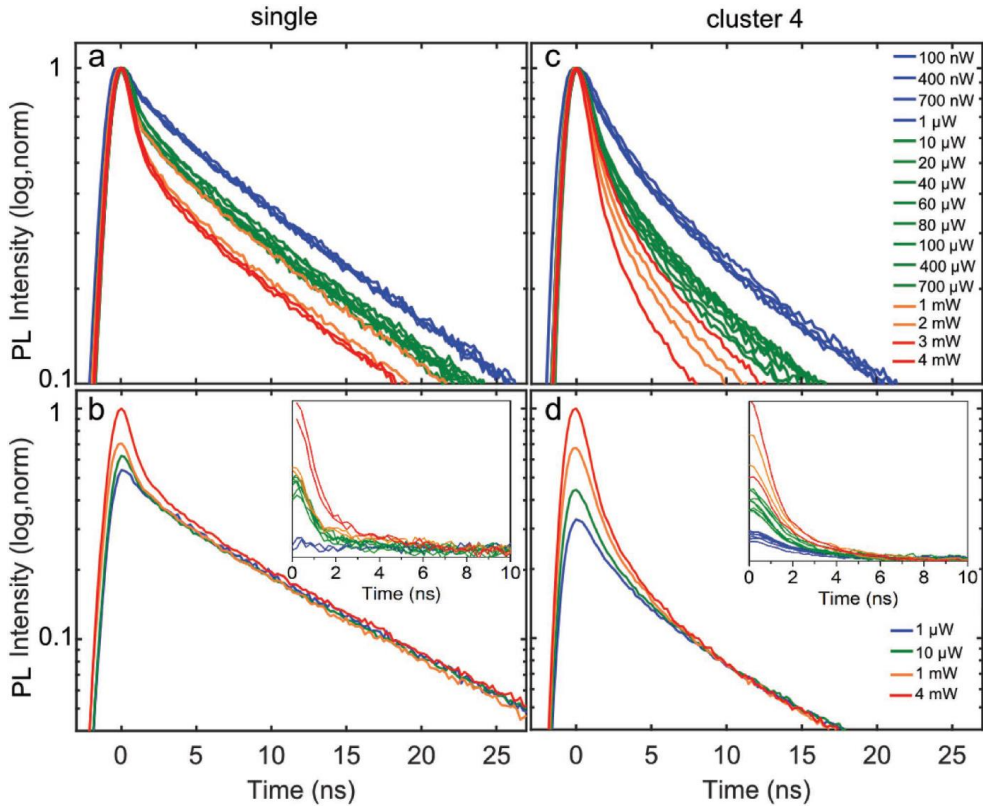


Figure 7.6 a) Spectral integrated PL decays of single NCs for different excitation powers, normalized to the maximum intensity and b) selected data from a, normalized to the tail of the PL decay. For the inset, the slow decay component was removed in order to highlight the onset of biexciton recombination. There, the complete data set is plotted, refer to (c). c,d) Spectral integrated PL decays of cluster 4 for different excitation powers, normalized the same way as in (a) and (b).

Figure 7.7 displays an excerpt of the data presented in the inset of Figure 7.6b. The biexponential component of the decay was removed in order to highlight the onset of the three exciton regime at 20 μW .

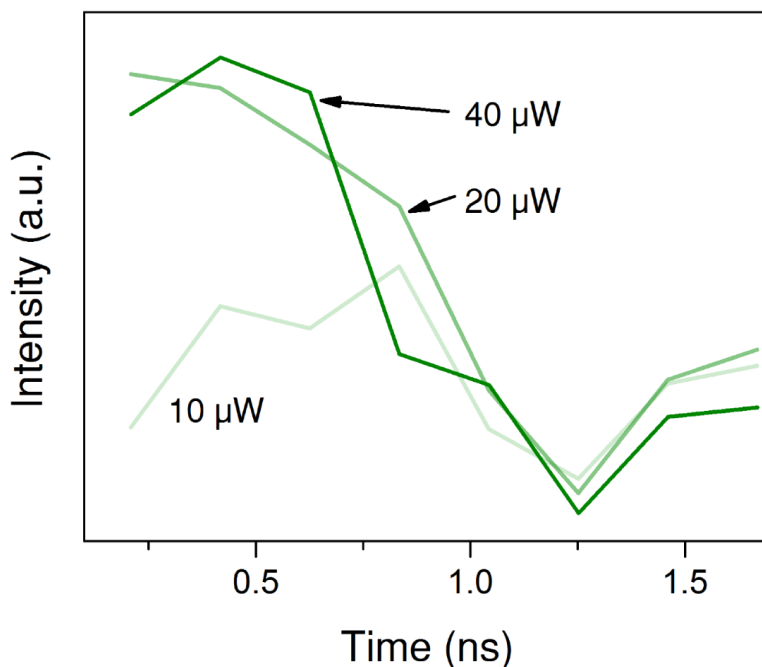


Figure 7.7 Spectral integrated PL decays of single NCs for different excitation powers. The data was normalized to the maximum intensity and the monoexponential and biexponential components were removed.

The power-dependent PL decays of the dense clusters 4 normalized similarly show a different behavior (Figure 7.6c,d). We also observe the onset of biexciton recombination with increasing power, but it is much more pronounced and sets in at lower power. Performing a multiexciton analysis similar to the single NCs (inset of Figure 7.6d) clearly shows that biexciton recombinations are already occurring at powers that lead to monoexponential decays in single NCs. Higher order exciton recombinations can also be observed at reduced powers. Figure 7.8 Figure 7.15 presents a comparison of the PL decays of the blue and red NCs as single NCs and in the dense cluster 4. The single blue and red NCs behave as the spectral integrated ensemble of single NCs (Figure 7.6): 10 μW is the threshold for observing multiexciton recombination. The same is valid for the blue NCs in the dense cluster. For the red NCs in cluster 4, a biexponential behaviour can already be observed at 1 μW, 10 μW of excitation power results in higher-order multiexciton recombinations.

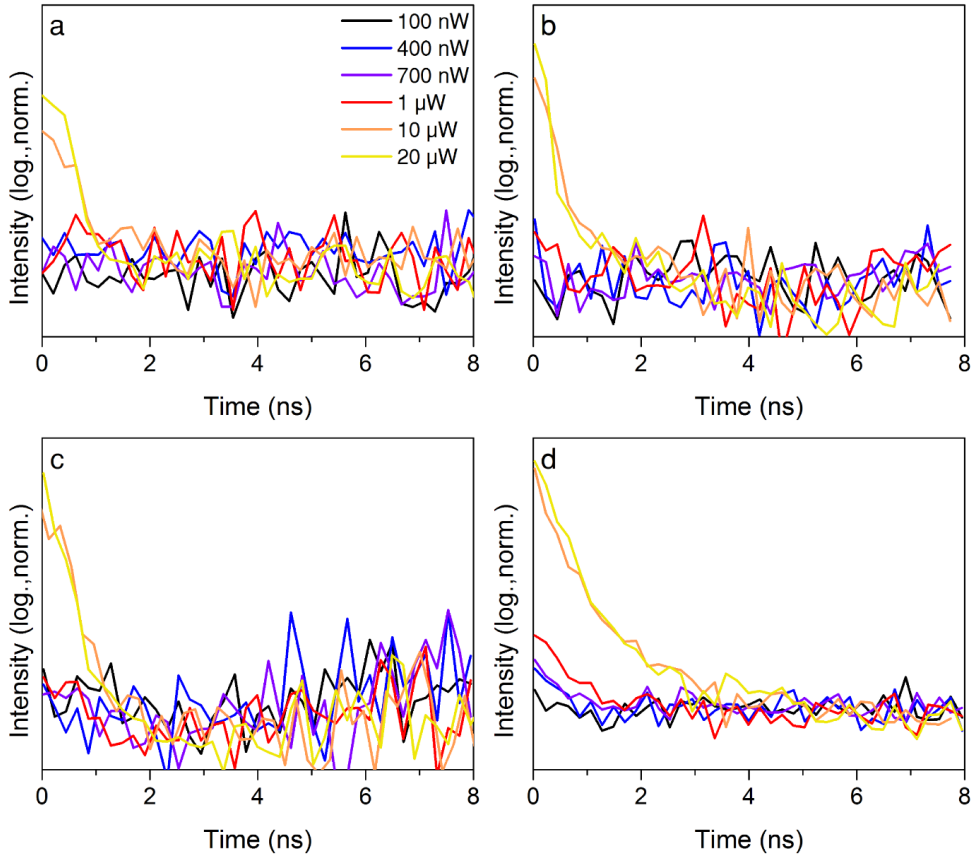


Figure 7.8 PL decays of a) the blue and b) red spectral component of single NCs and the blue c) and red d) spectral component of cluster 4. The data was normalized the same way as the inset of Figure 7.6.

It seems as if the clustered NCs were higher excited in average than the single NCs. This difference is distance-dependent. Figure 7.9 displays the spectral-integrated PL decays of clusters 1-3. The decays were normalized the same way as for cluster 4 in Figure 7.6. Cluster 1 behaves as the single NCs.

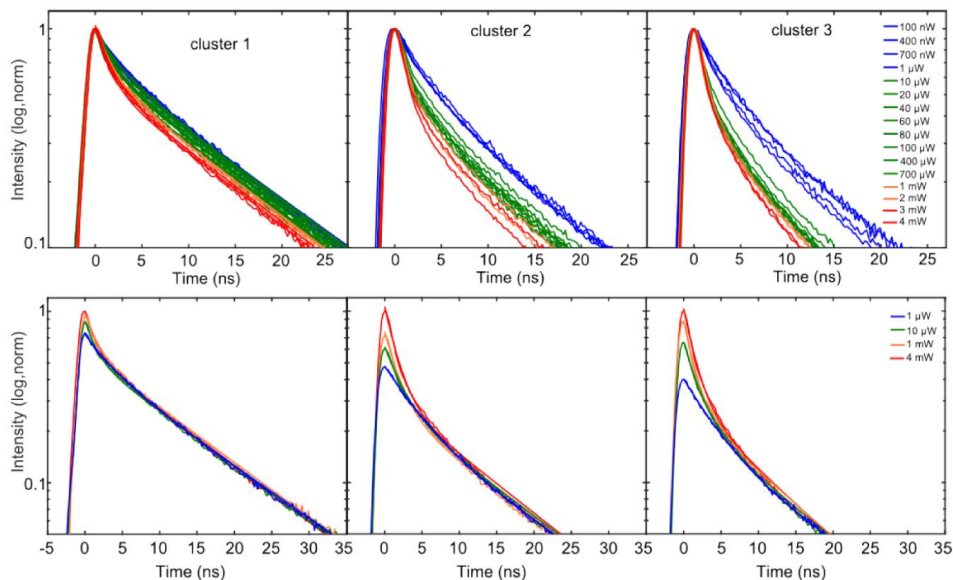


Figure 7.9 Spectral-integrated PL decays of cluster 1,2 and 3. The bottom row presents the same decays, normalized to the long-duration PL decay tail.

In addition, the same analysis is done for clusters 5 and 6 (Figure 7.10a, b). Again, the PL decays demonstrate that the interparticle distance is the main parameter for changing the clusters ensemble dynamics.

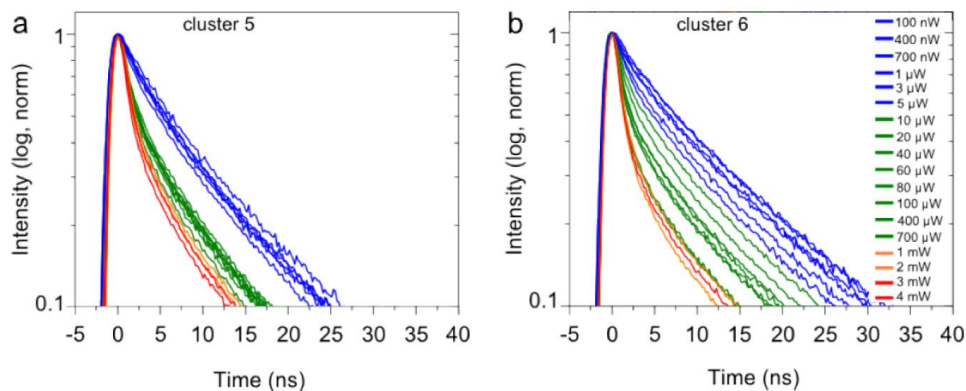


Figure 7.10 a,b) Time-resolved, spectral-integrated PL decays for increasing excitation powers.

The onset of multiexciton recombinations sets in at lower excitation powers for decreasing distances as apparent from the decays normalized to the long-duration tail of the decay.

As the excitation conditions are unchanged, the initial average exciton population per NC is the same. Multiexciton Auger recombination is generally not distance-dependent^[33], thus energy transfer must contribute to the changed decays. For an understanding of the impact of energy transfer on the PL decays, the distance dependence is important. Our micelle platform allows an increase of the NC interparticle distance in gradual steps. Experiments with both, spectral and time sensitivity allow for a more detailed analysis of energy transfer than the steady state PL presented in Figure 7.3c. An energy transfer into a nonradiative channel such as multiexciton recombination must not necessarily lead to a broadening of the spectra: in this case, the spectra would just decrease in overall intensity. In time-resolved experiments, the energy transfer to a nonradiative channel would be visible by a fastening in the PL decays of both donor and acceptor. Figure 7.11 summarizes experiments on the NCs in the single-exciton ($\langle N \rangle \leq 1$) regime with a streak camera for spectral- and time-resolved PL. Following photoexcitation, the single NCs feature a mostly monoexponential PL decay with a lifetime of 11 ns across the emitted spectrum. The decays of cluster 1 almost resembles the one of the single NCs. The large interparticle distances ensured by the polymer ligands reduce the energy transfer and the increased amount of NCs per micelle seems to have little impact. Reducing the interparticle distances (clusters 2-4) results in a splitting of the spectral components. The blue part of the spectrum decays faster, while the red part is less changed. This behaviour can be fully explained by Förster resonant energy transfer (FRET).^[34] The larger the NC bandgap, the higher the relative amount of neighbouring NCs with smaller bandgap acting as energy transfer acceptors and the higher the probability for an energy transfer contributing to the energy relaxation.

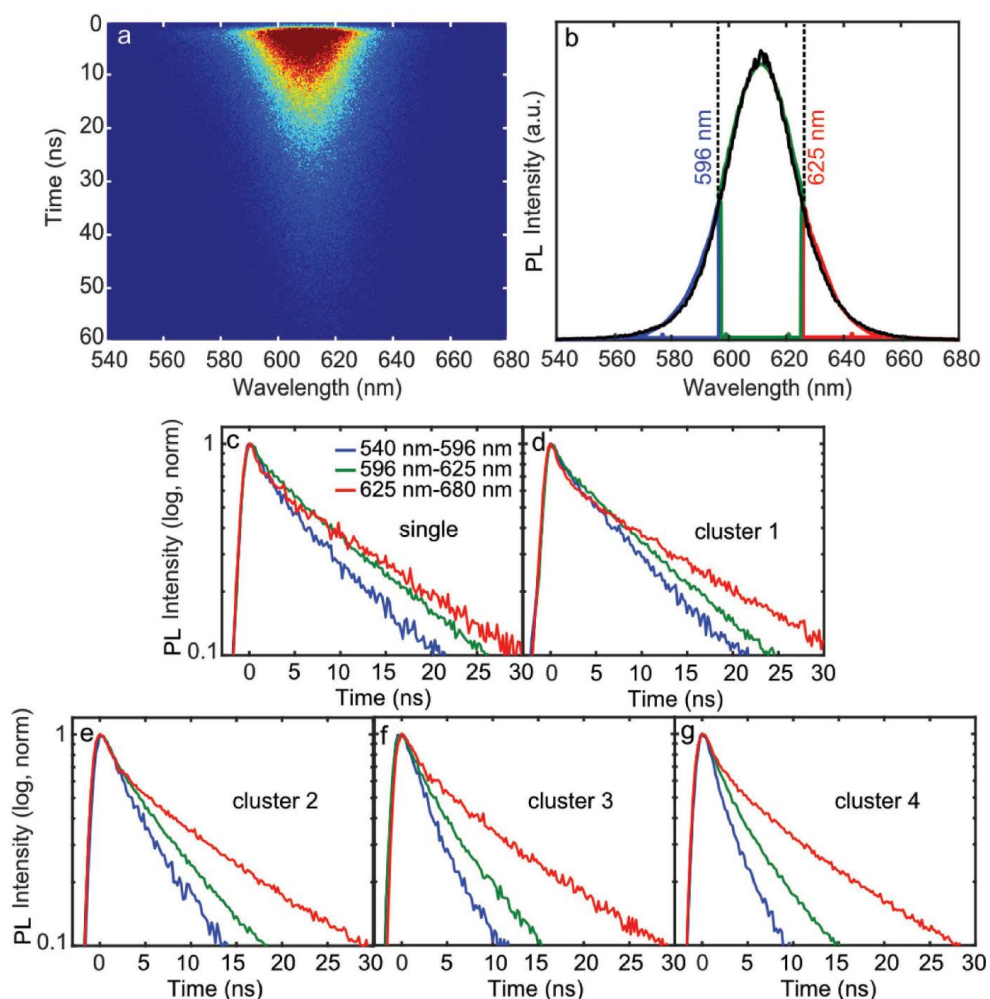


Figure 7.11 a) Streak camera map of single NCs. b) Time-integrated PL spectrum from the data set presented in (a). The three regions used for the spectral-resolved analysis are indicated: the spectrum was split in three parts at the full-width of half maximum. Spectral-resolved PL decays of c) single NCs, d) cluster 1, e) cluster 2, f) cluster 3, and g) cluster 4. All samples were excited with $1 \mu\text{W}$ at 418 nm ($N = 0.1$).

Assuming that all adjacent NCs of the blue NCs have smaller bandgaps and are potential acceptors, the observed change in the decay of the blue part of the spectrum allows an estimation of the average interparticle distance within the micelle. Typically, the probability of FRET scales with r^{-6} for point dipole-dipole interaction,^[35,36] where r is the distance between the interacting constituents. However the FRET rate also depends on the relative orientations of donors and acceptors. In case of QDs/QRs, the shape strongly affects the FRET rate. This results in an r^{-4} dependence.^[17,37-39] Under the assumption of no Förster resonance transfer occurring in the single NC samples, the decay time constant of the single NCs at low excitation

power was set as the unperturbed radiative time constant τ_{rad} which has a value of 9.7 ns. For clustered NCs we assumed $\frac{1}{\tau_{\text{tot}}} = \frac{1}{\tau_{\text{rad}}} + \frac{1}{\tau_{\text{nrad}}}$, where the total time constant is obtained from a fit to the measured decays and results in 9.1 ns for cluster 1, cluster 2: 5.7 ns, cluster 3: 4.3 ns and for cluster 4: 3.7 ns. The FRET-related non-radiative time constants τ_{nrad} are then 161.3 ns for cluster 1, cluster 2: 13.8 ns, cluster 3: 7.7 ns and cluster 4: 5.9 ns. The extracted distances are summarized in Table 7.1. Because of the large average interparticle distance within cluster 1, the differences of the PL decays between this cluster and the single NCs is so small that it does not allow a distance determination. Compared to the other clustered NCs, cluster 1 behaves as (almost) noninteracting. The good agreement between the different experiments confirms the extracted distances and demonstrates that the modified encapsulation approach results in a good distance control.

To investigate the interplay of energy transfer and multiexciton recombination, we performed power- and wavelength dependent studies on all samples. Figure 7.12 summarizes the experiments. The data are sorted such, that the excitation power increases from left to right, while the interparticle distance shortens from top to bottom. As discussed above, an increase of $\langle N \rangle$ in the single NCs (first row) leads to multiexciton Auger recombination and a multiexponential decay with no strong spectral sensitivity. The clusters behave different. The red part of the spectrum is more strongly changed upon increasing the power, the blue part shows the least power dependence. This is distance-dependent as evidenced by comparing the different clusters (rows). For cluster 1, interaction signatures appear at higher exciton populations. Still, this sample is more similar to the single NCs than to the other clusters. In general, the PL decay of the blue NCs can be completely described by contributions of energy transfer (as observed isolated at low-power excitation) and Auger recombination (observed in single NCs).

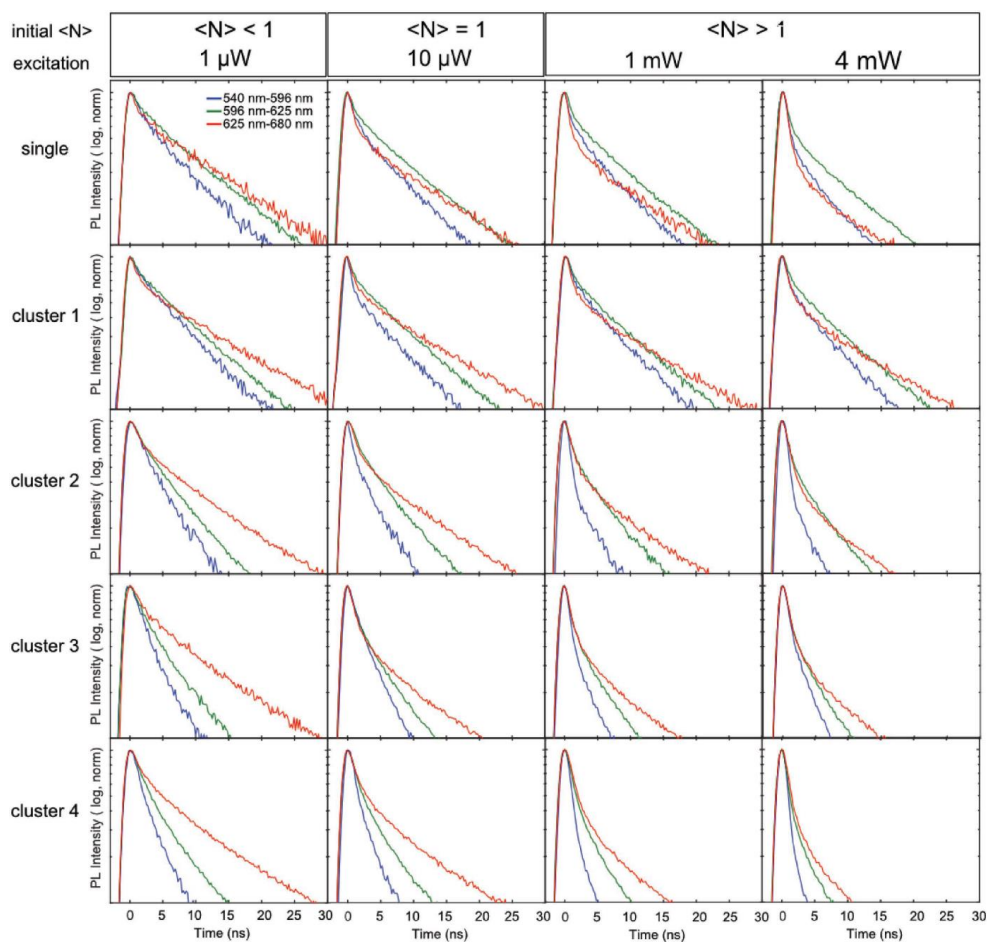


Figure 7.12 Spectral-resolved PL decays (wavelength regimes selected the same way as for Figure 7.11b of each sample in different initial exciton population regimes).

The blue and red single NCs show the same behaviour as the spectral integrated data in Figure 7.6 and thus have the same exciton population under the same excitation conditions. This means that there is no spectral sensitivity for the onset of multiexciton recombination. The blue clustered NCs also show no difference to the single NCs: crossing 10 μW excitation power generates more than one exciton per NC and multiexciton recombination sets in. This is different for the red clustered NCs. There, we observe an onset of multiexciton recombination already at 1 μW excitation power and 10 μW results in higher order multiexciton recombination.

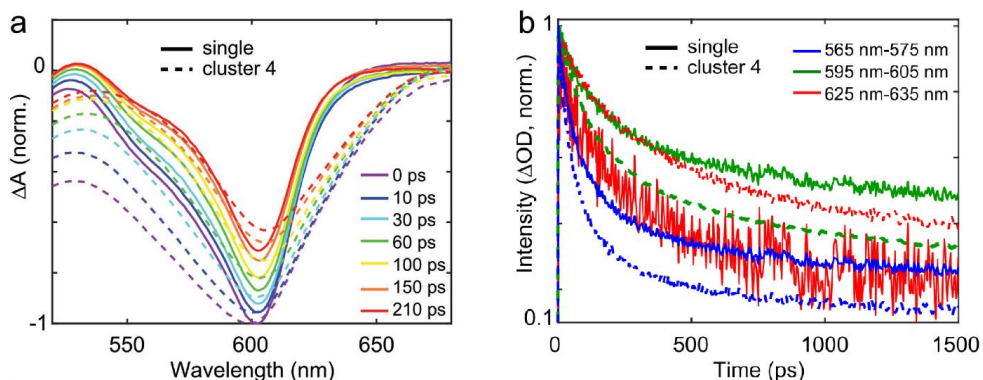


Figure 7.13 a) TA spectra around the CdSe IS spectral region of single NCs (solid lines) and cluster 4 (dashed lines) for different delay times. The spectra were normalized relative to the bleach maximum, set to $t=0$. b) TA dynamic traces for three representative spectral regimes of single NCs and cluster 4 in the $\langle N \rangle = 1$ regime.

For a more direct access to the exciton population, we performed transient absorption (TA) pump–probe experiments. The TA bleach signal is representative for the band edge carrier population and does, unlike PL, not rely on the radiative exciton recombination. Multiexciton populations can be directly detected and do not rely on changes of the decay.^[40] In CdSe NCs, after intraband relaxation, the TA signal is dominated by the electron filling the lowest-energy IS state.^[41] The corresponding contribution Δa is directly proportional to the occupation of the IS carrier level, enabling an estimation of the exciton population.

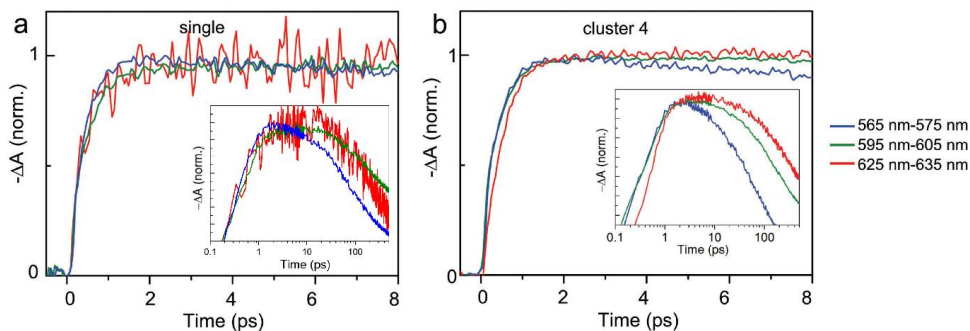


Figure 7.14 TA dynamic traces for three representative spectral regimes of a) single NCs and b) cluster 4. $t = 0$ was set to the moment of photoexcitation. The samples were excited with conditions leading to $\langle N \rangle = 1$. The insets show the TA dynamic traces with a logarithmic time axis.

Figure 7.13 presents the experiments on single NCs and cluster 4, excited in the $\langle N \rangle = 1$ regime. For the single NCs, the spectrum narrows during the first hundred picoseconds and then decays homogeneously. The cluster's initial spectrum features a shoulder in the blue part

of the spectrum, which decays faster than the other parts, resulting in a narrowing and a shift of the spectrum's centre of mass. Figure 7.13b displays a comparison of TA dynamic traces of single NCs and cluster 4 for different spectral regimes. Upon clustering, the decay of the blue NCs is fastened. The energy transfer leads to an in average longer exciton population of the red NCs. The corresponding TA dynamic traces at shorter timescales of the IS central bleach and its long- and short-wavelength shoulders are displayed in Figure 7.14. For the single NCs, no spectral sensitivity can be observed. For the clusters, a fast energy transfer is evidenced. The transfer leads to a fastened dynamic of the blue spectral component (blue NCs). The red NCs are effectively higher excited, resulting in an increased bleach intensity and a delayed bleach maximum, followed by a fast dynamic due to the onset of multiexciton recombination (Figure 7.14b, inset). Figure 7.15 displays spectrally integrated TA dynamic traces of single NCs and cluster 4 for increasing excitation powers. In the PL decays, the biexciton lifetime is instrument limited. From a biexponential fit to the TA traces, we can resolve an average lifetime of $\tau_{\text{Aug}} = 190$ ps.

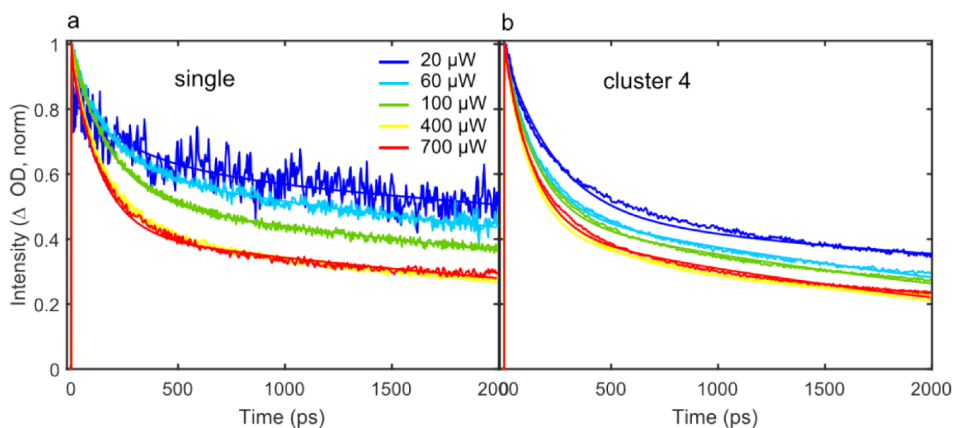


Figure 7.15 Spectrally integrated (around the IS central bleach) TA traces for different excitation powers of a) single QD/QRs and b) cluster 4.

The processes explaining our observations are summarized in Figure 7.16.

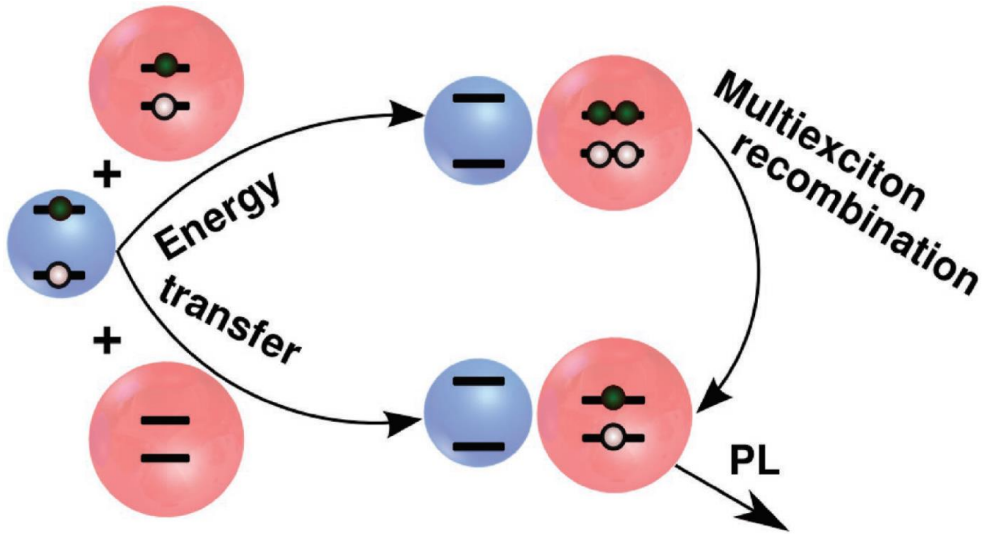


Figure 7.16 Schematic illustration of the processes contributing to the energy relaxation of clustered NCs. In the low-excitation regime, an excited blue NC transfers its energy to a groundstate red NC, which is followed by a radioactive decay. In the $\langle N \rangle = 1$ regime, the energy transfer results in a biexciton population in the red NC, resulting in a multiexciton recombination.

In the low-exciton regime, an efficient energy transfer moves the exciton from blue NCs to red NCs, shortening the lifetime of the blue NCs and increasing the amount of radiative recombinations in the red NCs, shifting the spectrum's center of mass to the red (Figure 7.3c). For $\langle N \rangle = 1$, the probability of a red NC energy transfer acceptor already being excited is high and an almost immediate multiexciton recombination follows (the biexciton lifetime is below 200 ps, according to the TA analysis). The effective recombination time then depends on the amount of triggered recombinations, which is governed by the FRET rate of the blue NCs. These collective processes happen until the $\langle N \rangle < 1$ regime is reached. The relative amount of the “triggered multiexciton recombination” scales with the amount of excitations (excitation level) and the probability of the energy transfer (distance). We start observing signatures of the effect at interparticle distances below 10 nm. This can have a significant impact for current device considerations: light sources become more and more compact. To not change the spatial emission profile, thin and dense QD films are employed as colour converters. However, when increasing the lamp brightness, the $\langle N \rangle = 1$ regime can be reached, where the triggered multiexciton recombination lowers the relative amount of radiative recombinations, reducing the efficiency. The same applies for solar energy light conversion with solar concentrators. In regimes with high light intensities, triggered multiexciton recombination might annihilate photogenerated carriers before they can be extracted. Low QD concentrations and large interparticle distances can ensure suppressing triggered multiexciton recombinations but result

in a reduced amount of absorbed light. Thus, the NC concentrations within the active materials have to be designed carefully.

7.3 Conclusions

In conclusion, we have developed a platform that allows investigating excitation-power and interparticle-distance dependent exciton dynamics between NCs. QDs/QRs were clustered in amphiphilic micelles with an interparticle distance control by a polymer spacer ligand. The resulting constructs are long-term stable and enable high-power excitation experiment. Under low excitation power, the cluster's dynamic is influenced by energy transfer. At high powers, multiple excitons are generated by NCs and multiexciton recombination can be observed. In dense clusters and at average excitons populations around 1, energy transfer can trigger multiexciton recombination in neighboring NCs. This effect sets in at interparticle distances below 10 nm and changes the collective properties, where the highest bandgap constituent governs the ensemble dynamics. The occurrence of the effect strongly depends on the interparticle distance and the excitation level, which opens ways to avoid or enhance the effect.

7.4 Experimental Section

7.4.1 Materials

The following chemicals were used as received: Tetrahydrofuran (THF, 99.7%), n-hexane (96%) and ethanol (99.98%) were purchased from VWR. 2,2'-Azobis(2-methylpropionitrile) (AIBN, 98%). Water was purified using an ELGA PURELAB flex 2 system (18.2 M Ω). QDs/QRs were synthesized according to the protocol used earlier.^[27] The syntheses of the polymers are described elsewhere.^[42-44] Table 7.4 summarizes the molecular weight characterization of the employed polymers.

Table 7.4 Molecular weight characterization of the used polymers. M_n (kDa): number average molar mass, M_w : mass average molar mass and M_w/M_n : dispersity.

Polymer	M_n [kDa]	M_w/M_n	wt% PEO
PI-DETA	1.1	1.19	-
PB-PA	2.2	1.03	-
PB-PA	4.8	1.00	-
PI- <i>b</i> -PEO	13.4	1.07	70
PB- <i>b</i> -PEO	14.8	1.01	67

7.4.2 Micellar Encapsulation

QDs/QRs were incubated with a 2000-fold excess of polymer ligand in n-hexane for more than 20 h. As polymer ligand PI-DETA or PB-PA was used. Before encapsulation, the QDs/QRs were precipitated with ethanol and centrifuged. The polymer-coated QDs/QRs were solved in THF and mixed with either a 200-fold excess of PB-*b*-PEO or a 500-fold excess of PI-*b*-PEO and AIBN (1/3 of isoprene and butadiene units present in the diblock copolymer) in THF. The concentration of QDs/QRs in THF was $4 \cdot 10^{-6}$ M. The QDs/QRs-polymer-AIBN-THF solution was slowly injected into the 12-fold of water and heated up to 80 °C. After 4 h, the QDs/QRs solution was washed with water in centrifugal filter units (Amicon Ultra15, 100 kDa membrane). To remove empty micelles and to separate different QDs/QRs micelle fractions, a sucrose gradient centrifugation was performed. To remove the sucrose, the fractions were washed again with water in centrifugal filter units.

7.4.3 Sample Characterisation

TEM experiments were performed using a Jeol JEM-1011 microscope (100 keV). UV-vis absorption spectra were recorded on Cary 50. DLS data were collected with a Zetasizer Nano ZS system (Malvern). The sample concentration was always $2 \cdot 10^{-6}$ M.

7.4.4 SAXS

For SAXS measurements the gallium anode low angle X-ray instrument (GALAXI) was used at the Jülich Centre for Neutron Science.^[45] SAXS experiments were performed in the Q-

range from 0.02 to 2.2 nm⁻¹. The samples were measured in sealed glass capillaries of 2 mm inner diameter at room temperature.

7.4.5 Optical Spectroscopy

Optical spectroscopy Pump-probe TA spectroscopy was performed using a commercial TA setup (Helios; Ultrafast Systems). A commercial amplified Ti-sapphire laser system (Spitfire-Ace, 800 nm, 6 W, 1 kHz, 35 fs; Spectra Physics) was employed to generate the pump and probe pulses. The pump pulses were transformed within an optical parametric amplifier (TOPAS-Prime; Light Conversion) with frequency mixer (NirUVis; Light Conversion) and chopped at 500 Hz. The probe beam was a broadband continuum white-light with a spectral range of 420-750 nm. The instrument response in this wavelength regime was estimated to be below 200 fs. For the reported experiments, the excitation wavelength was set 418 nm. The samples were excited in aqueous solution within a quartz cuvette. The estimated spot diameter within the liquid was 457 μm . The reported laser powers are all the cw-equivalent of the kHz pulse sequence. The time-resolved PL spectroscopy was performed with the same excitation source as for the TA and a universal streak camera (C 5680, Hamamatsu photonics) with a M 5675 Synchroscan and Single-Sweep-unit for detection. There, the excitation wavelength was also set to 418 nm and the spot diameter in solution was 204 μm .

7.5 Acknowledgements

M.R. and R.K. contributed equally to this work. The authors acknowledge financial support from the German Research Foundation (DFG) *via* the Cluster of Excellence “Center of Ultrafast Imaging (CUI).” L.S.F. acknowledges financial support from the DFG Priority Program SPPI681 (project KR 3929/2-1). The authors acknowledge Johannes Ostermann and Marcus Janschel for support with polymers and Alf Mews for spectroscopy lab access.

7.6 References

- [1] Y. E. Panfil, M. Oded, U. Banin, *Angew. Chemie Int. Ed.* **2018**, *57*, 4274.
- [2] F. Di Stasio, J. Q. Grim, V. Lesnyak, P. Rastogi, L. Manna, I. Moreels, R. Krahne, *Small* **2015**, *11*, 1328.
- [3] H. Zhao, D. Benetti, L. Jin, Y. Zhou, F. Rosei, A. Vomiero, *Small* **2016**, *12*, 5354.
- [4] J. M. Pietryga, Y.-S. Park, J. Lim, A. F. Fidler, W. K. Bae, S. Brovelli, V. I. Klimov, *Chem. Rev.* **2016**, *116*, 10513.
- [5] C. R. Kagan, E. Lifshitz, E. H. Sargent, D. V. Talapin, *Science (80-.)*. **2016**, *353*, aac5523.
- [6] G. H. Carey, A. L. Abdelhady, Z. Ning, S. M. Thon, O. M. Bakr, E. H. Sargent, *Chem. Rev.* **2015**, *115*, 12732.
- [7] B. S. Mashford, M. Stevenson, Z. Popovic, C. Hamilton, Z. Zhou, C. Breen, J. Steckel, V. Bulovic, M. Bawendi, S. Coe-Sullivan, P. T. Kazlas, *Nat. Photonics* **2013**, *7*, 407.
- [8] H. Huang, A. Dorn, V. Bulovic, M. G. Bawendi, *Appl. Phys. Lett.* **2007**, *90*, 023110.
- [9] R. Ghosh Chaudhuri, S. Paria, *Chem. Rev.* **2012**, *112*, 2373.
- [10] P. Reiss, M. Protière, L. Li, *Small* **2009**, *5*, 154.
- [11] K. Wu, Y.-S. Park, J. Lim, V. I. Klimov, *Nat. Nanotechnol.* **2017**, *12*, 1140.
- [12] Z. Zhang, Y. Ye, C. Pu, Y. Deng, X. Dai, X. Chen, D. Chen, X. Zheng, Y. Gao, W. Fang, X. Peng, Y. Jin, *Adv. Mater.* **2018**, *30*, 1801387.
- [13] M. Scheibner, T. Schmidt, L. Worschech, A. Forchel, G. Bacher, T. Passow, D. Hommel, *Nat. Phys.* **2007**, *3*, 106.
- [14] F. Montanarella, M. Biondi, S. O. M. Hinterding, D. Vanmaekelbergh, F. T. Rabouw, *Nano Lett.* **2018**, *18*, 5867.
- [15] A. Olaya-Castro, G. D. Scholes, *Int. Rev. Phys. Chem.* **2011**, *30*, 49.
- [16] C.-P. Hsu, Z.-Q. You, H.-C. Chen, *J. Phys. Chem. C* **2008**, *112*, 1204.
- [17] S. Halivni, A. Sitt, I. Hadar, U. Banin, *ACS Nano* **2012**, *6*, 2758.
- [18] J. B. Hoffman, H. Choi, P. V. Kamat, *J. Phys. Chem. C* **2014**, *118*, 18453.
- [19] S. W. Clark, J. M. Harbold, F. W. Wise, *J. Phys. Chem. C* **2007**, *111*, 7302.

- [20] A. J. Mork, M. C. Weidman, F. Prins, W. A. Tisdale, *J. Phys. Chem. C* **2014**, *118*, 13920.
- [21] A. J. Nozik, *Annu. Rev. Phys. Chem.* **2001**, *52*, 193.
- [22] V. I. Klimov, A. A. Mikhailovsky, D. W. McBranch, C. A. Leatherdale, M. G. Bawendi, *Science (80-.)*. **2000**, *287*, 1011.
- [23] V. I. Klimov, D. W. McBranch, C. A. Leatherdale, M. G. Bawendi, *Phys. Rev. B* **1999**, *60*, 13740.
- [24] Y. Gao, C. S. S. Sandeep, J. M. Schins, A. J. Houtepen, L. D. A. Siebbeles, *Nat. Commun.* **2013**, *4*, 2329.
- [25] C. E. Rowland, I. Fedin, H. Zhang, S. K. Gray, A. O. Govorov, D. V. Talapin, R. D. Schaller, *Nat. Mater.* **2015**, *14*, 484.
- [26] A. Sánchez-Iglesias, M. Grzelczak, T. Altantzis, B. Goris, J. Pérez-Juste, S. Bals, G. Van Tendeloo, S. H. Donaldson, B. F. Chmelka, J. N. Israelachvili, L. M. Liz-Marzán, *ACS Nano* **2012**, *6*, 11059.
- [27] M. Rafipoor, C. Schmidtke, C. Wolter, C. Strelow, H. Weller, H. Lange, *Langmuir* **2015**, *31*, 9441.
- [28] C. Schmidtke, E. Pösel, J. Ostermann, A. Pietsch, H. Kloust, H. Tran, T. Schotten, N. G. Bastús, R. Eggers, H. Weller, *Nanoscale* **2013**, *5*, 7433.
- [29] R. J. Hickey, A. S. Haynes, J. M. Kikkawa, S.-J. Park, *J. Am. Chem. Soc.* **2011**, *133*, 1517.
- [30] Y. Yin, A. P. Alivisatos, *Nature* **2005**, *437*, 664.
- [31] J. Maes, N. Castro, K. De Nolf, W. Walravens, B. Abécassis, Z. Hens, *Chem. Mater.* **2018**, *30*, 3952.
- [32] J. Oberdisse, P. Hine, W. Pyckhout-Hintzen, *Soft Matter* **2007**, *3*, 476.
- [33] I. Robel, R. Gresback, U. Kortshagen, R. D. Schaller, V. I. Klimov, *Phys. Rev. Lett.* **2009**, *102*, 177404.
- [34] S. A. Crooker, J. A. Hollingsworth, S. Tretiak, V. I. Klimov, *Phys. Rev. Lett.* **2002**, *89*, 186802.
- [35] T. Förster, *Discuss. Faraday Soc.* **1959**, *27*, 7.
- [36] T. Förster, *Ann. Phys.* **1948**, *437*, 55.
- [37] S. Jander, A. Kornowski, H. Weller, *Nano Lett.* **2011**, *11*, 5179.

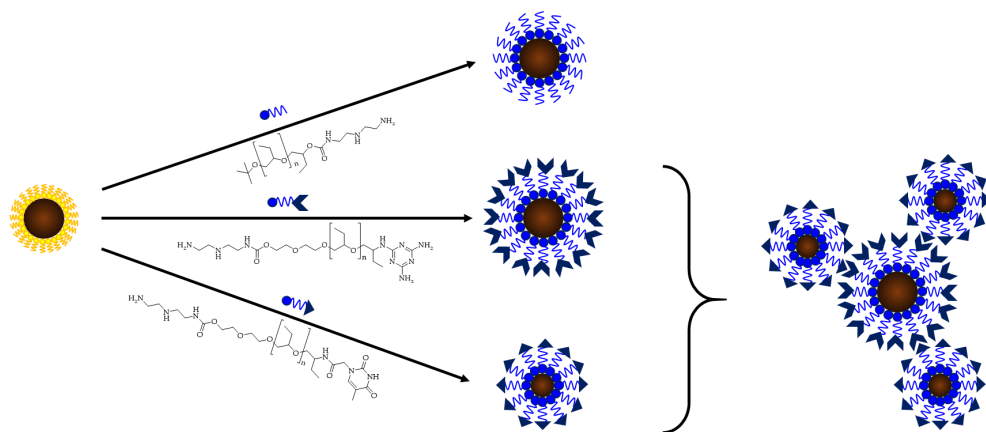
- [38] A. Sitt, N. Even-Dar, S. Halivni, A. Faust, L. Yedidya, U. Banin, *J. Phys. Chem. C* **2013**, *117*, 22186.
- [39] R. R. Chance, A. Prock, R. Silbey, in *J. Mol. Struct.*, **2007**, pp. 1–65.
- [40] A. H. Proppe, J. Xu, R. P. Sabatini, J. Z. Fan, B. Sun, S. Hoogland, S. O. Kelley, O. Voznyy, E. H. Sargent, *Nano Lett.* **2018**, *18*, 7052.
- [41] D. A. Wheeler, J. Z. Zhang, *Adv. Mater.* **2013**, *25*, 2878.
- [42] E. Pöselt, C. Schmidtke, S. Fischer, K. Peldschus, J. Salamon, H. Kloust, H. Tran, A. Pietsch, M. Heine, G. Adam, U. Schumacher, C. Wagener, S. Förster, H. Weller, *ACS Nano* **2012**, *6*, 3346.
- [43] A. Feld, R. Koll, L. S. Fruhner, M. Krutyeva, W. Pyckhout-Hintzen, C. Weiß, H. Heller, A. Weimer, C. Schmidtke, M.-S. Appavou, E. Kentzinger, J. Allgaier, H. Weller, *ACS Nano* **2017**, *11*, 3767.
- [44] J. Köhler, H. Keul, M. Möller, *Chem. Commun.* **2011**, *47*, 8148.
- [45] E. Kentzinger, M. Krutyeva, U. Rücker, *J. large-scale Res. Facil. JLSRF* **2016**, *2*, A61.

8 Synthesis and Characterisation of Polymer Coated Supramolecular Magnetic Nanocrystals

I synthesised one batch of the iron oxide nanocrystals (NC_{8.61}) and did the full synthesis of the supramolecular polymer ligand (including non-successful syntheses). The evaluation of the NMR data of the polymers was done by me. I performed all DLS measurements and most of the SAXS experiments. I evaluated all the SAXS data and analysed the TEM measurements. This manuscript was written by me. Jürgen Allgaier provided the polymer *t*Bu-PBO5k-OH which was used for the synthesis of the DETA-PBO5k as well as the Bn-PEO20k-OH. He established the usage of the benzyl protective group and supervised me during the synthesis of the polymers. Martin Dulle performed some of the SAXS experiments on his own and assisted me in all the others. Vanessa Leffler and Sascha Ehlert performed the TEM measurements and provided valuable information regarding the ligand exchange. Sascha Ehlert assisted me during the synthesis of the NCs and provided the second batch of NCs (NC_{4.35}). He showed me how to do the TGA measurements and performed most of them. Andreas Raba synthesised the HO-PBO5k-OH polymer and the DAT-F precursor. Jürgen Allgaier, Margarita Kruteva and Stephan Förster supervised the investigations.

8.1 Introduction

Supramolecular nanocomposites are versatile materials as they combine the functionalities of nanocrystals, polymers and supramolecular chemistry. Fundamental as well as application-oriented research is conducted towards the exploration of these systems and potential applications like artificial skin, sensors, drug delivery or artificial nacre have already been discussed in the literature.^[1-7]



Scheme 8.1 Scope of this chapter. Synthesised polymer ligands with and without supramolecular functionalities are attached to two different batches of iron oxide nanocrystals. The supramolecular nanocrystals are then mixed, leading to cluster formation due to the hydrogen bonds between the polymer shells.

To study the interactions between nanocrystals functionalised with supramolecular polymers, we target iron oxide nanocrystals coated with a poly(1,2-butylene oxide) (PBO) ligand (Scheme 8.1). One chain end was equipped with the ligand head group for anchoring the molecule on the NP surface and the other chain end was carrying the hydrogen bonding pair of thymine (Thy) and 2,6-diaminotriazine (DAT). Iron oxide nanocrystals are among the most used nanocrystals as they are the go-to choice for bioapplications like magnetic hyperthermia, drug delivery or contrast agents.^[8] They can be obtained by thermal decomposition in high quantities with a very narrow size distribution.^[9] Anionic ring opening polymerisation of butylene oxide (BO) leads to polymers with narrow molecular weight distribution if done in the presence of crown ethers in non-polar solvents like toluene at low temperatures.^[10] PBO has a low glass transition temperature of about $-70\text{ }^{\circ}\text{C}$ and is a semipolar polymer, which suppresses the cluster formation that is usually encountered in materials containing supramolecular groups.^[11] It contains by nature one or two alcohol end groups suitable for functionalisation. The hydrogen bonding pair Thy and DAT was chosen as supramolecular functionality due to their

strong hetero-association^[12] and the connection to PBO being an already established synthesis procedure.^[13]

This bonding motif has already been used for the synthesis and investigation of supramolecular nanocomposites. Boal *et al.* employed the Thy-DAT pair to assemble gold nanocrystals with thiol ligands of which a few were functionalised with thymine.^[14] These particles were then combined with polymers carrying the DAT functionality, resulting in spherical agglomerates in non-competitive solvents like dichloromethane or chloroform with a temperature dependent size. The sample precipitated and was insoluble in non-polar solvents but partially soluble in polar solvents. When the head group of the Thy ligand is replaced by a diol, this system can be employed to iron oxide nanocrystals resulting in tunable magnetic interactions between the nanocrystals.^[15] Using a diblock copolymer where only one block is DAT functionalised instead, leads to the formation of micellar structures where the supramolecular block and the Thy-functionalised nanocrystals form the core and the non-functionalised polymer block the shell of the micelles.^[16,17] Although the binding between Thy and DAT is much weaker in water than compared to non-polar organic solvents, CdSe nanocrystals grafted with a PEG-Thy ligand were able to attach to a DAT-functionalised polymer which were incorporated into lipid membranes.^[18]

To study the interactions between supramolecularly functionalised nanocrystals (NCs), suitable polymer ligands needed to be prepared. The target material was an α,ω -functionalised PBO equipped with a ligand head group and a supramolecular group. Additionally, a PBO was synthesised, containing only a ligand head group at one chain end to compare supramolecularly functionalised with non-functionalised NPs. As ligand group, either diethylenetriamine (DETA) or phosphonic acid functionalities were used due to their high affinity towards the surface of iron oxide nanocrystals.^[19]

The synthesised polymers were investigated *via* nuclear magnetic resonance (NMR) spectroscopy and size exclusion chromatography (SEC). Although it is a standard analysis technique for organic compounds, the usage of NMR to obtain the functionalisation degree of polymers is not trivial, especially for higher molecular weight products. Low concentrations and high scan rates increase the signal to noise ratio and pyridine- d_6 as solvent makes the protons of hydroxy groups visible in the spectrum. SEC is a commonly used technique for the evaluation of polymer sizes and size distribution. However, functional groups like amino groups can interact with the solvent material, which complicates the analysis of the polymers synthesised here. Transferring these groups into non-interacting ones as well as the correct choice of the eluent are necessary to gain reliable information about the analysed polymers.

8.2 Results and Discussion

8.2.1 Synthesis of DETA-PBO5k-Thy and DETA-PBO5k-DAT

Both Thy and DAT possess amino groups, however, these groups have a completely different chemical nature than the amino groups in DETA. Nevertheless, to make sure that there is no competitive situation between the ligand head group and the supramolecular group, PBOs functionalised with either DETA (DETA-PBO5k) or thymine/DAT (PBO5k-Thy/PBO5k-DAT) were added to oleic acid coated iron oxide nanocrystals (NC_{4.35}). The hydrodynamic radii were determined by DLS and compared to the one of the oleic acid (OA) coated nanocrystals (Figure 8.1).

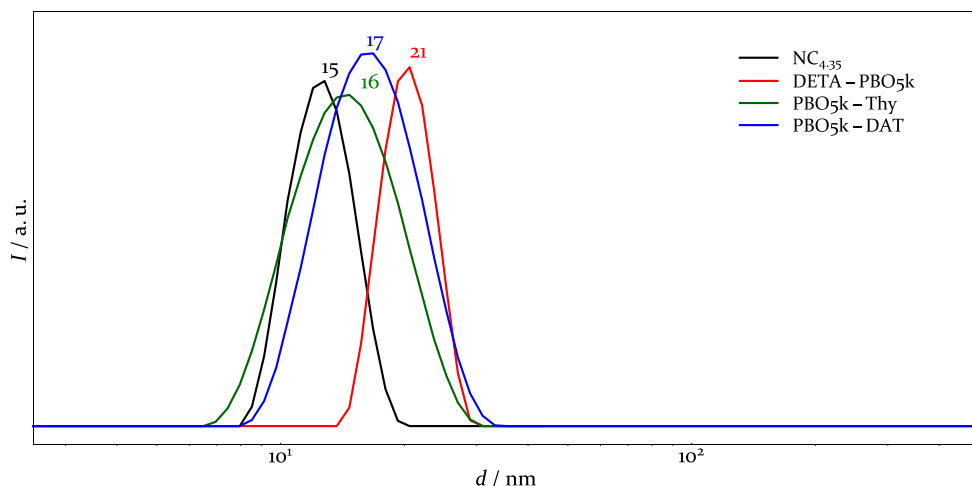
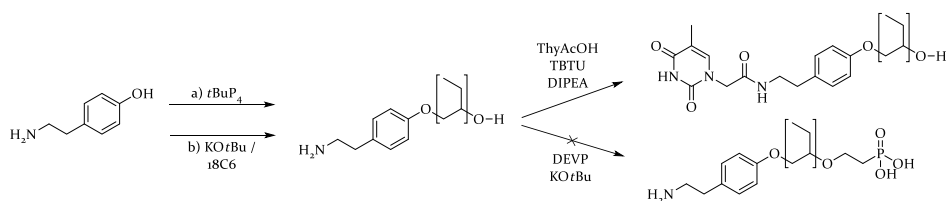


Figure 8.1 DLS measurements to check the affinity of the different groups for the iron oxide surface. Numbers represent the peak diameters in nm.

A strong shift of the peak maximum from OA stabilised NCs to the sample containing DETA-PBO5k due to the replacement of OA by the polymeric ligand. For the Thy and DAT samples mainly peak broadening is found in combination with a minor shift, indicating not more than small interactions with the NC surface.

The first attempt for the synthesis of the α - ω -functionalised PBO was to be based on the use of an initiator containing two different functionalities which allow the introduction of ligand and supramolecular group (Scheme 8.2). The chosen initiator was tyramine which had already been successfully used for the synthesis of poly(ethylene oxide) (PEO) *via* anionic

polymerisation.^[20] Tyramine is a phenol derivative with an aminoethyl group in para position. Deprotonating the hydroxy group should lead to initiation only at this group, resulting in a PBO containing an initial amino group and a secondary hydroxy end group. The latter one can be quantitatively functionalised with DETA as had been tested in prior experiments. For this reaction, the hydroxy end group is activated by 1,1'-carbonyldiimidazole (CDI) and then coupled with one of the amino groups of DETA. However, the tyramine amino group at the other chain end would react with CDI as well and prevent a selective functionalisation of both chain ends. Therefore this method was not considered. As an alternative to DETA, a phosphonic acid head group was taken into consideration. For this we chose an already tested synthesis route which was originally developed by Köhler *et al.*^[21,22] Here, the phosphonic acid is attached *via* the deprotonation of an OH group and a following oxa-Michael addition using diethyl vinylphosphonate (DEVP). As this compound is well-known to also react with amino groups in an aza-Michael reaction^[23,24], the amino group of tyramine has to be functionalised with thymine before introducing the phosphonate.



Scheme 8.2 First synthesis attempt towards supramolecular ligands using a tyramine initiator. Deprotonation was done via a) the phosphazene base $t\text{BuP}_4$ or b) potassium *tert*-butoxide KOtBu .

For the polymerisation reaction two routes were chosen to deprotonate the hydroxyl group of tyramine using a) the phosphazene base 1-*tert*-butyl-4,4,4-tris(dimethylamino)-2,2-bis[tris(dimethylamino)-phosphoranylideneamino]-2 λ^5 ,4 λ^5 -catenadi(phosphazene) ($t\text{BuP}_4$) and b) potassium *tert*-butoxide (KOtBu) together with the crown ether 18-crown-6 (18C6). Both polymerisation reactions were performed at room temperature in toluene. Higher temperatures as well as the use of other solvents like tetrahydrofuran (THF) cause significant side reactions during the polymerisation. The phosphazene base was used originally for polymerising ethylene oxide with tyramine^[20] and Misaka *et al.* successfully used the phosphacene base in combination with different alcohol initiators for polymerising butylene oxide.^[25] The initiator formed by the $t\text{BuP}_4$ option was soluble, and the reaction was done at room temperature according to the literature procedures. The SEC measurement of the polymer revealed two peaks and in addition a higher molecular weight fraction, indicating initiation at both ends of tyramine (Figure 8.2). Amino groups, especially primary ones, are known to act as nucleophilic centres being able to

perform the ring opening of alkylene oxides.^[26] To avoid this, highly reactive alcoholates are needed for example potassium alcoholates.^[26] Although the combination of tyramine and *t*BuP₄ was successfully used for PEO in THF, it was not a suitable initiator for PBO in toluene.

The potassium salt of tyramine, obtained from the reaction with KO*t*Bu, was not completely soluble neither in THF nor toluene. The polymerisation resulted in a rather high polydispersity ($M_w/M_n = 1.15$). The SEC measurement (Figure 8.2) reveals a strong tailing at lower molecular weights. The reason for that is the low solubility of the initiator and therefore a long initiation period.

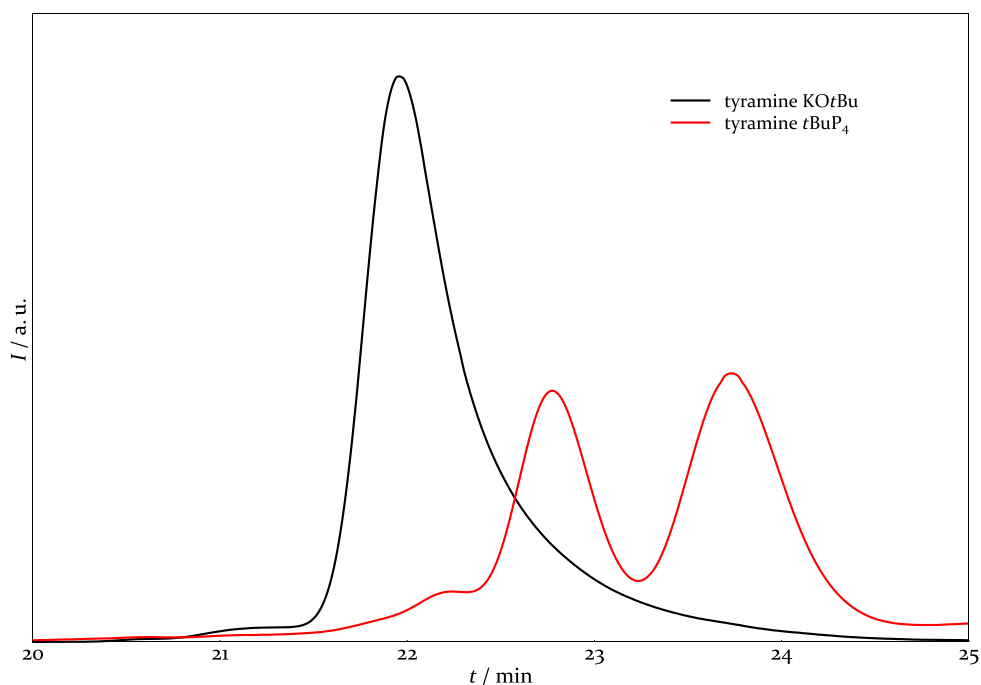
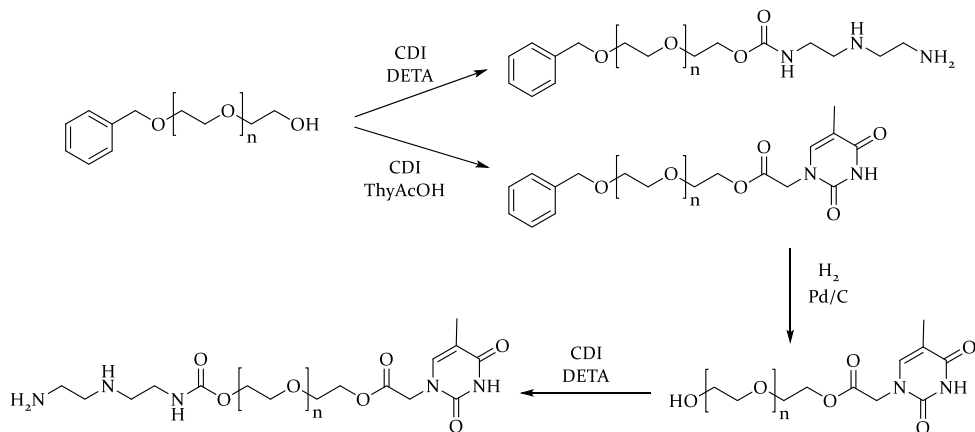


Figure 8.2 SEC traces of PBO initiated with tyramine.

Because of the significantly better result for the KO*t*Bu activation procedure, the polymer resulting out of this process was used for tests regarding further functionalisation. A part of the polymer was used to introduce the Thy group *via* the formation of an amide bond with the commercially available thymine-1-acetic acid (ThyAcOH) and another part of it was used to introduce a phosphonate moiety. In addition to the absence of amino groups, the phosphonic acid shows an increased affinity towards the iron oxide surface.^[27] While thymine could be successfully attached to the amino end group, no reaction could be observed between

the deprotonated secondary alcohol end group and diethyl vinylphosphonate. In addition to the unsatisfying result of the polymerisation, tyramine was not considered as a suitable initiator.

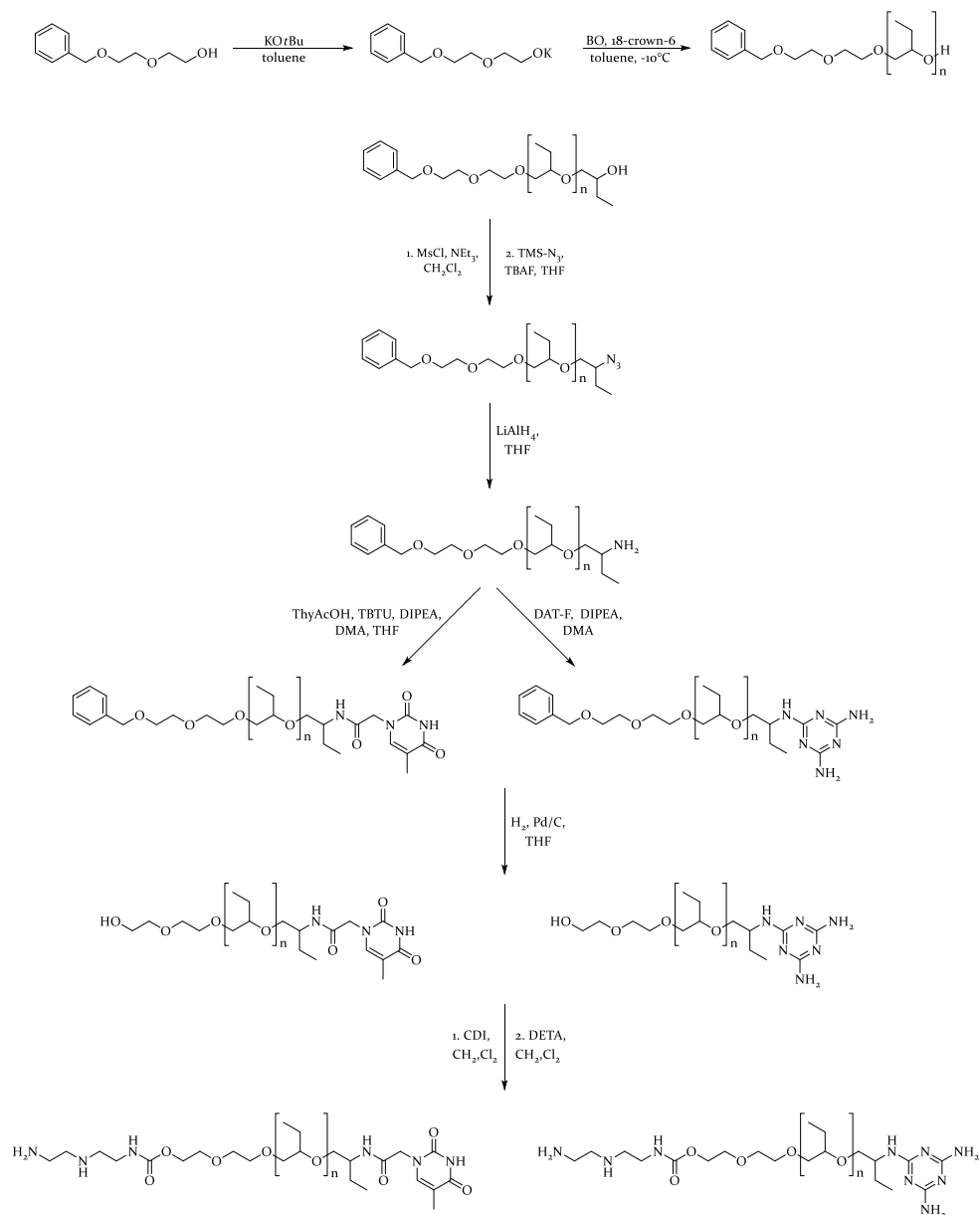


Scheme 8.3 Second approach towards supramolecular PBO ligands.

In the second approach to obtain the α,ω -functionalised PBO, a diol initiator was used where one hydroxy group was protected using a benzyl ether initiator. The benzyl group can be removed later by hydrogenation. In first feasibility tests, the functionalisation of an already existing polymer with such an end group was tested: Bn-PEO20k-OH. This polymer could successfully be functionalised with either the Thy (Bn-PEO20k-Thy) or a DETA functionality (Bn-PEO20k-DETA). DETA was chosen instead of the phosphonic acid because of the previously described difficulties in functionalising PBO with this ligand. Only Bn-PEO20k-Thy was used for further functionalisation. The successful hydrogenation yielded HO-PEO20k-Thy which was then reacted with CDI and DETA to obtain the target molecule DETA-PEO20k-Thy. The product showed a loss of 75 % of Thy functionality, most likely due to a cleavage of the ester bond between Thy and the polymer by DETA. Therefore, we chose to connect thymine *via* a more stable amide group for the next step.

In this synthesis route PBO is equipped with a benzyl ether and a secondary hydroxy end group. The hydroxy end group can then be transformed into an amino group *via* an azide intermediate. Reacting the amino group with ThyAcOH leads to one of the desired supramolecular functionalisations.^[B] To obtain the DAT functionality, a new procedure was applied including 2-fluoro-4,6-diamino-1,3,5-triazine (DAT-F). Cleaving the benzyl group yields a primary hydroxy end group that can be converted to a DETA head group as shown before.^[28] The whole procedure is displayed in Scheme 8.4.

8 Synthesis and Characterisation of Polymer Coated Supramolecular Magnetic Nanocrystals



Scheme 8.4 Synthesis route towards supramolecular PBO ligands.

To synthesise PBO with a benzyl ether functionality, benzyl alcohol was reacted with potassium metal. Although the deprotonation was possible, the alcoholate proved to be insoluble in toluene. Di(ethylene glycol) benzyl ether was chosen as the initiator instead due to its higher solubility arising from the two ethylene glycol moieties. Polymerisation at -10°C in

the presence of 18C6 resulted in the desired polymer. SEC reveals a M_n of 4990 g/mol and a narrow molecular weight distribution of 1.01 (Figure 8.3 and Table 8.4).

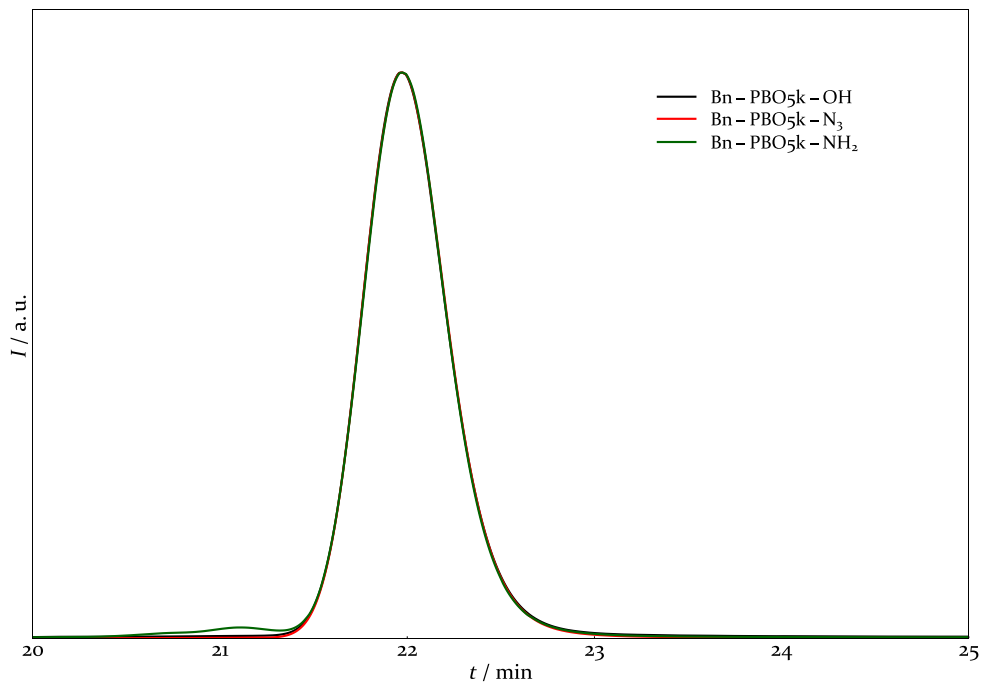


Figure 8.3 SEC trace of Bn-PBO5k-OH, Bn-PBO5k-N₃ and Bn-PBO5k-NH₂.

The ¹H NMR spectra of the so obtained polymer (Bn-PBO5k-OH) in pyridine-d₅ can be seen in Figure 8.4. The CH₂ unit of the benzyl group was chosen as the reference signal. To calculate the molecular weight, the signal for the polymer backbone (including the ethylene glycol protons) was used, resulting in a polymerisation degree of 63.6 monomer units and a molecular weight of 4760 g/mol. The other signals of the benzyl group can be found in the aromatic region between two of the pyridine peaks. The position of the single proton coincides with a satellite of one of the pyridine protons. At 5.66 ppm, the proton signal of the secondary hydroxy group can be found. The ratio between the intensity of the hydroxy proton and the reference signal revealed quantitative functionalisation within the error bars of this method.

In the next step, the secondary hydroxy group was converted into an azide group by first introducing a mesylate function to create a good leaving group which was then replaced by an azide functionality. The signal of the hydroxy proton has vanished in the resulting NMR spectrum but due to the mesylation beforehand, complete functionalisation cannot be

determined in this step. The signal of the CH-proton of the last BO unit moved from 4.00 ppm (signal 21) in Bn-PBO5k-OH into the PBO signal between 3.35-4.05 ppm.

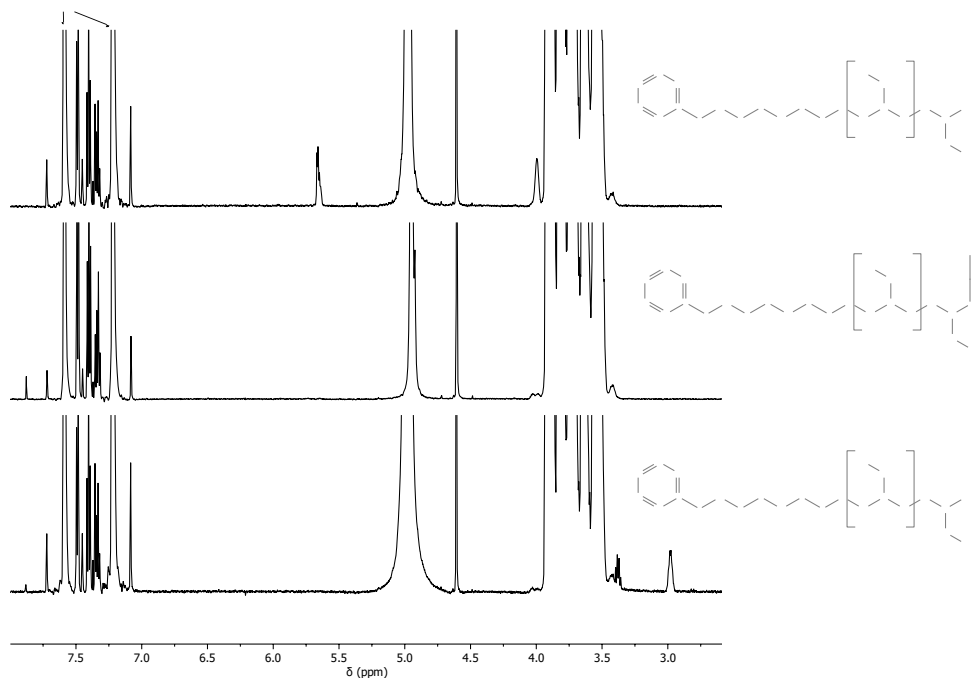


Figure 8.4 NMR spectra of Bn-PBO5k-OH, Bn-PBO5k-N₃ and Bn-PBO5k-NH₂ in pyridine-d₅ (from top to bottom).

The functionalisation degree of the final product could be determined after the azide group was reduced to an amino group using lithium aluminium hydride (LiAlH₄). In case of incomplete functionalisation of the hydroxy group, the alkaline conditions during the removal of the excess LiAlH₄ would cleave any remaining mesylate groups. No trace of the hydroxy proton could be found in the NMR spectrum of Bn-BPO5k-NH₂ (Figure 8.4). Instead, the signal of the C-H proton next to the amino group appeared at 2.98 ppm. The ratio of the intensities between this signal and the reference signal of the CH₂-protons from the benzyl group showed 97 % functionalisation. SEC analysis reveals 1 % of coupling product.

The amino end group was used to attach either Thy or DAT to the polymer (Scheme 8.4). The Thy group is introduced using ThyAcOH as described before. The signal of the methine proton next to the amino group therefore shifts to 4.38 ppm (Figure 8.5). Due to the ThyAcOH coupling, three new signals appear in the NMR spectrum: the methyl protons at 1.93 ppm, the CH₂-group of the acid which is split into two doublets at 4.59-4.62 and 4.86-4.92 ppm and the proton of the methine carbon inside the ring at 7.48 ppm which overlaps with

two of the benzyl protons. Additionally, there is a signal of the amide proton at around 8.9 ppm. These Thy signals are difficult to evaluate due to their overlapping with neighbouring signals. The absence of the methine signal from the amino group as well as the comparison between the signals introduced by the Thy group, especially the new methine signal (21) and the reference signal revealed 99 % of functionalisation with Thy.

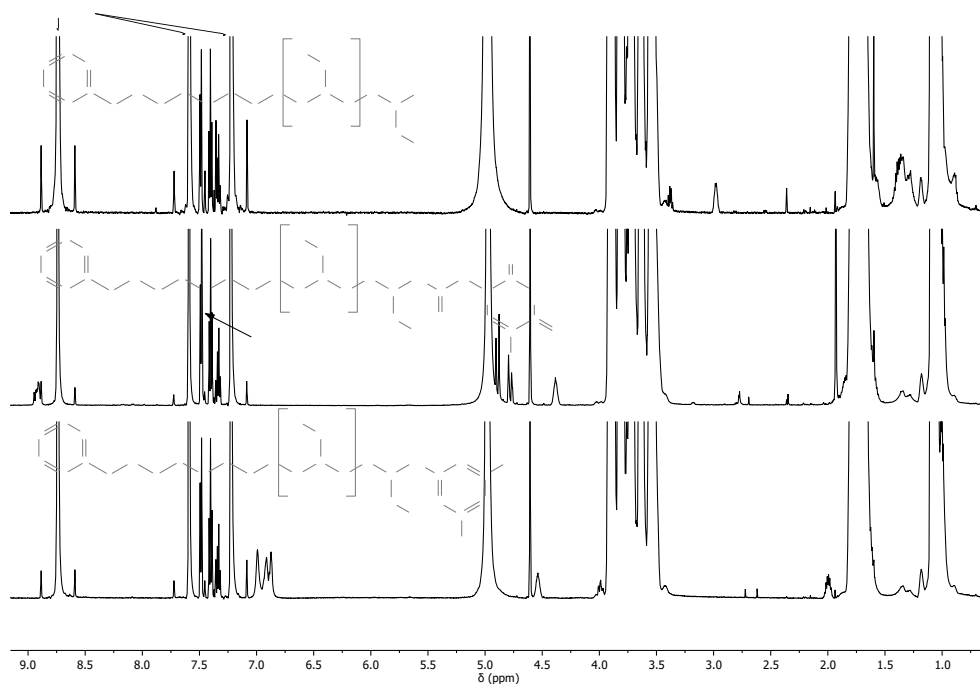


Figure 8.5 NMR spectra of Bn-PBO5k-NH₂, Bn-PBO5k-Thy and Bn-PBO5k-DAT in pyridine-d₅ (from top to bottom).

For the DAT coupling, DAT-Cl is known to bind to amino end-groups of polymer chains via nucleophilic aromatic substitution (S_NAr)^[29]. In this work, DAT-F was used instead of DAT-Cl. The chlorine equivalent is commercially available, however, it lead to about 5 % of chain-coupling in earlier studies.^[13] Due to fluoride being a better leaving group than chlorine the reactivity of DAT-F in a S_NAr is increased. Therefore, a lower reaction temperature of 70 °C instead of 100 °C could be used in the reaction to reduce the amount of coupling product. SEC analysis revealed 1 % of coupled chains after the reaction. A functionalisation degree of 94 % could be obtained from NMR spectroscopy by comparing the signal of the methine proton (signal 21) and the reference signal. Between 6.80 and 7.1 ppm, the signal of the amino protons (22, 31, 32) can be found.

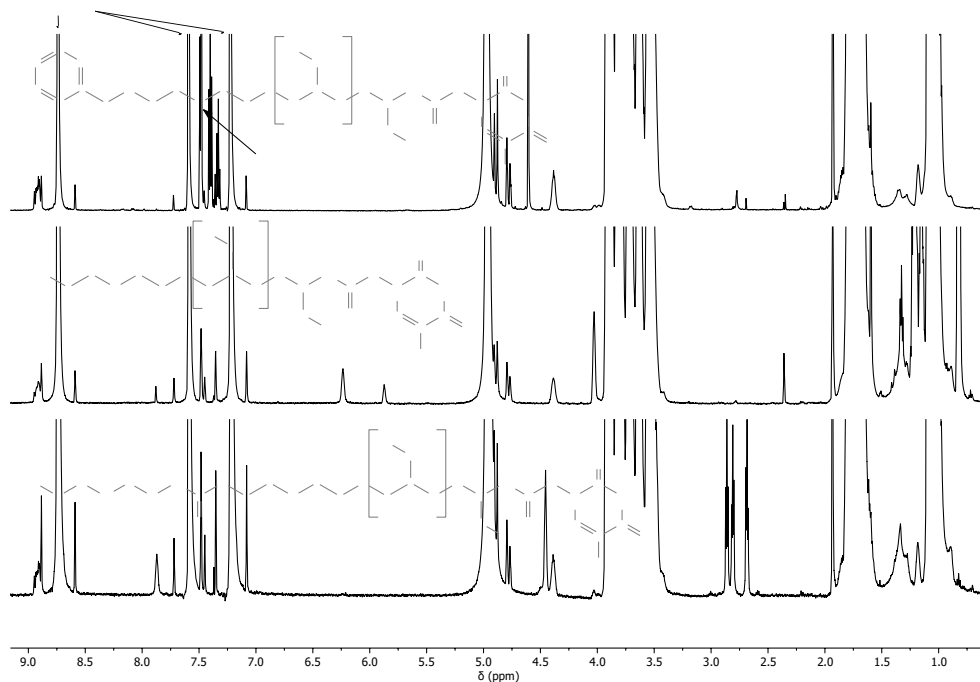


Figure 8.6 NMR spectra of Bn-PBO5k-Thy, HO-PBO5k-Thy and DETA-PBO5k-Thy in pyridine- d_5 (from top to bottom).

To cleave the benzyl group, hydrogenation with a Pd/C catalyst was used. After two hours the completion of the reaction for Bn-PBO5k-Thy could be determined *via* NMR spectroscopy. The signal at 4.61 ppm of the CH₂ protons from the benzyl group (signal I) disappeared completely (Figure 8.6). For Bn-PBO5k-DAT, the cleavage was not complete after the same time. Even after five hours in total, a signal from the benzyl group remained, indicating 11 % of remaining benzyl functionality (Figure 8.7). A possible reason is the high interaction between the catalyst and the supramolecular group. Removal of the catalyst also turned out to be more difficult than in prior reactions for example for Bn-PEO-Thy where simple mixing with Celite and separation *via* centrifugation was enough. Here, the catalyst had to be removed *via* filtration through silica. Ethanol was chosen as solvent for this procedure as a polar solvent reduces the interactions between silica and the polymer. The catalyst stuck to the column material and could be separated from the product. The signal of the CH₂-unit next to the hydroxy group now resides very close to the polymer backbone, which makes the NMR analysis more difficult (Figure 8.6 and Figure 8.7). Semi-quantitative analysis of the Thy and DAT signals showed no reduction of the double bonds in Thy or DAT.

The head group DETA was added in two steps. First, the polymer was mixed with CDI to functionalise the hydroxy group, yielding an acylimidazole derivative. The usual procedure

involves a high excess of CDI^[28] and was also employed for HO-PBO5k-Thy as the amino group of thymine is very electron poor due to the electron withdrawing nature of the neighbouring carbonyl groups. SEC analysis revealed 24 % of higher molecular weight fractions. This arises from chain coupling due to more than one polymer chain binding to one DETA molecule.

As the DAT group carries two primary amino groups, a reaction between these amino groups and CDI is a possibility. There is no equivalent reaction described in the literature, though there are some that show similarities to the reactants used in this work. Aniline can be coupled *via* CDI in a simple reaction.^[30] 2-Amino pyrimidine is deprotonated by a strong non-nucleophilic base and reacts with a secondary amino group which was activated prior to this by CDI.^[31] A *tert*-butyloxycarbonyl protecting group is introduced to an amino group of a triazine derivative *via* CDI.^[32] Another procedure reports the coupling of N²-(4-aminobutyl)-1,3,5-triazine-2,4,6-triamine *via* CDI but only the aliphatic amino group reacted in this process.^[33]

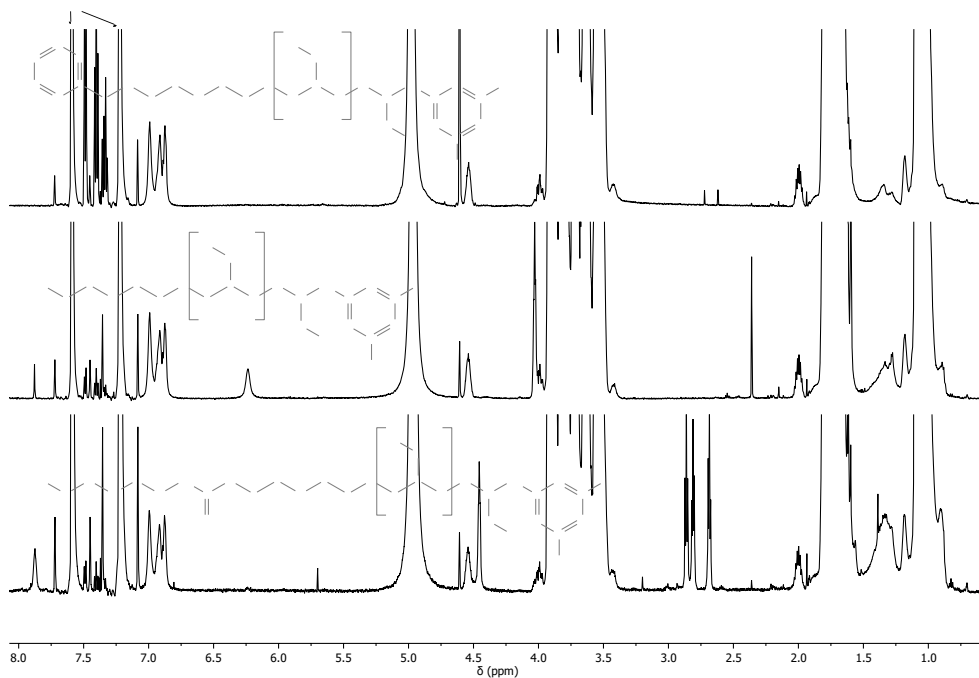


Figure 8.7 NMR spectra of Bn-PBO5k-DAT, HO-PBO5k-DAT and DETA-PBO5k-DAT in pyridine-*d*₅ (from top to bottom).

Therefore, only a small excess of CDI should be used to avoid side reactions of the DAT amino groups. To prove that the small excess of CDI is sufficient to provide a complete reaction of the hydroxy groups, HO-PEG2k-OH was used as testing material and successfully converted to the acylimidazole product. The full conversion of the hydroxy group of HO-PBO5k-DAT was

checked by isolating the acylimidazole intermediate for NMR spectroscopy. The spectrum shows no trace of the hydroxy proton. The CH₂ protons next to it are shifted to 4.62 ppm. Additionally, the signals of the imidazole ring can be observed. After the second step of the reaction, the NMR spectrum revealed complete conversion of the HO-PBO5k-DAT to the target molecule DETA-PBO5k-DAT. SEC analysis showed 6% of coupled chains.

8.2.2 Nanocomposites and self-assembly

Iron oxide nanocrystals (NCs) in two different sizes were chosen for the nanocomposite samples. The NCs were characterised *via* SAXS and TEM measurements (Figure 8.8 & Figure 8.9).

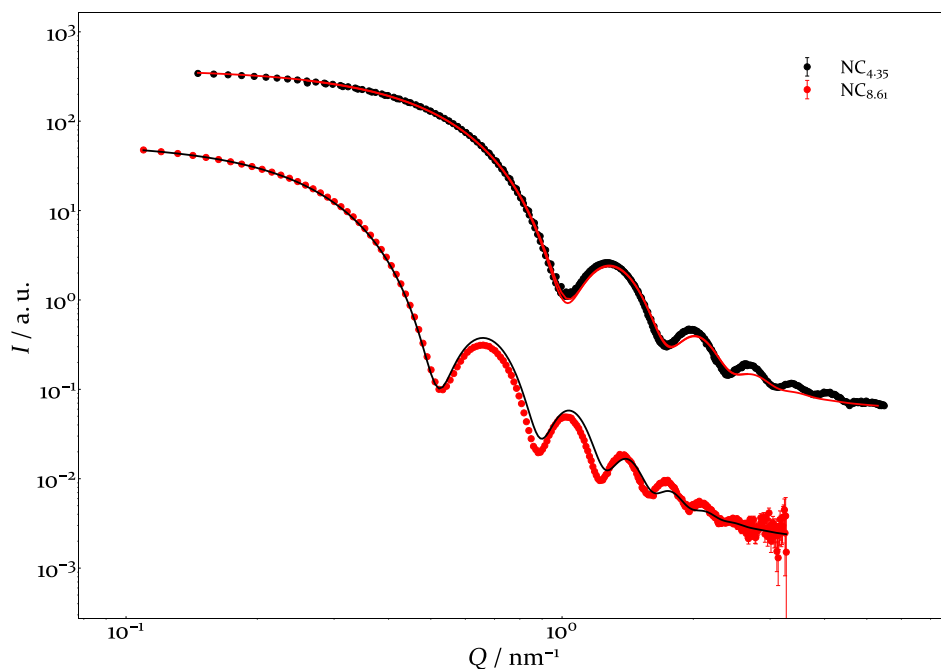


Figure 8.8 SAXS data of oleic acid coated NCs. The Solid lines represent the fit with the polydisperse sphere form factor.

For SAXS, a polydisperse sphere with a normal distribution for the radius of the NC was used to describe the data. This model describes the smaller NCs very well but deviates from the data of the larger NCs. This is due to a high fraction of the NCs which are not sufficiently spherical, as can be seen in Figure 8.9.

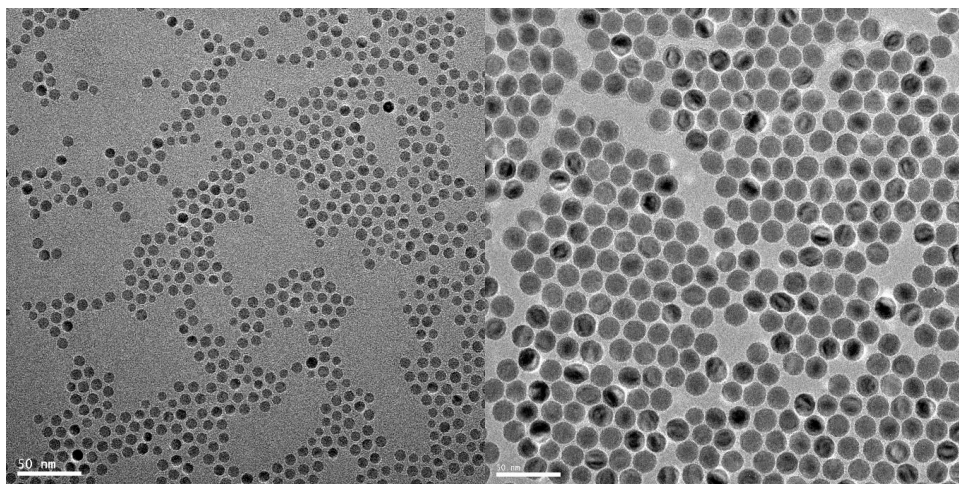


Figure 8.9 TEM images of $NC_{4.35}$ and $NC_{8.61}$ coated by oleic acid in the dried state.

The determined radii can be found in Table 8.1. The values obtained by SAXS and TEM coincide nicely within the estimated error bars.

Table 8.1 Radii of the NCs as determined from TEM and SAXS with their respective standard deviations.

	R_{SAXS} [nm]	R_{TEM} [nm]
$NC_{4.35}$	4.35 ± 0.35	4.07 ± 0.40
$NC_{8.61}$	8.61 ± 0.52	8.66 ± 0.62

Nanocomposites were prepared *via* ligand exchange of the synthesised polymer ligands DETA-PBO5k, DETA-PBO5k-Thy and DETA-PBO5k-DAT against the native oleic acid. For the used amounts of NCs and ligands, a maximum grafting density GD_{max} of 1 nm^{-2} was calculated. Interestingly, the time it takes for the dissolution of the supramolecular coated NCs after the purification step is much higher than for the NCs coated with DETA-PBO5k. This indicates additional interaction between the supramolecular NCs. Toluene was chosen as a solvent as its low polarity is beneficial for the interactions between Thy and DAT.^[34]

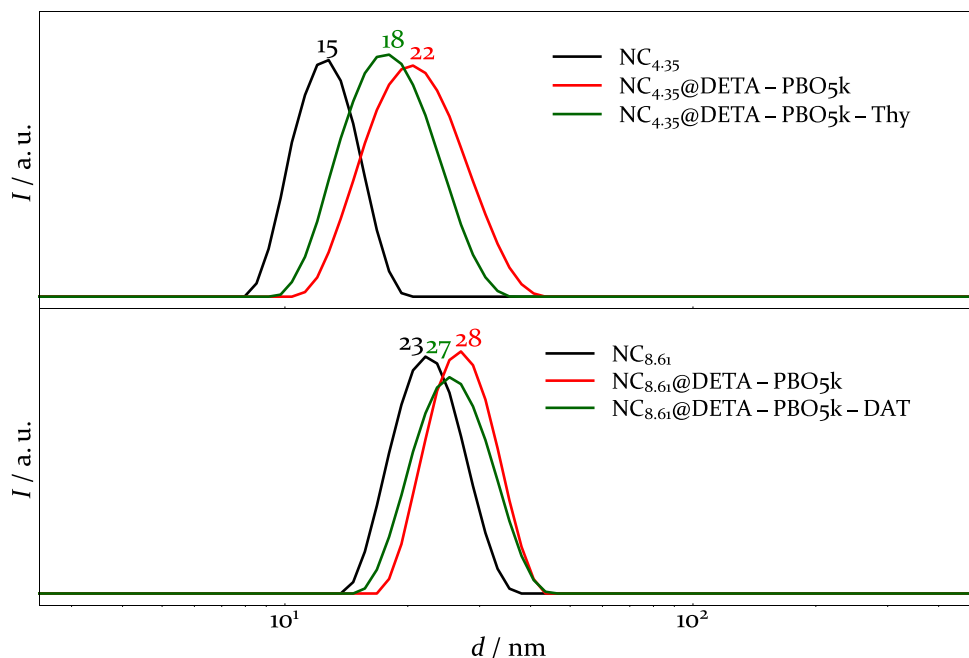


Figure 8.10 DLS measurements to confirm the successful ligand exchange.

The ligand exchange was checked *via* DLS (Figure 8.10). The increase of the hydrodynamic diameter confirms the successful ligand exchange. The hydrodynamic diameter of the non-supramolecularly functionalised NCs are larger than those of the Thy or DAT-containing samples. This indicates a higher grafting density for the non-supramolecularly functionalised NCs. TGA experiments were performed for a more precise study of this phenomenon (Figure 8.11 TGA curves of polymer coated NCs. Figure 8.11).

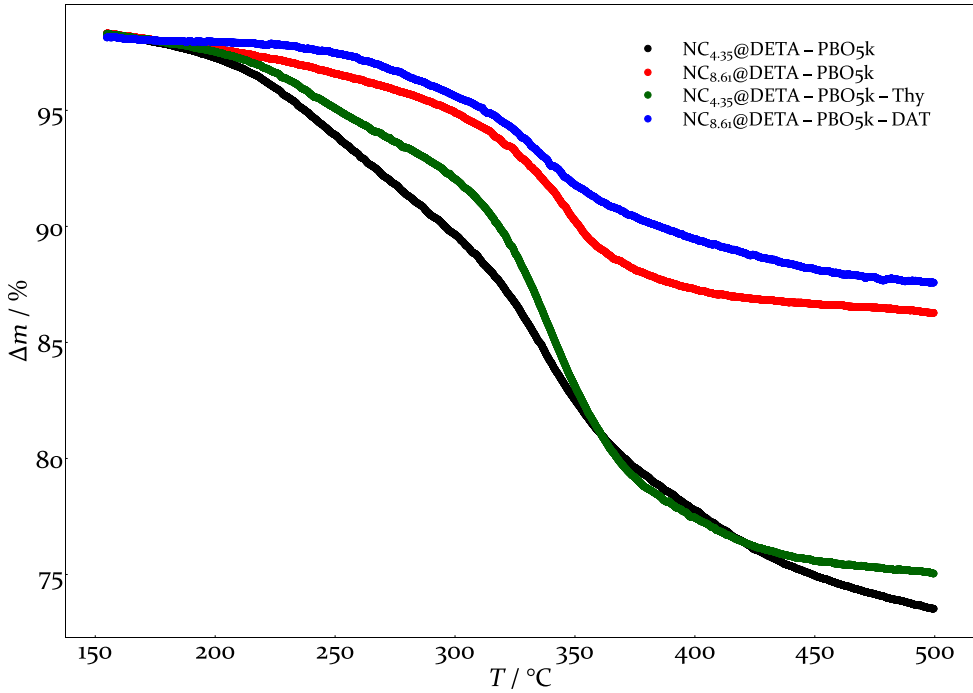


Figure 8.11 TGA curves of polymer coated NCs.

Assuming the measured mass loss to be equivalent to the polymer mass fraction, the grafting density GD can be calculated:

$$GD = \frac{\rho_{NC} N_A r_{NC} \Delta m}{3M_{polymer}(\Delta m - 100)} \quad (8.1)$$

with $\rho_{NC} = 5.2 \text{ g/cm}^3$ the density of magnetite, Fe_3O_4 ^[35], N_A the Avogadro constant, r_{NC} the radius of the NC, Δm the mass loss measured by TGA and $M_{polymer}$ the molar mass of the polymer ligand. The measured mass losses, the number of polymer ligands per NC and the resulting GD s are displayed in Table 8.2.

Table 8.2 TGA analysis.

sample	Δm [%]	$M_{n,polymer}$ [g/mol]	ligands / NP	GD_{TGA} [nm ²]	$t_{polymer}$ [nm]
NC _{4.35} @DETA-PBO5k	24.79	5070	70.19	0.30	1.72
NC _{4.35} @DETA-PBO5k-Thy	23.26	5340	61.28	0.26	1.61
NC _{8.61} @DETA-PBO5k	12.04	5070	226.07	0.24	1.69
NC _{8.61} @DETA-PBO5k-DAT	10.56	5770	171.37	0.18	1.49

Indeed, the GDs of the DETA-PBO5k samples are higher than their respective supramolecular counterparts. The obtained GDs are rather low compared to the desired value of 1 nm². Possible reasons are the high amount of coupled chains of the polymer ligand, especially for DETA-PBO5k and DETA-PBO5k-Thy (see Table 8.4 in the Supporting Information), which are sterically disadvantaged to attach to the iron oxide surface. For DETA-PBO5k-DAT, the amount of coupled chains is much smaller but the incomplete removal of the initiator results in about 10 % of polymer chains without DETA functionality which cannot attach to the NC surface. Assuming compact polymer shells, an approximate value for the shell thickness can be calculated.

Each solution of ligand exchanged NCs was checked for particle agglomeration by SAXS (Figure 8.12). All datasets could be described by a polydisperse spherical form factor, revealing no signs of agglomeration.

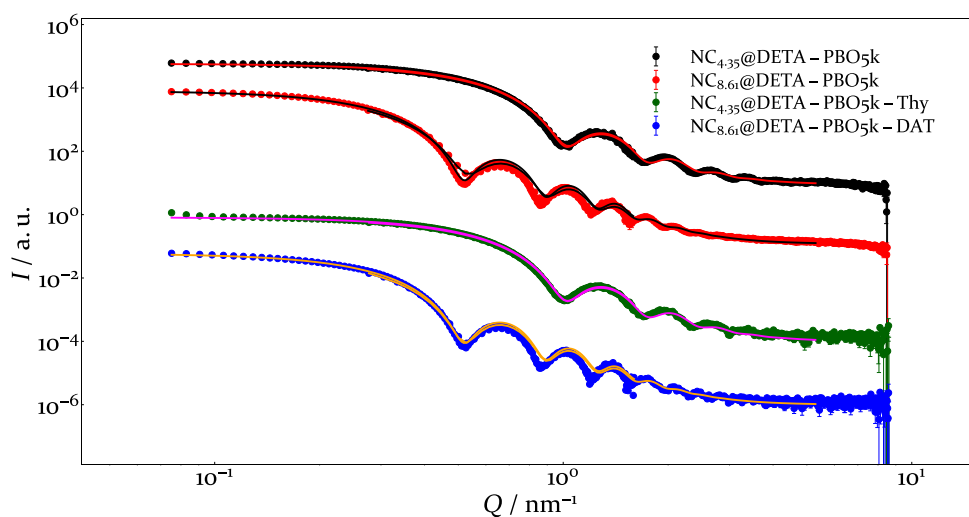


Figure 8.12 SAXS data of NCs after ligand exchange (solid lines represent the fits for the data)

Four samples were created by mixing small and large NCs carrying polymer ligands (Table 8.3). First, the non-supramolecularly functionalised NCs were used and mixed in NC ratios of 1 : 6.5 and 1 : 33 as reference material. The small Thy and large DAT functionalised NCs were mixed with the same ratios. Considering the obtained radii and calculated shell thicknesses gives a maximum amount of about 22 small NCs can stick to the surface of one large NC. Due to the different number of supramolecular groups per NC, the ratio between DAT and Thy groups in the mixtures do not coincide with the NC ratios, resulting in ratios DAT : Thy of 1 : 2.3 and 1 : 11.8 for PBO-ThyDAT_{1:6.5} and PBO-ThyDAT_{1:33} respectively.

Table 8.3 Mixture samples

sample	NC	polymer ligand	NC ratio
PBO _{1:6.5}	NC _{4.35}	DETA-PBO5k	1 : 6.5
	NC _{8.61}	DETA-PBO5k	
PBO _{1:33}	NC _{4.35}	DETA-PBO5k	1 : 33
	NC _{8.61}	DETA-PBO5k	
PBO-ThyDAT _{1:6.5}	NC _{4.35}	DETA-PBO5k-Thy	1 : 6.5
	NC _{8.61}	DETA-PBO5k-DAT	
PBO-ThyDAT _{1:33}	NC _{4.35}	DETA-PBO5k-Thy	1 : 33
	NC _{8.61}	DETA-PBO5k-DAT	

The NCs of the sample PBO-ThyDAT_{1:33} precipitated after a few hours while all other samples remained stable. All samples were investigated *via* SAXS (Figure 8.13). For PBO-ThyDAT_{1:33} the precipitated NCs were measured while for all other samples their solution was used for the measurement.

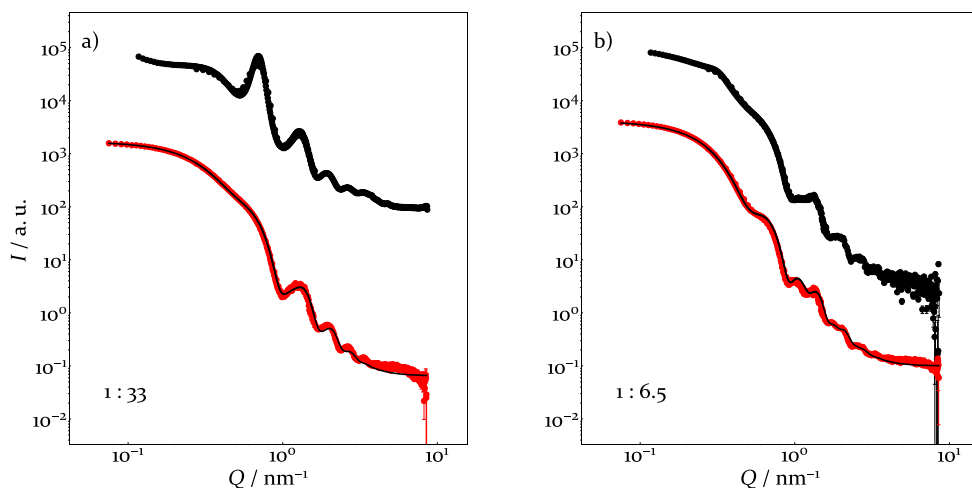


Figure 8.13 SAXS data of NC mixtures. a) Ratio of 1 : 33, b) ratio 1 : 6.5. Black curves are the supramolecular samples, red curves represent the NCs with simple PBO ligands, solid line: fit.

The data of the NCs coated with DETA-PBO5k were fitted with a model consisting of the sum of two polydisperse spherical form factors with different fractions φ :

$$I(Q) = \varphi_{4.35} \cdot P_{4.35}(Q) + (1 - \varphi_{4.35}) \cdot P_{8.61}(Q) \quad (8.2)$$

For PBO_{1:33}, a fraction of 0.953 of the smaller NCs was determined and for PBO_{1:6.5} a fraction of 0.795 corresponding to a ratio of 1 : 20.4 for PBO_{1:33} and 1 : 3.9 for PBO_{1:6.5}. This is a good agreement to the targeted ratios, especially if the non-trivial concentration determination of the original NC solution is considered. The data of the supramolecular mixtures differentiate from the non-supramolecular samples and therefore could not be described by this simple model. As can be seen in Figure 8.13a, for PBO-ThyDAT_{1:33} a peak can be found at 0.69 nm⁻¹ which corresponds to 9.11 nm in real space. This value indicates that a lot of the smaller NCs are close to each other as it is only a little higher than their diameter due to the polymer shell. The slope at the lowest Q values hints at larger structures being present which makes sense as the NCs precipitated due to agglomeration. For PBO-ThyDAT_{1:6.5} (Figure 8.13b), the most significant features are the slope at low Qs which can be described by a power law of $Q^{-0.8}$, indicating small linear agglomerates and the lack of the pronounced double peak at 1.0 and 1.3 nm⁻¹. A reason for the latter are interference cross-terms changing the form of the scattering curve. In addition, the sharp kink at 0.32 nm⁻¹ represents a distance of 19.63 nm. This is just 2.41 nm more than the centre-to-centre distance between two large NCs but 6.67 nm more than between a large and a small NC. The thickness of the polymer shell cannot be determined from SAXS measurements, but for a polymer ligand with a molecular weight of around 5000 g/mol a value between those

two numbers is reasonable. A mixture of large-large and large-small combinations is thus the logical reason for this peak.

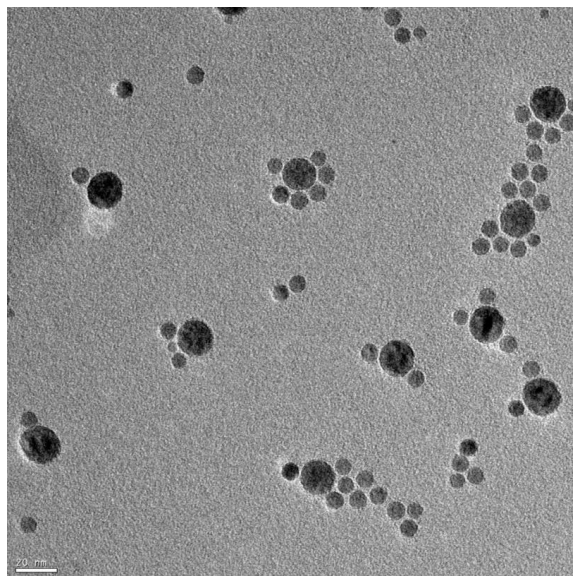


Figure 8.14 TEM image of PBO-ThyDAT_{1.6.5}

Additionally, TEM images were taken of the sample PBO-ThyDAT_{1.6.5}. The structures that can be seen in Figure 8.14 indicate ordering of the NCs. Several small NCs attach to the large NCs. In addition, the smaller NCs tend to form clusters between each other as well. This finding implies preferred supramolecular Thy-DAT and Thy-Thy interactions.

The formation of bonds between Thy and DAT in solution is favoured compared to the homo-association due to the higher association constant.^[34,36] However, the behaviour in the melt state is different. For polymer melts different preferences are found depending on the polymers used in the studies.^[36-38]

8.3 Conclusion and Outlook

A new synthesis route was developed for the polymer ligands DETA-PBO5k-Thy, DETA-PBO5k-DAT and DETA-PBO5k. The synthesis of the supramolecular ligands used a protected

initiator to introduce the α,ω -functionality of ligand head group and supramolecular group. Each synthesis step was investigated *via* NMR spectroscopy as well as SEC, revealing functionalisation degrees above 90 %. The native oleic acid was replaced by the polymer ligands to coat the iron oxide NCs with a polymeric shell. SAXS measurements revealed ordering effects of the supramolecular ligands with a preference for the Thy-DAT and Thy-Thy association if large DAT functionalised NCs were mixed with small Thy functionalised NCs.

To obtain more detailed information, a model needs to be developed to describe the attachment of the NCs to each other. An existing model on the basis of simple ordering of the smaller NCs around a large NC exists but does not correctly describe the data as the homo-associations are non-negligible in our samples. This needs to be represented in the model which complicates the calculations.

A higher excess of polymer ligand might improve the result for the grafting density. In addition, another ligand head group like a phosphonic acid could be used to avoid the chain coupling and increase the affinity for the iron oxide surface. An easier replacement for DETA could be pentaethylenehexamine (PEHA) with up to five free amino groups to connect to the iron oxide surface instead of two for DETA. Chain coupling of PEHA at both primary amino groups would then still allow the connection of four amino groups to the NC. The coupling reaction between DETA and PEHA could be improved by a more controlled addition of the polymer solution to the amine for example *via* a syringe pump (this could not be done here due to the small amount of the material).

The combination of the supramolecular NC and supramolecularly functionalised linear polymers like DAT-PBO-DAT or Thy-PBO-Thy could be used to compare the influence of the NC on the system for example with star polymers. In addition, the iron oxide NCs introduce the response to an external field to the system, which could be exploited towards anisotropic material properties. In addition, the interaction of Thy- or DAT-functionalised NCs and nucleotides could be interesting towards an efficient magnetic extraction system for nucleotides or even DNA as has been shown by studies on larger particles.^[39]

8.4 Materials and Methods

8.4.1 Nanocrystal synthesis

Materials. Iron(III) chloride hexahydrate (Merck, $\geq 99.0\%$), sodium oleate (TCI, $>97.0\%$), *n*-heptane (Merck, 99%), ethanol (Merck, 96%), oleic acid (Aldrich, 90%), 1-octadecene (Merck, $\geq 91.0\%$), tetrahydrofuran (THF) (Merck, $\geq 99.0\%$) and acetone (Merck, $\geq 99.5\%$) were used as received.

Synthesis. The iron oxide nanocrystals were synthesised according to a procedure by Park et al.^[9] The smaller nanocrystals (4.34 nm) were taken from an older batch, given to me by Dr. Sascha Ehlert. For the larger nanocrystals (8.55 nm) 37 g of iron oleate were obtained by reacting iron(III) chloride hexahydrate (10.93 g) and sodium oleate (36.97 g) in a mixture of *n*-heptane (140 ml), ethanol (80 ml) and water (60 ml) at 70 °C for four hours. The phases were separated and the organic phase was washed with water. The iron oleate was mixed with 11.3 g of oleic acid and 200 ml of 1-octadecene. The heating rate was 2 K/min and the temperature was held at 320 °C for 30 minutes. The solution was diluted with THF and around 1 l of acetone were added to precipitate the nanocrystals. After decanting the solvent, the nanocrystals were dissolved in 200 ml of THF and 400 ml of acetone were added to precipitate the nanocrystals again. The nanocrystals were isolated by centrifugation, dissolved in THF and stored in a fridge.

8.4.2 Polymer synthesis

General procedures. All manipulations were carried out at a high vacuum line or in a glove box filled with Argon (M Braun, Unilab). The water level in the glove box was below 1 ppm and the oxygen level below 0.1 ppm. The flasks for all manipulations were equipped with Teflon stopcocks (Young® or Gebr. Rettberg GmbH), which allowed the transfer of materials between the vacuum line and glove box without contamination with air. The flasks that were exposed to overpressure were pressure-tested to 4-12 bar depending on the size of the flask.

Materials. Toluene (Merck, 99.9%) was degassed, distilled into another flask which contained sodium metal, stirred over the sodium for at least 24 hours before being degassed

again and heated to 110-115 °C for 3-4 hours. Triethylamine (Sigma-Aldrich, ≥99%) was degassed and distilled into a flask containing solvent-free *n*-butyllithium. Tetrahydrofuran (THF) (Sigma-Aldrich, ≥99.9%) was degassed and distilled into a flask containing potassium metal and benzophenone. Dichloromethane (Sigma-Aldrich, ≥99.9%) was dried over molecular sieve (4 Å) for 2 days. After the drying procedures the solvents were distilled into storage flasks equipped with Teflon stopcocks. Di(ethylene glycol) benzyl ether (Sigma-Aldrich, 97%) was degassed prior to use. 1,2-Butylene oxide (BO) (Aldrich, 99%) was degassed and stirred twice over calcium hydride (CaH₂) for several days. Crown ether 18-crown-6 (18C6) (Sigma-Aldrich, 99%) was freeze dried with benzene prior to use under high vacuum conditions. Methanesulfonyl chloride (Fluka, ≥98%) was distilled into another flask without additional drying step. 2-Fluoro-4,6-diamino-1,3,5-triazine (DAT-F) was synthesised according to a literature procedure^[40]. Potassium *tert*-butoxide (KO*t*Bu) (Sigma-Aldrich 99.99%), acetic acid (Sigma-Aldrich ≥99.8%), methanol (VWR, ≥99.8%), THF (VWR, ≥99.5%), azidotrimethylsilane (Sigma-Aldrich, 95%), tetrabutylammonium fluoride (TBAF) solution (Sigma-Aldrich, 1.0 M in THF), Silica60 (Merck), Chloroform (VWR, ≥99.0%), lithium aluminium hydride solution (Sigma-Aldrich, 2.0 M in THF), *N,N*-dimethylacetamide (DMA) (Aldrich, ≥99.8%), *N,N*-diisopropylethylamine (DIPEA) (Sigma Aldrich, ≥99%), thymine-1-acetic acid (ThyAcOH) (Sigma Aldrich, 98%), *o*-(benzotriazole-1-yl)-*N,N,N',N'*-tetramethyluronium tetrafluoroborate (TBTU) (Sigma-Aldrich, ≥97%), *N,N*-dimethylformamide (DMF) (Sigma-Aldrich, 99.8%), palladium/charcoal activated (Pd/C) (Merck 10% Pd), Celite®535 (Sigma-Aldrich), ethanol (Merck, ≥99.9%) used as received, 1,1'-carbonyldiimidazole (CDI) (Aldrich, ≥97%), diethylenetriamine (DETA) (Aldrich, 99%), *n*-pentane (Sigma-Aldrich, ≥99%), magnesium sulfate (Merck, ≥99.5%) and hydrogen (Air Liquide, 99.999%) were used as received.

Synthesis of Bn-PBO5k-OH. 1.068 g (5.44 mmol) of di(ethylene glycol) benzyl ether was filled into a Schlenk flask and degassed under high vacuum. Inside a glove box, 0.568 g (5.06 mmol) KO*t*Bu and 15 ml of dry toluene were added to the flask. After stirring for 30 min an orange solution was obtained. The initiator was dried under high vacuum conditions at 60 °C for eleven days yielding a brown liquid. 1.338 g (5.06 mmol) of 18C6 and 20 g of dry toluene were added inside a glovebox. The pre-determined amount of BO (22.225 g, 308.21 mmol) was distilled into the reaction flask at the vacuum line. The dark brown solution was left for six days at -10 °C, after one day the viscosity had significantly increased. The reaction was terminated with 10 eq of acetic acid. The polymer was precipitated into a mixture of methanol and water (volume ratio 2 : 1) and washed twice with the same mixture. After drying under high vacuum

conditions 18.558 g of Bn-PBO5k-OH was obtained. ¹H-NMR (600 MHz, pyridine-d₅): 0.90-1.25 m (191 H), 1.50-1.95 m (127 H), 3.35-4.05 m (199 H), 4.59-4.62 s (2 H), 5.62-5.68 m (1 H), 7.31-7.36 m (1 H), 7.38-7.42 t (2 H), 7.47-7.50 d (2 H).

Synthesis of Bn-PBO5k-N₃. The functionalisation reaction to obtain Bn-PBO5k-N₃ was done according to a procedure described elsewhere^[13] with slight changes. After four days of reacting, half of the previously used amounts of azidotrimethylsilane and TBAF were added again to the flask to ensure complete functionalisation. In total, the reaction was stirred for seven days at 50 °C. The polymer was washed three times with a mixture of methanol and water (volume ratio 8 : 2). ¹H-NMR (600 MHz, pyridine-d₅): 0.90-1.25 m (190 H), 1.55-1.9 m (128 H), 3.35-4.05 m (198 H), 4.59-4.62 s (2 H), 7.31-7.36 m (1 H), 7.38-7.42 t (2 H), 7.47-7.50 d (2 H).

Synthesis of Bn-PBO5k-NH₂. The functionalisation reaction to obtain Bn-PBO5k-NH₂ was done according to a procedure described elsewhere^[13] with slight changes. The polymer was washed three times with a mixture of methanol and water (volume ratio 8 : 2). ¹H-NMR (600 MHz, pyridine-d₅): 0.90-1.25 m (200 H), 1.55-1.9 m (131 H), 2.94-3.02 m (1 H), 3.35-4.05 m (202 H), 4.59-4.62 s (2 H), 7.31-7.36 m (1 H), 7.38-7.42 t (2 H), 7.47-7.50 d (2 H).

Synthesis of Bn-PBO5k-Thy. The functionalisation reaction to obtain Bn-PBO5k-Thy was done according to a procedure described elsewhere^[13] with slight changes. Instead of DMF, DMA was used due to a better solubility of the polymer in DMA and the mixture was stirred for seven days at 40 °C. ¹H-NMR (600 MHz, pyridine-d₅): 0.90-1.25 m (189 H), 1.55-1.9 m (125 H), 1.90-1.94 m (3 H), 3.35-4.05 m (195 H), 4.34-4.43 m (1 H), 4.59-4.62 s (2 H), 4.75-4.81 m (1 H), 7.31-7.36 m (1 H), 7.38-7.42 t (2 H), 7.47-7.50 m (3 H), 8.89-8.95 m (1 H).

Synthesis of Bn-PBO5k-DAT. Bn-PBO5k-DAT was synthesised using 1.002 g of Bn-PBO5k-NH₂ (0.21 mmol) which was filled into a Schlenk flask together with 0.194 g (1.5 mmol) of DAT-F. After degassing, 70 µl of DIPEA and 3 ml of DMA were added inside a glovebox. The mixture was degassed and stirred for seven days at 70 °C. The reaction was terminated by removing the solvent under high vacuum, yielding a slightly pinkish product. The product was dissolved in *n*-pentane and the solid by-products were removed by centrifugation. The polymer was washed five times with a mixture of DMF and water (volume ratio 9 : 1) and dried under

high vacuum conditions. 1.014 g of product were obtained. $^1\text{H-NMR}$ (600 MHz, pyridine- d_5): 0.90-1.25 m (194 H), 1.55-1.9 m (128 H), 3.35-4.05 m (201 H), 4.48-4.58 s (1 H), 4.59-4.62 s (2 H), 6.80-7.04 (5 H), 7.31-7.36 m (1 H), 7.38-7.42 t (2 H), 7.47-7.50 d (2 H).

Synthesis of HO-PBO5k-Thy. HO-PBO5k-Thy was synthesised using 0.799 g of Bn-PBO5k-Thy (0.17 mmol). 0.259 g of Pd/C was filled into a Schlenk flask. The polymer was dissolved in 30 ml of THF and added to the catalyst. Hydrogen was added *via* a balloon and the reaction was stirred at room temperature. After two hours the hydration was complete. The solution was centrifuged to remove the solid parts of the catalyst. The dispersed catalyst was removed by column chromatography using ethanol as the solvent. After drying under high vacuum conditions, 0.639 g of product were obtained. $^1\text{H-NMR}$ (600 MHz, pyridine- d_5): 0.90-1.25 m (200 H), 1.55-1.9 m (130 H), 1.90-1.94 m (3 H), 3.35-4.05 m (195 H), 4.00-4.06 s (2 H), 4.34-4.43 m (1 H), 4.75-4.81 m (1 H), 6.20-6.26 s (1 H), 7.47-7.50 m (1 H), 8.89-8.95 m (1 H).

Synthesis of HO-PBO5k-DAT. HO-PBO5k-DAT was synthesised using 0.949 g of Bn-PBO5k-DAT (0.19 mmol) and the method described for HO-PBO5k-Thy. The reaction time was extended to five hours to achieve maximal functionality. 0.645 g of product were obtained. $^1\text{H-NMR}$ (600 MHz, pyridine- d_5): 0.90-1.25 m (198 H), 1.55-1.9 m (133 H), 3.35-4.05 m (201 H), 4.00-4.06 s (2 H), 4.48-4.58 s (1 H), 4.59-4.62 s (0.24 H), 6.20-6.26 s (1 H), 6.80-7.04 (5 H), 7.31-7.36 m (0.12 H), 7.38-7.42 t (0.21 H), 7.47-7.50 d (0.21 H).

Synthesis of DETA-PBO5k-Thy. DETA-PBO5k-Thy was synthesised using 0.625 g of HO-PBO5k-Thy (0.11 mmol). 0.414 g CDI (2.55 mmol) and 15 g of dry dichloromethane were added to the polymer in a Schlenk flask. The mixture was stirred over night. To remove unreacted CDI, the mixture was washed three times with 20 ml of water. After removal of the solvent, the polymer was dried under high vacuum conditions. In a glovebox, 0.404 g DETA (3.92 mmol) were dissolved in 10 g dry dichloromethane. The polymer was dissolved in 5 g dichloromethane and slowly poured into the flask containing DETA. The mixture was stirred over night. Most of the solvent was removed and the product was precipitated into a mixture of methanol and water (volume ratio 8 : 2). The polymer was washed with the same mixture and the solvent was removed. The polymer was dissolved in *n*-pentane to remove last small traces of the hydration catalyst *via* centrifugation and dried under high vacuum conditions to obtain 0.445 g of the product. $^1\text{H-NMR}$ (600 MHz, pyridine- d_5): 0.90-1.25 m (198 H), 1.55-1.9 m (131

H), 1.90-1.94 m (3 H), 2.65-2.72 m (2 H), 2.77-2.90 m (4 H), 3.35-4.05 m (201 H), 4.34-4.43 m (1 H), 4.42-4.52 m (2 H), 7.47-7.50 m (1 H), 8.89-8.95 m (1 H).

Synthesis of DETA-PBO5k-DAT. DETA-PBO5k-DAT was synthesised using 0.624 g HO-PBO5k-DAT (0.12 mmol) and the method described for DETA-PBO5k-Thy with slight changes. Only 1.5 eq of CDI were used to avoid the reaction between CDI and the amino groups of the DAT functionality. For the same reason, the reaction time between polymer and CDI was reduced to two hours. As the separation of the two phases was incomplete, the organic phase was dried with Magnesium sulfate to remove remaining water. In the end, 0.474 g of the product were obtained. ¹H-NMR (600 MHz, pyridine-d₅): 0.90-1.25 m (193 H), 1.55-1.9 m (126 H), 2.65-2.72 m (2 H), 2.77-2.90 m (4 H), 3.35-4.05 m (191 H), 4.42-4.49 m (1.7 H), 4.50-4.58 s (1 H), 4.59-4.62 s (0.23 H), 6.80-7.04 m (5 H), 7.38-7.42 t (0.25 H), 7.47-7.50 d (0.23 H).

Synthesis of DETA-PBO5k. DETA-PBO5k was synthesised according to the procedure described above starting from ^tBu-PBO5k-OH, a PBO that was synthesised using potassium *tert*-butoxide as an initiator^[10]. ¹H-NMR (600 MHz, pyridine-d₅): 0.86-1.15 m (211 H), 1.21-1.25 s (9 H), 1.51-1.94 m (141 H), 2.54-3.08 m (6 H), 3.37-4.07 m (213 H).

8.4.3 Exchange of oleic acid against the (supramolecular) polymer ligands

Four samples of polymer coated nanocrystals were produced: 1) 27 mg of DETA-PBO5k-Thy was dissolved in THF and mixed with 0.5 ml of the smaller nanocrystals in THF ($m_{\text{NPs}} = 20$ mg). After shaking for five minutes, ~45 ml of methanol were added to precipitate the nanocrystals. The nanocrystals were separated *via* centrifugation (one hour at 4000 rpm) and dissolved in 3 ml of toluene. 2) 25 mg of DETA-PBO5k-DAT was dissolved in THF and mixed with 2 ml of the larger nanocrystals in THF ($m_{\text{NPs}} = 40$ mg). Precipitation and separation were done as described for 1). 6 ml of toluene were used to disperse the nanocrystals. 3) 57 mg of DETA-PBO5k was dissolved in THF and mixed with 1 ml of the smaller nanocrystals in THF ($m_{\text{NPs}} = 40$ mg). Precipitation and separation were done as described for 1). 6 ml of toluene were used to disperse the nanocrystals. 4) 53 mg of DETA-PBO5k was dissolved in THF and mixed with 4 ml of the larger nanocrystals in THF ($m_{\text{NPs}} = 80$ mg). Precipitation and separation were done as described for 1). 12 ml of toluene were used to disperse the nanocrystals.

8.4.4 Polymer characterisation:

The molecular weights M_n were determined *via* ^1H NMR spectroscopy. NMR spectra were collected on a Bruker Avance III 600 MHz spectrometer equipped with a Prodigy cryoprobe. The samples were dissolved in pyridine- d_5 and measured at 295 K.

The molecular weights M_n and the molecular weight distributions M_w/M_n of the polymers were determined by size exclusion chromatography (SEC) using a SEC instrument consisting of Agilent 1260 Infinity pump (G1310B) and autosampler (G1329B), three Agilent PlusPore GPC columns with a continuous pore size distribution, a Shimadzu CTO-20AC column oven and a differential refractive index (Wyatt Optilab T-rEX) as well as a light scattering detector (Wyatt DAWN Heleos-2). The eluent was a mixture of THF and DMA (85 : 15 by volume) at a flow rate of 1 mL/min at 50 °C. The data were evaluated using the ASTRA6.1 software, determining the refractive index increment from the polymer peak and calculating the absolute molecular weights from the light scattering signal. For all samples containing amino groups (all samples besides the first two steps) it was necessary to acetylate them before doing the SEC measurements to avoid interactions between the amino groups and the SEC columns. In a typical experiment, 5 mg of polymer are dissolved in 100 μL of dichloromethane. 1.4 μL of triethylamine and 1.4 μL of acetyl chloride were added and shaken for ten minutes. Afterwards all compounds besides the polymer were removed under high vacuum conditions.

8.4.5 Transmission electron microscopy (TEM)

TEM experiments were performed using a Philips CM20 (200 kV) at the Ernst Ruska-Centre Jülich. The standard procedure for sample preparation includes partial drying of a diluted nanocrystal solution on a carbon-coated copper grid and the removal of excess solution. For the experiments with longer drying times, two procedures were performed: a) a drop of a strongly diluted solutions of the nanocrystals in THF was dried completely on the grid and b) strongly diluted solutions of the nanocrystals in toluene were filled into a small metal spoon containing the grid and dried completely taking advantage of the slower evaporation of toluene in contrast to THF. To determine the radii of the nanocrystals, the length of 200 nanocrystals on one image were measured with ImageJ. Average and standard deviation were calculated from these data.

8.4.6 Dynamic light scattering (DLS)

DLS measurements were performed on a Malvern Zetasizer Nano ZS instrument (4 mW He-Ne laser, $\lambda = 633$ nm, $\theta = 173^\circ$). The nanocrystal solutions were diluted with solvent (THF or toluene) until the solutions were only slightly colourful and measured in Quartz or glass cells.

8.4.7 Small-angle X-ray scattering (SAXS)

The scattering patterns were recorded with the SAXS system “Ganesha-Air” from (SAXSLAB/XENOCS). The X-ray source of this laboratory based system is a D2-MetalJet (Excillum) with a liquid metal anode operating at 70 kV and 3.57 mA with Ga- K_α radiation (wavelength $\lambda = 0.1314$ nm) providing a very brilliant and a very small beam (<100 μm). The beam is slightly focused with a focal length of 55 cm using a specially made X-ray optic (Xenocs) to provide a very small and intense beam at the sample position. Two pairs of scatterless slits are used to adjust the beam size depending on the detector distance. Samples were measured in borosilicate capillaries with an inner diameter of 2 mm. All data was radially averaged and normalized with respect to measurement time and background subtracted.

8.5 Acknowledgements

This work was supported by SPP 1681 (projects KR 3929/2-1 and KR 3929/2-2) of the German Research Foundation (DFG). The authors acknowledge Marlies Hintzen for SEC measurements and Michael Krinninger, Silke Nyholt and Dr Sabine Willboldt for NMR measurements.

8.6 Supporting Information

Table 8.4 Characterisation of synthesised polymers by NMR and SEC.

polymer	NMR		SEC		mass fraction of coupled chains [%]
	M_n [g/mol]	M_n [g/mol]	M_n [g/mol]	M_w/M_n	
Bn-PBO5k-OH	4760	4990		1.01	-
Bn-PBO5k-N ₃	4720	5190		1.02	-
Bn-PBO5k-NH ₂	4850	5340		1.02	2
Bn-PBO5k-Thy	4780	6090		1.02	0
Bn-PBO5k-DAT	4940	6040		1.01	1
HO-PBO5k-Thy	5600	5590		1.02	1
HO-PBO5k-DAT	5060	5920		1.03	6
DETA-PBO5k-Thy	5340	6180		1.01	24
DETA-PBO5k-DAT	5770	6300		1.01	6
DETA-PBO5k	5070	5550		1.02	26

8 Synthesis and Characterisation of Polymer Coated Supramolecular Magnetic Nanocrystals

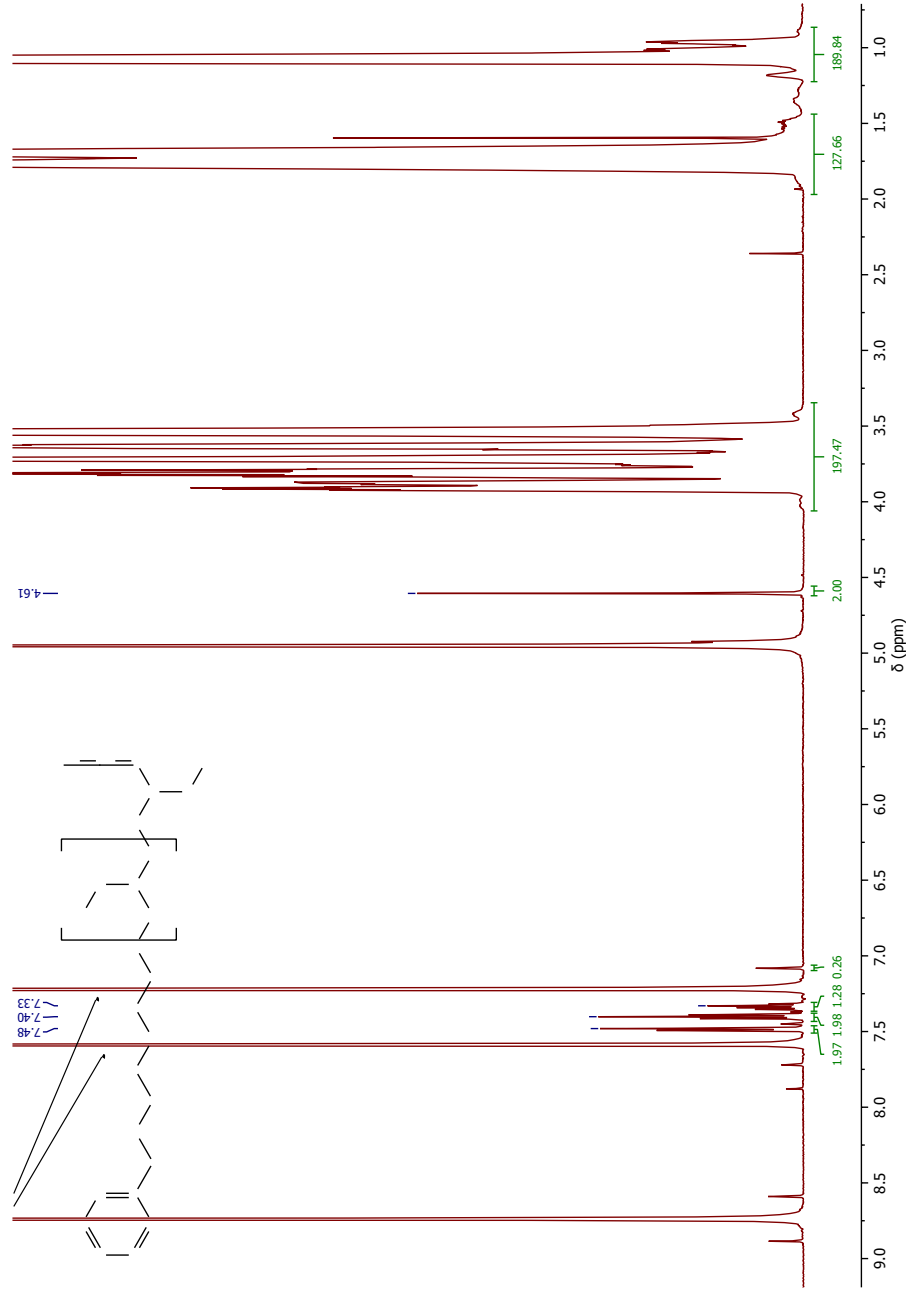


Figure 8.16 NMR spectrum of Bn-PBO5k-N₃ in pyridine-d₅.

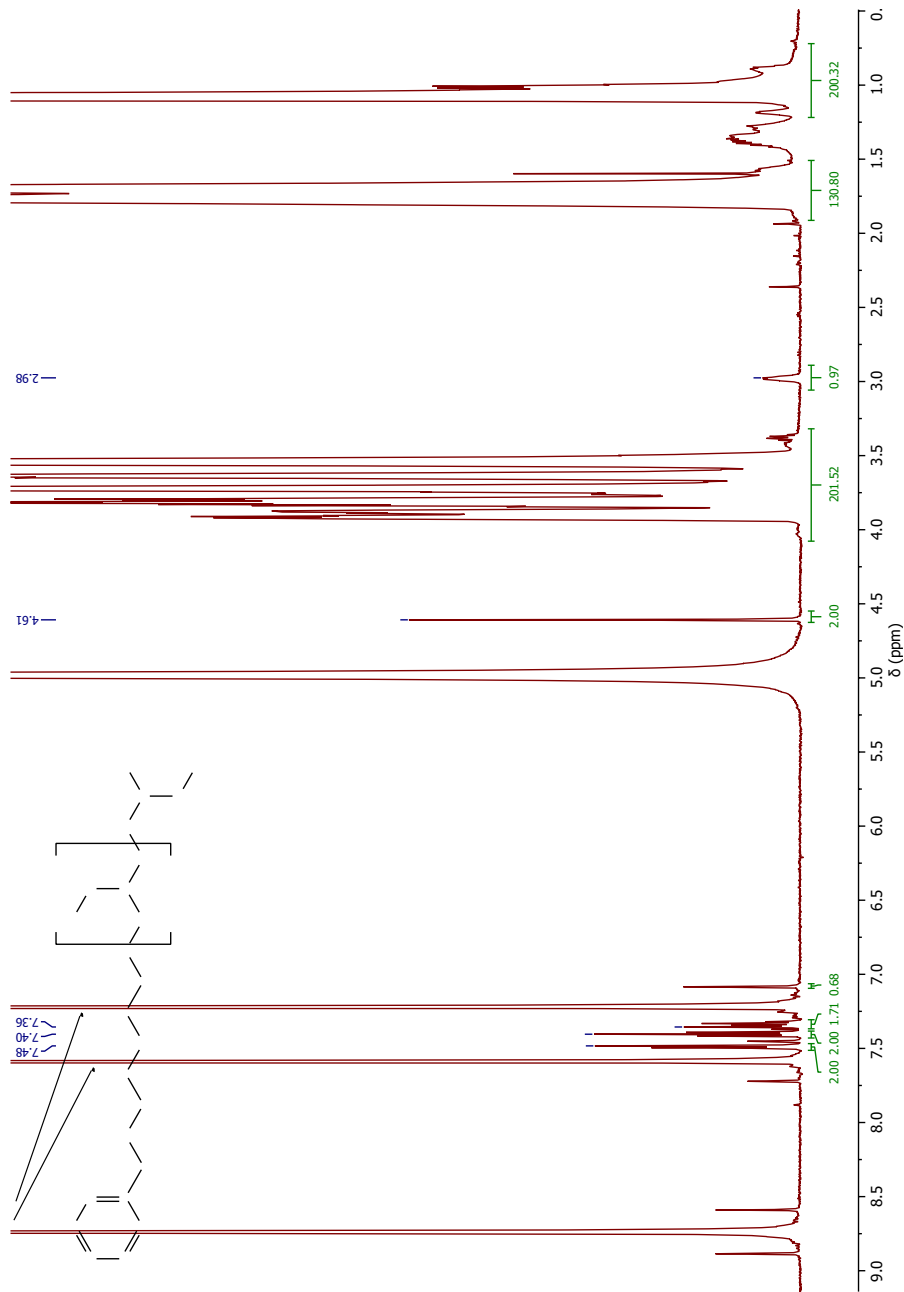


Figure 8.17 NMR spectrum of Bn-PBO5k-NH₂ in pyridine-*d*₅.

8 Synthesis and Characterisation of Polymer Coated Supramolecular Magnetic Nanocrystals

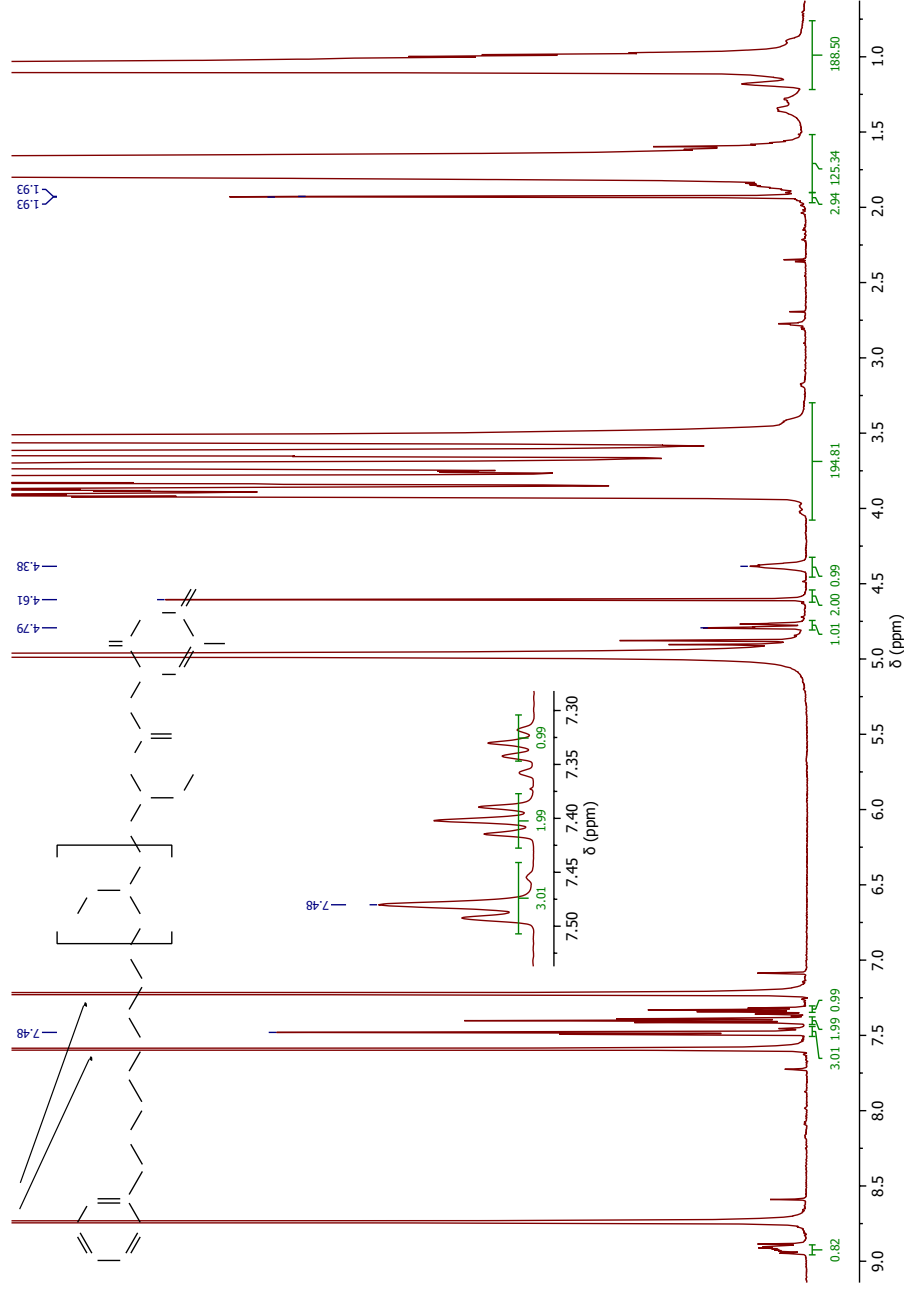


Figure 8.18 NMR spectrum of Bn-PBO5k-Thy in pyridine- d_5 .

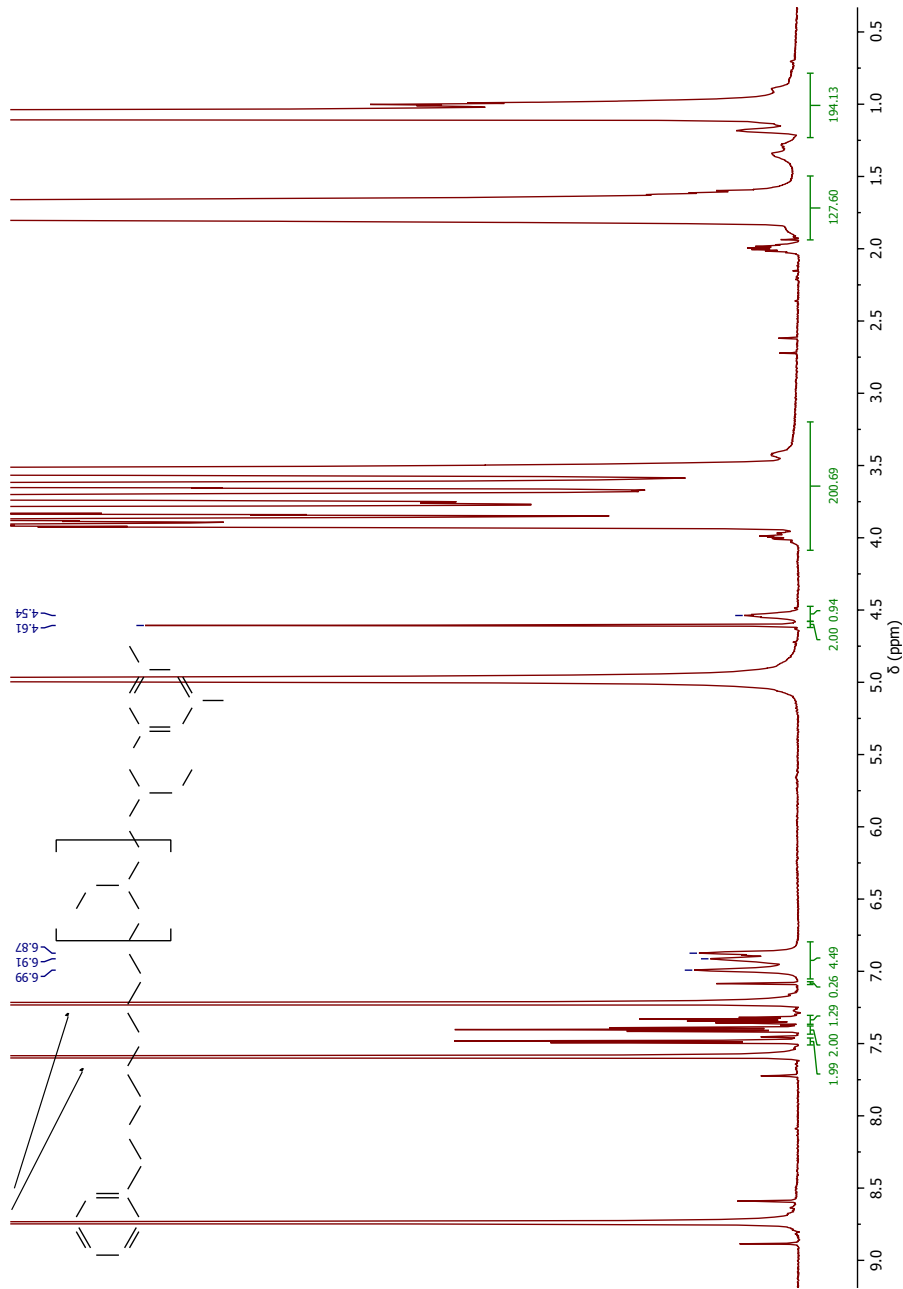


Figure 8.19 NMR spectrum of Bn-PBO5k-DAT in pyridine- d_5 .

8 Synthesis and Characterisation of Polymer Coated Supramolecular Magnetic Nanocrystals

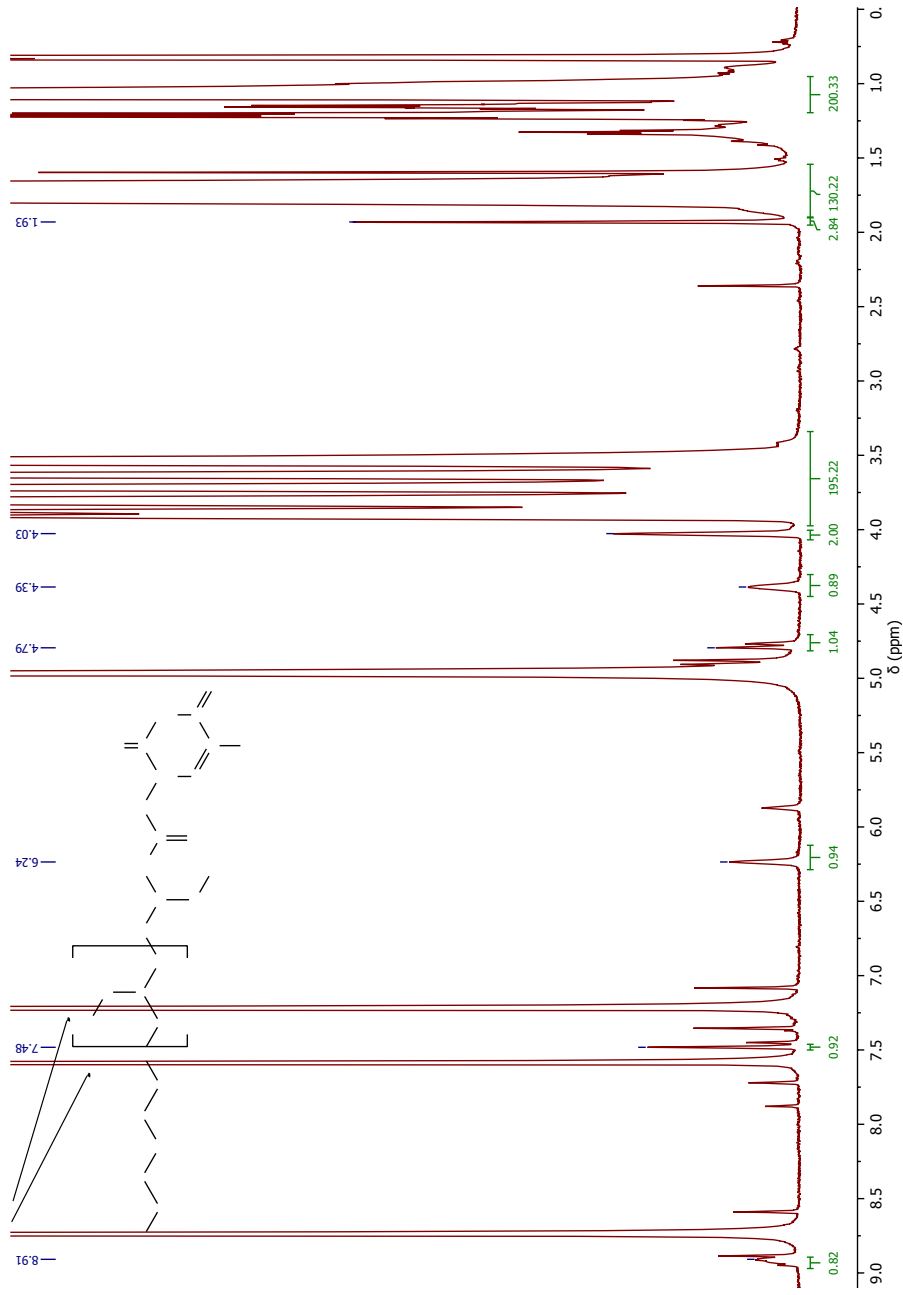


Figure 8.20 NMR spectrum of HO-PBOSk-Thy in pyridine- d_5 .

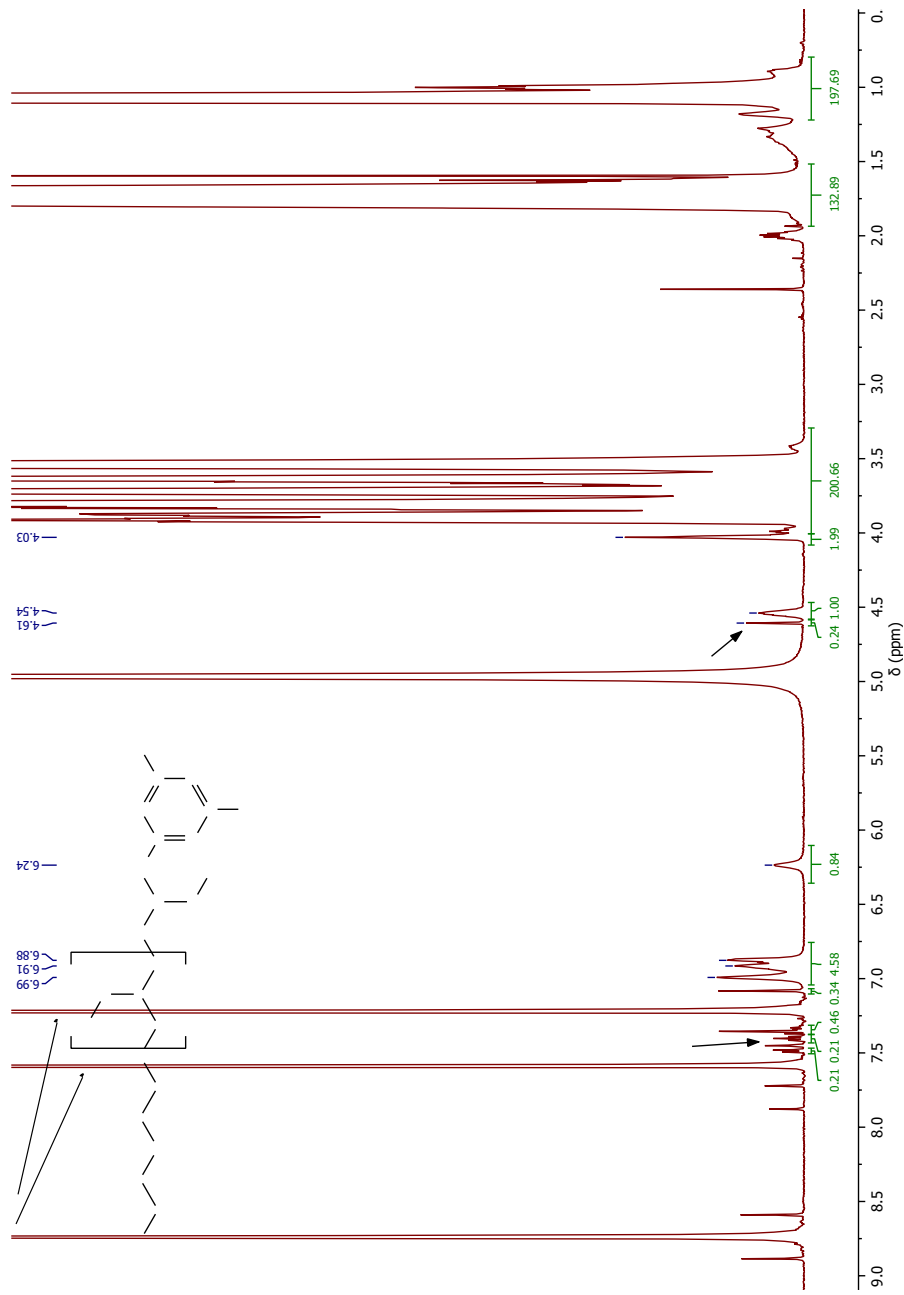


Figure 8.21 NMR spectrum of HO-PBO5k-DAT in pyridine- d_5 .

8 Synthesis and Characterisation of Polymer Coated Supramolecular Magnetic Nanocrystals

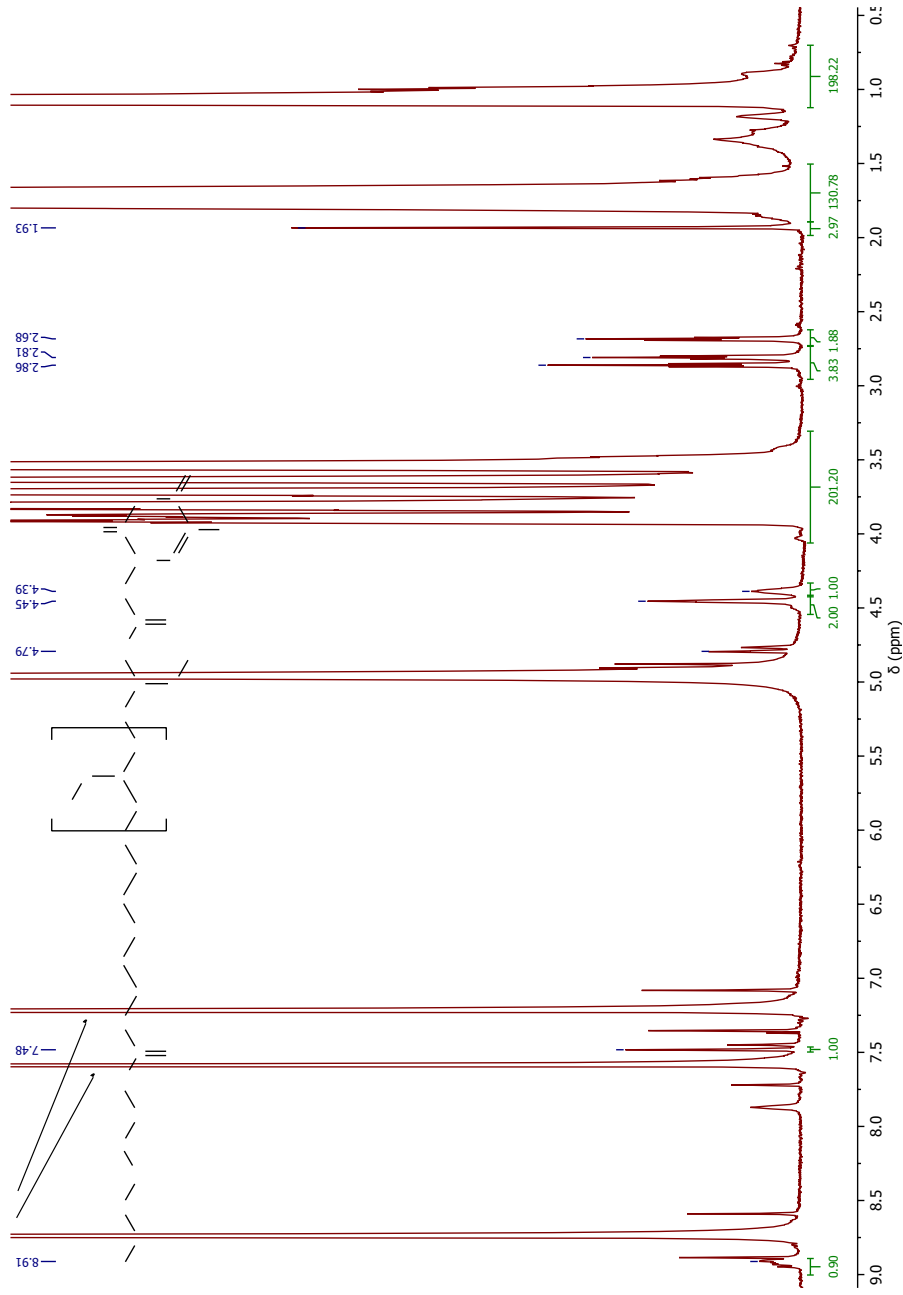


Figure 8.22 NMR spectrum of DETA-PBO5k-Thy in pyridine- d_5 .

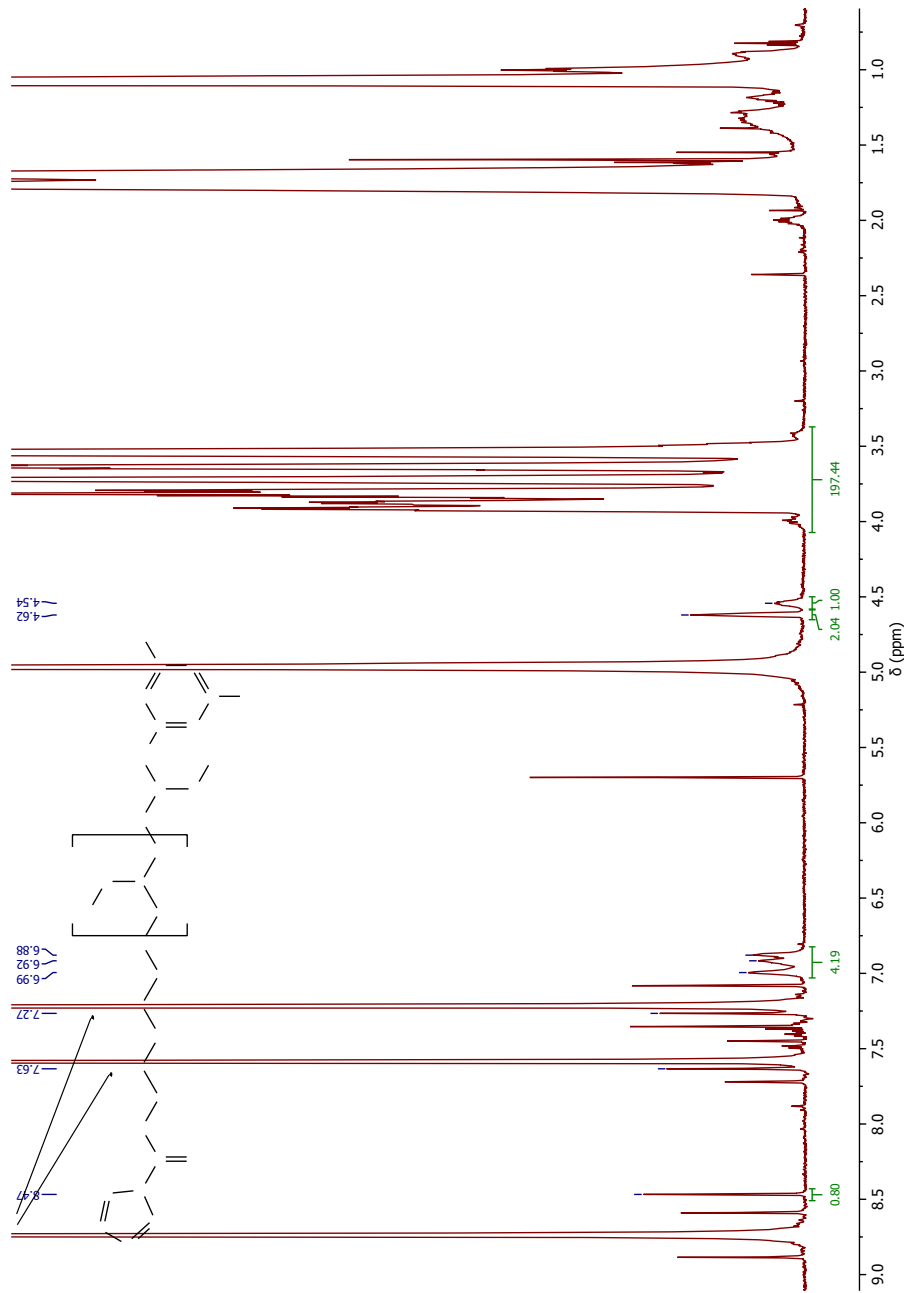


Figure 8.23 NMR spectrum of Acylimidazol-PBOSk-DAT in pyridine- d_5 .

8 Synthesis and Characterisation of Polymer Coated Supramolecular Magnetic Nanocrystals

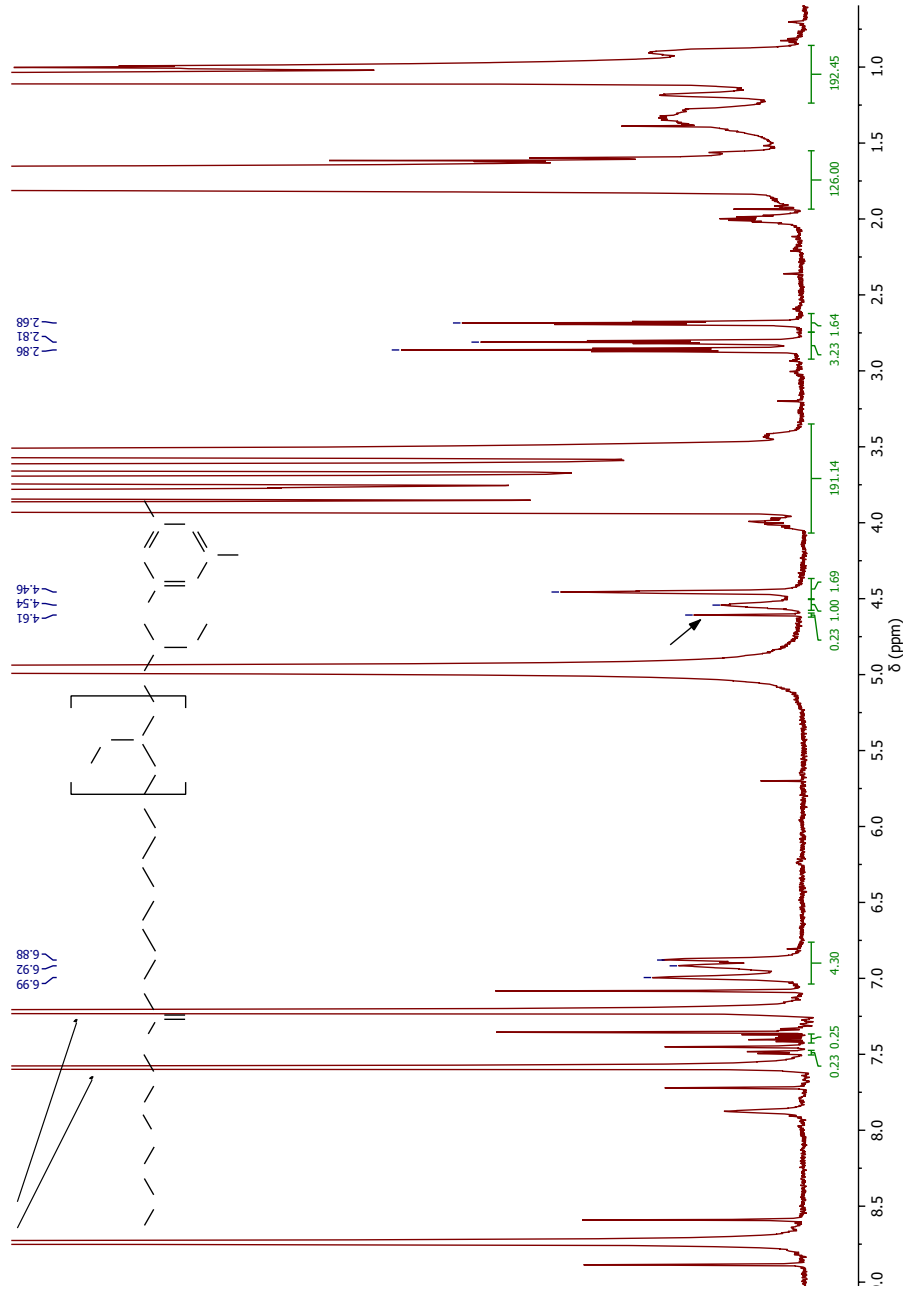


Figure 8.24 NMR spectrum of DETA-PBO5k-DAT in pyridine- d_5 .

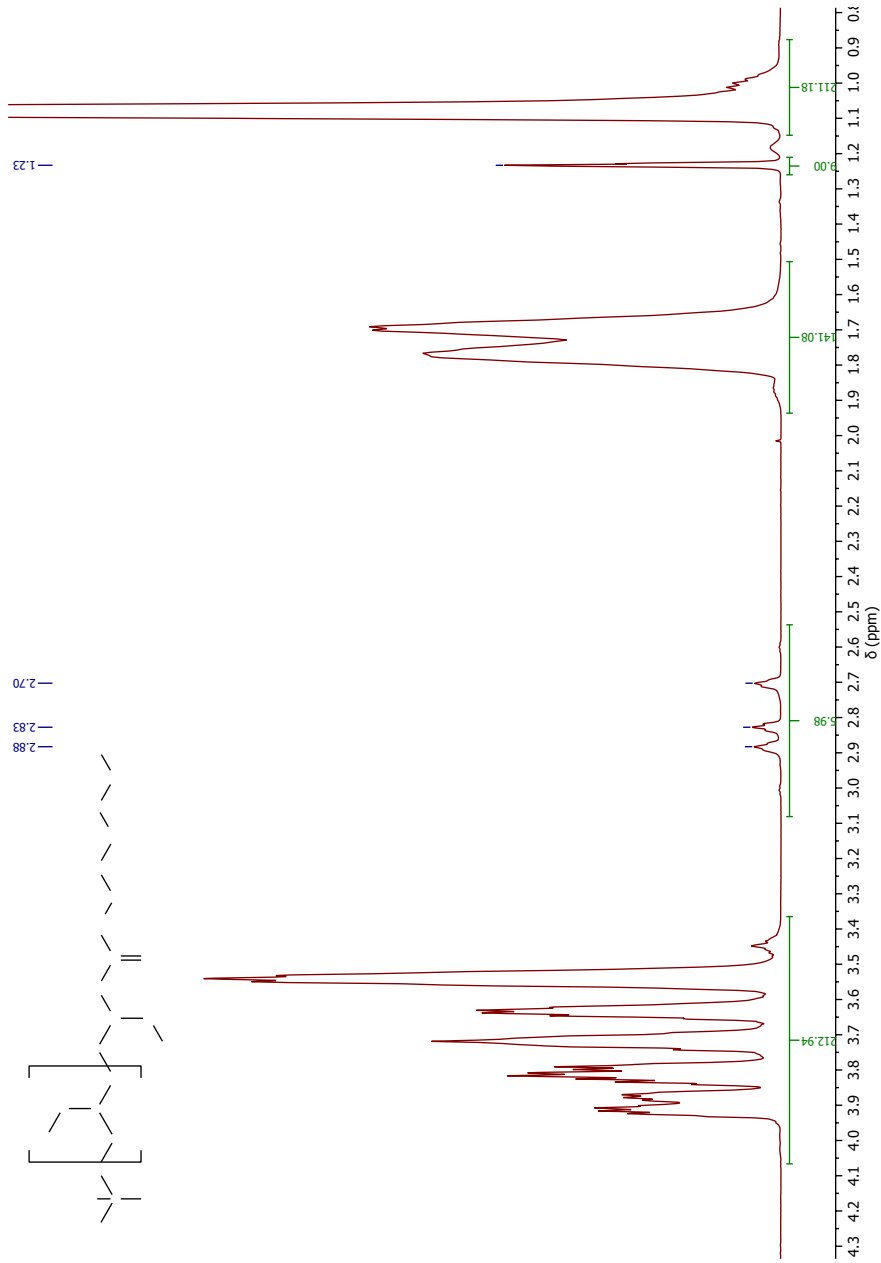


Figure 8.25 NMR spectrum of DETA-PBO5k in pyridine- d_5 .

8.7 References

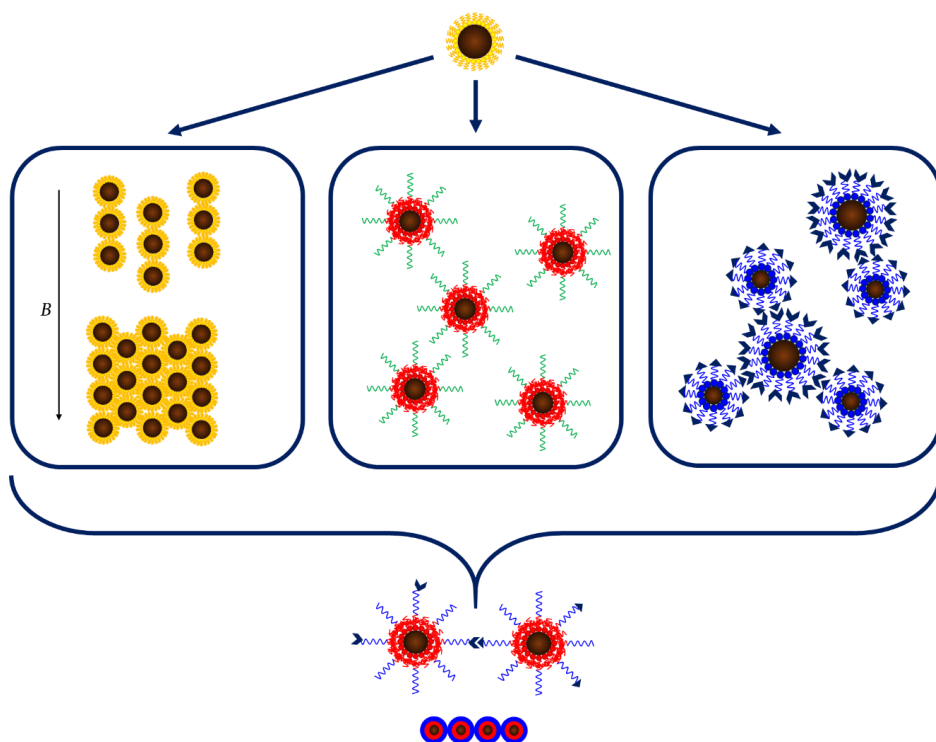
- [1] C. Hou, T. Huang, H. Wang, H. Yu, Q. Zhang, Y. Li, *Sci. Rep.* **2013**, *3*, 3138.
- [2] B. C. K. Tee, C. Wang, R. Allen, Z. Bao, *Nat. Nanotechnol.* **2012**, *7*, 825.
- [3] Y. Chen, W. Cheng, L. Teng, M. Jin, B. Lu, L. Ren, Y. Wang, *Macromol. Mater. Eng.* **2018**, *303*, 1700660.
- [4] G. Cai, J. Wang, K. Qian, J. Chen, S. Li, P. S. Lee, *Adv. Sci.* **2017**, *4*, 1600190.
- [5] J. Cao, C. Lu, J. Zhuang, M. Liu, X. Zhang, Y. Yu, Q. Tao, *Angew. Chemie Int. Ed.* **2017**, *56*, 8795.
- [6] X. Ran, Q. Qu, X. Qian, W. Xie, S. Li, L. Li, L. Yang, *Sensors Actuators B Chem.* **2018**, *257*, 362.
- [7] Y. Wang, T. Li, P. Ma, S. Zhang, H. Zhang, M. Du, Y. Xie, M. Chen, W. Dong, W. Ming, *ACS Nano* **2018**, *12*, 6228.
- [8] E. Polo, P. del Pino, A. Pardo, P. Taboada, B. Pelaz, in *Nanooncology. Nanomedicine and Nanotoxicology* (Ed: T.G. Gonçalves G.), Springer, Cham, **2018**, pp. 239–279.
- [9] J. Park, K. An, Y. Hwang, J.-G. Park, H.-J. Noh, J.-Y. Kim, J.-H. Park, N.-M. Hwang, T. Hyeon, *Nat. Mater.* **2004**, *3*, 891.
- [10] J. Allgaier, S. Willbold, T. Chang, *Macromolecules* **2007**, *40*, 518.
- [11] J. Lal, G. S. Trick, *J. Polym. Sci. Part A-1 Polym. Chem.* **1970**, *8*, 2339.
- [12] H. Asanuma, T. Ban, S. Gotoh, T. Hishiyama, M. Komiyama, *Macromolecules* **1998**, *31*, 371.
- [13] J. Allgaier, C. H. Hövelmann, Z. Wei, M. Staropoli, W. Pyckhout-Hintzen, N. Lühmann, S. Willbold, *RSC Adv.* **2016**, *6*, 6093.
- [14] A. K. Boal, F. Ilhan, J. E. DeRouchey, T. Thurn-Albrecht, T. P. Russell, V. M. Rotello, *Nature* **2000**, *404*, 746.
- [15] A. K. Boal, B. L. Frankamp, O. Uzun, M. T. Tuominen, V. M. Rotello, *Chem. Mater.* **2004**, *16*, 3252.
- [16] B. L. Frankamp, O. Uzun, F. Ilhan, A. K. Boal, V. M. Rotello, *J. Am. Chem. Soc.* **2002**, *124*, 892.
- [17] O. Uzun, B. L. Frankamp, A. Sanyal, V. M. Rotello, *Chem. Mater.* **2006**, *18*, 5404.

- [18] A. Olubummo, M. Schulz, R. Schöps, J. Kressler, W. H. Binder, *Langmuir* **2014**, *30*, 259.
- [19] S. Ehlert, S. M. Taheri, D. Pirner, M. Drechsler, H.-W. Schmidt, S. Förster, *ACS Nano* **2014**, *8*, 6114.
- [20] M. Stolzenburg, *Synthese Und Funktionalisierung von Biokompatiblen Homopolymeren Und Amphiphilen Blockcopolymeren Zur Potentiellen Anwendung Als Medikament-Transport-Systeme*, Görlich & Weiershäuser, Marburg, **2009**.
- [21] J. Köhler, H. Keul, M. Möller, *Chem. Commun.* **2011**, *47*, 8148.
- [22] R. Koll, L. S. Fruhner, H. Heller, J. Allgaier, W. Pyckhout-Hintzen, M. Kruteva, A. Feoktystov, R. Biehl, S. Förster, H. Weller, *Nanoscale* **2019**, *11*, 3847.
- [23] A. Burger, W. H. Shelver, *J. Med. Pharm. Chem.* **1961**, *4*, 225.
- [24] E. V. Matveeva, P. V. Petrovskii, I. L. Odinet, *Tetrahedron Lett.* **2008**, *49*, 6129.
- [25] H. Misaka, E. Tamura, K. Makiguchi, K. Kamoshida, R. Sakai, T. Satoh, T. Kakuchi, *J. Polym. Sci. Part A Polym. Chem.* **2012**, *50*, 1941.
- [26] M. Mosquet, Y. Chevalier, P. Le Perche, J.-P. Guicquero, *Macromol. Chem. Phys.* **1997**, *198*, 2457.
- [27] K. Davis, B. Qi, M. Witmer, C. L. Kitchens, B. A. Powell, O. T. Mefford, *Langmuir* **2014**, *30*, 10918.
- [28] E. Pösel, C. Schmidtke, S. Fischer, K. Peldschus, J. Salamon, H. Kloust, H. Tran, A. Pietsch, M. Heine, G. Adam, U. Schumacher, C. Wagener, S. Förster, H. Weller, *ACS Nano* **2012**, *6*, 3346.
- [29] J. Cortese, C. Soulié-Ziakovic, S. Tencé-Girault, L. Leibler, *J. Am. Chem. Soc.* **2012**, *134*, 3671.
- [30] T. Rawling, A. M. McDonagh, B. Tattam, M. Murray, *Tetrahedron* **2012**, *68*, 6065.
- [31] S. Y. Huang, A. D. Adams, *Therapeutic Compounds for Treating Dyslipidemic Conditions*, **2004**, US 2005/0113419 A1.
- [32] D. H. Ly, K. Gopalsamy Suresh, A. Manna, *Divalent Nucleobase Compounds and Uses Therefor*, **2014**.
- [33] T. Asaka, M. Kashimura, A. Matsuura, T. Sugimoto, T. Tanikawa, *Erythromycin A 11,12-Carbamate Derivatives*, **1999**, WO 99/21870.

- [34] J. Cortese, C. Soulié-Ziakovic, L. Leibler, *Polym. Chem.* **2014**, *5*, 116.
- [35] J. W. Anthony, R. A. Bideaux, K. W. Bladh, M. C. Nichols, Eds. , *Handbook of Mineralogy*, Mineralogical Society Of America, Chantilly, **2001**.
- [36] F. Herbst, W. H. Binder, *Polym. Chem.* **2013**, *4*, 3602.
- [37] M. Staropoli, A. Raba, C. H. Hövelmann, M. Krutyeva, J. Allgaier, M.-S. Appavou, U. Keiderling, F. J. Stadler, W. Pyckhout-Hintzen, A. Wischnewski, D. Richter, *Macromolecules* **2016**, *49*, 5692.
- [38] M. Krutyeva, A. R. Brás, W. Antonius, C. H. Hövelmann, A. S. Poulos, J. Allgaier, A. Radulescu, P. Lindner, W. Pyckhout-Hintzen, A. Wischnewski, D. Richter, *Macromolecules* **2015**, *48*, 8933.
- [39] K. Köse, *Process Biochem.* **2016**, *51*, 1644.
- [40] D. Grisley, Jr, E. Gluesenkamp, S. Heininger, *J. Org. Chem.* **1958**, *23*, 1802.

9 Conclusion and Outlook

Nanocomposites are an important class of functional materials. Their diverse properties enable various applications that already improve our everyday life. Responsive materials in which structure formation can be induced by external stimuli are particularly interesting.^[1] The aim of this thesis was to develop a pathway towards magneto-elastomeric nanocomposites with supramolecular activity. It is structured into three parts as presented in Scheme 9.1:



Scheme 9.1 Steps on the way towards magneto-elastomeric nanocomposites with supramolecular activity. From left to right: Self-assembly of surfactant stabilised nanoparticles in magnetic fields. Nanoparticles encapsulated in diblock copolymer with crosslinked inner polydiene shell. Supramolecular interactions between nanoparticles coated with supramolecular polymer ligands equipped with hydrogen bonding thymine and DAT groups.

The first part deals with the self-assembly of superparamagnetic iron oxide nanoparticles (maghemite, $\gamma\text{-Fe}_2\text{O}_3$) in magnetic fields. The diameter of the nanoparticles used in these experiments were about 20 nm and they were coated with oleic acid as stabilising

surfactant. Dispersions of these nanoparticles in deuterated toluene were studied in magnetic fields up to 3 T *via* SAXS and SANS. In a first experiment, it was shown that the nanoparticles form chain-like structures already at a low field of 0.1 T while higher field strengths led to the nanoparticles forming a body-centred tetragonal crystal lattice. Increasing the field strength forced the nanoparticles closer together due to field inhomogeneities. The results indicated that the oleic acid shell was compressed due to the nanoparticles approaching each other. A more detailed study with smaller field steps revealed the transition from chain-like structures to a dominating crystalline phase to take place at around 0.5 T. To continue the investigation concerning the influence of the field gradient on the self-assembly of magnetic nanoparticles, a new sample holder for SAS experiments based on a Halbach array is currently under construction, enabling the precise control of field strength and gradient.

The dispersion of nanoparticles in polymer matrices is the focus of the second part of this thesis. Using ligand exchange, the nanoparticles could be coated with a polydiene shell due to the polymers being equipped with a head group like DETA which coordinates to the surface of the nanoparticle. An encapsulation procedure was used relying on polydiene-PEO diblock copolymers which form micellar structures around the nanoparticles when transferred from organic medium to water.^[2] The inner polydiene shell could be crosslinked to form a network around the nanoparticle while the outer PEO shell allowed the dispersion of the nanoparticles in water or PEO matrix. Detailed investigation of this encapsulation procedure showed that 1,2-PB as the polydiene block proved to be slightly advantageous compared to 3,4-PI. The use of different crosslinking reactions documented the broad applicability of this method. While the use of only AIBN as a radical initiator resulted in insufficient stabilisation of the nanoparticles, the combination of AIBN and the crosslinker HDT improved the results significantly, leading to highly monodisperse nanocomposites. As alternatives, initiation via UV light and a redox reaction were carried out, yielding well-dispersed nanoparticles.^[3] The diblock copolymer shell was investigated via SANS and EA, indicating a rather compact structure. SAXS studies for each step of the encapsulation revealed the phase transfer into water to be the crucial step of this method, leading to a small amount of agglomeration of the nanoparticles. The stability of the nanoparticles dispersed in a PEO matrix depends on the molecular weight ratio of PEO block to matrix. If the ratio deviates strongly from one, a higher degree of agglomeration can be detected which is in agreement to results found in the literature.^[4] The encapsulation procedure could also be applied to create clusters of QDs.^[5] Different lengths and amounts of polymer ligand were used to vary the distance between the QDs inside the cluster, which correlated to their optical properties. The clusters were highly stable and showed interparticle distance dependent exciton dynamics. At low excitation powers, energy transfer was dominating while

at high powers, the generation and recombination of multiexcitons occurred. This encapsulation procedure produced well-dispersed nanoparticles with a high stability. Due to the high forces inside the polymer matrix induced by field gradients or shear forces a chemically fixated polymer shell is better suited than a physically grafted ligand. As could be seen from the experiments of oleic acid coated nanoparticles in magnetic fields, the shell is influenced which could lead to permanent aggregation of the nanoparticles in the sample. Therefore, a chemically fixated shell is a more reliable coating than physical grafting. However, this process is based on the use of PEO and a thick inner shell.

Therefore, an alternative process was developed in the third part of this thesis to take a further step forward towards elasticity and probe the interactions of supramolecularly functionalised nanoparticles by coating the nanoparticles with PBO. A challenging task was the synthesis of an α - ω -functionalised PBO ligand containing both anchor and supramolecular group. In the successful method a protected initiator allowed the synthesis of a PBO with a terminal hydroxy group. The supramolecular group Thy or DAT was coupled to this end of the polymer chain. After deprotection of the other chain end, a DETA head group was attached. These ligands were combined with differently sized nanoparticles to study the structure formation based on the Thy-DAT interactions between the nanoparticles *via* SAXS and TEM. While no interactions could be observed for the nanoparticles without supramolecular functionality, the samples containing the small Thy- and large DAT-functionalised nanoparticles showed cluster formation. Depending on the relation between these two types of nanoparticles, small clusters or large agglomerates were obtained.

In the scope of this work, the important proofs of concepts were achieved towards the realisation of the targeted material of magneto-elastomeric nanocomposites with supramolecular activity. In the last part, supramolecularly functionalised nanoparticles were obtained. With further experiments the interactions and properties could be tuned, for example by varying the content of supramolecular groups. The combination with a suitable matrix material to obtain nanocomposites needs to be investigated as well as the additional structure formation by external fields or mechanical forces. Thy could already be successfully attached to the PEO ends of the iron oxide nanoparticles encapsulated with the diblock copolymer. The resulting nanocomposites showed a dispersion state of the nanoparticles that was as good as for the non-supramolecular samples. First investigations of the magnetically induced structure formation of the nanocomposites obtained by this procedure have already been carried out and revealed a chain formation of the magnetic nanoparticles inside the polymer melt. These results are currently being analysed. In the next step, these results can be transferred to the PBO system

either by adapting the encapsulation procedure to a PB-*b*-PBO diblock or by synthesising an α , ω -functionalised PB-*b*-PBO diblock copolymer.

The final system of magneto-elastomeric nanocomposites with supramolecular activity as well as its components are of high relevance for future applications. Assemblies of magnetic nanoparticles are considered to be promising candidates for high density data storage.^[6] Iron oxide nanoparticles encapsulated in a water-soluble shell which is permanently attached are of high interest, especially for bioapplications like contrast agents.^[7] Adding supramolecular groups like Thy or DAT, which can bind to nucleotides, could be used for DNA extraction.^[8] Exchanging these groups for other functionalities would allow the connection to cancer cells or other targets inside the body. A possible application for the targeted smart composite material is dynamic sealing. Seals in motors or other devices with high friction often have to withstand huge forces in one particular direction. Stabilising the seal by fillers aligned to this direction enhances the properties of the material like its modulus and increases their lifetimes.^[9] Magnetic nanoparticles are highly promising for this purpose due to their diameter being in the range of the mesh size of the polymeric materials. Their ability to form chains in an external field allows their usage as anisotropic fillers. Fixating the chain-like structures by supramolecular hydrogen bonds increases the flexibility of these materials as the structures can be dispersed and recreated. In addition, the strength of the fixation can be influenced by the temperature.

9.1 References

- [1] M. A. Cohen Stuart, W. T. S. Huck, J. Genzer, M. Müller, C. Ober, M. Stamm, G. B. Sukhorukov, I. Szleifer, V. V. Tsukruk, M. Urban, F. Winnik, S. Zauscher, I. Luzinov, S. Minko, *Nat. Mater.* **2010**, *9*, 101.
- [2] A. Feld, R. Koll, L. S. Fruhner, M. Krutyeva, W. Pyckhout-Hintzen, C. Weiß, H. Heller, A. Weimer, C. Schmidtke, M. S. Appavou, E. Kentzinger, J. Allgaier, H. Weller, *ACS Nano* **2017**, *11*, 3767.
- [3] R. Koll, L. S. Fruhner, H. Heller, J. Allgaier, W. Pyckhout-Hintzen, M. Kruteva, A. Feoktystov, R. Biehl, S. Förster, H. Weller, *Nanoscale* **2019**, *11*, 3847.
- [4] C. Chevigny, F. Dalmas, E. Di Cola, D. Gigmes, D. Bertin, F. Boué, J. Jestin, *Macromolecules* **2011**, *44*, 122.
- [5] M. Rafipoor, R. Koll, J. Merkl, L. S. Fruhner, H. Weller, H. Lange, *Small* **2019**, *15*, 1803798.
- [6] A. K. Boal, in *Nanoparticles Build. Blocks Nanotechnol.* (Ed: V.M. Rotello), Springer Science+Business Media, New York, **2004**, pp. 1-27.
- [7] E. Pösel, C. Schmidtke, S. Fischer, K. Peldschus, J. Salamon, H. Kloust, H. Tran, A. Pietsch, M. Heine, G. Adam, U. Schumacher, C. Wagener, S. Förster, H. Weller, *ACS Nano* **2012**, *6*, 3346.
- [8] K. Köse, *Process Biochem.* **2016**, *51*, 1644.
- [9] Y. Li, J. Li, W. Li, H. Du, *Smart Mater. Struct.* **2014**, *23*, 123001.

Acknowledgements

This work was funded by the DFG as part of the SPPI681 for which I am very grateful.

Bringing my PhD to a successful finish would have been impossible without the continuous support of a huge amount of people.

First of all, I want to thank my direct supervisors, Dr Margarita Kruteva and Dr Jürgen Allgaier. Thank you for introducing me to small-angle scattering, polymer synthesis, functionalisation and characterisation, as well as teaching me how to present my work on conferences and what it takes to be a good scientist. Thank you for your trust in me and your helpfulness regarding whatever big or small problems encountered during this time.

I would like to express my sincerest gratitude towards Prof Dr Stephan Förster for his willingness to be my Doktorvater and his support for this project. I want to thank Prof Dr Walter Richtering for the co-supervision of this thesis.

Dr Ralf Biehl deserves a huge thank you for all his effort towards teaching me how to work with Python, for troubleshooting all problems with Python or Linux and for patiently answering all my questions regarding scattering, coding and everything else. Thank you, Ralf!

Another thank you belongs to Laura Kleebank for taking care of all the organisational and bureaucratic affairs as well as her general helpfulness concerning all sorts of issues.

I want to thank Dr Claas Hövelmann, Dr Andreas Raba and Dr Sascha Ehlert for assisting me in polymer or nanoparticle synthesis and characterisation. In addition, thank you to Dr Sascha Ehlert and Vanessa Leffler for TEM and TGA measurements, as well as all the information about nanocomposites.

Dr Wim Pyckhout-Hintzen helped me to understand a lot about scattering and polymers. Thank you for your willingness to help me with any question I came up with.

Marlies Hintzen and Dr Lutz Willner are thanked for SEC measurements and evaluations. Marlies, thank you for taking care of all the orders for needed chemicals and laboratory equipment!

I would like to thank the NMR team of Dr Sabine Willboldt (ZEA-3), especially Silke Nyholt and Michael Krinninger, for countless NMR measurements and the great cooperation towards urgent measurements.

Thank you to Dr Herbert Feilbach and his team as well as the workshop for designing and manufacturing custom-made sample holders or smaller construction units.

For great support during SANS beamtimes, I want to thank Dr Artem Feoktystov and Dr Lester Barnsley from the KWS-I team. Thank you for teaching me so much about neutron scattering and the handling of the instrument. I also want to express my gratitude to the MLZ for providing these beamtimes. I thank Dr Emmanuel Kentzinger, Dr Ulrich Rücker and Dr Martin Dulle for providing SAXS beamtime at GALAXI and Ganesha as well as their immediate support to solve any instrument-related issues. Thank you to all the instrument scientists for trusting me to work on my own with their instrument.

I would like to say thank you to my cooperation partners at the University of Hamburg, namely Dr Rieke Koll, Dr Hauke Heller, Dr Artur Feld, Dr Agnes Weimer and Prof Dr Horst Weller. First and foremost, a huge thank you belongs to Dr Rieke Koll for the great cooperation, for countless mails and phone calls to drive this project forward. I am equally grateful towards our cooperation partners at the University of Cologne in the group of Prof Dr Annette Schmidt. Thank you to Dr Melissa Hess for working with me on another project and to her and her colleagues for “adopting” me several times on workshops or conferences.

Thank you to Dr Walter Van Herck for his collaboration towards the SANS data evaluation with BornAgain!

I want to thank Dr Andreas Wischnewski for listening to any kind of questions and his advice in many situations.

My time at the JCNS-I was made enjoyable due to my great colleagues. I want to thank Vanessa Leffler, Dr Sascha Ehlert, Dr Barbara Gold, Nico König, Benjamin Reineke, Dr Charlotte Lorenz, Dr Matthias Amann and Joanna Michalska in no specific order and as representatives for many more for countless lunch and coffee breaks, traveling together on business trips and for a lot of after-work-activities. Thank you for being not only colleagues but friends. I would like to extend this thank you to the JCNS-2 colleagues for the good cooperation inside the JCNS.

Sascha, Vanessa, Nico and Babsi are thanked for sharing office 331 with me during my PhD time and for always being available for any support needed. Thank you for finding solutions with me for all sorts of questions or problems.

I am very thankful towards all the colleagues who proofread parts of this thesis: Dr Margarita Kruteva, Dr Jürgen Allgaier, Dr Ralf Biehl, Dr Sascha Ehlert, Vanessa Leffler and Prof Dr Stephan Förster, as well as my husband Dr Chris-Julian Fruhner.

Although geographically apart, another thank you belongs to my friends and former colleagues at Clausthal University of Technology. Especially to Maria, Heike, Lisa and Rebecca: thank you for the great time and for being friends that I could and can always rely on.

Last but definitely not least, I want to thank my family for supporting me all the way towards where I stand now. Especially to Chris, Pjakkur, Emily and Tom for being my emotional support and compensation from work. Chris, thank you for being there for me and believing in me all this time. Thank you to my parents for laying the foundations for me to become the person I am now, as well as their support during my whole life. Thank you as well to Lukas and Jessica, especially for providing bed and breakfast during beamtimes and other business trips to Garching. Similarly, thank you to Benjamin and Luise on the same account and sorry for scaring you by leaving the house in the middle of the night during beamtime. Thank you to my grandparents, my aunts and uncles, my cousins and my family in law for your support and simply for being a part of my life.

Curriculum Vitae

Personal Details

Name: Lisa Sarah Fruhner (née Müller)

Date of birth: 08.06.1990

Place of birth: Duisburg, Germany

Education

2016 - today PhD Physical Chemistry
Jülich Centre for Neutron Science (JCNS-1/ICS-1), Forschungszentrum
Jülich GmbH & Institute of Physical Chemistry, RWTH Aachen

2012 – 2016 Chemistry M.Sc.
Institute of Physical Chemistry, Technische Universität Clausthal

2009 – 2012 Chemistry B.Sc.
Institute of Physical Chemistry, Technische Universität Clausthal

2000 – 2009 Abitur
Liebfrauegymnasium Büren

Band / Volume 221

High spatial resolution and three-dimensional measurement of charge density and electric field in nanoscale materials using off-axis electron holography

F. Zheng (2020), xix, 182 pp

ISBN: 978-3-95806-476-8

Band / Volume 222

Tools and Workflows for Data & Metadata Management of Complex Experiments

Building a Foundation for Reproducible & Collaborative Analysis in the Neurosciences

J. Sprenger (2020), X, 168 pp

ISBN: 978-3-95806-478-2

Band / Volume 223

Engineering of *Corynebacterium glutamicum* towards increased malonyl-CoA availability for polyketide synthesis

L. Milke (2020), IX, 117 pp

ISBN: 978-3-95806-480-5

Band / Volume 224

Morphology and electronic structure of graphene supported by metallic thin films

M. Jugovac (2020), xi, 151 pp

ISBN: 978-3-95806-498-0

Band / Volume 225

Single-Molecule Characterization of FRET-based Biosensors and Development of Two-Color Coincidence Detection

H. Höfig (2020), XVIII, 160 pp

ISBN: 978-3-95806-502-4

Band / Volume 226

Development of a transcriptional biosensor and reengineering of its ligand specificity using fluorescence-activated cell sorting

L. K. Flachbart (2020), VIII, 102 pp

ISBN: 978-3-95806-515-4

Band / Volume 227

Strain and Tool Development for the Production of Industrially Relevant Compounds with *Corynebacterium glutamicum*

M. Kortmann (2021), II, 138 pp

ISBN: 978-3-95806-522-2

Band / Volume 228

**Complex magnetism of nanostructures on surfaces:
from orbital magnetism to spin excitations**

S. Brinker (2021), III, 208 pp
ISBN: 978-3-95806-525-3

Band / Volume 229

**High-throughput All-Electron Density Functional Theory Simulations
for a Data-driven Chemical Interpretation of X-ray Photoelectron Spectra**

J. Bröder (2021), viii, 169, XL pp
ISBN: 978-3-95806-526-0

Band / Volume 230

Molecular tools for genome engineering of *Corynebacterium glutamicum*

C. K. Sonntag (2021), VIII, 111 pp
ISBN: 978-3-95806-532-1

Band / Volume 231

**Interface Functionalization of Magnetic Oxide Fe₃O₄/SrTiO₃
Heterostructures**

M. H. A. Hamed (2021), xvii, 151 pp
ISBN: 978-3-95806-535-2

Band / Volume 232

Optically induced magnetization reversal in Co/Pt multilayers

Role of domain wall dynamics
U. Parlak (2021), ix, 162, XII pp
ISBN: 978-3-95806-536-9

Band / Volume 233

Application of Silicon Photomultipliers in Neutron Detectors

S. Kumar (2021), xxvi, 157 pp
ISBN: 978-3-95806-537-6

Band / Volume 234

**Towards Magneto-Elastomeric Nanocomposites with Supramolecular
Activity**

L. S. Fruhner (2021), XVI, 213 pp
ISBN: 978-3-95806-538-3

Weitere **Schriften des Verlags im Forschungszentrum Jülich** unter
<http://www.zb1.fz-juelich.de/verlagextern1/index.asp>

Schlüsseltechnologien / Key Technologies

Band / Volume 234

ISBN 978-3-95806-538-3